UNIVERSITY of the
WESTERN CAPE

CONSTRAINTS ON THE GENESIS OF THE SANDAMAP GOLD PROSPECT, NAMIBIA: FLUID INCLUSION, GEOCHRONOLOGY AND STABLE ISOTOPE STUDIES

By

Kamwi Rector Siseho

B.Sc. (UNAM), B.Sc. (Hons) (UJ), M.Sc. (UNAM)

A thesis submitted in fulfilment of the requirements for the degree of **Doctor of Philosophy in Applied Geology** in the Faculty of Natural Sciences, Department of Earth Sciences, The University of the Western Cape, South Africa

Supervisor: Dr Russell Bailie

Co-supervisor: Dr Lynnette Greyling

Date

April 2020

ABSTRACT

The Sandamap gold prospect is a metaturbidite shear zone-hosted gold mineralization located in the Neoproterozoic Damara Orogen 30 km northwest of the town of Usakos in Namibia with an estimated gold content of 240 000 t at 3.6 g/t up to 40 m below surface. This research project was aimed at constraining the age, crustal level of formation, pressure-temperature conditions during formation, sources of the mineralizing fluids, and by implication, the metal sources of the Sandamap gold mineralization. Fluid inclusion, geochronological and isotopic studies were carried out on quartz veins hosting the ore. The presence of kaolinite, alunite and jarosite suggest post-hydrothermal weathering of sulfides. Various sources of data from this study, giving rise to depths of entrapment of 4 to 14 km, temperature range of entrapment of fluids of 187 – 594 °C, stable isotope data ($\delta^{13}C$ and $\delta^{18}O$), δD values and a δD vs. $\delta^{18}O_{H2O}$ plot are all in favour of an orogenic gold deposit. Additionally, the dominant CO_2-rich and CH_4-rich fluids observed at Sandamap do not contradict this interpretation. The calculated depth of entrapment of mineralization covers the lower portion of the epizonal zone to the upper portion of the hypozonal zone of gold deposits. The Sandamap mineralization's δD values of -35‰ to -49‰ fall within the range of most published data for typical orogenic gold deposits which varies from -20 to -80‰. Moreover, the calculated $\delta^{18}O_{water}$ values of the ore-fluids (+6.6 to +11.3‰) of the higher temperature aqueous group from the Sandamap mineralization fall within the range observed in typical orogenic gold deposits found in Phanerozoic terrains (+7 to +13‰). The schist hosting the mineralized shear zone with a gold content of 0.05 ppm Au or its higher grade equivalent at depth, is a possible gold source candidate. Two mechanisms of deposition were possibly at play: (i) the cooling below 500 °C and possible sulfidation (resulting from fluid-rock interaction), lowered the solubility of pyrite causing S_3^- and $Au(HS)S_3^-$ (possible main Au carriers) to breakdown resulting in decreased Au solubility and its subsequent deposition and (ii) the elevated amount of CO_2 (e.g. trench 14 where CO_2-rich fluid inclusions are dominant) led to a sharp decrease in the $Au(HS)_2^-$ and $Au(HS)S_3^-$ concentrations, causing decreased Au solubility and its subsequent deposition. The age of mineralization obtained from $^{40}Ar/^{39}Ar$ dating of the muscovite associated with the ore-hosting quartz veins is placed at 472 ± 3 Ma. The mineralization is younger than the shear zone, which acted as a conduit for ore-fluid migration and it has no age relationship with proximal plutonic bodies. The mineralization is younger than the foliated granite (FG), which exhibits a metamorphic fabric in the form of mineral segregation, but older than the non-foliated granite (GT) which hosts a mineralized xenolith.

DECLARATIONS

I, the undersigned, hereby declare that this thesis entitled **Constraints on the genesis of the Sandamap gold prospect, Namibia: fluid inclusion, geochronology and stable isotope studies**, is my own original work, that this work, or part thereof has not been submitted for a degree in any other institution of higher education, and that all sources I used or quoted are indicated and acknowledged as complete references.

Kamwi Rector Siseho **Date**……23/04/2020……..

……
Signature

DEDICATION

I am dedicating this research work to my late mother in remembrance and appreciation of her consistent reminder of the importance of education. “Cikolo kacizaniswa” was her phrase whenever she noticed that one was taking education lightly. It would literally mean “Don’t play with education”, an expression of disapproval to one who do not seem to take education seriously. The second dedication of this research work goes to my young boy Kamwi Ethan Siseho for the company during writing and for inevitable breaks amidst writing and to my daughters Aimee Namasiku Siseho and Kamila Maria Siseho.

ACKNOWLEDGEMENTS

Firstly my gratitude of the highest order goes to my main supervisor Dr Russell Bailie for his critical assessments and his great responsive supervisory skills; I really had a ball working with you and a big thank you. My second vote of thanks and gratitude goes to my co-supervisor Dr Lynnette Greyling (University of Cape Town - UCT) for her critical assessments on the fluid inclusion chapter, her words of encouragement and her openness to give credit where credit was due, greatly appreciated. I must mention my deep sense of appreciation for Professor Chris Harris (UCT) for his timely turnaround time for every sample submitted to his lab (the world would be very efficient if all operated like him). Further, I am grateful to Professor Jan Kramers (University of Johannesburg – UJ) for $^{40}Ar/^{39}Ar$ isotope dating analysis. I am also very grateful to Dr Rudolf Erasmus (University of the Witwatersrand) for Raman spectroscopy analysis and the notes. I also wish to express my gratitude to the Central Analytical Facilities (CAF) Stellenbosch University and, in particular, Mrs Mareli Grobbelaar and Dr Laura Bracciali. I am also very grateful to Mr Lisias Negonga for his input on fluid inclusion calculations. A vote of appreciation also goes to Ms Cristofina Kanyama for her encouragement and the support during the long but adventurous journey. Lastly my warmest sincere and wholehearted gratitude goes to the German Academic Exchange Service (DAAD) for the scholarship, without which this project would not have been completed and many thanks to Mrs Martina Williams, the Scholarship Administrator at TUCSIN. I am equally and greatly thankful to Mr Aphary Muyongo for the role he played and for believing in the project, “thanks man it’s greatly appreciated”.

TABLE OF CONTENTS

LIST OF FIGURES

LIST OF TABLES

APPENDICES

LIST OF ACRONYMS

AFOT:	Autseib Fault and Otjohorongo Thrust
Aq-type:	Aqueous-rich fluid inclusion type
AqC-type:	Aqueous-carbon dioxide-rich fluid inclusion type
Ar:	Argon
Au:	Gold
BABI:	Basaltic Achondrite Best Initial
CAF:	Central Analytical Facility (Stellenbosch University, SA)
CH_4:	Methane
CL:	Cathodoluminescence
C-type:	Carbon dioxide-rich fluid inclusion type
CKZ:	Central Kaoko Zone
CO_2:	Carbon dioxide
CZ:	Central Zone
$D_{1, 2, 3, 4}$:	Deformation event 1, 2, 3, 4
DMS:	Degrees, minutes, seconds
EKZ:	Eastern Kaoko Zone
FI:	Fluid inclusion
GRL:	Gomab River Line

IA:	Alkalinity index
IT:	Temperature index
L:	Liquid
Ma:	Million years ago
MN-type:	Methane-nitrogen-rich fluid inclusion type
MNC-type:	Methane-nitrogen-carbon dioxide-rich fluid inclusion type
MSWD:	mean square weighted deviation
nCZ:	northern Central Zone
NMZ:	Northern Margin Zone
NP:	Northern Platform
NZ:	Northern Zone
OL:	Okahandja Lineament
OML:	Omaruru Lineament
PDB:	Pee Dee Belemnite
Pb:	Lead
sCZ:	Southern Central Zone
SF SC ICP-MS:	Single-collector sector-field Inductively Coupled Plasma Mass Spectrometry
SuF:	Summas Fault
SF:	Southern Foreland (Front)
SKZ:	Southern Kaoko Zone
SMOW:	Standard Mean Ocean Water
SMZ:	Southern Margin Zone
SZ:	Southern Zone
TBE:	Tetrabromoethane
T_d:	Decrepitation temperature
T_e:	Eutectic temperature
T_f:	Final melting temperature
T_h:	Total homogenization temperature
$T_{h(CO2)}$:	Carbon dioxide homogenization temperature
T_i:	Initial melting temperature
$T_{m(Cl)}$:	Clathrate melting temperature
$T_{m(CO2)}$:	Carbon dioxide melting temperature
$T_{m(ice)}$:	Ice melting temperature
T_t:	Temperature of entrapment
UCT:	University of Cape Town
UJ:	University of Johannesburg
U:	Uranium
UWC:	University of the Western Cape
V:	Vapour
WKZ:	Western Kaoko Zone
WT:	Waterberg Thrust

LIST OF SYMBOLS

δD:	delta-Deuterium
$\delta^{13}C$:	delta-C-13
$\delta^{16}O$:	delta-O-16
$\delta^{18}O$:	delta-O-18
°C:	degree Celsius
µm:	micro meter
%:	percent (meaning parts per hundred)
‰:	per mil (meaning parts per thousand)

CHAPTER 1

INTRODUCTION

1.1 BACKGROUND

The Sandamap gold prospect is a metaturbidite-hosted gold mineralization confined within a shear zone located in the Neoproterozoic Damara Orogenic belt in central Namibia, north of the collision zone between the Congo and Kalahari cratons. The deposit was estimated to hold 240,000t grading at 3.6 g/t gold to a depth of 40m (Steven, 1999). The prospect is located 30 km northwest of the town of Usakos in Namibia, on the farm Sandamap Noord 115. The 3.4 km long mineralization zone is open along strike and has only been tested to a depth of 40 m (Steven, 1999). The mineralization is hosted by sheared biotite-sillimanite-K-feldspar schist of the upper Kuiseb Formation which forms part of a highly deformed Neoproterozoic deep marine sedimentary succession consisting of metagreywackes and graphitic metaturbidites. The gold mineralization is contained in quartz veins, gossan stringers and mylonite rocks.

The deposit is in the NE-trending, Damara orogenic belt which has been divided into several different zones on the basis of stratigraphy, metamorphic grade, structure, geochronology, plutonic rocks and aeromagnetic expression (Miller, 1983, 1998). The zones are separated by tectonic lineaments and these are, from north to south: the Northern Platform (NP), Northern Margin Zone (NMZ), Northern Zone (NZ), Central Zone (CZ), Southern Zone (SZ), Southern Margin Zone (SMZ) and the Southern Foreland (Fig.1.1). The Central Zone is divided into northern (nCZ) and southern (sCZ) zones. The Okahandja Lineament zone (OLZ) is routinely regarded as part of the SZ (Miller, 2008). The Sandamap prospect is located in the nCZ, to the immediate north of the Omaruru lineament and 10 km east of the Welwitschia lineament (Fig. 1.1). The regional geology of the central zone of the Damara belt, where the prospect is located, is characterised by mainly marble, schist and quartzite of the Swakop and Nosib groups of the Damara Supergroup (Fig. 1.2).

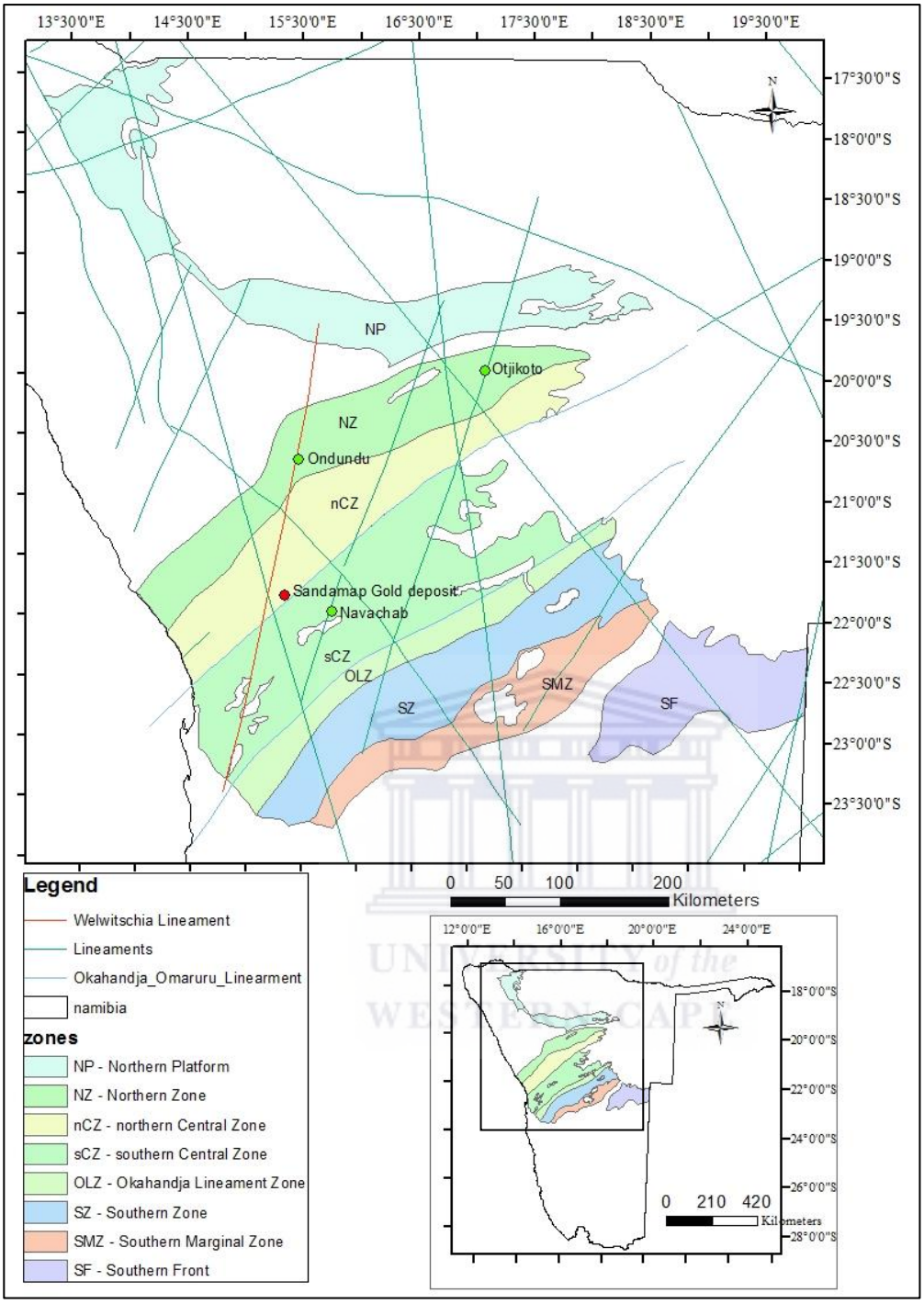

Fig. 1.1. Tectonic zones of the Damara orogenic belt, structural lineaments, the location of the Sandamap gold prospect and those of other gold deposits within the Damara belt (Navachab, Ondundu and Otjikoto) (Shape files are from the Geological Survey of Namibia).

The prospect was initially explored and trenched by Solar Exploration (Pty.) Ltd. in the 1930s and the first written account of the deposit was given by Frommurze *et al.* (1942). In spite of that the gold potential was only realized from 1988 (Steven, 1988, 1991, 1993; Petzel, 1990; Steven *et al*., 1993, 1994). From 1988 the prospect was investigated by Gold Fields Namibia and Genmin before being acquired by Namibia Mineral Development Company (NMDC) in

1992. In 1993 NMDC signed an agreement with Australian-financed Namaust Exploration (Pty.) to undertake drilling and metallurgical work. The target of the agreement was to assess the viability of a shallow open-cast operation on the oxidized zone.

A total of 8 holes were drilled to a vertical depth of 40m on three anomalies. At trench 15, the deposit was estimated to contain 45 000t at 3.6 g/t gold to a depth of 40 m (Steven, 1999). Bottle roll and column leach tests were carried out on core from 4 drill holes. Results indicated that a recovery of 55 – 65% is easily achievable with simple cyanide leaching if ore is crushed to a size of between 4 and 11 mm (Steven, 1999). Even though the metallurgical results were encouraging, the delineated resource at the time was found to be too small to justify gold extraction (Steven, 1999). Regarding potential for future mining, the mineralization remains open along strike and remains untested below 40m.

Limited published work done on the genesis of the Sandamap prospect to date (Pirajno et al., 1993; Steven, 1999) has not resolved uncertainties pertaining to the deposit's origin. The overall aim of this research project was to assess the potential of the deposit at depth by carrying out a systematic examination of the genesis of the deposit. The study encompassed fluid inclusion, geochronological and isotopic studies on the ore. Results from this study indicated the source of the mineralizing fluids and, an inference pointing towards a metamorphic origin as opposed to magmatic, would be indicative of an orogenic gold deposit type whose mineralization commonly extends to great depths (Groves et al., 1998).

Steven (1999) reported on ^{18}O and ^{13}C isotopic values (from both calcite and graphite, respectively) of a sample from the Sandamap prospect. The value from calcite was found to fall within a range observed in the Yilgarn Block and the Abitibi Belt gold deposits, which are typical orogenic deposits, and the ^{18}O isotopic value was found to fall within a range for marine carbonates, possibly derived from fragments of the Karibib Formation marble. Pirajno et al. (1993) analysed two samples from the farm Sandamap Noord 115 for ^{34}S isotopic values; one value was from galena hosted in vein quartz cutting the Kuiseb schist, and the other was from pyrite in a pocket within a pegmatite dyke cutting marble rocks of the Kuiseb Formation. The results thereof were found to be related to intracratonic rifting in a convergent tectonic setting similar to those of Mississippi Valley Type (MVT) mineralization or possibly of skarn affinity. The locality of the sampling positions in relation to the locality

of the Sandamap gold prospect could, however, not be established and, as such, their proximity to the prospect under investigation could not be determined.

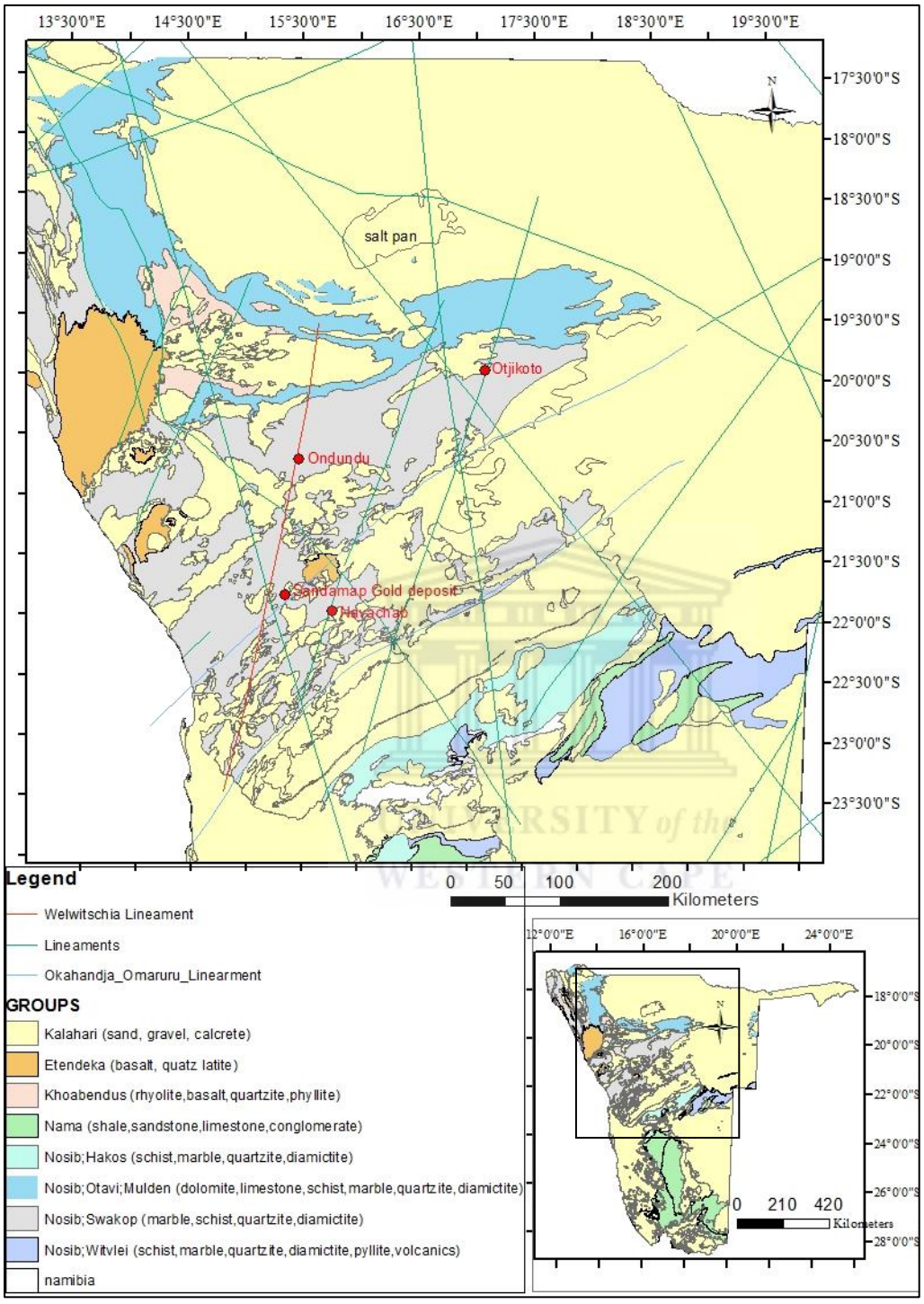

Fig. 1.2. Location of the Sandamap prospect, structural lineaments and regional geology of the Damara orogenic belt (Shape files are from the Geological Survey of Namibia).

The tectonic evolution of the Damara belt, as given in Miller (2008), is as follows: the formation of the Damara belt started with initial intracontinental rifting between 900 and 800

Ma, a period which also forms a portion of the time which marks the breakup of the supercontinent of Rodinia (Li et al., 2008). Rifting ended between 766 and 752 Ma, with initiation of the transition from rifting to spreading between 759 to 746 Ma. This was followed by the formation of deep seas (Outjo and Khomas seas) and the concurrent sedimentation in these seas. Spreading ended roughly 600 Ma. Subduction of the Kalahari craton beneath the Congo Craton was initiated between 600 and 580 Ma. Continental collision in the Damara Belt, final closure of the Khomas Sea and the age of final collision of the Kalahari and Congo Cratons is placed at 542 Ma, an age which falls within the formation period (600–530 Ma) of the supercontinent of Gondwana (Li et al., 2008).

The period from 542 to 535 Ma is characterised by erosional activity of the elevated areas of the Damara belt and deposition of the debris in southern distal areas (Miller, 2008). The period between 535 and 495 Ma is characterised by regional metamorphism, deformation, extensive partial melting and generation of anatectic granites as well as the emplacement of various granites and pegmatites in some parts of the Damara belt (Miller, 2008). This was followed by the detachment of the subducting slab and full development of a back-arc region of the nCZ (Fig. 1.3), D_3, D_4 deformation, diapiric rise of hot marble domes and extensive granite emplacement in the nCZ that took place between 490 to 460 Ma (Miller, 2008).

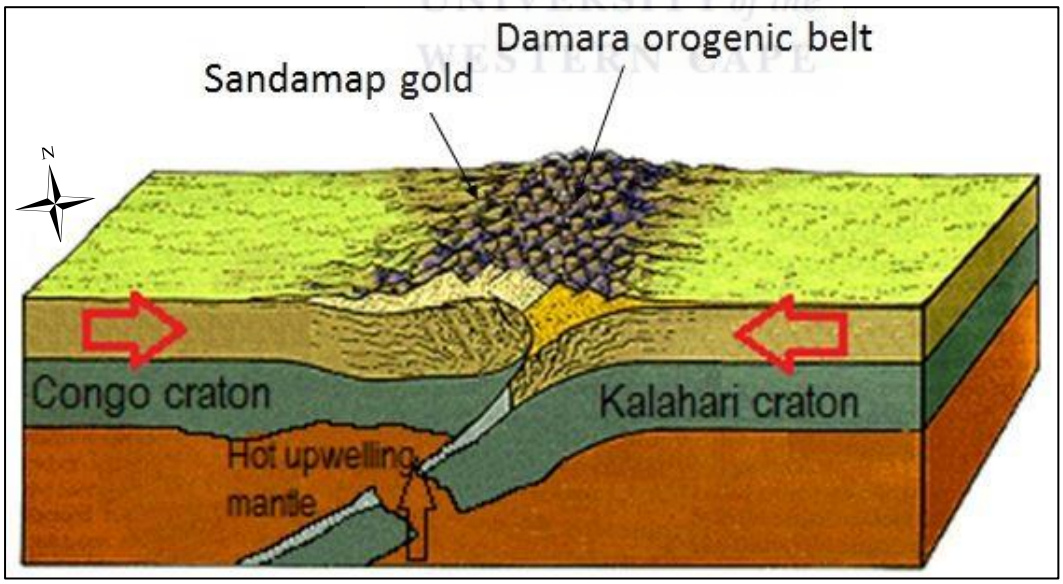

Fig. 1.3. The back arc of the nCZ became fully developed following the detachment of the subducting slab, the subsequent rise of hot mantle and thinning of the crust (modified after "Convergent Plate Boundaries," 2018).

The development of the Sandamap shear zone and emplacement of mineralization are also believed to have taken place during this period. Formation of the Sandamap shear zone, which acted as a zone of weakness through which mineralizing fluids circulated, is either related to the D_3 and D_4 deformations (Steven, 1993), or the sinistral rotation of the dolomite dome in its adjacency as it rose to the surface. Mylonitic shear zones are common in the margins of the dolomite domes of the nCZ (Miller, 2008). Steven (1993) states that the Au fluids were either expelled from the stanniferous pegmatites (with a Rb-Sr whole rock age of 468 ±14 Ma) or mobilised from metasediments. Steven et al. (1994) reported Pb-Pb model ages of galena from the mineralized zone of 469 – 464 Ma.

1.2 LITERATURE REVIEW

1.2.1 OROGENIC GOLD DEPOSITS

One of the consistent characteristics of orogenic gold deposits is that they are associated with deformed metamorphic terranes of all ages (Groves et al., 1998; Goldfarb and Groves, 2015) (Fig. 1.4). Many deposits that occur in Archaean greenstone belts and in Phanerozoic metamorphic belts have been observed to have a strong association with greenschist facies rocks. However, a notable number of deposits have been observed in higher and lower metamorphic grade rocks around the world (Groves et al., 1998).

Orogenic deposits may be syn- and post-orogenic in terms of age. The deposits are subdivided according to their depth of formation (Fig. 1.5): epizonal deposits (forming at depths of <6 km from the surface and at temperatures of 150–300°C), mesozonal deposits (forming at depths of 6–12 km and at temperatures of 300–475°C), and hypozonal deposits, forming below 12 km at temperatures above 475°C (Groves et al., 1998).

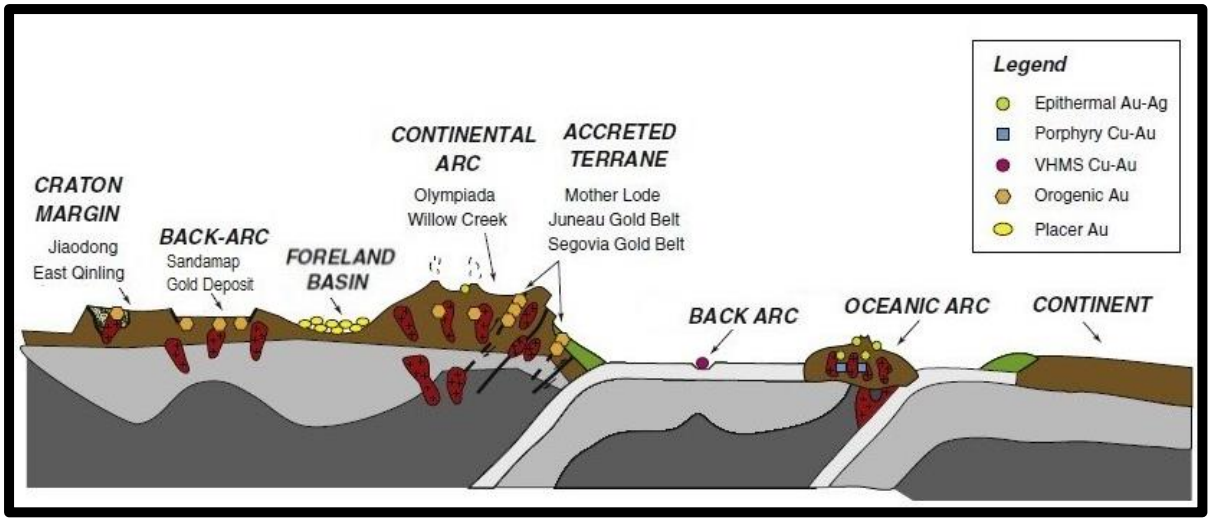

Fig. 1.4. Tectonic setting of orogenic and other gold deposit types. The orogenic gold deposits may be located in metamorphosed fore-arc and back-arc regions (the latter as is the case for the **Sandamap prospect**) of active continental margins, as well as along the sheared margins to continental arc batholiths (after Goldfarb and Groves, 2015).

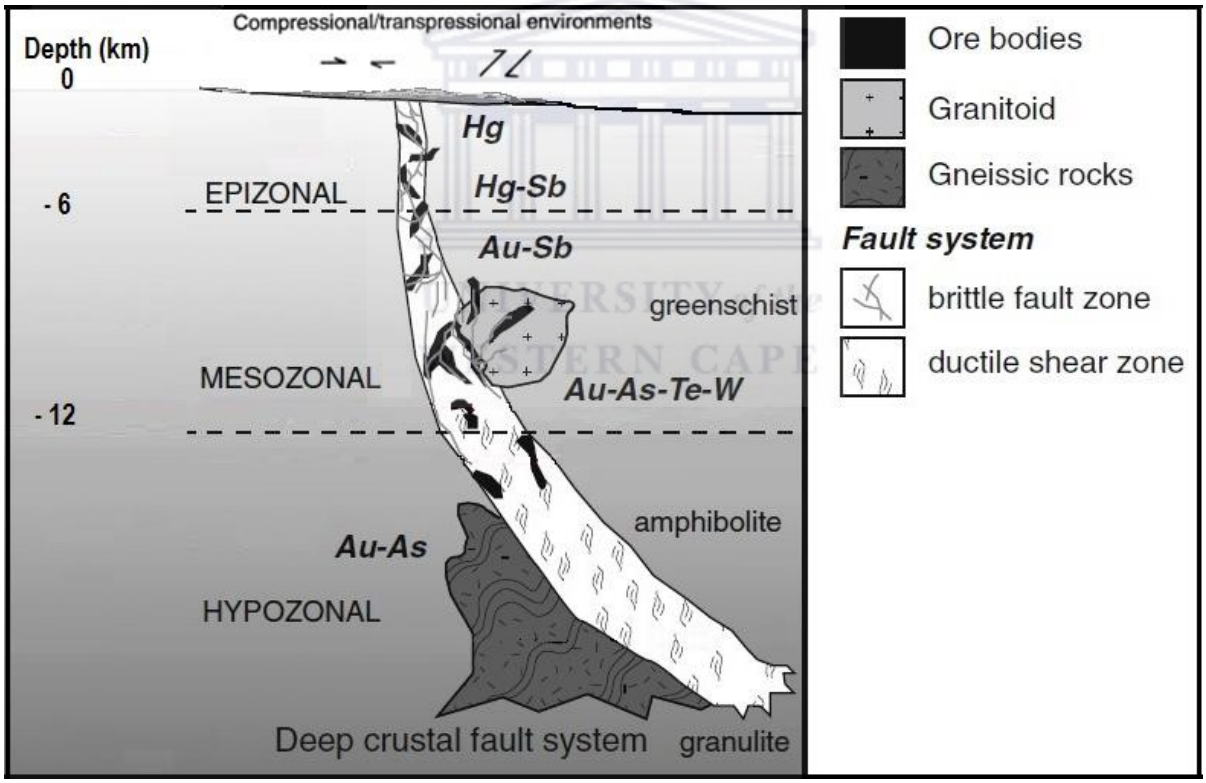

Fig. 1.5. Orogenic gold deposits can form over a variety of depths. The majority of deposits form in the greenschist facies or at the greenschist–amphibolite facies boundary. Modified after Goldfarb & Groves (2015).

The gold is carried from depth along zones of weakness in the form of a reduced sulphur complex in aqueous-carbonic fluids, with typically 5–20 mol.% CO_2; however, much more CO_2-rich fluid inclusions may be entrapped as a result of unmixing during extreme pressure

fluctuation (Goldfarb and Groves, 2015). The mineralizing fluids are characterised by near-neutral pH (5.5) and low-salinity (3–7 wt.% NaCl equiv.), where Na > K >> Ca and Mg (Goldfarb and Groves, 2015; Groves et al., 1998). The consistency in fluid composition of orogenic gold deposits supports an ore fluid produced from a single source area and implying that mixing of fluids from multiple sources does not play a significant role in their formation (Goldfarb and Groves, 2015). Fluid compositions of orogenic gold deposits are identified by the following ranges in stable isotopes: (a) δD and $\delta^{34}S$ values that are extremely variable; (b) $\delta^{15}N$ of +10 to +24‰ for the Neoarchean, +6.5 to +12‰ for the Paleoproterozoic, and +1.5 to +10‰ for the Phanerozoic; (c) $\delta^{18}O$ for Precambrian ores of +6 to +11‰, and +7 to +13‰ for Phanerozoic ores, and (d) $\delta^{13}C$ values that range from −11 to −2‰ (Goldfarb and Groves, 2015). There is a lack of significant orogenic gold ores that formed between 1.8 and 0.6 Ga and as such only few significant gold resources are recorded in this geological period (Goldfard et al., 2001) and this may be the possible explanation for lack of $\delta^{15}N$ data for the Meso- and Neoproterozoic.

Mineralization is structurally controlled, and deposits are located in second or third order structures. Controlling structures are commonly ductile to brittle in character ranging from brittle faults to ductile shear zones, fracture arrays, stock-work networks or breccia zones in competent rocks, foliated zones (pressure solution cleavage), and fold hinges in ductile turbidite sequences. The vein system may continue vertically for up to 2 km with little or no change in gold grade or mineralogy (Groves et al., 1998).

These deposits display meter scale lateral alteration zonation. The extent, intensity and mineralogy of the alteration zones depend on the wall rock type and crustal level. The common alteration minerals are: (i) carbonate minerals (dolomite, ankerite, calcite), (ii) sulfides (pyrite, pyrrhotite or arsenopyrite), (iii) alkali-rich silicates (sericite and less commonly, fuchsite, K-feldspar, biotite, albite, paragonite, chlorite). Carbonates are less abundant at deeper crustal levels while amphiboles or diopsides are more common with progressing depth.

The deposits are dominantly composed of quartz veins with ≤ 3–5% sulfide minerals (dominantly Fe-sulfides) and ≤ 5–15% carbonate minerals. Common gangue minerals are albite, white mica or fuchsite, scheelite, tourmaline and chlorite. Gold commonly occurs in association with sulfide minerals, including pyrite, pyrrhotite, arsenopyrite, chalcopyrite,

sphalerite and galena. Gold grades are relatively high and Au:Ag ratios range from 10 (normal) to 1 (less common) (Groves et al., 1998). Veins containing gold are enriched with variable amounts of As, B, Bi, Hg, Sb, Te and W; Cu, Pb and Zn contents are slightly elevated relative to regional backgrounds (Groves et al., 1998).

There is worldwide agreement that the main complex responsible for transportation of gold in orogenic gold deposits is $Au(HS)_2^-$ (Seward, 1984; Mikucki, 1998). According to Benning and Seward (1996), $Au(HS)^0$ may become predominant under low pH conditions. In general gold-chloride complexes are regarded as negligible under the physical and chemical conditions prevailing in orogenic gold deposits. However, Mikucki's (1998) thermodynamic calculations suggest that $AuCl_2^-$ is the dominant gold-complex at temperatures above 550°C even in low-salinity fluids.

1.2.2 TECHNIQUES FOR CHARACTERISING OROGENIC GOLD DEPOSITS

Classification of gold deposits in orogenic environments has proven to be problematic due to a number of uncertainties. The uncertainties include the sources of the ore fluids and metals, and the role that spatially related granitic bodies play with regard to their formation. Widely applied methods aimed at constraining the sources of the ore fluids and associated metals include analyses of stable isotopes (C, S and O), fluid inclusion studies, and geochronological studies.

Hydrogen, oxygen, sulphur and carbon isotopes are universally accepted for constraining the source of the fluids of orogenic gold deposits (Lambert-Smith et al., 2016; Wang et al., 2016; Shen et al., 2016). Fluid inclusion microthermometry has been extensively utilised to characterize fluid compositions, pressure-temperature conditions and ore-forming processes. CO_2-rich fluids have been used in many studies as a signature for fluids of metamorphic origin (Fyon et al., 1989; Phillips and Powell, 1993). Radiometric dating methods, such as $^{40}Ar/^{39}Ar$, and U-Pb zircon can be utilized to establish absolute time relationships between tectonic, metamorphic, magmatic, and ore formation events (Chai et al., 2016; Groves et al., 1998).

1.3 AIMS OF THE RESEARCH

This research project is aimed at constraining the age, crustal level of formation, pressure-temperature conditions during formation, and the sources of the mineralizing fluids, and, by implication, the metal sources of the Sandamap gold mineralization.

1.4 OBJECTIVES OF THE STUDY

The objective of this study is to carry out fluid inclusion, geochronological and isotopic studies on the ore, as well as investigate the role played by spatially related magmatic bodies in the formation of the deposit. These undertakings will be used to constrain the age of the deposit, the pressure-temperature conditions during formation, and the nature and source of the mineralizing fluids, as demonstrated for other orogenic deposits elsewhere (Groves et al., 2003, 2005; Goldfarb and Groves, 2015).

1.5 RATIONALE

There are a limited number of published works on the genesis of the Sandamap gold deposit (Pirajno et al., 1993; Steven et al., 1999), and earlier researchers (Steven et al., 1994; Steven, 1993; Petzel, 1990) assume a magmatic fluid origin due to the presence of a number of intrusive bodies in the proximity of the mineralization and a calcite $\delta^{13}C_{PDB}$ value obtained from one sample (Steven, 1999). Besides the spatial relationship that the mineralization has with these intrusive bodies, it shares numerous similarities with orogenic gold deposits and it is therefore equally likely that the mineralizing fluids are of metamorphic origin. This study tests this notion.

According to Steven (1999), a stable isotope investigation on a sample from the Sandamap deposit showed that pure calcite has a $\delta^{13}C_{PDB}$ value of -5.4‰ and a $\delta^{18}O_{SMOW}$ value of +24‰, whereas the graphite has a $\delta^{13}C_{PDB}$ value of -10.0‰. The calcite $\delta^{13}C_{PDB}$ value of -5.4‰ falls within the range of -2 to -8.5‰ which was observed in the Yilgarn Block and the Abitibi Belt gold deposits. Steven (1999) stated that the $\delta^{18}O_{SMOW}$ value of +24‰ is too high to be of magmatic origin and, since the value falls within the range for marine carbonates (21 - 28‰), the oxygen may have been possibly derived from fragments of the Karibib Formation marble. Steven (1999), however, cautioned that due to the limited number of sample analyses carried out, not many conclusions can be drawn, as it appears that the stable

isotope investigation was only carried out on one sample, and he further remarked that the genesis of the Sandamap turbidite-hosted gold mineralization is debatable.

Work done by earlier researchers and mineral explorers alike concentrated on the characterization of the deposit in terms of geology and mineralogical associations (Steven et al., 1994; Steven, 1993; Petzel, 1990) and not much was done on constraining the genesis. This study is aimed at filling that knowledge gap. The new knowledge from this study may help in understanding the environment of formation of this and other deposits in similar environments within the Damara Orogenic belt and will also serve as a research tool for future researchers and mineral explorers in search of new discoveries falling within similar environments in the Damara belt.

1.6 STATEMENT OF THE PROBLEM

There are uncertainties regarding the sources of the ore fluids and metals at the Sandamap gold deposit, and the role that spatially related granitic bodies played during the formation of the deposit. This deposit has only been drilled to a depth of 40m and what lies below that is unknown. Knowing the source of the mineralizing fluids and metals would play a pivotal role in assessing the potential of the deposit at depth before embarking on an expensive drilling programme. This would also serve as an important preliminary exploration tool but would however, not preclude some important structural and other studies required in gold exploration. For instance, finding out that the fluids are of metamorphic origin would imply that the existence of mineralization at depth is highly probable since orogenic gold deposits are known to extend vertically up to 2 km (Groves et al., 1998).

1.7 THESIS OUTLINE

- **Chapter 1 Introduction:** Presents the introduction of the research project which includes the background of the project, literature review, aims of the research, objectives of the research, rationale, statement of the problem and research design.
- **Chapter 2 Geological setting:** Presents the description of the area which includes tectonic evolution and geological setting of the area, sampling and petrographic studies.

- **Chapter 3 Geochemistry:** Presents the chemical compositions of the rocks of the area of study.
- **Chapter 4 Fluid inclusions:** Presents research materials, methods and the results of fluid inclusion studies.
- **Chapter 5 Stable isotopes:** Presents research materials, methods and the results of stable isotope studies.
- **Chapter 6 Geochronology:** Presents research materials, methods and the results of geochronological studies.
- **Chapter 7 Discussion, Conclusions and recommendations:** Presents a discussion section, conclusion and recommendations derived from the results of this study.

The last part of the thesis will be appendices. At the end of each chapter is a reference list.

1.8 REFERENCES

Benning, L. G., & Seward, T. M. (1996). Hydrosulphide complexing of Au (I) in hydrothermal solutions from 150–400^{o}C and 500–1500 bar. *Geochimica et Cosmochimica Acta, 60*(11), 1849-1871.

Chai, P., Sun, J. G., Xing, S. W., Li, B., & Lu, C. (2016). Ore geology, fluid inclusion and $^{40}Ar/^{39}Ar$ geochronology constraints on the genesis of the Yingchengzi gold deposit, southern Heilongjiang Province, NE China. *Ore Geology Reviews, 72*, 1022-1036.

Convergent Plate Boundaries. (2018, June 02). Retrieved from http://www.geosci.usyd.edu.au/users/prey/ENG-1/HTML.Lect1/sld010.htm

Fyon, J. A., Troop, D. G., Marmont, S., & Macdonald, A. J. (1989). Introduction of gold into Archean crust, Superior Province, Ontario - Coupling between mantle-initiated magmatism and lower crustal thermal maturation. *Economic Geology Monograph, 6*, 479-490.

Frommurze, H. F., Gevers, T. W., Rossouw, P. J. 1942. *The geology and mineral deposits of the Karibib area, South West Africa*. Explanation to Sheet 79, Geological Survey of South Africa, 172 pp.

Goldfarb, R. J., & Groves, D. I. (2015). Orogenic gold: common or evolving fluid and metal sources through time. *Lithos, 233*, 2-26.

Goldfarb, R. J., Groves, D. I., & Gardoll, S. (2001). Orogenic gold and geologic time: a global synthesis. *Ore Geology Reviews, 18*(1-2), 1-75.

Groves, D. I., Goldfarb, R. J., Gebre-Mariam, M., Hagemann, S. G., & Robert, F. (1998). Orogenic gold deposits: a proposed classification in the context of their crustal

distribution and relationship to other gold deposit types. *Ore Geology Reviews*, *13*(1), 7-27.

Lambert-Smith, J. S., Lawrence, D. M., Vargas, C. A., Boyce, A. J., Treloar, P. J., & Herbert, S. (2016). The Gounkoto Au deposit, West Africa: Constraints on ore genesis and volatile sources from petrological, fluid inclusion and stable isotope data. *Ore Geology Reviews*, *78*, 606-622.

Li, Z. X., Bogdanova, S. V., Collins, A. S., Davidson, A., De Waele, B., Ernst, R. E., ... & Karlstrom, K. E. (2008). Assembly, configuration, and break-up history of Rodinia: a synthesis. *Precambrian Research*, *160*(1-2), 179-210.

Mikucki, E. J. (1998). Hydrothermal transport and depositional processes in Archean lode-gold systems: A review. *Ore Geology Reviews*, *13*, 307-321.

Miller, R. M. (1983). The Pan-African Damara Orogen of South West Africa/Namibia. Pp. In: R. M. Miller, (ed.) *Evolution of the Damara Orogen of South West Africa/Namibia*. Geological Society of South Africa Special Publication 11:431-515

Miller, R. M. (2008). Neoproterozoic and early Palaeozoic rocks of the Damara Orogen. In: Miller, R.M. (Ed.), The Geology of Namibia. Geological Survey of Namibia, Windhoek vol. 2, 13-1–13-410.

Petzel, V. F. W. (1990). Progress report on geological exploration conducted on the farm Sandamap Noord 15 - Damaraland District. Unpubl. rep., Gold Fields Namibia Ltd, 1-37.

Phillips, G. N., & Powell, R. (1993). Link between gold provinces. *Economic Geology*, *88*(5), 1084-1098.

Pirajno, F., Kinnaird, J. A., Fallick, A. E., Boyce, A. J., & Petzel, V. F. W. (1993). A preliminary regional sulphur isotope study of selected samples from mineralised deposits of the Damara Orogen, Namibia. *Communications of the Geological Survey of Namibia*, *8*, 81-97.

Seward T. M. (1984). The transport and deposition of gold in hydrothermal systems. In: Foster RP (Ed.) Gold 82: *The geology, geochemistry and genesis of gold deposits.* Balkema, Rotterdam, 165–181.

Shen, P., Pan, H., & Zhu, H. (2016). Two fluid sources and genetic implications for the Hatu gold deposit, Xinjiang, China. *Ore Geology Reviews*, *73*, 298-312.

Steven, N. M. (1988). *Intermediate report on grant M46/3/1614: Exploration conducted on the farms Sandamap Noord 115, Sandamap 64 and Eureka 99, central Namibia*. Goldfields Namibia.

Steven, N. M. (1991). Turbidite-hosted gold mineralisation at the Sandamap Noord prospect, central Namibia. *Journal-Namibia Scientific Society*, *44*, 109-118.

Steven, N.M. (1993). A study of epigenetic mineralization in the Central Zone of the Damara Orogen, Namibia, with special reference to gold, tungsten, tin and rare earth elements. *Memoirs of the Geological Survey of Namibia*, **16**, 166pp.

Steven, N. M. (1999). Evaluation of the Sandamap Noord turbidite-hosted gold prospect, central Namibia, for a heap-leach gold operation: Implications for regional gold exploration in the Navachab district. Information Circular No. 337. Economic geology research unit, University of the Witwatersrand, Johannesburg.

Steven, N. M., Armstrong, R. A., Moore, J. M. (1993). The Sandamap Noord gold prospect, central Namibia: Discovery of a new style of turbidite-hosted gold mineralisation. *International Geology Review*, 35, 840-854.

Steven, N. M., Badenhorst, F. P., and Petzel, V. F. W. (1994). A review of gold occurrences in the Northern and Central Zones of the Damaran Orogen and the underlying mid-Proterozoic basement, central Namibia. *Communications of the Geological Survey of Namibia*, *9*, 63-77.

Wang, Y. H., Xue, C. J., Gao, J. B., Zhang, F. F., Liu, J. J., Wang, J. P., & Wang, J. C. (2016). The genesis of the ores and granitic rocks at the Hongshi Au deposit in Eastern Tianshan, China: constraints from zircon U–Pb geochronology, geochemistry and isotope systematics. *Ore Geology Reviews*, *74*, 122-138.

CHAPTER 2

DESCRIPTION OF THE AREA

2.1 GEOLOGICAL SETTING OF THE SANDAMAP GOLD DEPOSIT

The Sandamap shear hosted gold deposit is located in the Damara Orogenic belt in central Namibia, to the immediate north of the Omaruru lineament (Fig. 1.1). The Damara belt forms part of the Pan-African collisional belts in southern Africa representing the formation of the Gondwana supercontinent (Miller, 2008). The Damara Orogen is a Neoproterozoic orogen consisting of three arms, the NNW-trending coastal arm (the Kaoko Belt) extending into Angola, the NE-trending arm (the Damara Belt) which extends through central Namibia, across Botswana to the Zambezi belt (Miller, 2008), and the Gariep Belt to the south extending into north-western South Africa. The Kaoko, Damara and Gariep Belts evolved through phases of intracontinental rifting, spreading, subduction and continental collision lasting from approximately 800 or 900 Ma to ~460 Ma. In the Damara Belt, the Kalahari Craton was subducted beneath the Congo/Angola Craton and continental collision is dated at ~542 Ma (Miller, 2008).

The central zone of the Damara Belt is a high-temperature, low-pressure zone with metamorphic grade increasing from middle amphibolite facies in its eastern parts to lower granulite facies in its western parts (Miller, 2008). The northern (nCZ) and southern central (sCZ) zones are separated by the Omaruru lineament to the west and the Waterberg fault in the east. In terms of lithology, the central zone is characterized by mainly schist, marble and quartzite of the Swakop and Nosib groups of the Damara sequence with numerous syn- to post-tectonic granitic plutons (Fig. 2.1). The zone is also typified by major magnetic lineaments (Welwitschia and Erongo) and minor magnetic lineaments (Abbabis and Otjikoto) (Fig. 2.1).

Peak regional metamorphism in the central zone (CZ) is syn-D_2 and occurred at ~520 Ma (Haack *et al.*, 1980; Miller, 1983). On the other hand Miller (2008) places the peak of post-tectonic M_2 regional metamorphism throughout the Damara belt at 535 Ma. Both andalusite and sillimanite are abundant in the CZ, and Steven (1993) stated that since the sillimanite-

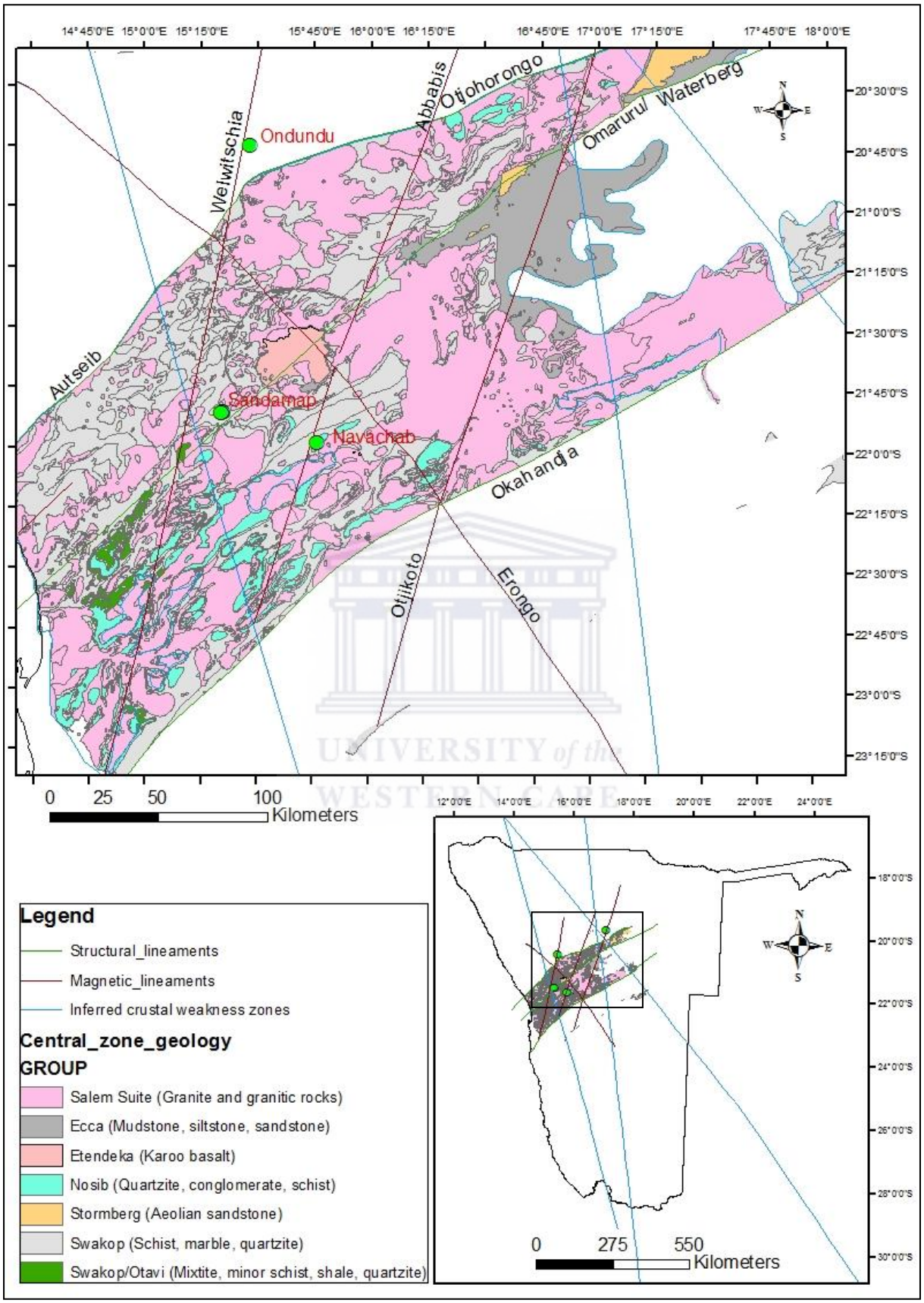

Fig. 2.1. Geology and structural lineaments of the central zone of the Damara orogenic belt as well as gold deposit locations (Sandamap, Navachab and Ondundu).

bearing assemblages seem to have originated from essentially isobaric heating, it is deemed unlikely for the peak metamorphic pressures at any stage in the evolution of the CZ to have exceeded the Al_2SiO_5 triple-point value of 3.76±0.3 kbar (Holdayway, 1971). The CZ is a high-temperature–low-pressure metamorphic belt, hence the abundance of andalusite and sillimanite which is presumably an M_2 assemblage. In the sCZ the peak-M_1 assemblages are syn-D_1 and characterised by s_1-parallel sillimanite knots and staurolite. The period of M_1 metamorphism in the sCZ is placed from 575 to around 565 Ma where M_1 pressure-temperature conditions may have been ~6 kbar and ~700°C (Miller, 2008). According to Miller (2008), staurolite predating sillimanite was found by Nash (1971), Jacob (1974) and Downing (1982) in the sCZ which these authors suggested indicated an early, relatively high-pressure phase of M_1 metamorphism in this region.

D_1 and D_2 deformation events were marked by isoclinal (F_1) and tight (F_2) folding across the CZ (Steven, 1993). The earliest reliably dated granites in the sCZ post-dates D_1 and have ages between 564 and 558 Ma (Miller, 2008). Syn-D_3 granites place D_3 deformation in the sCZ at 542 Ma and the D_2 deformation event in the northern zone (NZ), southern central zone (sCZ), southern zone (SZ), southern margin zone (SMZ) (but not in the nCZ) is placed at approximately 555 to 550 Ma while the earlier deformation event (D_1) has been found to be older than the Okongava diorite which was emplaced at approximately 560 Ma (Miller, 2008). The nCZ is dominated by the highest stratigraphic unit of the Swakop Group (the Kuiseb Formation) and marbles from lower stratigraphic levels were forced upward into the Kuiseb schist during D_3 deformation resulting in the formation of domes. These anticlinal marble domes of various sizes are scattered throughout the nCZ and the age of D_3 deformation is placed between 480 and 460 Ma (Miller, 2008). The Rb-Sr whole-rock age of garnetiferous leucogranites places the D_2 deformation event in the nCZ at 514 ±11 Ma (Haack *et al.*, 1980). According to the above given geochronology data, it appears that the some deformation events in the nCZ (D_1 is older than 564 Ma, D_2 at ~514 Ma, D_3 placed between 480 and 460 Ma) came later than those in the sCZ (D_1 is older than 564 Ma, D_2 at ~555 to 550 Ma, and D_3 at 542 Ma).

2.2. TECTONIC EVOLUTION OF THE NORTHERN CENTRAL ZONE (nCZ)

The Sandamap gold deposit is located in the nCZ (a back-arc region). The precursors of the Sandamap gold deposit host rocks (metaturbidites) were deposited as deep-water turbiditic facies in the Outjo Sea from around 625 to approximately 609 Ma (Miller, 2008). The deposit is located in a mylonitic shear zone in the margin of a marble dome which is associated with D_3 deformation (Steven, 1993; Steven et al., 1994). This deformation event was marked by the diapir-like rise of numerous hot, steep-sided marble domes of the Karibib Formation which produced their own wide thermal aureoles (where granites are absent) in the Kuiseb schist into which they rose (Miller, 2008). Sinistral rotation of the domes during their rise towards the surface produced mylonitic shear zones, in many instances on their margins.

According to Miller (2008), the northern part of the Central Zone was part of the deep northern graben, and it is likely that, although the crust beneath the graben did not rupture, it was very thin and the detachment of the subducting plate beneath this zone enabled hot mantle material to intrude the base of the crust. This provided the heat necessary for granite generation and heating of the deeply buried Karibib Formation.

The age of 542 Ma defines the final closure of the Khomas Sea and the age of continental collision in the Damara Belt (Miller, 1983, 2008). The Khomas Sea was located between the Congo and the Kalahari cratons in the east, while the Outjo Sea was situated on the Congo craton on the western side. The evolution of the nCZ appears to be a match with that of the sCZ up to around 550 Ma. D_3 deformation in the nCZ was typified by the formation of the numerous marble domes and was accompanied by the intrusion of numerous syn-D_3 granite plutons, with their ages ranging from 480 to 460 Ma (Miller, 2008). According to Miller (2008), the absence of more precise granite ages for the nCZ makes it impossible to establish the age at which D_3 deformation ended, and, as such, where uncertainty exists the notation D_3/D_4 will be used in this study. A synopsis of the deformation events of both the northern and southern central zones are given in section 2.1.

2.2.1 TIME FRAME OF EVENTS IN THE nCZ

This section covers an overview of the tectonic events in the nCZ covering a period of ~770 million years starting with intracontinental rifting from 900 Ma, followed by the formation of deep seas, the concurrent sedimentation and the subsequent subduction which led to the collision of tectonic plates at ~542 Ma. The section will close with post-collision events which include detachment of the subducting plate, development of a back-arc region in which the Sandamap gold deposit is located, and the rejuvenation of major thrusts and faults which caused extensive melting of basement rocks and resulted in the production of the prominent Etendeka volcanic rocks from 137 to ~128 Ma. These chains of events are summarized from Miller (2008) and are given in Table 2.2. The schematic diagrams (Figs. 2.3 – 2.9) given in this section, portraying the sequence of events through time, are illustrations taken from the location indicated in Fig. 2.2. Lithostratigraphic nomenclature referred to in this section and elsewhere in this study are given in Table 2.1.

Table 2.1 Lithostratigraphic nomenclature in the northern Central Zone (nCZ) of the Damara belt (after Miller, 2008).

Group	Subgroup	Formation	Member	Lithology
Swakop	Navachab	Kuiseb		Mica schist, ortho-amphibolite, marble, quartzite, graphitic schist
		Karibib	Arise River	Marble, schist, ortho-amphibolite, quartzite
			Otjongeama	
			Harmony	
	Usakos	Arandis	Oberwasser	Schist, calc-silicates
			Okawayo	
			Spes Bona	
		Chuos?		Mixtite, schist, ortho-amphibolite, iron-formation
	Ugab	Rossing		Marble, schist, quartzite
Nosib				Conglomerate, schist, marble

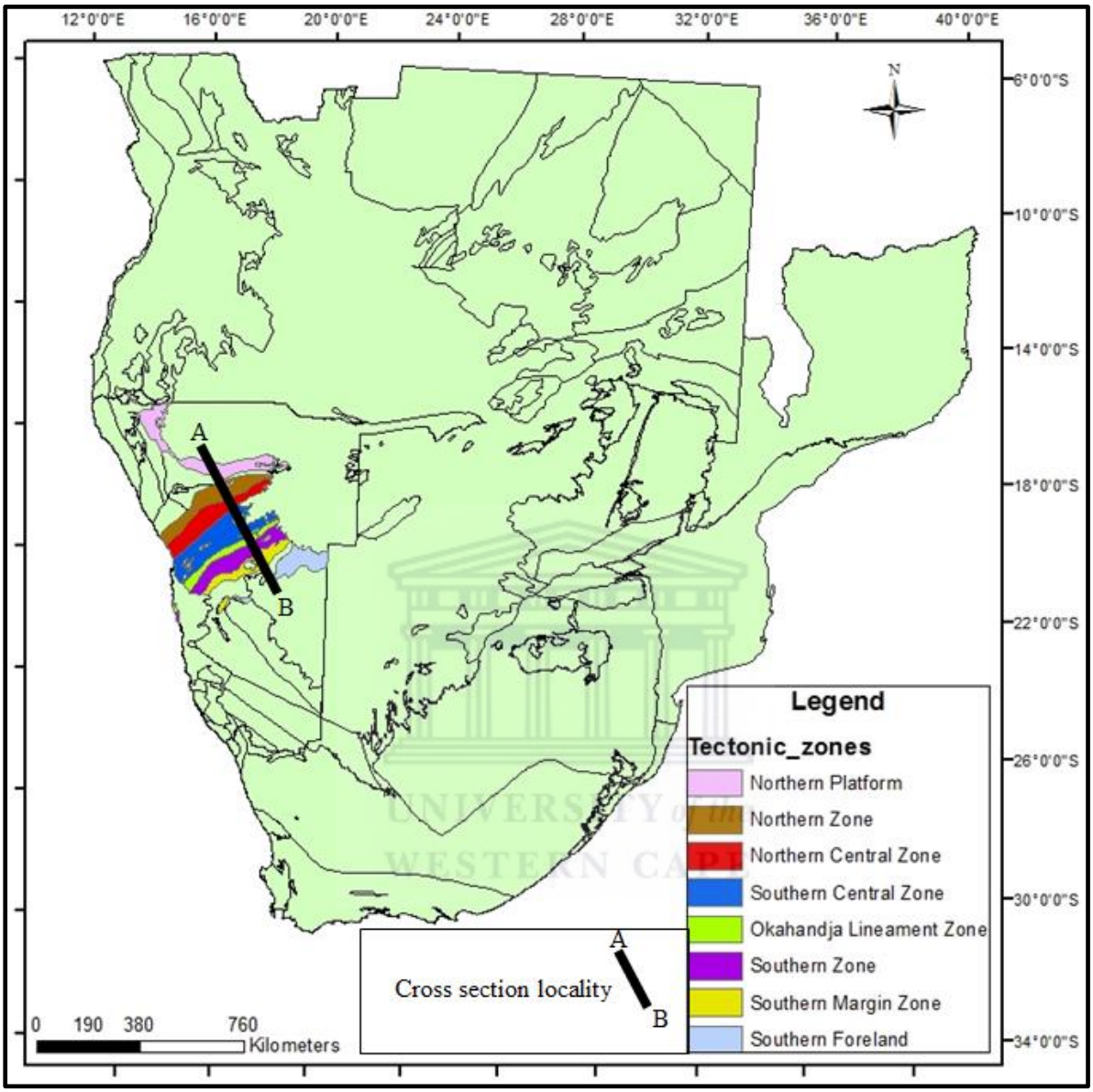

Fig. 2.2. The position of the cross-section across the Damara belt where illustrations given in Figs. 2.3 to 2.9 were taken.

Table 2.2 A summary of geological processes in the northern central zone nCZ from ~900 to 128 Ma

Period/ Date (Ma)	Geological process
~900 - 800	Intracontinental rifting and filling of the graben in the nCZ (Fig. 2.3a). Deposition of Nosib Group
740?	Covering of the nCZ by the Outjo Sea (Fig. 2.3b). Deposition of Rössing Formation
~730	Deep water in the Outjo Sea, turbidite and Chuos Formation deposition (Fig. 2.3c).
720 - 650	Deep water of the Outjo Sea (Fig. 2.4a). Arandis Formation deposition
~625	Entire Damara belt was under water (Fig. 2.4b). Arandis Formation deposition
~625 - ~609 Ma,	Damara belt was under water (Fig. 2.4b). Karibib Formation deposition
~600	Damara Ocean had narrowed (final deposition of turbidites) (Fig. 2.4c). Kuiseb Formation deposition
595 - 575	CZ uplifted and eroded
~565 - 560	Intrusion of post-D_1 – pre-D_2, diorites at the base of the Kuiseb schists in the CZ, erosion in the CZ.
560 - 550	Emplacement of pre- or syn-D_2, Salem-type granites in the CZ at the base of the Kuiseb Formation
542 - 535	Transportation of erosional debris from the CZ across the closed Khomas Sea and Adamastor Ocean and deposited as the distal, southern molasses, Cambrian Nomtsas Formation and Fish River Subgroup
542	Continental collision in the Damara Belt
~514	D_2 deformation event, peak metamorphism and leucogranite emplacement
515 - 510	Necking of the subducting plate below the nCZ and possible initial establishment of the nCZ as a back-arc region (Fig. 2.5a).
495	Initial detachment of the subducting plate below the nCZ and rise of hot mantle below the nCZ (Fig. 2.5b)
490-460	• The subducting plate fully detached and rise of hot mantle, • the nCZ fully develops into back-arc region (Fig. 2.6a) • nCZ pops-up on the Omaruru Lineament • Cooling of the orogen below 300°C
480 - 460	D_3 doming and the intrusion of numerous syn- to post-tectonic D_3 granites in the nCZ
~220	Post-Damara faulting, Omaruru Lineament was reactivated (possibly as a reverse fault)
137 - ~128	• Post-Karoo rejuvenation of the Waterberg Thrust, Autseib Fault and Otjohorongo Thrust (Figs. 2.1, 2.6b). • Damaran rocks were thrust over Karoo sedimentary rocks (Fig. 2.6b). • Eruption of Etendeka volcanic rocks, • Emplacement of abundant dolerite dykes in the western nCZ

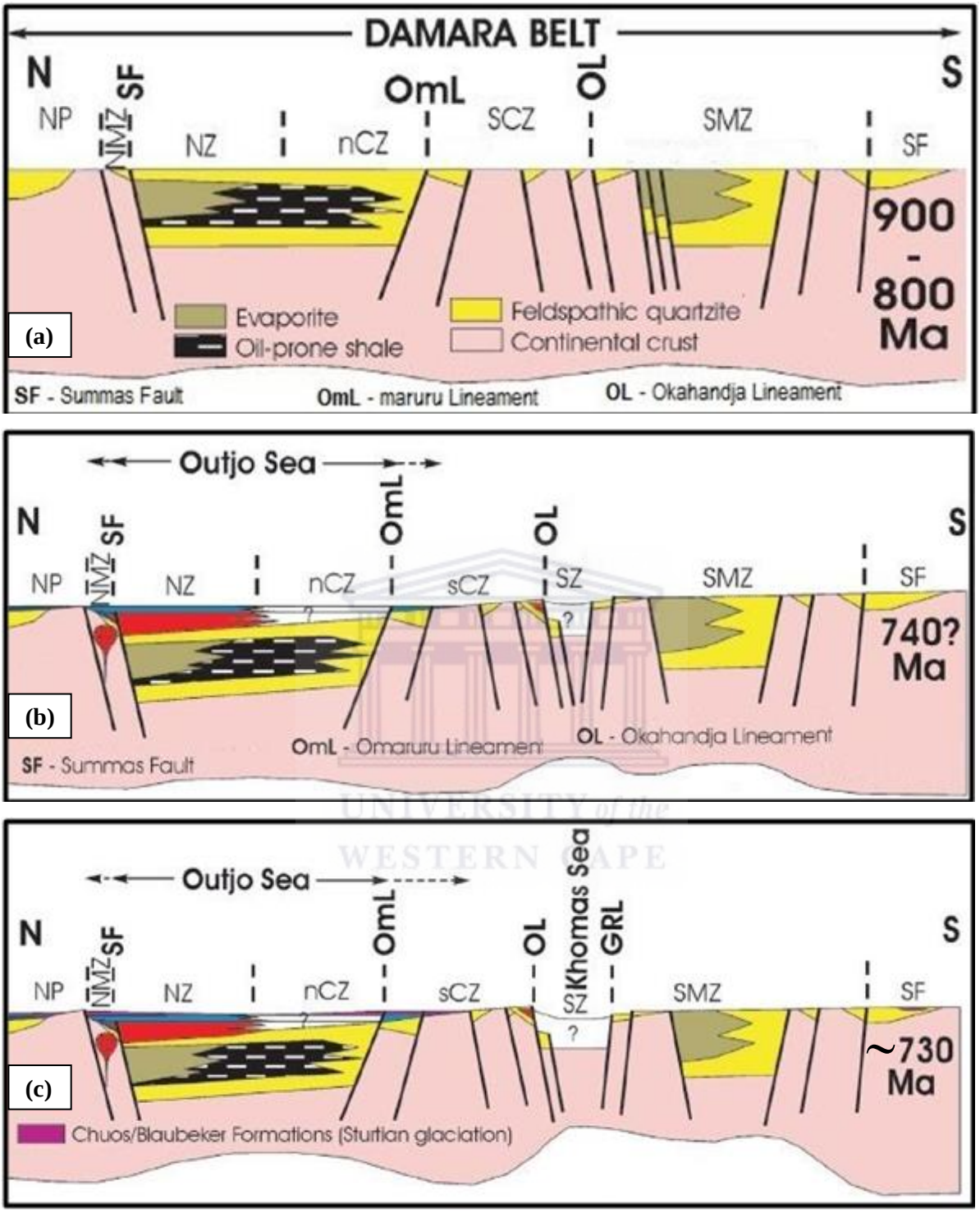

Fig. 2.3. Cross-sections across the Damara belt depicting (a) Intracontinental rifting and filling of the graben in the nCZ (which would give rise to the Outjo Sea), (b) Covering of the nCZ by the Outjo Sea and deposition of the Rössing Formation, (c) Turbidite and Chuos Formation deposition in the deep water of the Outjo Sea in the nCZ. Modified after Miller (2008).

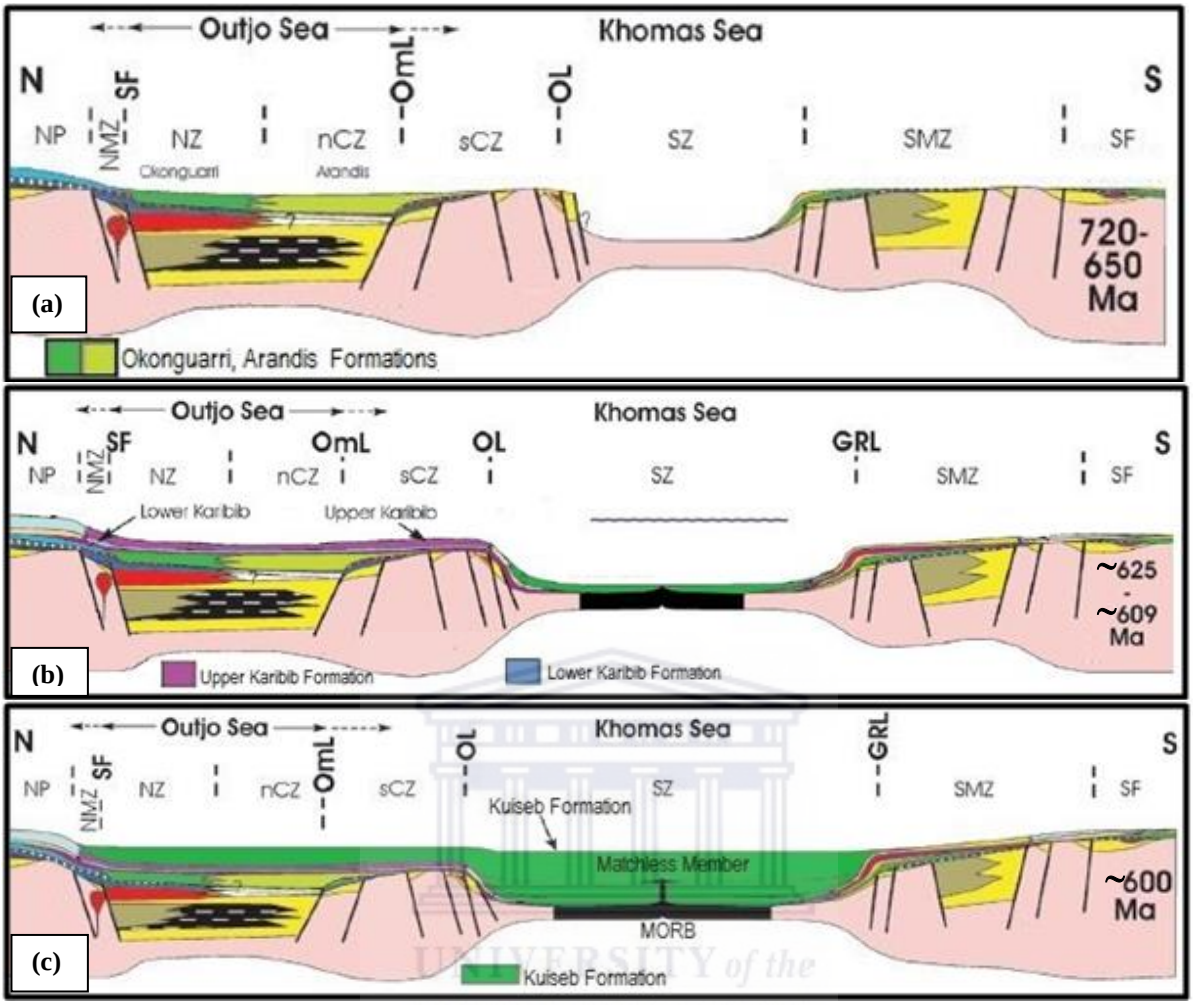

Fig. 2.4. The cross-sections show the following events in the nCZ: (a) Deposition of the Arandis Fm in the deep Outjo Sea, (b) The entire Damara belt was under water for the first time at ~625 Ma, and the deposition of the Karibib Formation occurred during the period ~625 - ~609 Ma, (c) At ~600 Ma the Damara Ocean had narrowed to only extend from the NMZ to the SZ and this period was also characterised by the final depositional stages of the Kuiseb Formation. Modified after Miller (2008).

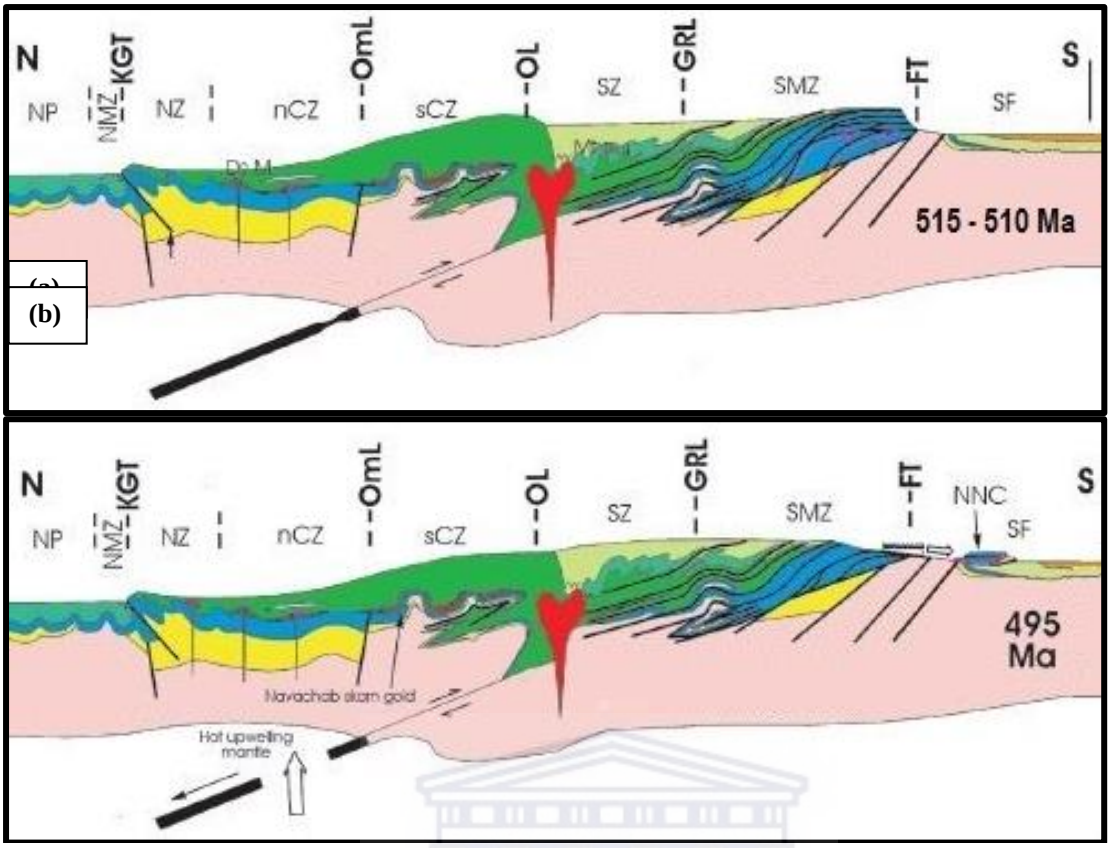

Fig. 2.5. (a) Necking of the subducting plate below the nCZ and possible initial establishment of the nCZ as a back-arc region, (b) Initial detachment of the subducting plate below the nCZ and rise of hot mantle below the nCZ as detachment progresses. Modified after Miller (2008).

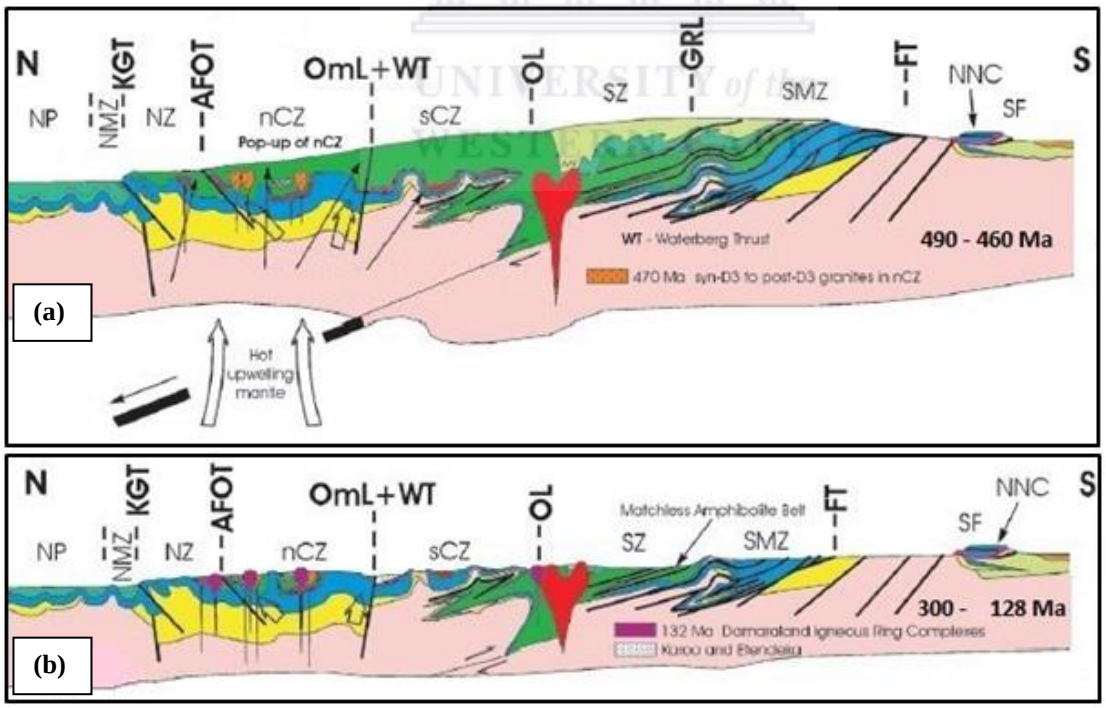

Fig. 2.6. (a) Full detachment of the subducting plate was followed by rise of hot mantle to the base of the crust below the nCZ and full development of the nCZ as a back-arc region (b) Deposition of the Etendeka volcanic rocks, intrusions of the Damaraland Igneous Ring Complexes at around 132 Ma and rejuvenation of the Waterberg Thrust (WT), Autseib Fault and Otjohorongo Thrust (AFOT) post-132 Ma. Modified after Miller (2008).

2.3 LOCAL GEOLOGICAL SETTING

The gold mineralization at Sandamap occurs to the immediate north of the Omaruru Lineament on the edge of a D_3/D_4 leucogranite dome (Fig. 2.7) which is related to the north-northeast trending Welwitschia Lineament zone situated roughly 10 km to the west (Fig. 2.1). According to Steven (1993) the mylonitisation in the vicinity of the mineralization is related to the D_3/D_4 movements on the Welwitschia Lineament zone. Steven (1993) relates the development of the unmineralised mylonitic shear zone in the schist to the diapiric intrusion of the leucogranite-cored dome and accompanying pegmatites (Fig. 2.7). It should, however, be also noted that the shear zone may have formed as a result of the sinistral rotation of the marble dome situated west of it (Fig. 2.7), since mylonitic shear zones have been observed to be common in the margins of the marble domes in the nCZ (Miller, 2008).

A synopsis of the events in the study area and immediate surroundings, as given by Steven (1993), is as follows: greywackes and turbidites of the Kuiseb Formation were regionally metamorphosed during isoclinal and tight folding (F_1 and F_2) resulting in the formation of biotite ± muscovite schists. The late D_3/early D_4 compression led to the formation of the domal structures which were, to a large extent, caused by the intrusion of granites and associated pegmatites. To the immediate west of the mylonitic shear zone hosting the Sandamap gold deposit is a marble dome (Fig. 2.7). The dome is associated with D_3/D_4 deformation which has been observed to be the final deformation event in the northern Central Zone (nCZ) (Miller, 2008). Very late Damara movement on the Welwitschia lineament zone led to the formation of sillimanite-bearing mylonitic rocks in late-tectonic pegmatites on the northwest side of the domal structure situated to the west of the Sandamap gold mineralization.

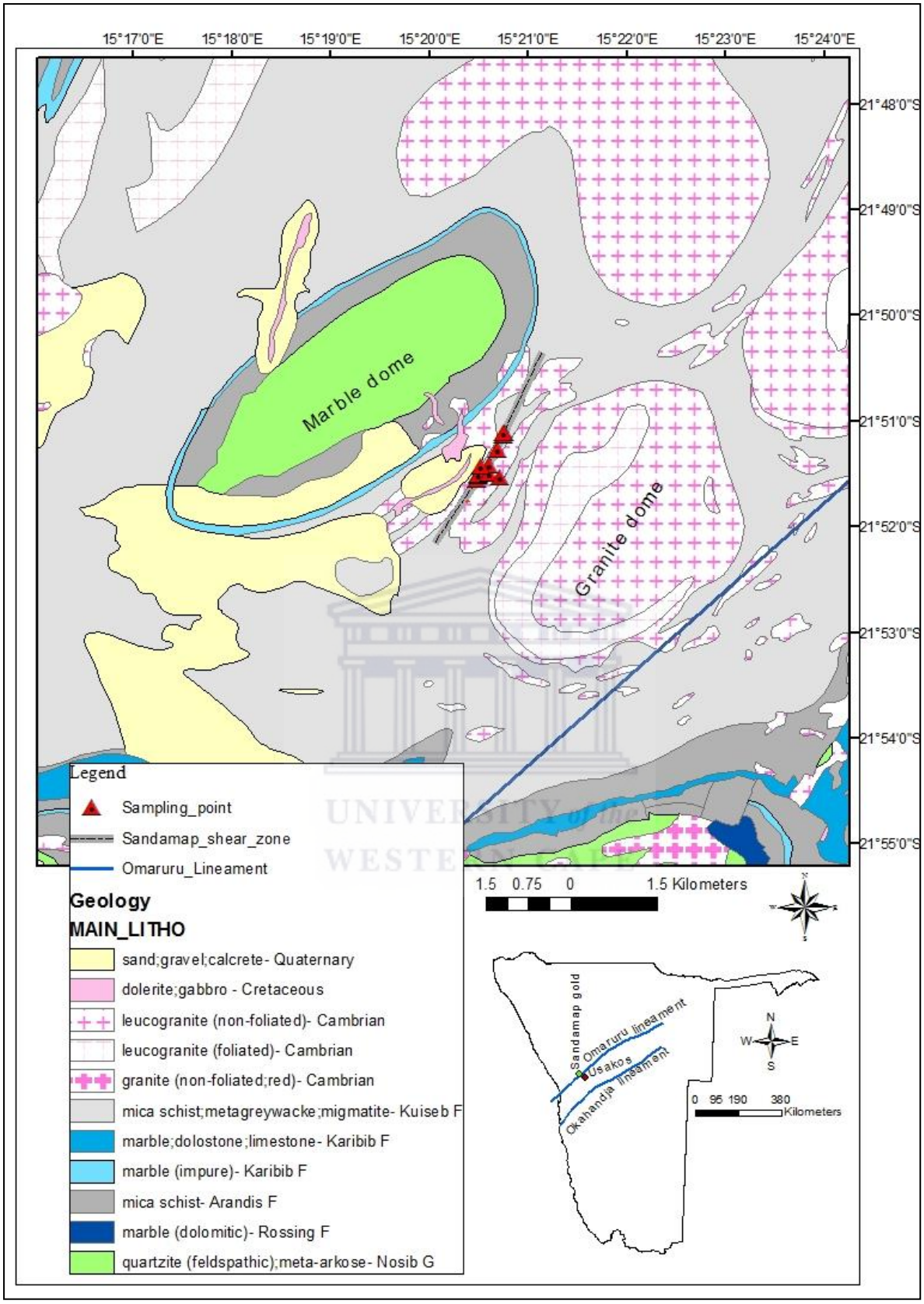

Fig. 2.7. The mylonitic shear zone hosting the gold mineralization is bounded by a marble dome on the north-western side and by a granite dome on the south-eastern side. Both are related to the D_3 deformational event. F in the legend stands for Formation and G stands for Group.

This deformation event was marked by the diapir-like rise of numerous hot, steep-sided marble domes of the Karibib Formation (a formation in the Central Zone of the Damara Belt which is dominantly carbonate). Thermal aureoles around these domes in the Kuiseb schist (the schist hosting the Sandamap shear zone), where granites are absent, are an indication of high temperature activity (Miller, 2008). Sinistral rotation of the domes during their rise towards the surface produced mylonitic shear zones, in many instances on their margins (Miller, 2008).

2.4 SANDAMAP GOLD DEPOSIT AND THE LOCAL GEOLOGY

The mineralization is hosted by sheared biotite-sillimanite-K-feldspar schist of the upper Kuiseb Formation which forms part of a highly deformed Neoproterozoic deep marine sedimentary succession consisting of metagreywackes and graphitic metaturbidites (Fig. 2.7). The gold mineralization is contained in quartz veins, gossan stringers and mylonite rocks. The ore minerals are native gold, loellingite, arsenopyrite, pyrrhotite, pyrite and galena with tourmaline, kaolinite, graphite, alunite, calcite, garnet, jarosite and brookite as gangue minerals (Steven, 1993). Alteration assemblages consist of calcite-graphite-tourmaline rocks and auriferous grunerite rocks (Steven, 1993).

Steven (1993) stated that the Au fluids were either expelled from the stanniferous pegmatites (with a Rb-Sr whole rock date of 468 ± 14 Ma), or mobilised from metasediments. A xenolith of altered mineralized schist hosted in the pegmatitic granite in one of the trenches (trench 9) indicates that the mineralization pre-dates the pegmatitic granite (Petzel, 1990). Steven et al. (1994) reported Pb-Pb model ages of galena from the mineralized zone of 469 – 464 Ma.

2.5 SAMPLING

2.5.1 TRENCH AND SAMPLING POINT LOCATIONS

Hydrothermal vein quartz and plutonic rock samples were collected from some trenches and their immediate surroundings. The trenches, which are 40 in total, were excavated by Solar Development Co. Ltd in 1931 across the gold-hosting shear zone (Frommurze et al., 1942; Petzel, 1990). Sampling coordinates are given in Table 2.3 and Fig. 2.8 shows the first 16 trenches and sampling points for this study.

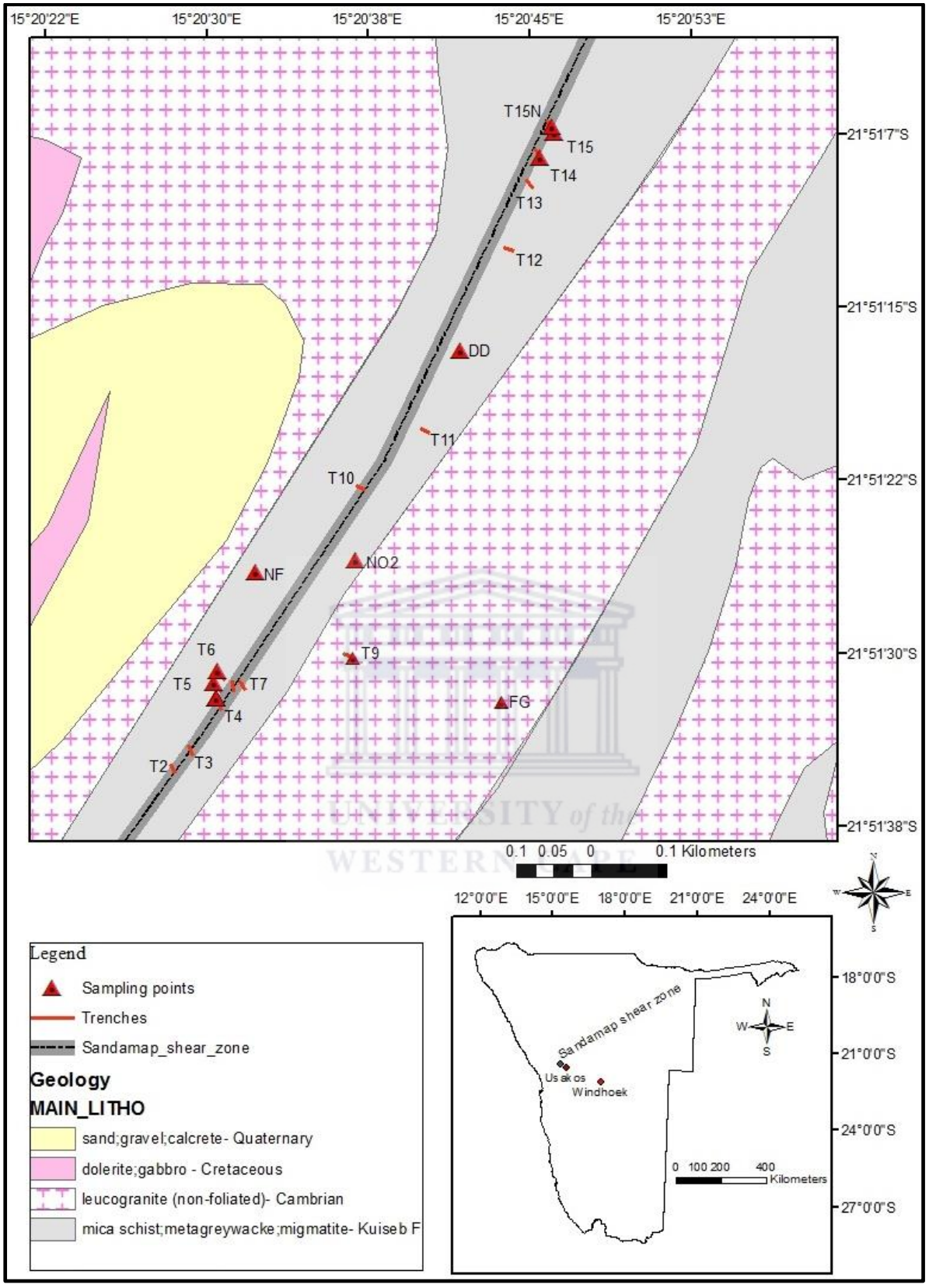

Fig. 2.8. Location of trenches and samples. The study area is located 30 km northwest of the town of Usakos in Namibia. Lithology shapefile scale is 1:250 000. Shapefiles are from the Geological Survey of Namibia.

Table 2.3 Trenches and sampling point coordinates. Samples were collected from trenches only where quartz veins were exposed.

Trench number	Latitude (DMS)	Longitude (DMS)	Trench strike	Sample number
Trench 1	21° 51' 46.5012" S	15° 20' 23.8200" E	------	None
Trench 2	21° 51' 35.3412" S	15° 20' 28.6188" E	------	None
Trench 3	21° 51' 34.0200" S	15° 20' 29.1588" E	------	None
Trench 4	21° 51' 32.0400" S	15° 20' 30.4800" E	112°	T4
Trench 5	21° 51' 31.3812" S	15° 20' 30.3612" E	127°	None
Trench 6	21° 51' 30.8412" S	15° 20' 30.5412" E	127°	T6
Trench 7	21° 51' 31.6800" S	15° 20' 31.8012" E	117°	None
Trench 8	21° 51' 31.2588" S	15° 20' 31.2000" E	097°	None
Trench 9	21° 51' 30.2400" S	15° 20' 36.8412" E	158°	T9
Trench 10	21° 51' 22.9788" S	15° 20' 37.3812" E	155°	None
Trench 11	21° 51' 20.5200" S	15° 20' 40.3800" E	152°	None
Trench 12	21° 51' 12.6000" S	15° 20' 44.2788" E	162°	None
Trench 13	21° 51' 9.9000" S	15° 20' 45.1212" E	129°	None
Trench 14	21° 51' 8.5788" S	15° 20' 45.4812" E	121°	T14
Trench 15	21° 51' 7.4988" S	15° 20' 46.1400" E	130°	T15, T15IZ, T15B & T153d
Trench 15N	21° 51' 7.2000" S	15° 20' 46.0212" E	135°	T15NT & T15NB

2.5.2 SANDAMAP GOLD HOSTING SHEAR ZONE

The sheared rock which hosts the gold mineralization is described as biotite-sillimanite-K-feldspar schists (Fig. 2.9) belonging to the upper Kuiseb Formation (Table 2.1). The gold mineralisation is in ferruginous quartz veins and altered schist. The shear zone is bounded by two domal features: the marble dome on the western edge and the granite dome on the eastern edge (Fig. 2.7). The shear zone, with a dip direction towards the granite, has a dip which varies from gently dipping 56° ESE at some outcrops to steeply dipping 80° ESE in some trenches (Fig. 2.10).

Fig. 2.9. Biotite sillimanite schist of the upper Kuiseb Formation which hosts the mineralized quartz veins.

It is not quite clear as to which of the two domal structures brought about the formation of the shear zone. According to Steven (1993), the unmineralised mylonitic shear zone in the schist is related to the diapiric intrusion of the leucogranite-cored dome which is on the eastern edge of the shear zone (Steven, 1993). On the other hand the marble dome on the western edge of the shear zone could also have potentially produced the shear zone. It has been observed that sinistral rotation of the marble domes in the nCZ produced mylonitic shear zones on their margins in many instances as they rose towards the surface (Miller, 2008). This is also supported by the following observations from the field: features observed at one of the outcrops would likely have resulted from sinistral rotation of the marble dome, and, secondly, the shear zone is dipping away from the marble dome.

Fig. 2.10. The shear dip is quite steep in some places and in this trench (trench 14) two different measurements were obtained: 70° ESE and 80° ESE.

2.5.3 SAMPLING POINT LITHOLOGICAL DESCRIPTION

It will be noticed that some sampling points fall in non-corresponding lithologies in Fig. 2.8 and this is due to the scale of the lithology data used which is 1:250 000 meaning 1 mm on the map represents 250 m on the ground. This implies that anything less than 250 m is not represented on the map and, as such, some sampling units i.e. foliated granite (FG), Non-foliated granite (NF) and dolerite dyke (DD) appear to be in different rock units (Fig. 2.8).

Trench 4: Exposed in the trench is sillimanite-biotite schist hosting ferruginous quartz veins. Images of samples from the trench are given in Fig. 2.11. The dominant minerals in the vein quartz samples are hematite and, of course, quartz.

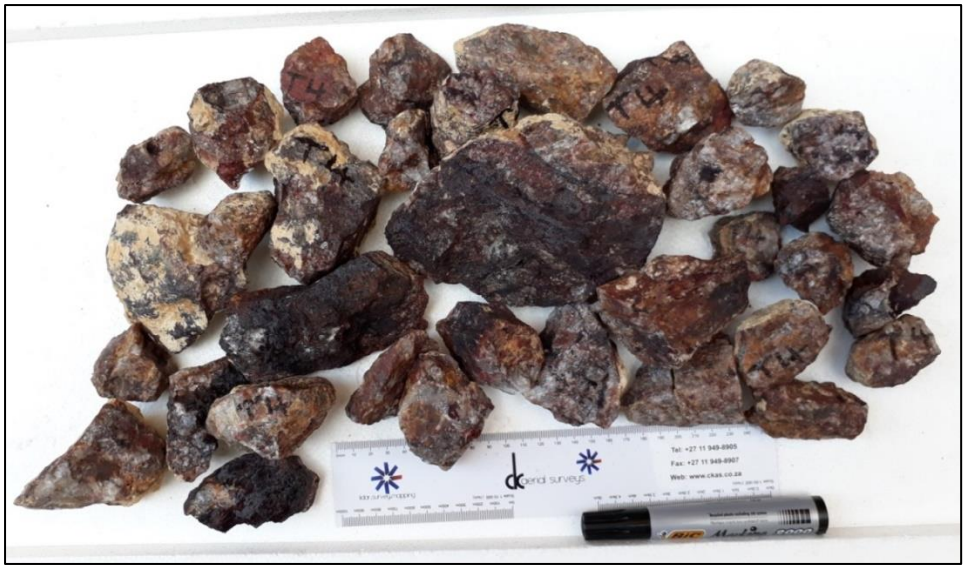

Fig. 2.11. Ferruginous vein quartz samples from trench 4 (T4). The dominant minerals are quartz and hematite.

Trench 6: A carbonate unit bounded by biotite schist is located in this trench and both the carbonate unit and schist were sampled for gold content, major and trace element analysis. The results from the carbonate unit indicate that the unit does not contain gold and does not have any notable abundance of other elements (Tables 3.2 – 3.4). Collected rock samples from the carbonate unit are shown in Fig. 2.12.

Fig. 2.12. Carbonate samples from trench 6 (T6). Major element analysis by fusion XRF indicates that these are dominantly CaO-rich and would thus be described as limestone (Table 3.3).

Trench 9: This contains a ferruginous amphibole schist xenolith (Fig. 2.13) hosted by pegmatitic granite. The xenolith sample (Fig. 2.14) yielded a gold concentration of 0.72 ppm while the hosting granite produced none (Table 3.2). Fig. 2.13 shows where samples were collected and the red dashed lined roughly indicates the partially debris-covered contact between the xenolith and the granite in the trench.

Fig. 2.13. Ferruginous amphibole schist xenolith within the pegmatitic granite in trench 9. The xenolith is partially covered by loose rock debris and some parts can be seen through the rock debris.

Fig. 2.14. Ferruginous amphibole schist xenolith samples from trench 9, hosted by pegmatitic granite.

Trench 14: Quartz veins are occurring within sillimanite-biotite schist in this trench. Samples from this trench (Fig. 2.15) yielded the highest gold content of 1.937 ppm (Table 3.2).

Fig. 2.15. Vein quartz samples from trench 14 (T14). Vein quartz occurs in the hosting biotite schist enclosures.

Trench 15: This trench is characterised by hydrothermally altered schist with layered thin quartz veins (Figs. 2.16, 2.17). Samples from this locality yielded the second highest gold content of 1.634 ppm (Table 3.2) and the gold assay was obtained from the whole rock (altered schist and vein quartz).

Fig. 2.16. Hydrothermally altered schist samples from trench 15 (T15) which, according to XRD results, are composed of quartz, cummingtonite, calcite, albite, muscovite, mimetite, kaolinite, alunite and dickite.

Fig. 2.17. A close up of the hydrothermal rock samples showing layered structures of vein quartz

NO2: A quartz vein parallel to the shear zone fabric within a sheared schist outcrop was sampled. This outcrop is not located in a trench hence a difference in the sampling point naming. Samples from the quartz vein are shown in Fig. 2.18 and these yielded a gold content of 0.018 ppm which is lower than the 0.05 ppm obtained from the hosting schist. This gave an $^{40}Ar/^{39}Ar$ plateau age of 472 ± 3 Ma (Fig. 6.2). This age constrains the age of the shear zone.

Fig. 2.18. Ferruginous vein quartz samples from a quartz vein in a sheared schist outcrop at sampling point NO2.

FG: Medium-grained granite, referred to as foliated granite in the literature, shows what appears to be a mineral foliation, as can be seen in the collected samples (Fig. 2.19). The patterns of mineral segregation have, however, been described by Steven (1993) as bands and not true foliations. These bands and the age of the pluton (Rb-Sr whole-rock age of 512 ± 19 Ma) coincide with F_2 folding in the nCZ and the peak regional metamorphism placed at approximately 520 Ma (Steven, 1993).

Fig. 2.19. Foliated granite samples located not far from the shear zone (locality FG, Fig. 2.8). The patterns of mineral segregation have, however, been described as bands rather than true foliations (Steven, 1993).

NF: The samples collected from the pegmatitic non-foliated granite are shown in Fig. 2.20. This is the body that hosts the amphibole xenolith schist which yielded a gold concentration of 0.72 ppm while none was obtained from the granite itself.

Fig. 2.20. Non-foliated pegmatitic granite samples from locality NF west of the shear zone (Fig. 2.8).

2.6 PETROGRAPHIC DESCRIPTIONS

Thin section and polished slab photomicrographic images are given in Figs. 2.21 – 2.28, 2.30 and the mineralogical data (mineralogy, grain sizes, abundances, textures, etc.) for each sample is given in Table 2.4.

Thin section examination of samples from trench 4 (T4) show the abundance and dominance of quartz and hematite (Fig. 2.21). This, as such, complements the obsevation in the hand specimens (Fig. 2.11). A closer observation of the quartz-hematite relations reveals that hematite either occupies areas which were initially occupied by quartz or covers quartz surfaces as a penetrative coat or surface coating (Fig. 2.21B). Fibrous crystal habit in cummingtonite is quite noticeable in Fig. 2.21C & D.

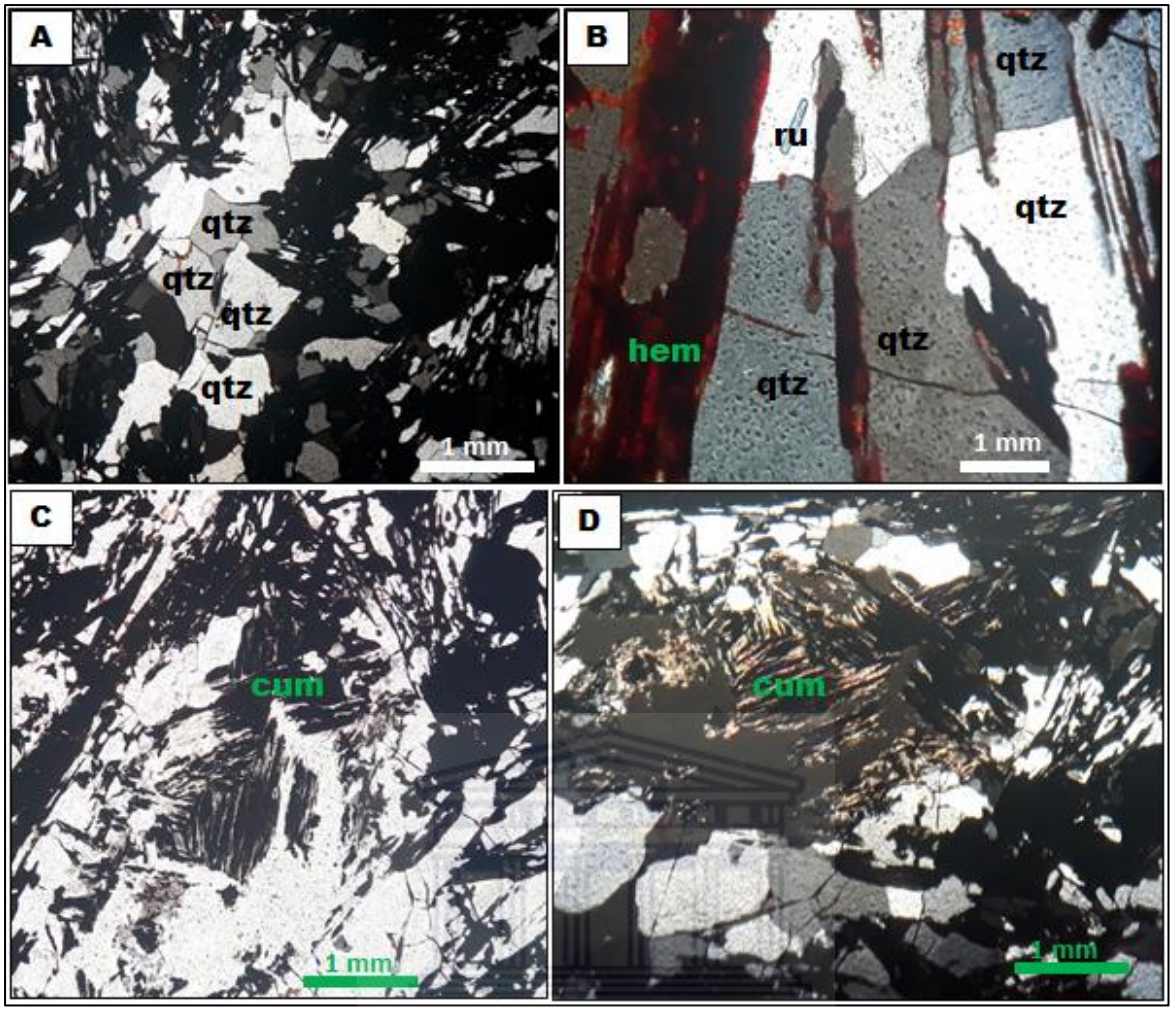

Fig. 2.21. Photomicrographs of samples from trench 4 viewed using transmitted light (PPL & XPL). A. In PPL, quartz (qtz) and opaque minerals (dark grey), presumably haematite, as the dominant minerals (at 4× MAGN). B. In XPL, quartz (qtz), along with hematite (hem) and rutile (ru) as inclusions in quartz (at 20× MAGN). C. In PPL & D. In XPL, notable in the center of the images is the fibrous habit of cummingtonite (cum) (at 4× MAGN). The cross-cutting textural relationship between quartz and haematite shows that the quartz formed earlier as seen in B).

Quartz is the dominant mineral with patchy skeletal micas in thin sections from trench 14 (Fig. 2.22), although at first glance the hand specimens (Fig. 2.15) may give the impression that micas are quite abundant in the samples while, in actual fact, the micas that are seen are restricted to the margins of the quartz veins. The skeletal and anhedral grain shapes of the micas suggest replacement by quartz probably during cooling. The skeletal and anhedral grain shapes could also mean a fast rate of crystallization (Raith et al., 2011). Tourmaline can be seen in the fine-grained matrix. The fine-grained matrix is believed to be clay which could be dickite reported in XRD results of samples from T14 (Fig. 2.23).

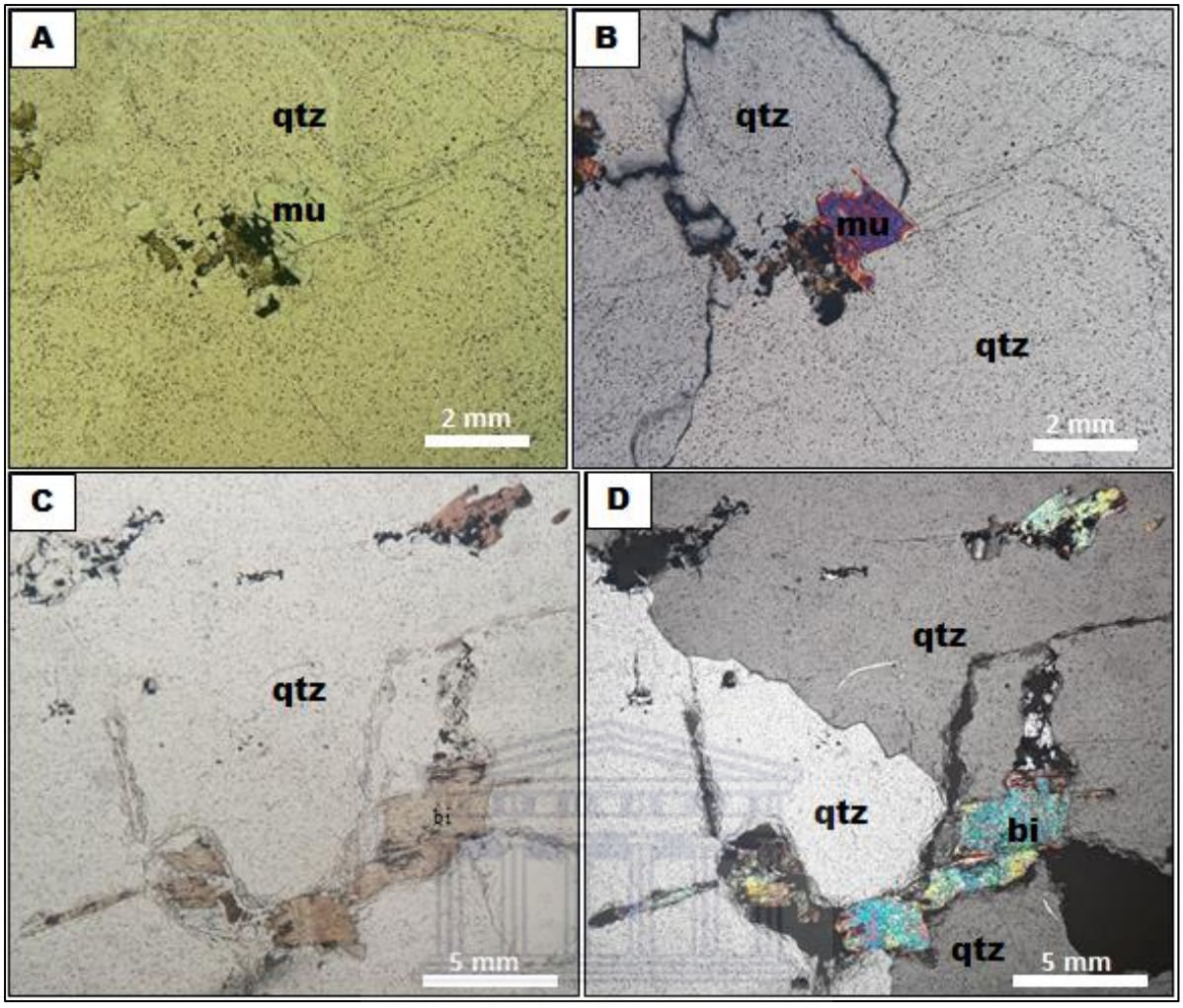

Fig. 2.22. Photomicrographs of samples from trench 14 using the transmitted light microscope. A. Muscovite (mu) and quartz (qtz) taken at 10× MAGN (under PPL) and B. The same minerals as in A under XPL. C. Biotite (bi) and quartz (qtz) taken at 4× MAGN (PPL), and D. The same minerals as in C under XPL.

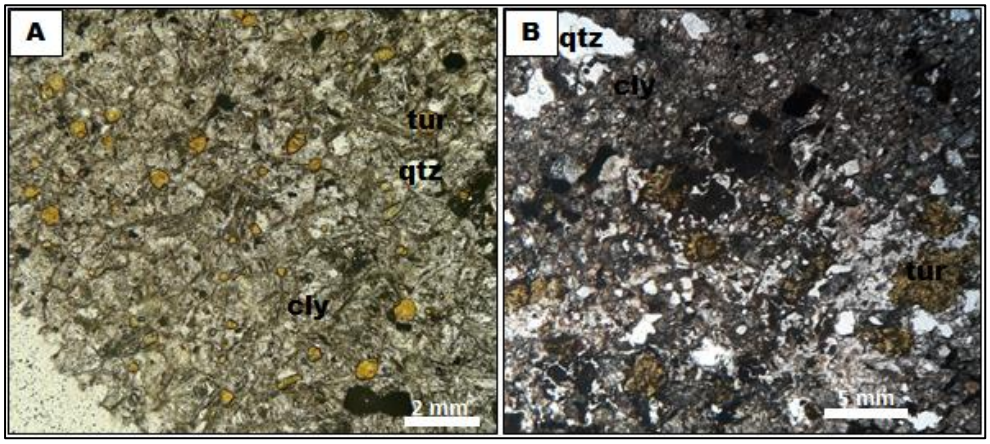

Fig. 2.23. Photomicrographs of hydrothermal rock sample from trench 14 under transmitted light microscope. A. Tourmaline (tur), quartz (qtz) and clay (kaolinite/ dickite) taken at 10× MAGN (under PPL) and B. The same minerals as in A taken at 4× MAGN under XPL.

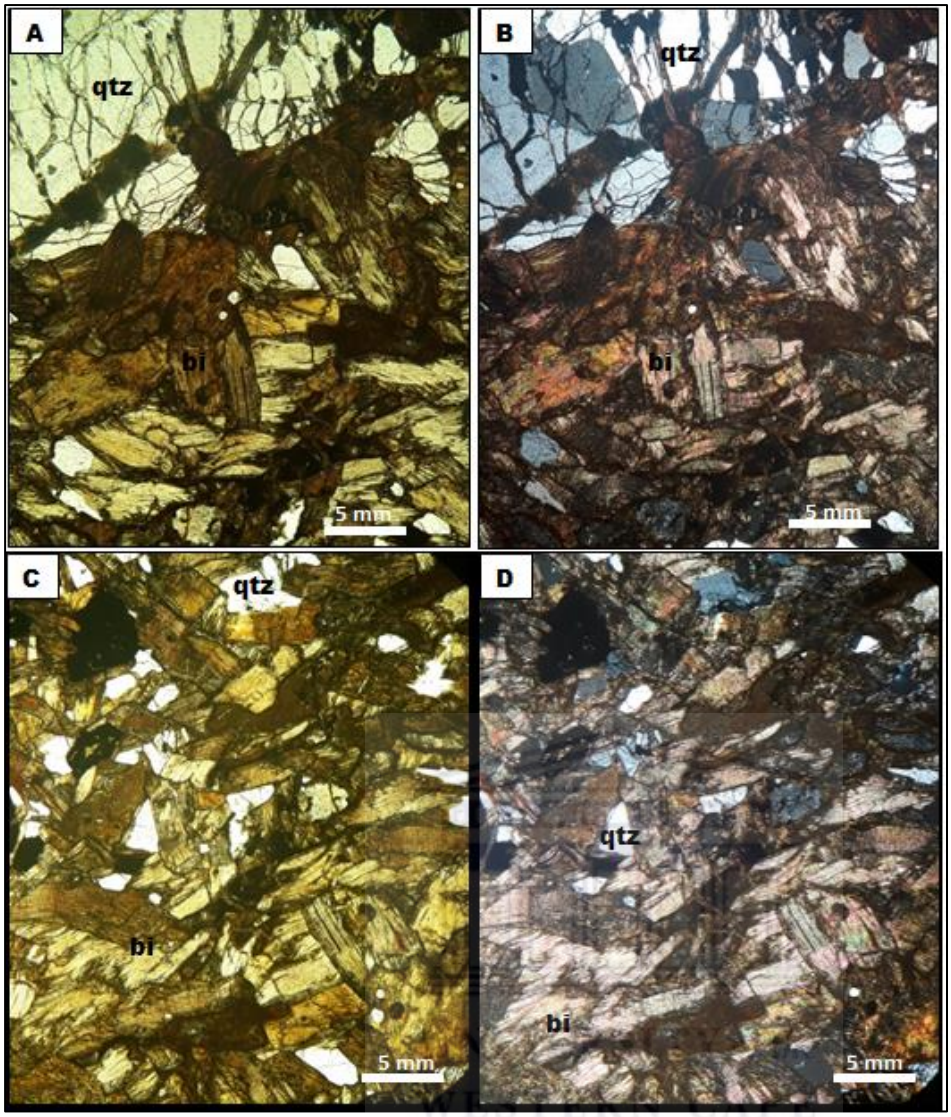

Fig. 2.24. Photomicrograph of hydrothermal rock sample from trench 15 using the transmitted light microscope. A. & C. Biotite (bi) and quartz (qtz) taken at 4× MAGN (under PPL – A and XPL - B), and B. & D. The same minerals on left hand side under XPL.

In samples from trench 15 (T15) micas are quite dominant (Fig. 2.24) and, in some portions of the samples, dominant micas can be seen bordering the quartz vein (Fig. 2.24A & B). In other portions quartz appears as isolated inclusions in biotite grains (Fig. 2.24C & D). A closer look at the relationship between the quartz and the micas suggest replacement of quartz by micas probably during hydrothermal heating.

Other samples from T15 show garnets within medium-grained micas together with some quartz grains (Fig. 2.25). The growth of the garnet is expected to have formed more likely during metamorphism or during hydrothermal fluid flow. Micas wrap around the garnets

indicating that the latter (the garnets) formed earlier and that the former (the biotite) grew around the earlier garnets during deformation and metamorphism (Fig. 2.25B, Fig. 2.29). Euhedral crystals of amphibole can be seen as inclusions in quartz in other samples from T15 (Fig. 2.26).

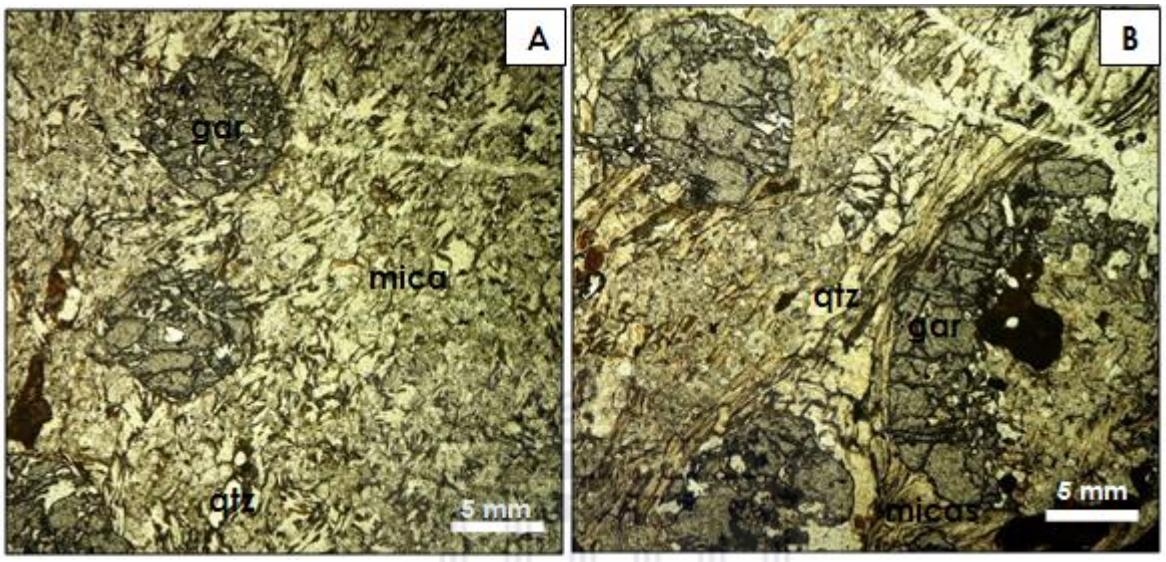

Fig. 2.25. Photomicrographs of hydrothermally altered schist rock samples from trench 15 using transmitted light microscope. A. & B. Garnet (gar), quartz and medium-grained micas. Samples taken at 4× MAGN (under PPL). Micas wrap around the garnet and partial replacement of the garnet by the micas in the right bottom corner of the image B.

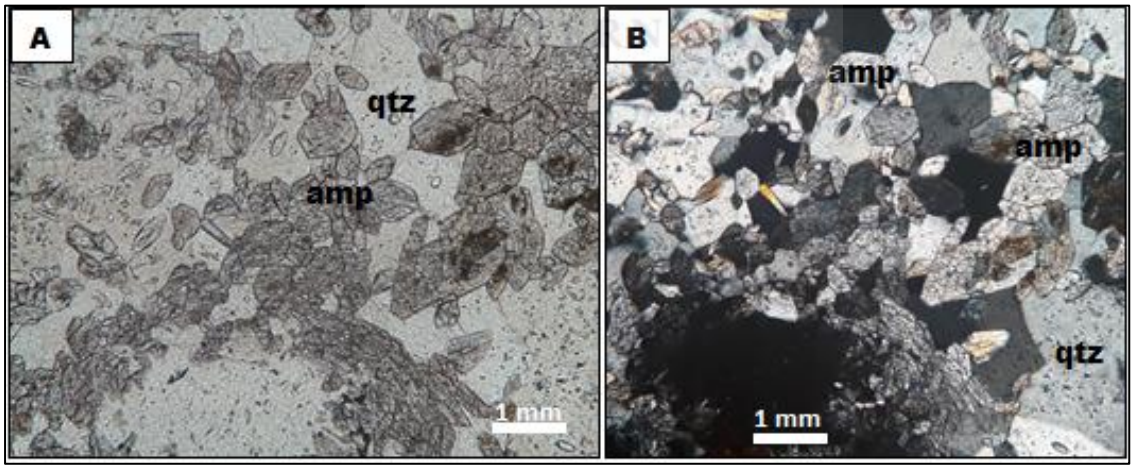

Fig. 2.26. Photomicrographs of hydrothermal rock samples from trench 15 under transmitted light microscope. A. & B. Quartz (qtz) and amphibole (amp) taken at 20× MAGN (A taken under PPL, while B is under XPL). The amphibole is cummingtonite. Euhedral crystal of cummingtonite in massive quartz, growing over quartz.

Examination of opaque minerals in polished slabs from trench 15 and 15N shows mainly iron oxides and pyrite where a subhedral pyrite cystal can be seen next to hematite in Fig. 2.27.

The gangue minerals (i.e. quartz) and ore mineral (i.e. pyrite) are expected to be contemporaneous (Fig. 2.27, Fig. 2.29). Goethite, hematite and quartz have been identified in Fig. 2.28. In Fig. 2.27, pyrite is partially replaced by haematite and goethite possibly filling a micro-fracture suggesting replacemnt of haematite by goethite (Fig. 2.28A & B).

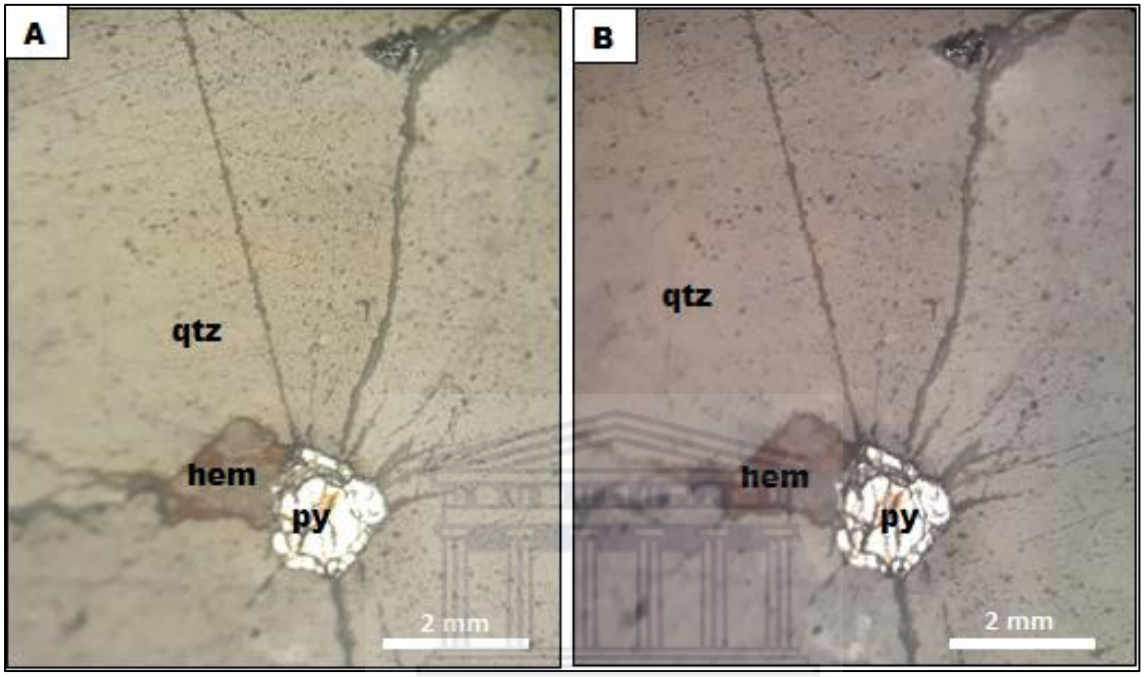

Fig. 2.27. Photomicrographs of a sample from trench 15N using reflected light microscopy. A. & B. Quartz (qtz), pyrite (py) and haematite (hem) taken at 10× MAGN (image on the left is under PPL and image on the right is XPL). Hematite replacing pyrite possibly through a change in anion. The gangue mineral (quartz) and Ore mineral (pyrite) are expected to be contemporaneous.

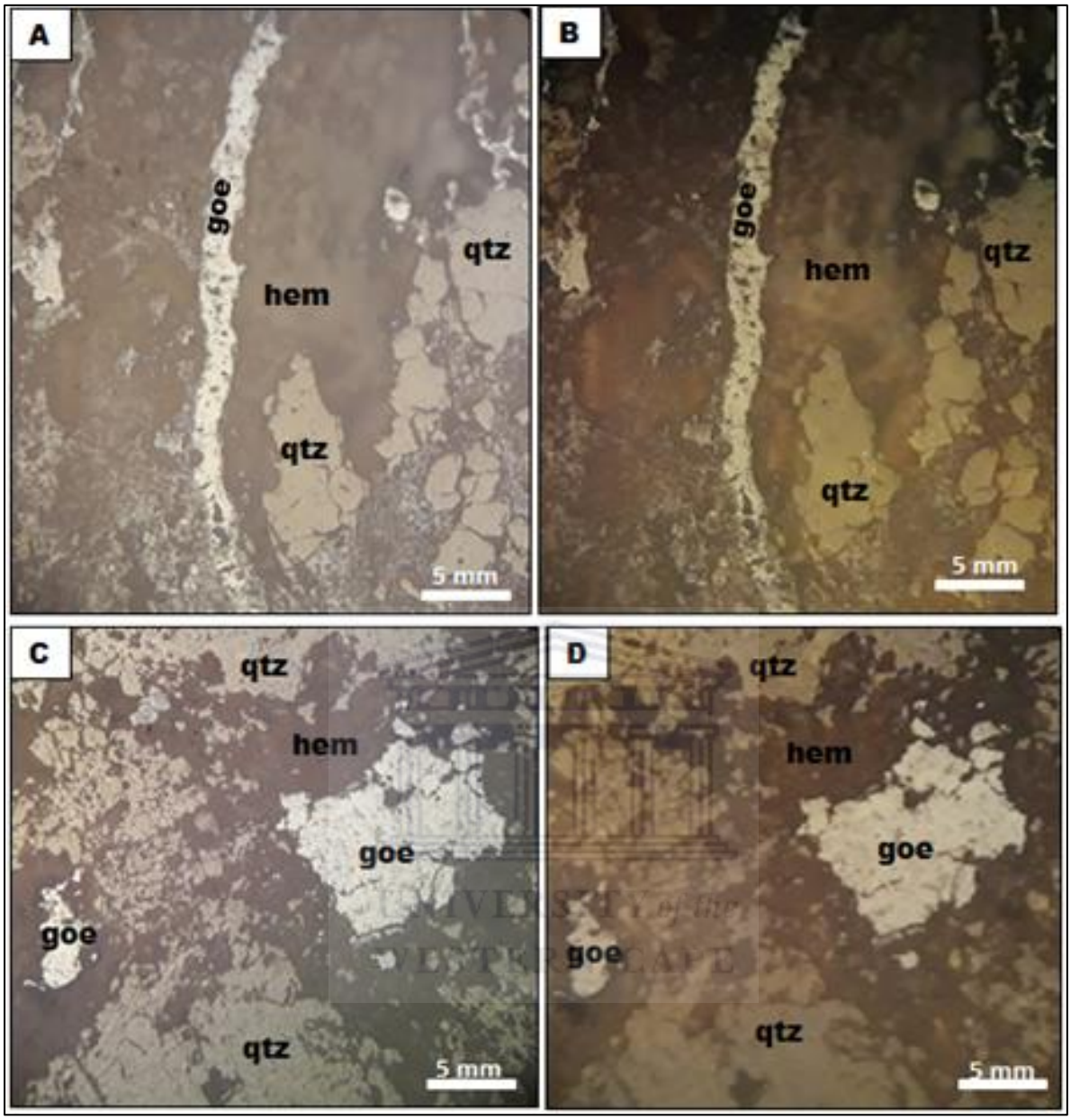

Fig. 2.28. Photomicrographs of a sample from trench 15 using reflected light microscopy. A.-D. Quartz (qtz), haematite (hem) and goethite (goe) taken at 4× MAGN (A & C under PPL and B & D under XPL). Goethite vein crosscutting haematite in A and B, indicting a younger age.

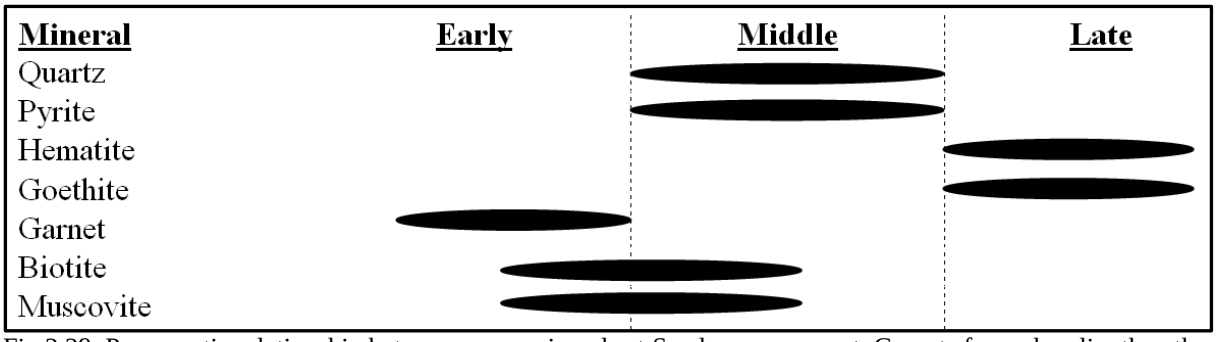

Fig.2.29. Paragenetic relationship between some minerals at Sandamap prospect. Garnets formed earlier than the micas. The skeletal textures of micas in quartz suggest retrograde hydration reactions, where quartz and mica were contemporaneous products or micas maybe relicts. Haematite and goethite formed later than pyrite.

Thin section images of non foliated pegmatitic granite (NF) show granular anhedral crystals of quartz, microcline and plagioclase interlocking with one another (Fig. 2.30). The grain relationships between quartz and the feldspars suggest that the quartz grains grew into the feldspar grains probably during cooling. The abundance and texture of minerals at Sandamap is given in Table 2.4.

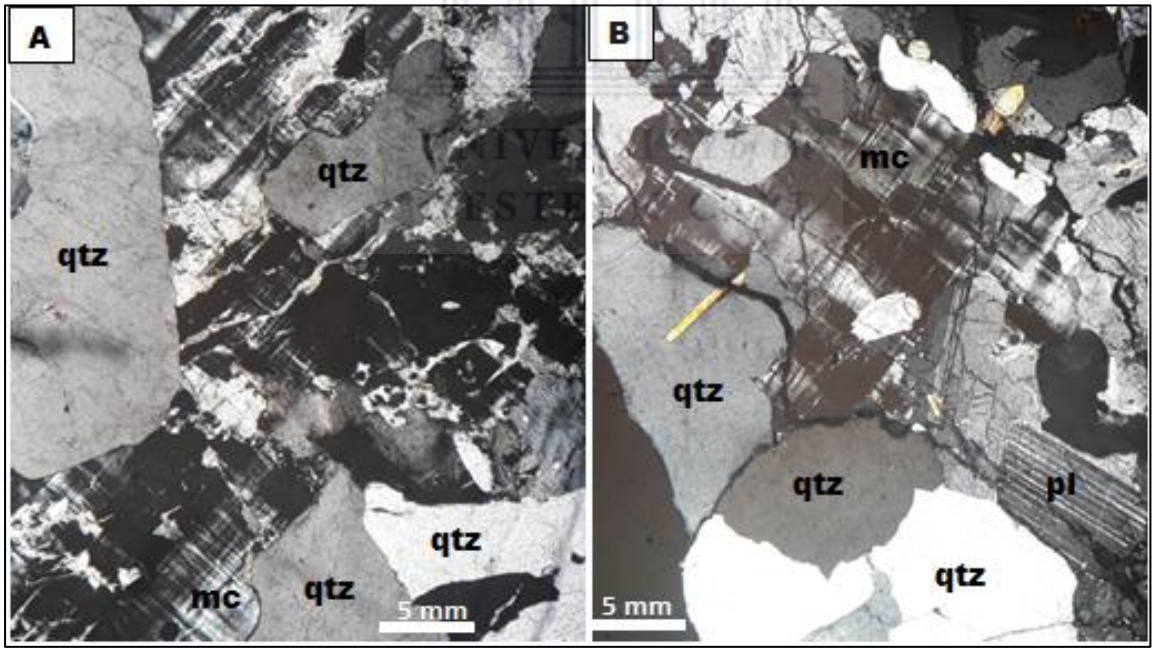

Fig. 2.30. Photomicrographs of a sample from the non-foliated granite using a transmitted light microscope. A. & B. Quartz (qtz), microcline (mc) and plagioclase (pl) taken at 4× MAGN (both images were taken under XPL).

Table 2.4 A summary of mineral abundance observed at the Sandamap prospect.

Sampling locality	Lithology Sampled	Mineral	Abundance (%)	Grain size	Texture
T4	Quartz vein	Quartz	50	Coarse	Massive
		Hematite	49	Coarse	Intergrowth
		Cummingtonite	1	Coarse	Fibrous
T14	Quartz vein	Quartz	70	Coarse	Massive
		Tourmaline	6	Medium	Fairly disseminated subhedral grains in clay
		Clay	15	Fine	Massive
		Biotite	5	Coarse	Skeletal
		Muscovite	4	Coarse	Skeletal
T15	Hydrothermal altered schist with quartz veinlets	Quartz	60	Coarse	Intergrowth/ massive
		Biotite	20	Coarse	Granular, massive, enveloping the garnet
		Cummingtonite	5	Medium	Granoblastic
		Hematite	4	Coarse	Intergrowth
		Goethite	2	Coarse	Intergrowth
		Garnet	3	Coarse	Skeletal
		Muscovite	5	Coarse	Granular /massive
		Pyrite	1	Medium	Sparsely disseminated subhedral grains in quartz
NF	Non-foliated leucogranite	Quartz	30	Coarse	Granular
		Plagioclase	20	Coarse	Granular
		Microcline	50	Coarse	Granular

2.7 QUARTZ VEIN SYSTEM

The general observation is that the quartz veins are roughly parallel to shear zone foliation, varying in thickness from roughly 1 or less cm to approximately 20 cm. The ferruginous quartz veins at trench 4 are parallel or roughly subparallel to the shear zone foliation and are characterized by notable quantity of haematite (Fig. 2.11). The quartz veins at sampling point NO 2 are parallel or subparallel to the shear zone foliation. Some portions of the vein quartz at this locality have noticeable reddish tint indicating the presence of haematite (Fig. 2.18). The quartz veins at trench 14 are lenticular shaped (Fig. 2.31) and lie parallel / subparallel to the shear zone foliation. The veins are void of visible haematite (Fig. 2.15). The veining system at trench 15 consists of quartz veins with a cross-cutting relationship; a set of top veins lying approximately perpendicular to the shear zone foliation and another set parallel to the shear zone foliation (Fig. 2.32). The quartz veins at this locality do not have noticeable haematite. The general observation is that the content of visible haematite increases southwest-wards while the analysed gold content is higher at localities in the opposite direction. The paragenetic sequence of the veins could not be established, but what has been

determined from type I fluid inclusions is that the veins contain fluids that have been deposited at different temperatures (Fig. 4.7) through fracturing and healing, translating into pressures and depths (Fig. 4.29) and this by implication means deposition at different times.

Fig.2.31. Lenticular shaped vein quartz samples from trench 14 (Sandamap), found lying subparallel to the shear-zone schistosity.

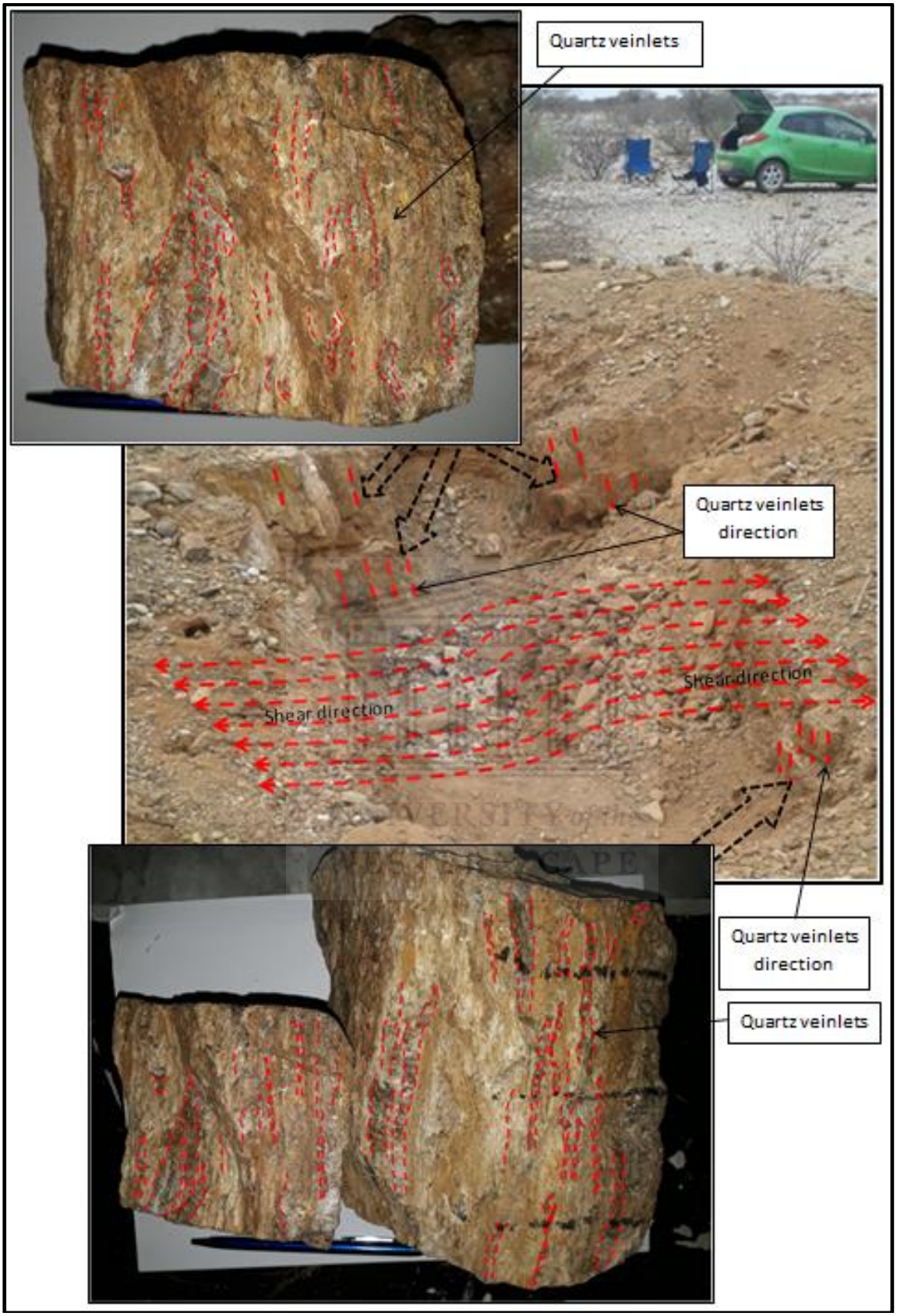

Fig. 2.32. Cross-cutting relationships between pre-failure extension veins and post-failure discharge veins; a common fault-valve behaviour feature. Noted at trench 15 are subhorizontal quartz veinlets lying perpendicular to subvertical shear zones (Sibson, 1990; Chi, and Guha, 2011).

2.8 ROCK ALTERATIONS /ALTERATION ZONES

In petrography, a kaolinite/ dickite alteration zone with tourmaline was observed in samples from trench 14 (Fig. 2.23) and at trench 15, a garnet bearing alteration zone was noted where micas wrap around (this is assumed to be a deformation feature) and partially replace garnet (Fig. 2.25). The garnets did not form during hydrothermal alteration and are interpreted remnants from past metamorphism and but it could not be established as to whether they are pre- or syn-tectonic. A number of zones were observed at trench 15; a zone with quartz veinlets, biotite-rich zone, muscovite-rich zone, Kaolinite/dickite and jarosite-rich zone (Fig. 2.33). XRD results indicated the presence of kaolinite, alunite and dickite at trench 15. Dickite, kaolinite and jarosite were observed at trenches 14 and 15. Alunite forms at temperatures between 15°C and 400°C by action of sulfate or solfataric action on aluminous rocks (Handbook of Mineralogy, 2001). Jarosite possibly formed at temperatures below 200 °C (Frost et al., 2005). Kaolinite form at low temperatures of less than 150-200°C (Corbett and Leach, 1998). Kaolinite forms by replacement of other aluminosilicate minerals during hydrothermal alteration and weathering (Handbook of Mineralogy, 2001). Dickite is an important alteration indicator which forms partly from the alteration of aluminosilicate minerals (Handbook of Mineralogy, 2001). Alunite, kaolinite and dickite are indicative of advanced argillic alteration (Corbett and Leach, 1998; Georgieva and Velinova, 2012). Hydroniumjarosite determined by XRD in a sample from trench 14 occur in oxidized zone of rapidly weathering sulfide−bearing rocks (Handbook of Mineralogy, 2001).

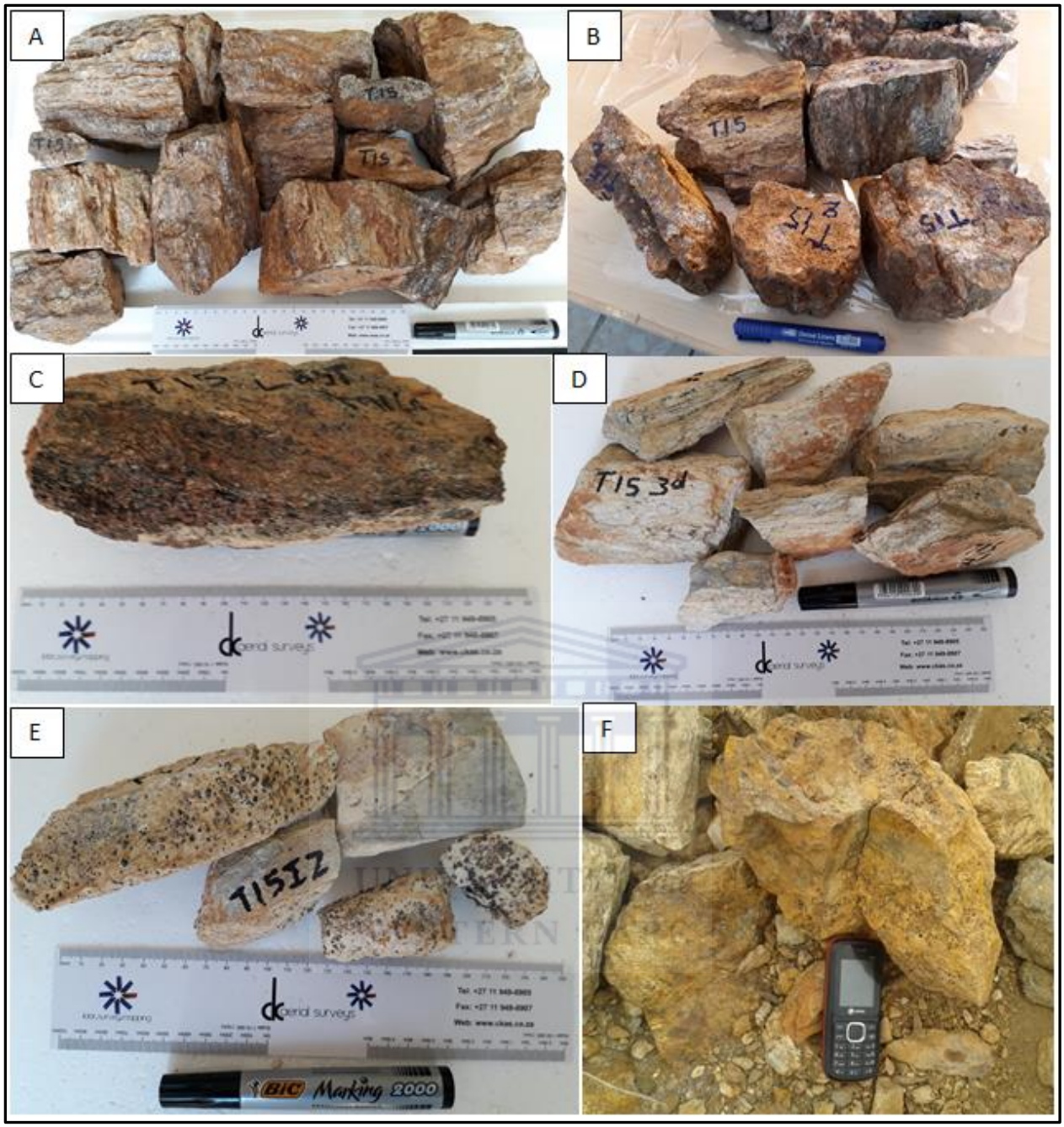

Fig.2.33. Hydrothermal zone samples from trench 15. Samples A and B are interpreted as from the outer most zone, followed in alphabetical order with sample F being from the inner most. A & B. Samples from a zone composed of quartz veinlets, cummingtonite, jarosite and mica, C. Sample from biotite-rich zone with iron oxide, D. Sample from muscovite-rich zone within quartz, alunite and calcite, E. Sample from kaolinite/dickite-rich zone with alunite, quartz and garnet, F. Sample from jarosite-rich zone with calcite veinlets.

2.9 REFERENCES

Corbett, G. J., & Leach, T. M. (1998). *Southwest Pacific Rim gold-copper systems: structure, alteration, and mineralization* (No. 6). Boulder, Co: Society of Economic Geologists.

Craig, J.R. and Vaughan, D.J. (1994). *Ore Microscopy and Ore Petrography (2nd edition).* Wiley Interscience, New York.

Downing, K.N. 1982. *The evolution of the Okahandja Lineament and its significance in Damaran tectonics (Namibia).* Unpubl. Ph.D. thesis, Univ. Leeds, 242 pp.

Frommurze, H.F., Gevers, T.W., Rossouw, P.J. 1942. *The geology and mineral deposits of the Karibib area, South West Africa*. Explanation to Sheet 79, Geological Survey of South Africa, 172 pp.

Georgieva, S., & Velinova, N. (2012). Alunite from the advanced argillic alterations in the Chelopech high-sulphidation epithermal Cu-Au deposit, Bulgaria: Chemistry, morphology and genetic significance. *Geochemistry, Mineralogy and Petrology*, *49*, 17-31.

Haack, U., Gohn, E. and Klein, J.A. 1980. Rb/Sr ages of granitic rocks along the middle reaches of the Omaruru River and the timing of orogenic events in the Damara belt (Namibia). *Contributions to Mineralogy and Petrology*, **74**, 349-360.

Handbook of Mineralogy. (2001). Mineral Data Publishing (version 1.2) [PDF file]. Retrieved from http://rruff.info/doclib/hom/

Holdaway, M.J. 1971. Stability of andalusite and the aluminium silicate phase diagrams. *American Journal of Science*, **271**, 97-131.

Jacob, R.E. 1974. Geology and metamorphic petrology of part of the Damara Orogen along the lower Swakop River, South West Africa. *Bull. Precambr. Res. Unit, Univ. Cape Town,* **17**, 185 pp.

Miller, R.M. 1983. The Pan-African Damara Orogen of S.W.A./Namibia. *Special Publication of the Geological Society of South Africa*, **11**, 431-515.

Miller, R.M., 2008. Neoproterozoic and early Palaeozoic rocks of the Damara Orogen. In: Miller, R.M. (Ed.). The Geology of Namibia. Geological Survey of Namibia, Windhoek vol. 2, pp. 13-1–13-410.

Nash, C.R. 1971. Metamorphic petrology of the SJ Area, Swakopmund District, South West Africa. *Bull. Precambr. Res.Unit, Univ. Cape Town*, **9**, 77 pp.

Petzel, V.F.W. 1990. Progress report on geological exploration conducted on the farm Sandamap Noord 15 - Damaraland District. Unpubl. rep., Gold Fields Namibia Ltd., 37 pp.

Raith, M.M., Raase, P.R., and Reinhardt, J.R. 2011. *Guide to thin section microscopy*. University of Bonn.

Steven, N.M. 1993. A study of epigenetic mineralization in the Central Zone of the Damara Orogen, Namibia with special reference to gold, tungsten, tin and rare earth elements. *Memoir of the Geological Survey of Namibia*, **16**, 166 pp.

Steven, N.M., Badenhorst, F.P. and Petzel, V.F.W. 1994. A review of gold occurrences in the northern and central zones of the Damara Orogen and the underlying mid-Proterozoic basement, central Namibia. *Communications of the Geological Survey of Namibia*, **9**, 63-77.

CHAPTER 3

GEOCHEMISTRY

This chapter mainly details the chemical composition of the ore and country rocks. The chapter covers: (i) mineral identification using X-ray powder diffraction (XRD) to identify minerals present in the samples of interest, (ii) gold content analysis using fire assay to examine the concentration of gold in the ore and country rocks, (iii) major element analysis using Fusion x-ray fluorescence (XRF) to carry out a comparative (correlation) assessment between the XRF and XRD results to assess the balance between major element geochemistry and the mineralogy present in the rocks, (iv) minor and trace element analysis using Inductively Coupled Plasma Optical Emission Spectroscopy (ICP-OES) to assess the existence of any trends and correlations between ore samples from different localities as well as (v) carrying out a correlation assessment between ore samples and the country rock to assess as to whether or not there was a likely influence on the ore content and composition by the surrounding country rock.

3.1 GEOCHEMICAL ANALYSIS

Ore samples, which are dominantly vein quartz samples, were crushed and pulverised at the Geological Survey of Namibia. Each sample was halved and the first halves were used to carry out XRD analysis at the aforementioned Geological Survey's lab. The other halves were sent to a commercial Lab (Scientific Services Pty. Ltd.) in Cape Town for fire assay, Inductively Coupled Plasma Optical Emission Spectroscopy (ICP-OES) and Fusion X-Ray Fluorescence (XRF) analysis.

3.1.1 X-RAY DIFFRACTION (XRD) ANALYSIS RESULTS

X-ray diffraction analyses were carried out on ore-samples to identify the minerals present, and to establish whether or not the identified minerals have any relationship with the envisaged hydrothermal origin interpretation. XRD analysis results of the ore samples (T4, T14, T15, NO2) and a non-ore sample (T6) are shown in Fig. 3.1 and are given in Table 3.1.

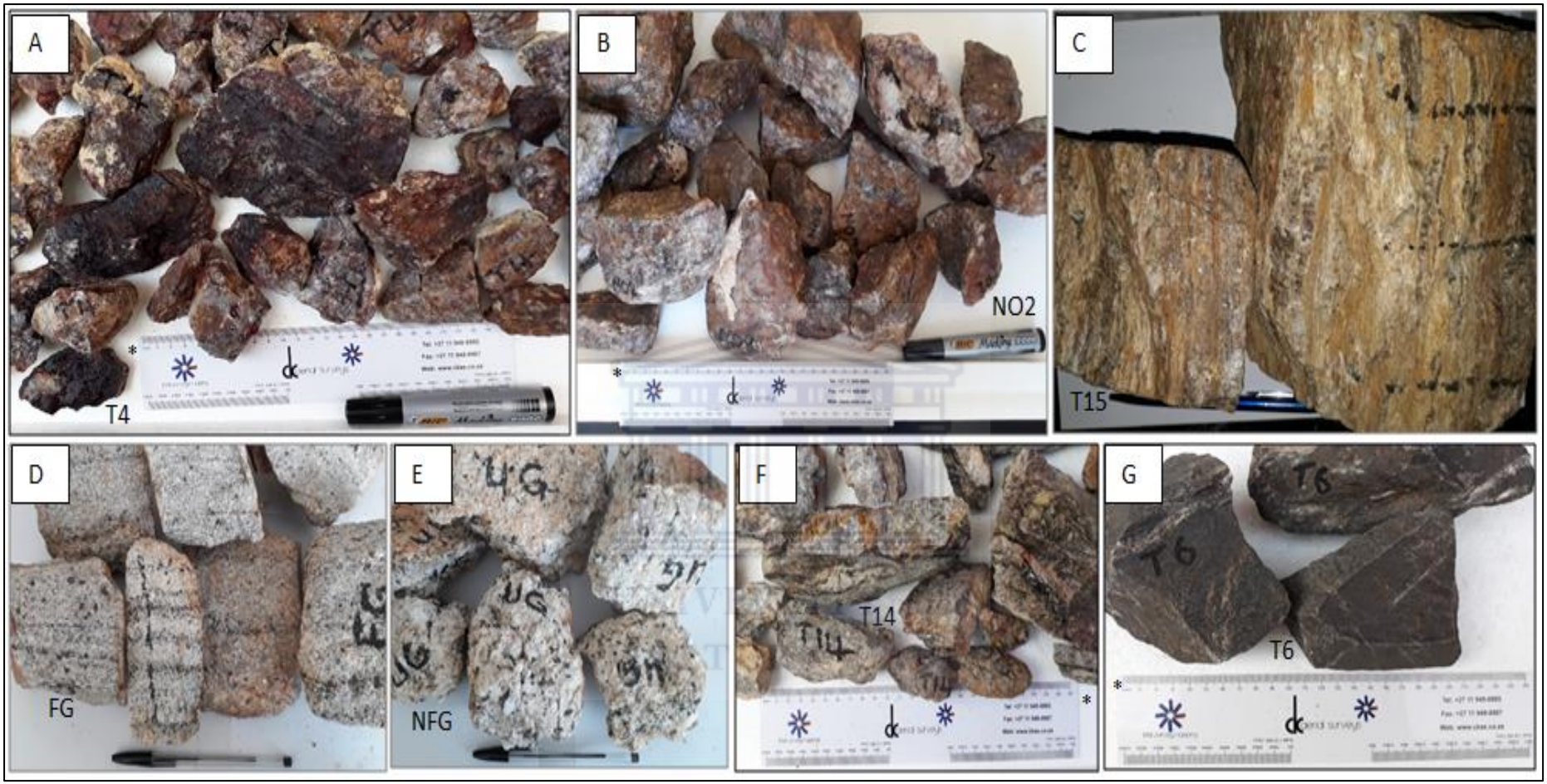

Fig. 3.1 Representative samples on which geochemical analysis were carried out. A. Ferruginous vein quartz from trench 4, B. Vein quartz (NO2), C. Hydrothermal rock showing layers of vein quartz from trench 15, D. Foliated granite, E. Non foliated pegmatitic granite, F. Vein quartz in association with schist from trench 14, G. Carbonate rock sample from trench 6. (*The ruler is 25 cm long, pen is 15 cm)

The ore samples are predominantly composed of vein quartz, and the quartz veins are hosted by sheared sillimanite biotite schist. The non-ore sample (T6) forms part of the country rock and was found within a proximal distance of the ore veins in trench 6 (Fig. 2.8). The sample is composed of mainly calcite, dolomite, quartz and almandine and may be described as a dark grey limestone which was sampled mainly for characterisation. Among the ore samples only NO2 is dominantly composed of vein quartz, with sample T4 composed of vein quartz and hematite, and T14 composed of vein quartz, dickite and jarosite (Table 3.1). T15 is composed of a variety of hydrothermal minerals which includes vein quartz, cummingtonite, calcite, albite, muscovite, mimetite, kaolinite, alunite and dickite (Table 3.1).

Table 3.1 XRD analytical results of the ore samples.

Sample No.	XRD analysis results
NO2	Quartz
T4	Quartz, hematite
T6	Calcite, dolomite, quartz, almandine
T14	Quartz, dickite, hydronium jarosite
T15	Quartz, cummingtonite, calcite, albite, muscovite, kaolinite, alunite, dickite

3.1.2 FIRE ASSAY, ICP-OES AND FUSION XRF METHODS

Pulverised vein quartz samples from trenches 4, 6, 14 and 15, and from vein quartz (NO2) in the shear zone were analysed for gold at a commercial laboratory in Cape Town (Scientific Services Pty Ltd) by fire assay. The results are given in Table 3.2. The samples were also analysed for trace elements at the same lab by Inductively Coupled Plasma Optical Emission Spectroscopy (ICP-OES) and Fusion X-Ray Fluorescence (XRF) methods and the results are given in Tables 3.3 and 3.4, respectively. For quality assessment standards (ST265 for Fire assay, AMIS 55 for XRF, GBM315-5 for ICP-OES) with certified values were analyzed and contamination was checked by analyzing a blank. Details of the analytical procedures are given in Appendix O.

3.1.3 RESULTS

3.1.3.1 ANALYTICAL RESULTS FOR FIRE ASSAY

Fire assay analysis was undertaken to assess the concentration of gold in the quartz veins and the results thereof are given in Table 3.2. Samples from trenches 14 (T14) and 15 (T15) gave the highest grades of 1.937 ppm and 1.634 ppm respectively (Table 3.2). This was followed by the amphibolite schist xenolith sample (T9AM) which was sampled from the fragment located within the non-foliated pegmatitic granite; this gave a grade of 0.72 ppm (Table 3.2). The non-foliated granite which hosts the amphibolite schist failed to yield any gold content. The lowest grades were recorded in samples from trench 4 and NO2 which gave 0.117 ppm and 0.018 ppm respectively (Table 3.2). Some country rock samples also yielded some gold contents of 0.07 ppm and 0.05 ppm from the foliated granite (FG) and schist (SCT) respectively (Table 3.2). Taking into account the gold concentration of 0.05 ppm in the schist the gold content of 0.018 ppm obtained from sample NO2 is thus regarded as background. Any gold concentration below the detection limit 0.05 ppm was not detected. The carbonate rock (T6) also failed to yield any gold content. Other elements which were analyzed together with gold by fire assay in the samples are platinum and palladium whose results proved negative.

Table 3.2 Fire assay analytical results for gold, platinum and palladium. ST265 is the standard used during analysis.

Sample ID	Au (ppm)	Pt (ppm)	Pd (ppm)
Blank	**<0.005**	**<0.005**	**<0.005**
ST265	**0.473**	**0.935**	**0.683**
T4	0.117	<0.005	<0.005
T6	<0.005	<0.005	<0.005
T14	1.937	<0.005	<0.005
T15	1.634	<0.005	<0.005
NO2	0.018	<0.005	<0.005
FG	0.07	-	-
NFG	<0.05	-	-
T9AM	0.72	-	-
SCT	0.05	-	-

3.1.3.2 MAJOR ELEMENT CONCENTRATIONS IN ORE SAMPLES: FUSION XRF

Major element analysis was carried out on the ore samples using fusion XRF to assess the concentration of major elements in the ore samples. The mineralization is hosted by vein quartz, however XRF results depict lower concentrations of SiO_2 (60 – 71.5 wt.% SiO_2) than would be expected in a dominantly quartz specimen, with an exception for sample NO2 which yielded 95 wt.% SiO_2 (Table 3.3). This is attributed to the following reasons: the lower concentration of SiO_2 in sample T4 is due to the dominant hematite which is notable in samples (Fig. 3.1A) and also identified by XRD (Table 3.1) and mirrored by the high concentration of Fe_2O_3 in the XRF results (Table 3.3). The lower concentration of SiO_2 in sample T14 is likely due to loss of water components from dickite and jarosite identified by XRD (Table 3.1). This loss is attributed to the Loss On Ignition (LOI) process and is accounting for 25.04 wt.% as seen in the XRF results (Table 3.3). The lower SiO_2 value in T15 is likely due to the presence of iron oxides and the loss of water during LOI determination potentially from cummingtonite, muscovite, kaolinite, alunite and dickite (T15 - Table 3.1). For the non-ore carbonate sample (T6) the high LOI value is due to the loss of CO_2 and the high CaO content reflects the carbonate-rich characteristic of the sample (Table 3.1).

Sample T4 is dominantly vein quartz and hematite and this is mirrored by the XRF results which are given as 70.75 wt.% SiO_2 and 25.61 wt.% Fe_2O_3 with the remaining analysed oxides giving measurements below 1 wt.% (Table 3.3). The silica content of sample T14 is 65.25 wt.% SiO_2 followed in abundance by LOI which accounted for 25.04 wt.% (attributed to loss of water from hydronium jarosite, dickite, muscovite and biotite) while other notable contents were obtained from Fe_2O_3 and Al_2O_3 which yielded 3.43 wt.% and 3.36 wt.% respectively (Table 3.3). The remainder of the analysed major oxides in T14 are below 1 wt.% (Table 3.3). The relatively notable wt.% values of Fe_2O_3 and Al_2O_3 in T14 are likely due to the presence of hydronium jarosite and dickite. Sample T15 yielded a silica content of 61.67 wt.% SiO_2 and an iron content of 23.18 wt.% Fe_2O_3 which is likely reflecting the presence of cummingtonite (Tables 3.1 & 3.3, Fig. 2.33) and iron oxides (Figs. 2.27 & 2.28). Two other pronounced oxide values in T15 are MgO and CaO with values of 3.56 wt.% and 1.11 wt.% respectively (Table 3.3). The remainder of the analysed oxides in T15 gave values

below 1 wt.%. The comparatively notable value of MgO in T15 is likely due to contributions from cummingtonite and the CaO value is likely due to contributions from calcite.

The silica content of sample NO2 reflects results which would be expected from a dominantly quartz specimen, yielding a value of 95.78 wt.% SiO_2 (Table 3.3). Other notable values yielded by NO2 are 1.43 wt.% Fe_2O_3 and 1.00 wt.% Al_2O_3, with the remaining analysed oxides recording values below 1 wt.% (Table 3.3). The oxides concentrations of the non-ore carbonate sample (T6) are as follows in their order of abundance: 30.89 wt.% CaO, 19.77 wt.% SiO_2, 7.39 wt.% Al_2O_3, 5.40 wt.% Fe_2O_3 and 1.96 wt.% MgO, with the remaining oxides yielding values below 1 wt.% (Table 3.3). The relatively elevated oxide values in T6 are likely attributed to the presence of the following minerals identified by XRD: CaO likely due to calcite and dolomite, SiO_2 likely due to quartz, Al_2O_3 and Fe_2O_3 are likely due to almandine, and, lastly, MgO is likely due to dolomite (Table 3.1).

Table 3.3 Major element analytical results of the ore samples which are visibly dominated by vein quartz (Analytical technique: Fusion XRF). The results are generally in agreement with the XRD results.

Sample ID	SiO_2 %	Al_2O_3 %	TiO_2 %	Fe_2O_3 %	MgO %	CaO %	Na_2O %	K_2O %	MnO %	P_2O_5 %	Cr_2O_3 %	SO_3 %	LOI %	Total
AMIS 55	36.00	4.70	0.20	3.60	0.59	27.00	0.34	0.69	0.10	21.25	0.07	0.18	3.39	98.12
T4	70.75	0.36	0.03	25.61	0.10	0.89	0.05	0.06	0.05	0.04	0.03	0.32	2.24	100.53
T6	19.77	7.39	0.41	5.40	1.96	30.89	0.36	0.64	0.03	0.10	0.01	0.10	31.61	98.67
T14	65.25	3.36	0.10	3.43	0.22	0.72	0.21	0.82	0.01	0.10	0.01	0.93	25.04	100.22
T15	61.67	0.42	0.03	23.18	3.56	1.11	0.37	0.26	0.40	0.03	0.02	0.84	5.28	97.15
NO2	95.78	1.00	0.03	1.43	0.09	0.06	0.00	0.27	0.01	0.01	0.03	0.05	0.26	99.01

3.1.3.3 **CORRELATION ASSESSMENT BETWEEN XRD AND XRF RESULTS**

The majority of the minerals identified in the ore samples (T4, T14, T15, NO2) are not uncommon in hydrothermal environments. The relationship between the observed minerals and Sandamap gold's environment of formation (hydrothermal system) is as follows: *Quartz* occurs in hydrothermal veins and in hydrothermal metal deposits; *hematite* may precipitate from mobile hydrothermal fluids seeping through a rock unit; *hydronium jarosite* occurs in oxidized zone of rapidly weathering sulfide−bearing rocks; *dickite* is commonly of hydrothermal origin formed partly from the alteration of aluminosilicate minerals and as such an important alteration indicator in hydrothermal systems; *cummingtonite* commonly occurs in metamorphosed magnesium−rich rocks and in amphibolites and there are also reports of

the mineral's occurrence in hydrothermal deposits, *calcite* occurs as gangue in hydrothermal veins; *albite* may occur in some hydrothermal vein deposits; *muscovite* is formed from other minerals under hydrothermal conditions, *kaolinite* forms by replacement of other aluminosilicate minerals during hydrothermal alteration and weathering; and lastly *alunite* is an analog of jarosite, where aluminium replaces Fe^{3+} and forms by action of sulfate or solfataric action on aluminous rocks (Handbook of Mineralogy, 2001).

Quartz and hematite identified by XRD in the sample from trench 4 (T4) are also mirrored by high concentrations of SiO_2 (71 wt.%) and Fe_2O_3 (26 wt.%) yielded from the same sample by XRF analysis. Calcite, dolomite, quartz, almandine identified in XRD from trench 6 (T6) are represented by CaO, MgO, SiO_2, Al_2O_3, Fe_2O_3 and a high LOI due to CO_2 loss in XRF results. Quartz, dickite, hydronium jarosite identified in XRD from trench 14 (T14) are represented by SiO_2, Al_2O_3, Fe_2O_3 and a high LOI due to water loss from dickite and hydronium jarosite in XRF results. Quartz, cummingtonite, calcite, albite, muscovite, kaolinite, alunite, dickite identified in XRD from trench 15 (T15) are represented by SiO_2, Fe_2O_3, MgO, CaO, Na_2O, Al_2O_3, and K_2O in XRF results.

3.1.3.4 MINOR AND TRACE ELEMENT CONTENTS IN ORE AND COUNTRY ROCK SAMPLES: ICP-OES

Trace element analyses were carried out on the country rocks and vein samples in an effort to establish whether or not there are some pronounced geochemical similarities between the ore samples and proximal country rock. Trace element ICP-OES analytical results are given in Tables 3.4 & 3.5.

There are no notable trace element content similarities between the ore samples and the surrounding country rock samples. Noteworthy are the elevated contents of arsenic in ore samples correlating with relatively high quantities of gold (samples T14, T15 & T9AM) (Table 3.4). Sample T4, whose gold content is 0.117 ppm, has relatively elevated quantities of base metals (Zn, Pb, Cu) with Zn concentrations as high as more than twentyfold that of the background which is given as 55 ppm (Table 3.4). Another noteworthy concentration is the amount of the minor element manganese in the schist which is roughly twofold (1021.3 ppm) the quantity of the second highest sample (T9AM: 511.4 ppm) (Table 3.5). Apart from the above none of the remainder of the analytical results are comparatively different to background concentrations (Tables 3.4 & 3.5).

Table 3.4 Minor and trace element analytical results of the ore samples which are visibly dominated by vein quartz (Analytical technique: ICP-OES).

Sample #	Ag (ppm)	As (ppm)	Ba (ppm)	Be (ppm)	Bi (ppm)	Cd (ppm)	Ce (ppm)	Co (ppm)	Cu (ppm)	La (ppm)	Mo (ppm)	Ni (ppm)	Pb (ppm)	Sc (ppm)	Th (ppm)	V (ppm)	Y (ppm)	Zn (ppm)
Blank	**0.2**	**0.0**	**0.1**	**0.0**	**0.8**	**0.0**	**1.0**	**0.0**	**0.6**	**0.0**	**0.0**	**1.2**	**0.0**	**0.0**	**0.4**	**0.0**	**0.0**	**1.5**
GBM315-5	**12.1**	**73.7**	**68.5**	**0.7**	**1.2**	**2.5**	**28.5**	**8.8**	**46.8**	**15.5**	**1.5**	**4.0**	**70.4**	**3.4**	**5.3**	**34.5**	**6.1**	**145.2**
T4	1.9	254.0	117.8	3.6	0.0	5.4	2.8	11.7	139.0	2.8	13.3	29.5	653.8	6.4	0.0	225.0	1.6	1535.3
T6	0.6	18.5	435.9	10.2	0.0	1.0	7.6	2.8	42.6	4.4	2.9	9.6	65.3	4.0	4.9	37.0	3.6	55.4
T14	0.2	1413.4	113.5	0.4	16.4	1.1	2.0	2.9	14.5	1.3	7.5	6.6	9.9	11.3	0.0	36.0	1.1	10.9
T15	1.0	16978.7	188.1	0.4	11.6	3.5	1.4	5.0	50.7	0.0	5.9	27.6	6.6	0.8	0.0	67.3	0.4	17.2
NO2	0.2	245.1	12.6	0.5	1.4	0.3	0.0	0.7	11.2	0.7	13.3	4.8	7.1	0.1	0.0	21.5	1.7	5.2
T9AM	<2.0	738.5	-	<2.0	4.7	<2.0	-	<2.0	48.9	-	2.0	14.4	<2.0	<2.0	<2.0	52.4	2.3	15.0

Table 3.5 Minor and trace element analytical results of the country rock (FG: foliated granite, NFG: non –foliated granite, T9AM: amphibolite schist xenoliths within FG, SCT: sillimanite biotite schist. (Analytical technique: ICP-OES).

Sample #	Ag (ppm)	As (ppm)	Be (ppm)	Bi (ppm)	Cd (ppm)	Co (ppm)	Cu (ppm)	Ge (ppm)	Mn (ppm)	Mo (ppm)	Ni (ppm)	Pb (ppm)	Re (ppm)	S (ppm)	Sb (ppm)	Sc (ppm)	Se (ppm)	Sr (ppm)	Th (ppm)	V (ppm)	Y (ppm)	Zn (ppm)
Blank	**<2.0**	**<2.0**	**<2.0**	**<2.0**	**<2.0**	**<2.0**	**<2.0**	**<2.0**	**<2.0**	**<2.0**	**<2.0**	**<2.0**	**<2.0**	**<10**	**<2.0**	**<2.0**	**<2.0**	**<2.0**	**<2.0**	**<2.0**	**<2.0**	**<2.0**
GBM315-5	**14.5**	**71**	**0.5**	**2**	**2.0**	**8.8**	**46.0**	**0.0**	**942**	**1.9**	**4.1**	**68.7**	**<2.0**	**9591**	**4.1**	**3.8**	**5.7088**	**64.4**	**3.1**	**36.1**	**6.1**	**144**
FG	<2.0	3.6	<2.0	3.6	<2.0	<2.0	3.0	<2.0	493.4	10.2	4.3	4.6	<2.0	48	<2.0	<2.0	<2.0	3.9	<2.0	10.1	2.8	4.9
NFG	<2.0	<2.0	<2.0	<2.0	<2.0	<2.0	2.4	<2.0	115.2	12.0	3.4	6.1	<2.0	24	<2.0	<2.0	<2.0	3.0	<2.0	11.3	3.1	4.5
T9AM	<2.0	738.5	<2.0	4.7	<2.0	<2.0	48.9	<2.0	511.4	2.0	14.4	<2.0	<2.0	261	<2.0	<2.0	3.1	35.9	<2.0	52.4	2.3	15.0
SCT	<2.0	50.9	2.0	<2.0	2.9	16.4	24.5	<2.0	1021.3	7.7	30.5	17.9	<2.0	280	4.8	15.6	10.5	53.7	10.1	109.6	9.8	44.4

3.1.3.5 HARKER BINARY PLOTS AND MASS-BALANCE PROCEDURES

The SiO_2 contents of the vein quartz samples from Sandamap vary from 61.67 to 95.78wt%. The Harkar binary plots (Fig. 3.2) of SiO_2 vs major oxides do not show any correlations, which point towards non-igneous origin. In igneous rocks, correlations are attributed to frationation during crystalisation (Cortés, 2009).

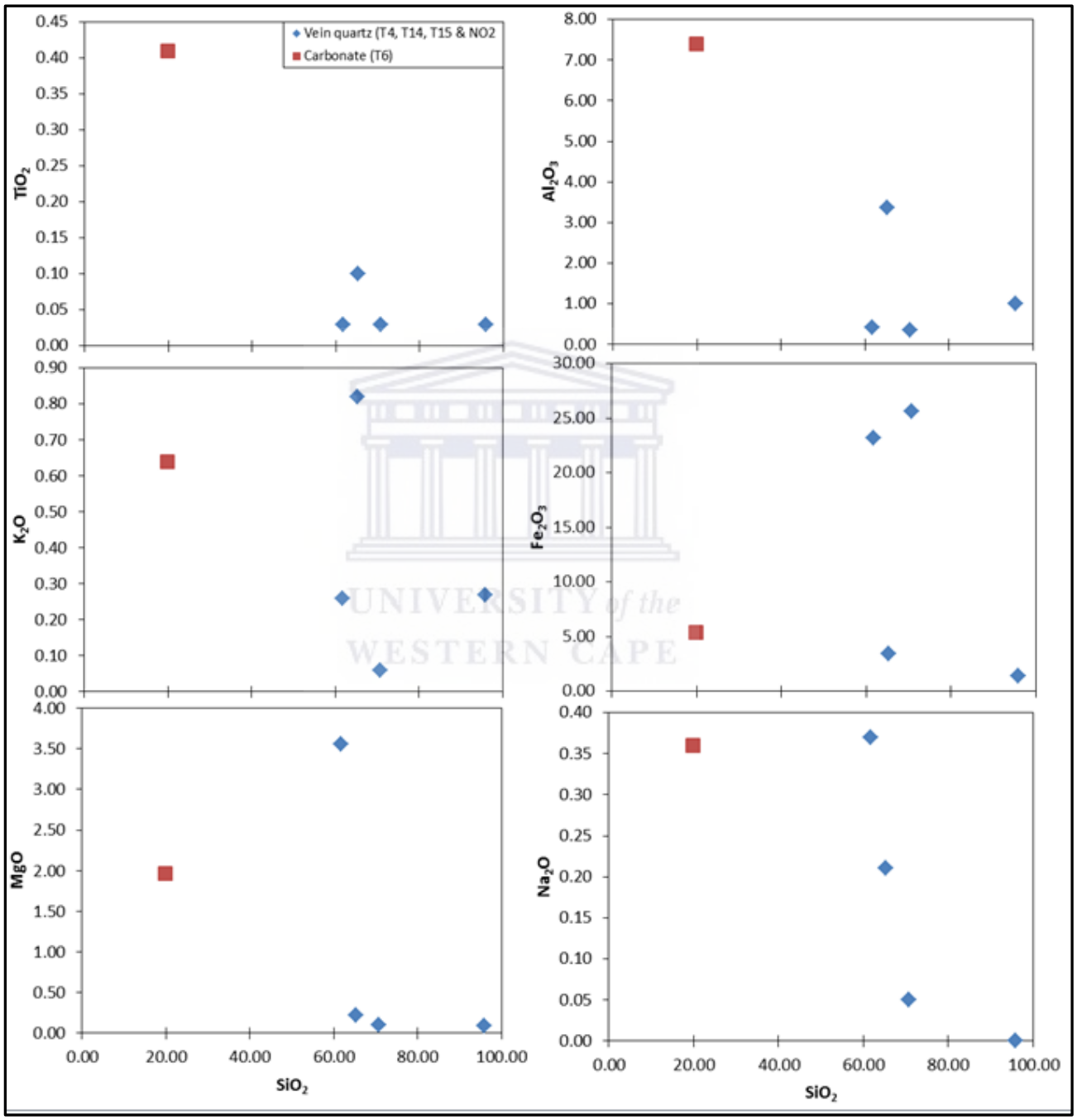

Fig. 3.2. Binary plots showing the geochemical variation of ore quartz vein samples from Sandamap deposit. The purpose of these plots is to indicate that correclation between SiO_2 and major oxides does not exist and the implication being that the quartz veins are of non-igneous origin.

3.2 REFERENCES

Benkó, Z., Mogessie, A., Molnár, F., Krenn, K., Poulson, S.R., Hauck, S., Severson, M. and Arehart, G.B. (2015). Hydrothermal alteration and Cu–Ni–PGE mobilization in the charnockitic rocks of the footwall of the South Kawishiwi intrusion, Duluth Complex, USA. *Ore Geology Reviews*, 67, 170-188.

Cortés, J. A. (2009). On the harker variation diagrams; a comment on "the statistical analysis of compositional data. Where are we and where should we be heading?" by Aitchison and Egozcue (2005). Mathematical Geosciences, 41(7), 817–828

Handbook of Mineralogy. (2001). *Mineral Data Publishing (version 1.2)* [PDF file]. Retrieved from http://rruff.info/doclib/hom/

Li, R., Albert, N. N., Yun, M., Meng, Y., & Du, H. (2019). Geological and Geochemical Characteristics of the Archean Basement-Hosted Gold Deposit in Pinglidian, Jiaodong Peninsula, Eastern China: Constraints on Auriferous Quartz-Vein Exploration. *Minerals*, *9*(1), 62.

Sein, M. M., van Leeuwen, W., & Glörfeld, P. (2017). Combination of Fire Assay and Modern Instrumental Techniques for Precious Metals Analysis. Retrieved from https://img-labor.de/wp-content/uploads/2017/09/Combination-of-Fire-Assay-and-Modern-Instrumental-Techniques-for-Precious-Metals-Analysis.pdf

Steven, N. M. (1993). A study of epigenetic mineralisation in the Central Zone of the Damara Orogen, Namibia with special reference to gold, tungsten, tin and rare earth elements. *Communications of the Geological Survey of Namibia*, *8*, 157-159.

CHAPTER 4

FLUID INCLUSION STUDIES

Fluid inclusions contain abundant clues that can help us understand the processes which produced the earth (Roedder & Bodnar, 1997). The study of fluid inclusions has provided us with important data on probable sources and paths of the ore fluids, and almost all of the known data on the composition, densities, temperatures and pressures of hydrothermal ore fluids (Roedder & Bodnar, 1997).

When studying fluid inclusions there are five basic assumptions that have to be taken into consideration (Roedder & Bodnar, 1997):

1) The inclusion is trapped as a single homogeneous phase for fluid inclusions having the same composition, or a heterogeneous phase for fluid inclusions having two immiscible fluids, boiling solution or saturated solution.
2) Nothing is added to, or removed from the inclusion after trapping,
3) The volume of the cavity surrounding the fluid does not decrease or increase after trapping,
4) The relationship of the fluid inclusion to the process being investigated is known, and
5) The effects of pressure are insignificant or are known.

4.1 SAMPLE PREPARATION AND ANALYSIS FOR MICROTHERMOMETRY

Doubly polished thick wafers (~200 μm thick) of vein quartz samples collected from trenches 4, 14, 15 and 15N were prepared at UCT, then sized to fit the diameter of the low temperature sample holder of the Linkam THMSG600 stage. The sampling points are T4, NO2, T14, T15 and T15N (Fig. 4.1). All samples were collected from historical trenches except those from sampling point NO2 that were collected from a quartz vein in a shear zone outcrop.

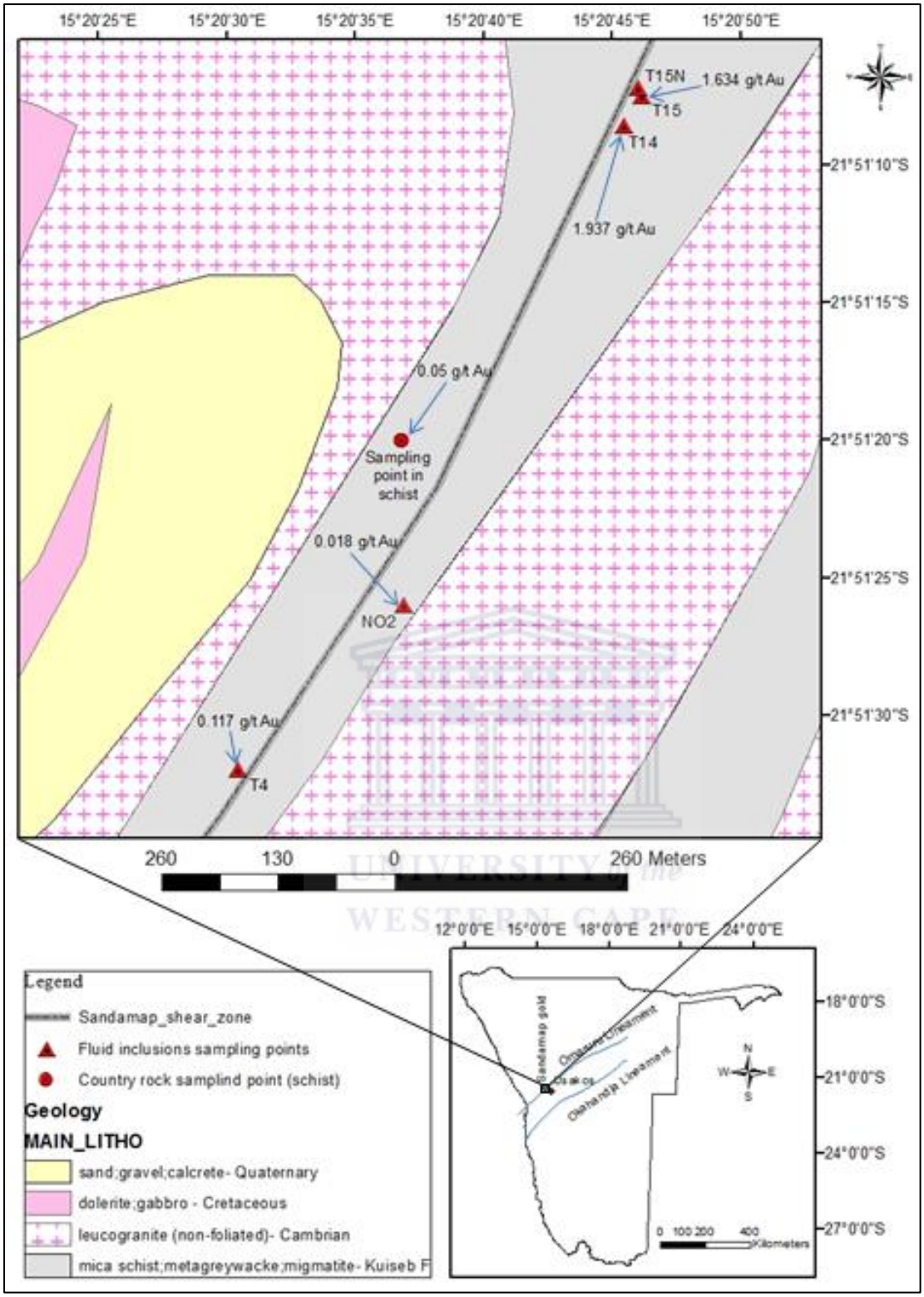

Fig. 4.1. Sampling points T4, NO2, T14, T15 and T15 N where vein quartz samples for fluid inclusion studies were collected. Note: the shear zone width is wider than indicated in the map. Fire assay gold grades are also indicated at some sampling localities along the shear zone.

Microscopic studies were carried out to determine phases, relative inclusion volume, shapes and sizes at UWC. Fluid inclusions were selected, sketches done and classification of fluid inclusions were carried out in terms of their relative ages (primary vs. secondary inclusions).

Microthermometry was carried out on selected inclusions and this involved cooling and heating experiments to determine final melting and homogenization temperatures. Images were captured at various temperatures. Inclusions were first cooled to −100°C or −180°C, depending on the final freezing temperature of the individual inclusions and phase transition temperature measurements were recorded during the heating process. **The following measurements were recorded:**

- **$T_{m(ice)}$:** The final temperature of ice melting in aqueous inclusions (solid + liquid + gas = liquid + gas),
- **$T_{m(CO2)}$:** The final temperature of CO_2 melting (solid + liquid + gas = liquid + gas),
- **$T_{m(cla)}$:** The final temperature of clathrate melting in aqueous inclusions (i.e. $CO_2 \cdot 6H_2O$), ($liquid_{(aq)}$ + $solid_{(cla)}$ + vapour = $liquid_{(aq)}$ + vapour),
- **$T_{h(CO2)(L)}$:** The final temperature of CO_2 homogenization to a fluid in the liquid phase (Liquid + Vapour = Fluid),
- **$T_{h(CO2)(V)}$:** The final temperature of CO_2 homogenization to a fluid in the vapour phase (Liquid + Vapour = Fluid) and
- **$T_{h\ tot(L)}$:** The temperature of total homogenization of an aqueous fluid inclusion to a liquid phase (Liquid + Vapour = Liquid).

These parameters are required to characterise the fluid inclusions and determine the P–T conditions under which the fluids were trapped as well as their compositions. The total homogenization temperature of aqueous fluid inclusions (T_h) provides an estimate of the minimum temperature of entrapment of the fluid inclusion (Goldstein & Reynolds, 1994). Homogenization temperature is the minimum temperature of entrapment of the fluid inclusion and can also be used to calculate fluid density and molar mass. The temperature of melting of carbon dioxide (T_{mCO2}) can be used to determine the composition of the fluid inclusion of CO_2-dominant fluid inclusions. Raman spectroscopy was also be used to determine and confirm the presence of aqueous ± carbonic components of fluid inclusions.

4.2 SAMPLES FOR MICROTHERMOMETRY

Samples for microthermometric studies were collected from five localities along the SW−NE strike of the shear zone. The sampling localities are trench 4 (Fig. 4.2), NO2 (Fig. 4.3), trench 14 (Fig. 4.4), trench 15 (Fig. 4.5) and trench 15N (Fig. 4.6) and sampling locations and the samples collected for fluid inclusion studies are shown in each figure. Rocks targeted for sampling were hydrothermal quartz veins which were presumed to be gold hosts and secondly are within the shear zone. All the quartz veins from which the samples were collected met the above stated sampling conditions, with the exception of the sample from locality NO2 that did not meet the first condition pertaining to gold content in that it yielded a grade equivalent to the background concentration (gold content in hosting schist).

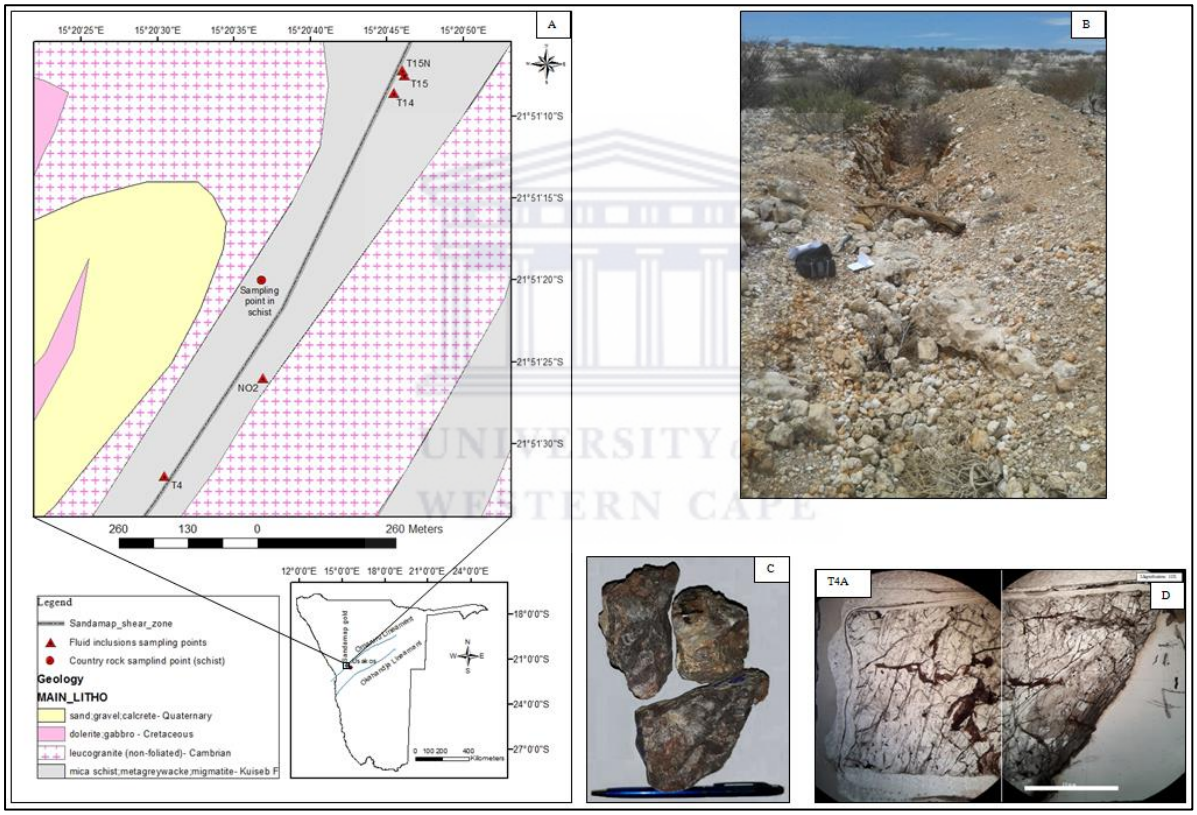

Fig. 4.2. Samples collected from trench 4 marked T4 on the map (A) and yielding a gold grade of 0.117g/t Au. B. Trench 4 from where samples shown in C were collected. The quartz samples in C appear darker due to the presence of haematite. The image with an inset T4A is a doubly polished wafer cut from the samples shown in C.

The quartz vein from trench 4 is hosted by biotite schist and the quartz samples have hematite between the quartz grains and on the surface of the grains making them appear slightly dark in some places (Fig. 4.2). The quartz vein at locality NO2 lies roughly 130 m NE of trench 4

(Fig. 4.3). The vein quartz samples from this locality contain relatively low hematite content and are clearer in comparison to those from trench 4 (Fig. 4.3).

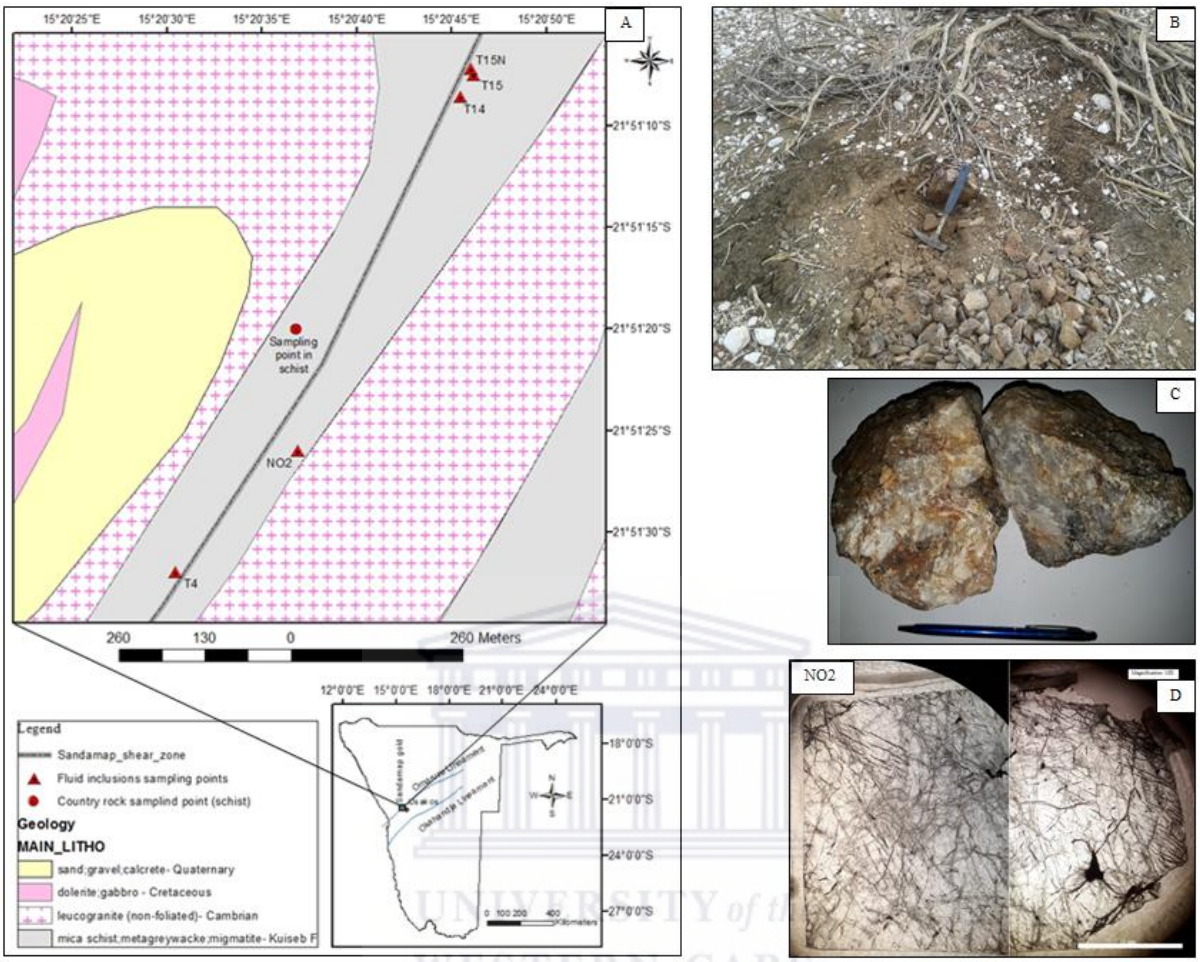

Fig. 4.3. A. Sampling map showing where the samples given in image marked C came from and the location of the Sandamap gold prospect in Namibia. B. NO2 sampling site outcrop showing quartz vein remnant in the schist hosted-shear zone, C. Vein quartz samples collected from locality NO2 which yielded a gold grade of 0.018g/t Au. D. Doubly polished vein quartz wafer cut from samples shown in C.

Trench 14, which lies roughly 300 m NE of NO2, is a shallow trench in which the biotite schist-hosted shear zone is exposed. The vein quartz samples from this trench are the clearest of all the samples from the study area and no iron oxide coating or staining is observed (Fig. 4.4). The next sampling point, trench 15, which is located roughly 20 m to the NE of trench 14, is characterized by hydrothermally altered schist consisting of numerous thin quartz veins (Fig. 4.5).

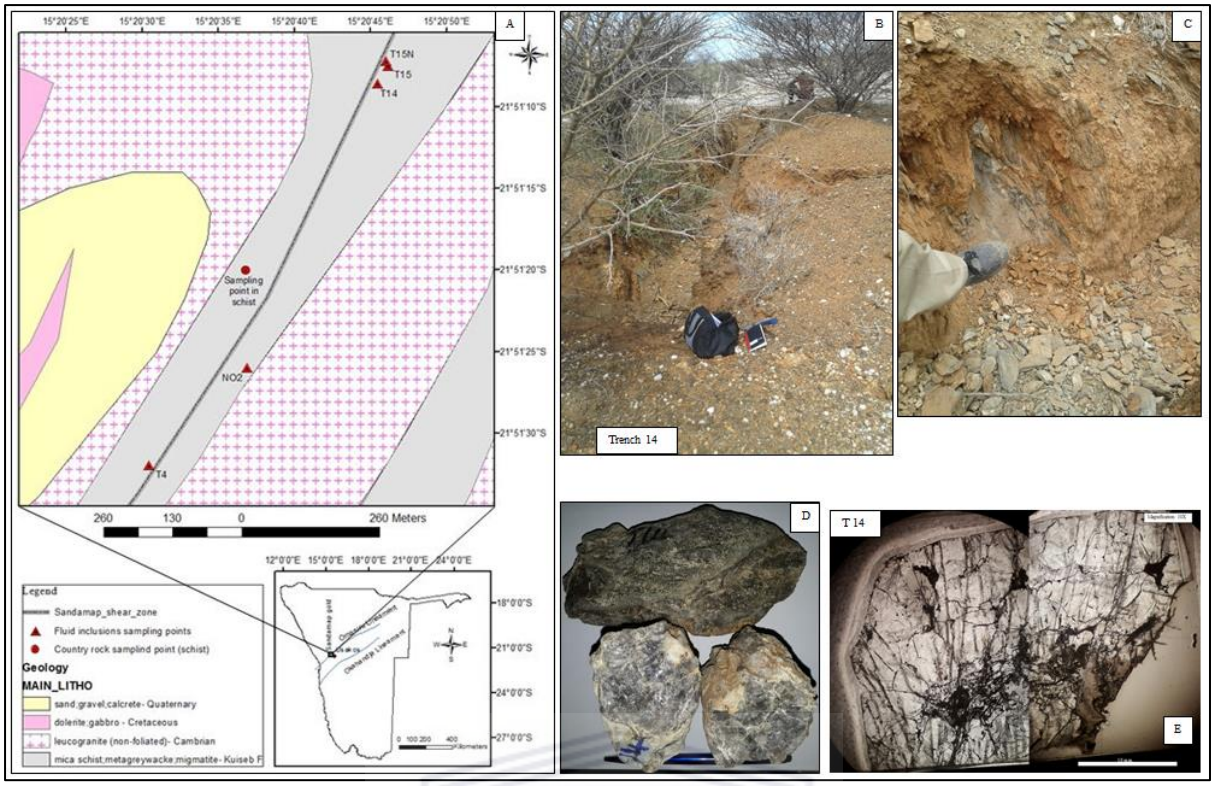

Fig. 4.4. A. Sampling map showing where the samples given in image marked D came from and the location of the Sandamap gold prospect in Namibia. B. Trench 14 from where the vein quartz samples were collected, C. An excavation in trench 14 where the samples shown in D where collected, D. Collected vein quartz samples which yielded a gold grade of 1.937g/t Au, E. Doubly polished wafer cut from the sample given in D. Quartz veins are in conformity with the shear fabric which is striking 030° and dipping 70° ESE.

The last sampling point is a very shallow and short trench located 2 m north of trench 15 (Fig. 4.6). Quartz veins from this trench are thicker than those in trench 15 but the fluid inclusions appear to be of the same character in terms of the type of fluid inclusion present (type IV), fluid inclusion phases at room temperature (vapour), range of fluid inclusion homogenization temperature (-130.0 to -71.4°C), fluid inclusion density range (0.0015 – 0.0216 g/cc), composition range of CH_4 (0.8 – 0.97), composition range of H_2O and N_2 (0.03 – 0.2) and fluid inclusion vapour percentage (100%).

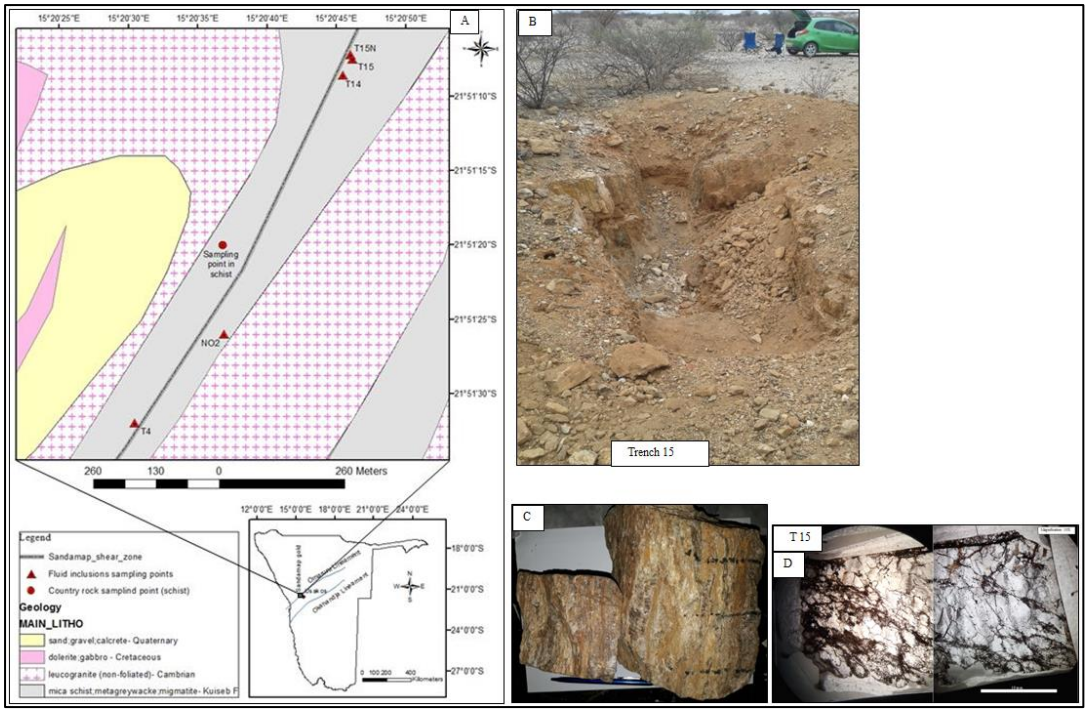

Fig. 4.5. A. Sampling map showing where the samples given in image marked C came from and the location of the Sandamap gold prospect in Namibia. B. Trench 15 from where the samples were collected, C. Samples collected from trench 15 showing thin quartz veinlets in association with hydrothermally altered sheared schist. The quartz veinlets lie parallel to the shear zone fabric with an orientation 040° and dipping 80° ESE. Samples from this locality yielded a gold grade of 1.634 g/t Au. D. Doubly polished wafer cut from the sample given in C.

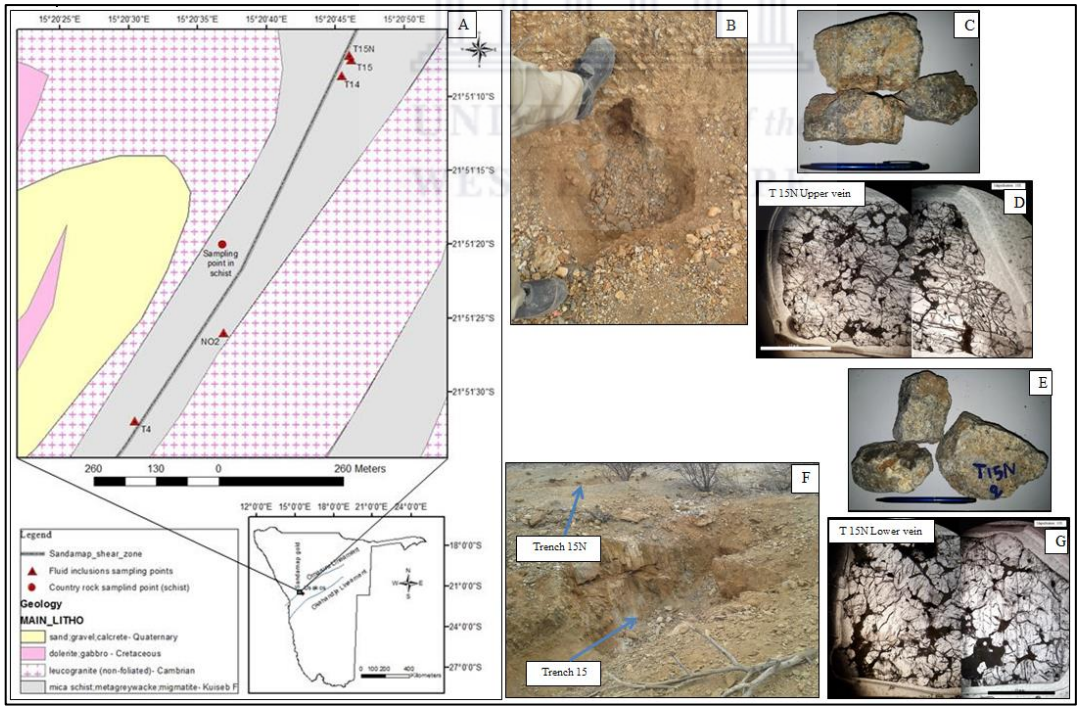

Fig. 4.6. A. Sampling map showing where the samples given in image marked C and E came from and the location of the Sandamap gold prospect in Namibia, B. An excavation in trench 15N from where the samples shown in C and E were collected and these were collected from two quartz veins lying one above the other within the hosting schist, C. Samples collected from the upper vein, D. Doubly polished wafer cut from a sample from the upper vein, E. Samples collected from the lower vein, F. Locality of trench 15N which lies 2 m north of trench 15 and the gold content here was assumed to be more or less similar to that of trench 15, G. Doubly polished wafer cut from a sample from the lower vein.

4.3 FLUID INCLUSION PETROGRAPHY

4.3.1 FLUID INCLUSION DISTRIBUTION PATTERNS

Doubly polished wafers were studied under the microscope to identify broad patterns between individual fluid inclusions and to classify inclusions into assemblages. Wafers were then broken into pieces small enough to fit the ring size of the Linkam stage after being soaked in acetone to detach the glass and remove the mounting resin. Each sample chip which was assessed by microthermometry was sketched and some noticeable fluid inclusion distribution patterns and individual fluid inclusions were also sketched and photomicrographs taken (Figs. 4.7 - 4.13). Petrographic assessment of the fluid inclusions in the study area revealed that the inclusions predominantly occur in trails (Figs. 4.7 - 4.13). Isolated fluid inclusions are rare and microthermometric assessment was carried out on the few isolated ones that were encountered.

Petrographic sketches of chip T4A from trench 4 in Fig. 4.7 shows bi- and mono-phase fluid inclusion trails. The bi-phase fluid inclusions are smaller and are less prevalent than the larger mono-phase inclusions. The focus of the sketches in Fig. 4.7 was placed on the less dominant trails containing bi-phase fluid inclusions. The more prevalent and dominant fluid inclusions are larger and mono-phase at room temperature (Fig. 4.8). Another chip (T4B) from trench 4 was petrographically assessed to establish the chronological relationship between the mono-phase and bi-phase fluid inclusions. Their locations in relation to each other, as shown in Fig. C9, suggests that the two fluid inclusion types are sychronous in trench 4. A total of 48 fluid inclusions of sizes varying from 3.8 to 24.6 µm with an average size of 11.0µm and having vapour percentages ranging from 10 to 100% were assessed for samples from trench 4.

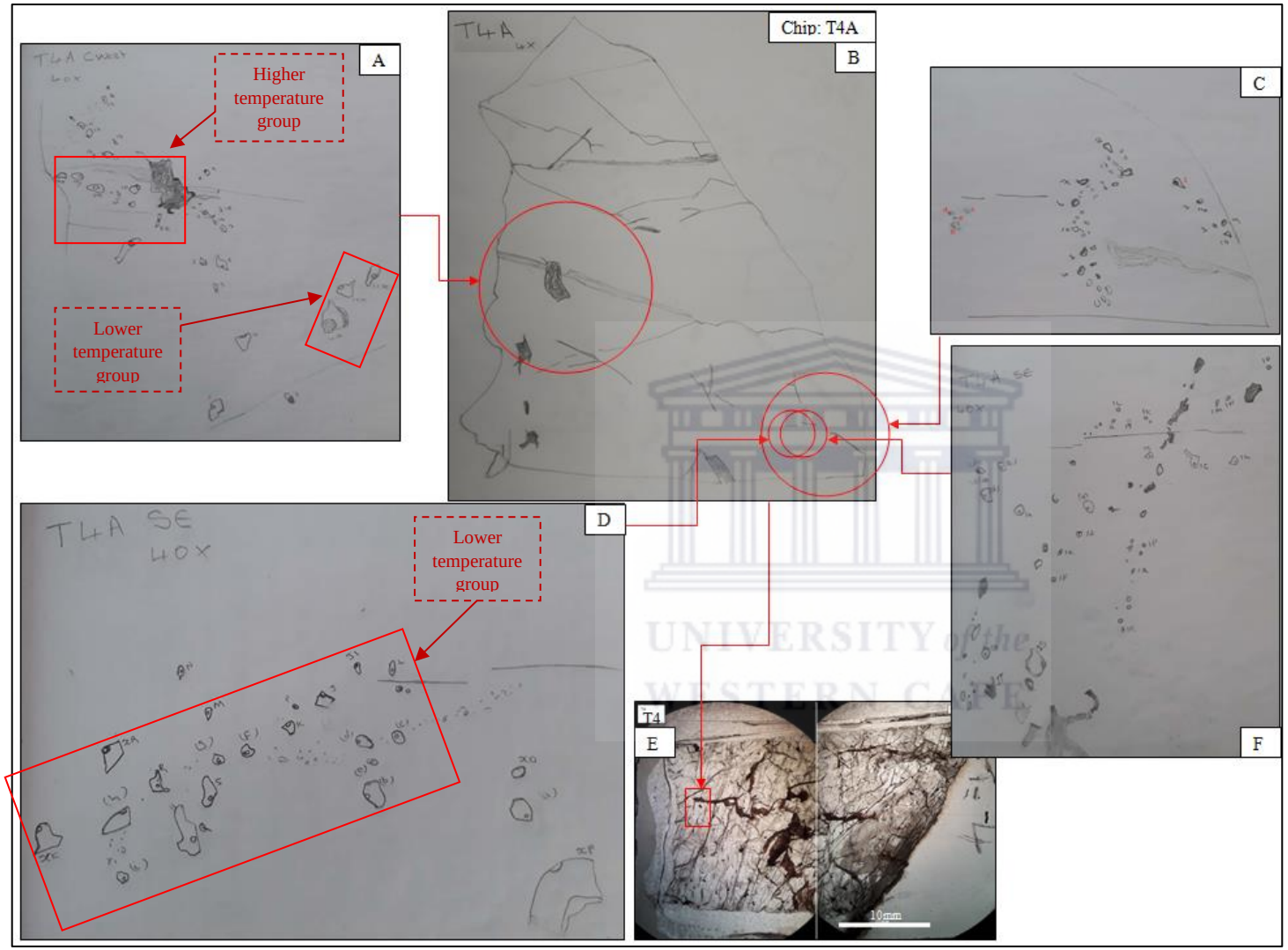

Fig. 4.7. Sketch of a chip broken from a doubly polished wafer cut from one of the samples collected from trench 4 and sketches of fluid inclusions in the chip, A, C, D and F. Close-ups of the chip reveal fluid inclusions trails containing mainly bi-phase fluid inclusions. The focus was placed mainly on parts of the chip depicting prevalence of this type of fluid inclusion, B. Chip T4A from trench 4, E. Doubly polished wafer from trench 4 showing the position of the chip T4A shown in B. Both lower and higher temperature fluid groups occur in same same chip (T4A) in B indicating different deposition episodes.

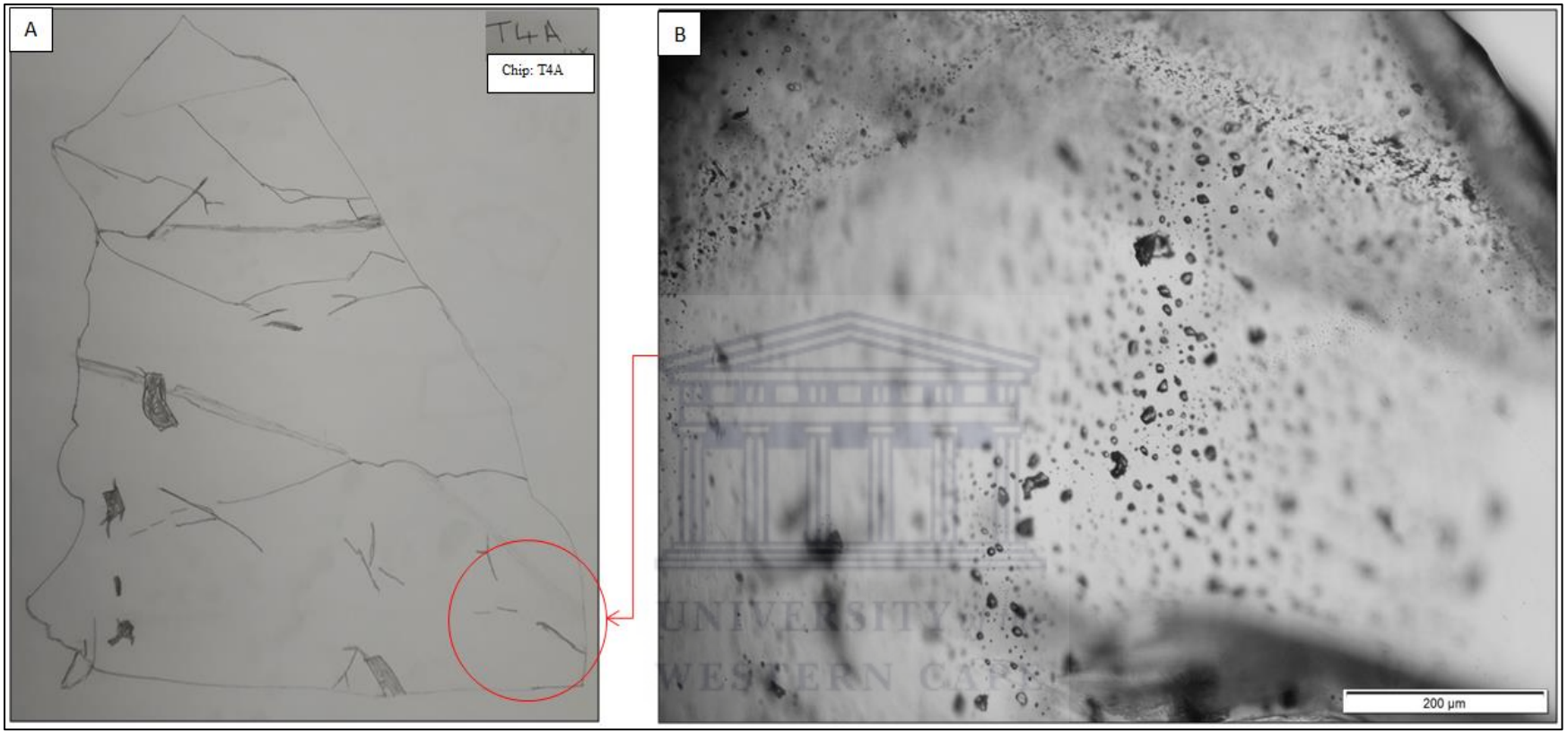

Fig. 4.8. Mono-phase fluid inclusions in chip T4A are large, pervasive and predominant. A. Chip T4A from trench 4, B. Photomicrograph of fluid inclusions depicting the pervasiveness and dominance of mono-phase fluid inclusions at 200 µm scale in which only larger fluid inclusions can be seen.

Fluid inclusions at the next sampling point (NO2) located 130 m NE of trench 4 show a distribution pattern similar to that observed at trench 4. Both mono- and bi-phase fluid inclusions occur as trails (Fig. 4.9). A total of 31 fluid inclusions of sizes varying from 7.0 to 31.9 µm, giving an average size of 15.1 µm, and having vapour percentages ranging from 0 to 50% were assessed at sampling point NO2.

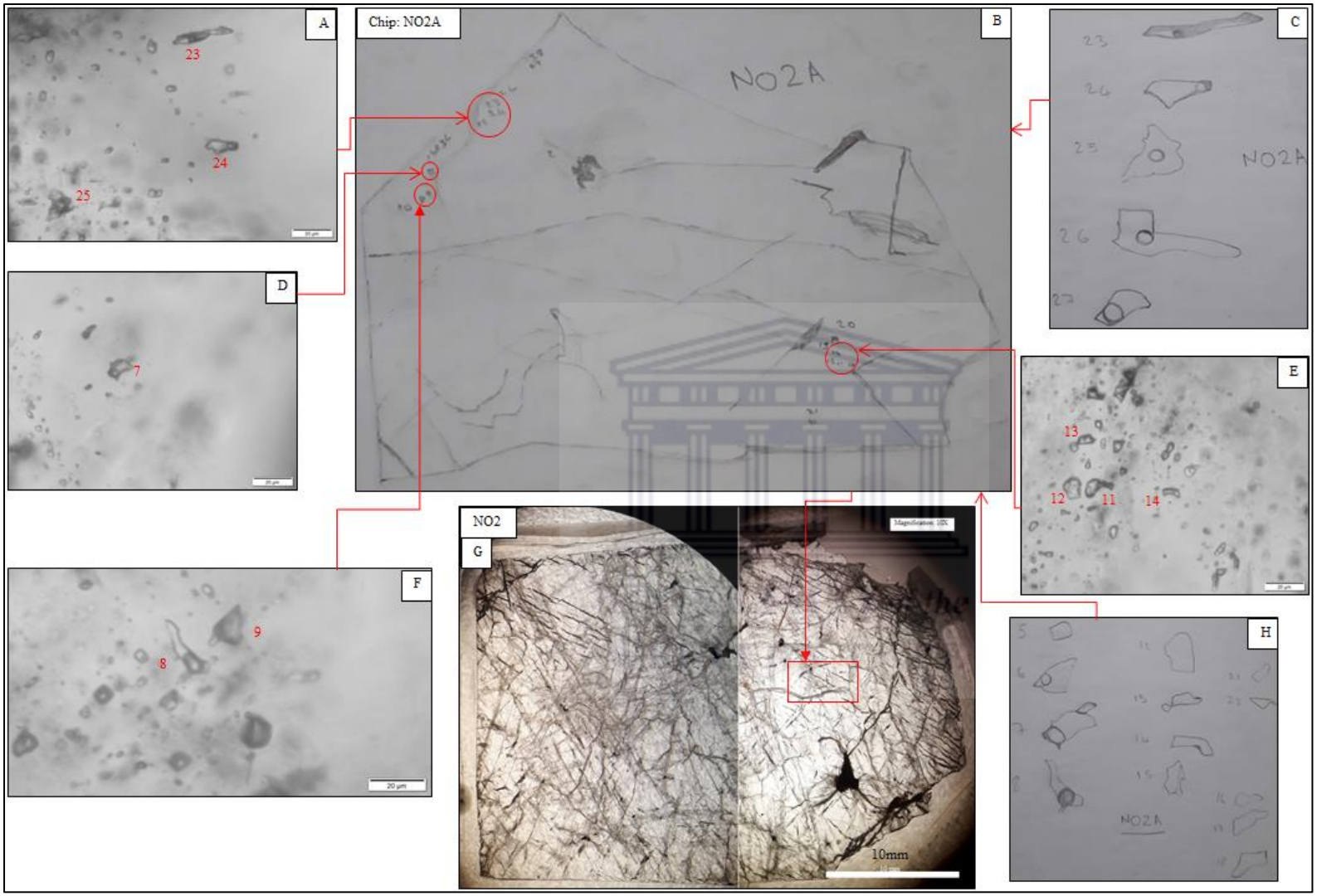

Fig. 4.9. Mono-phase and bi-phase fluid inclusions from sampling point NO2. A. Photomicrograph of a trail of bi-phase fluid inclusions, B. A sketch of a chip (NO2A) broken from a doubly polished wafer cut from samples collected from sampling point NO2, C. Sketches of fluid inclusions from chip NO2A, D. An isolated bi-phase fluid inclusion, E. Photomicrograph showing two fluid inclusion trails crossing, F. A trail of bi-phase fluid inclusions G. Image of a doubly polished wafer (NO2) from sampling point NO2, H. Sketches of fluid inclusions from chip NO2A.

A total of 33 fluid inclusions of sizes varying from 7.4 to 29.4 µm giving an average size of 16.4µm and having vapour percentages ranging from 0 to 100% were assessed at trench 14 which is located approximately 300 m NE of sampling point NO2. Most of the fluid inclusions occur in trails, as can be seen in Fig. 4.10.

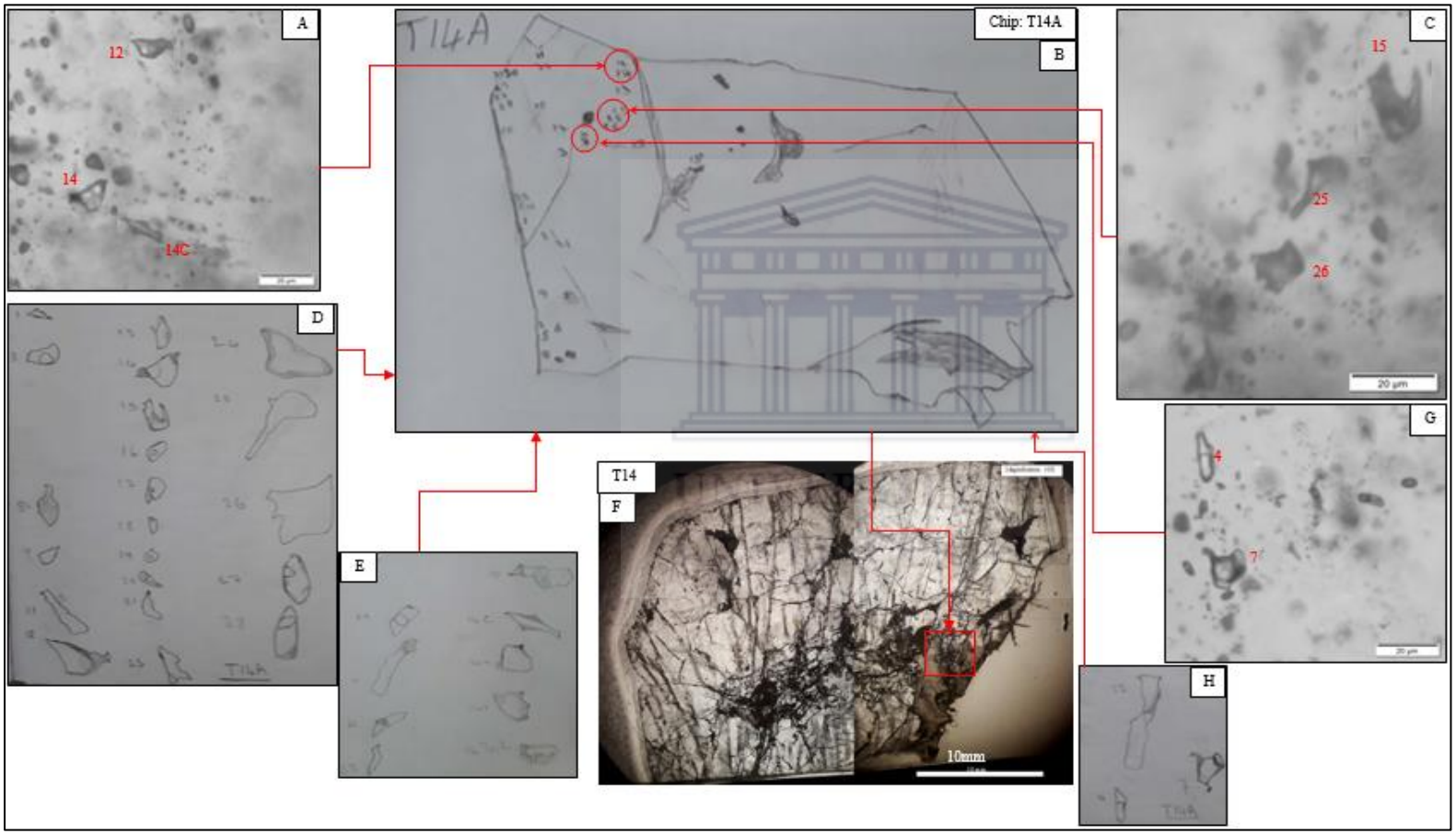

Fig. 4.10. Sketches and photomicrographs of fluid inclusions from trench 14. A, C & G. Photomicrographs showing trails of both mono- and bi-phase fluid inclusions; B. A sketch of a chip (T14A) broken from a doubly polished wafer (F) cut from samples collected from sampling point trench 14; D, E & H. Sketches of fluid inclusions from chip T14A; F. Image of a doubly polished wafer (T14) cut from samples collected from trench 14.

At trench 15, situated approximately 20 m NE of trench 14, a total 57 fluid inclusions (including those from trench 15N which is 2 m to the north) of sizes varying from 6.6 to 42.4 µm, giving an average size of 16.5 µm, and having vapour percentages ranging from 20 to 100%, were assessed. At these two locations, like at other previous sampling locations, most of the fluid inclusions occur in trails, as can be seen in Fig. 4.11 and Fig. 4.12.

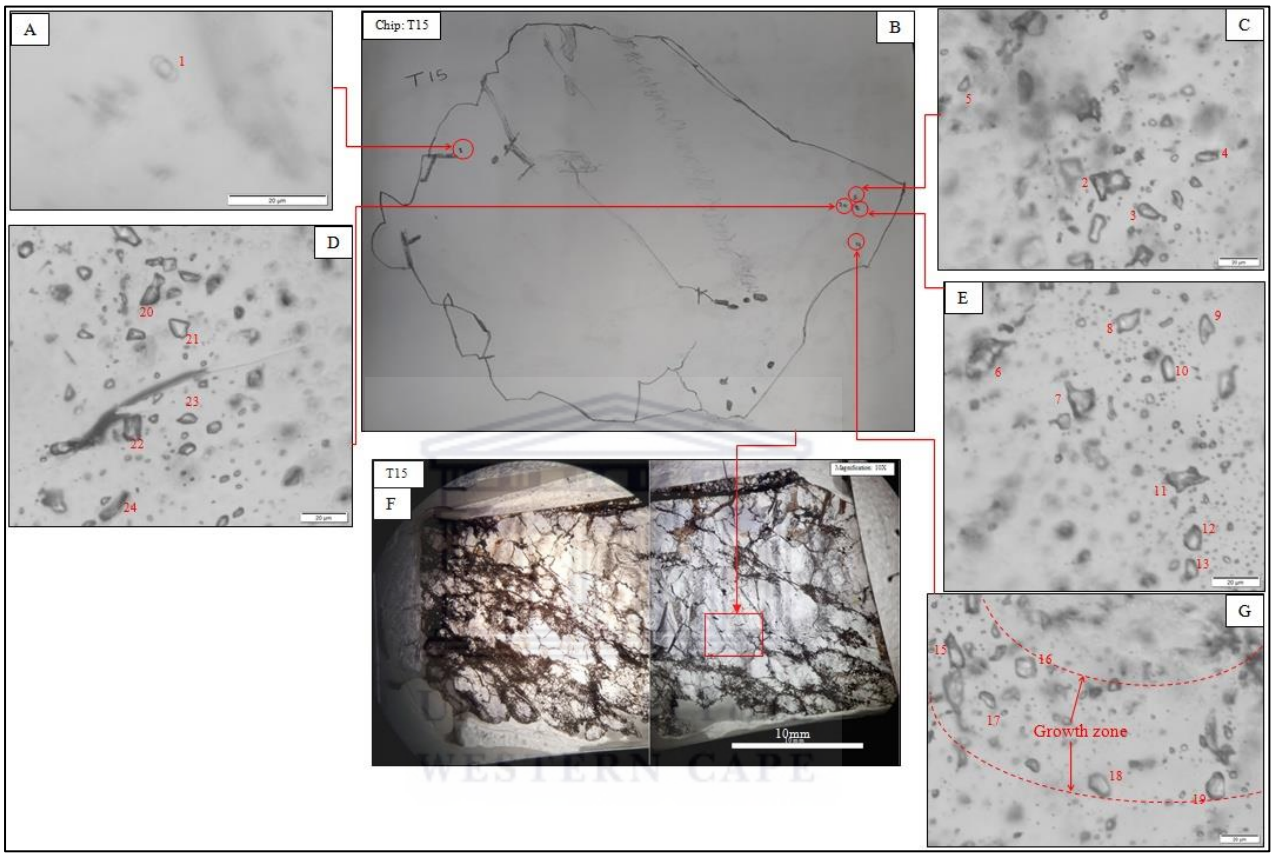

Fig. 4.11. Photomicrographs of fluid inclusions from trench 15. A, C, D & E. Photomicrographs showing trails of both mono-phase (C, D & E) and bi-phase (A) fluid inclusions; B. Sketch of a chip T15 broken from a doubly polished wafer (F) cut from samples collected from sampling point trench 15; G. Photomicrograph showing a trail of fluid inclusions along a growth zone, F. Image of a doubly polished wafer (T15) cut from samples collected from trench 15.

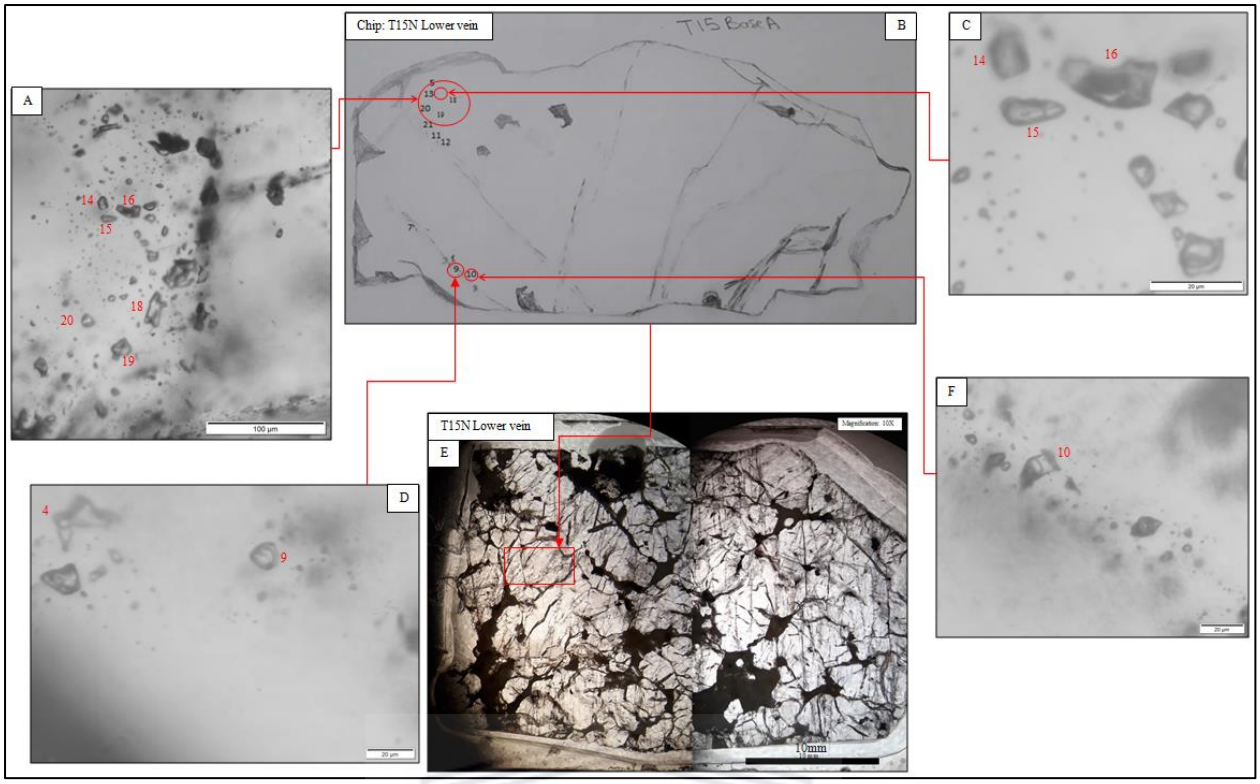

Fig. 4.12. Photomicrographs of fluid inclusions from trench 15N. A, C, D & F. Photomicrographs showing trails of fluid inclusions; B. Sketch of a chip (T15N Lower vein) broken from a doubly polished wafer (E) cut from samples collected from sampling point trench 15N; E. Image of a doubly polished wafer (T15N Lower vein) cut from samples collected from trench 15N.

4.3.2 FLUID INCLUSION TYPES, SPATIAL RELATIONSHIP AND TIMING

Generally, consistency in microthermometric data was observed within trails. Five types of fluid inclusions assemblages were identified. Microthermometry and Raman spectroscopy confirmed the presence of five types of fluids and these are given as follows:

(1) $H_2O \pm CH_4 \pm N_2$ (type I: aqueous-rich),

(2) $H_2O - CO_2 \pm CH_4 \pm N_2$ (type II: aqueous-carbonic-rich),

(3) $CO_2 \pm CH_4 \pm N_2$ (type III: carbon -rich),

(4) $CH_4 \pm H_2O \pm N_2$ (type IV: methane-rich),

(5) $CH_4 - CO_2 \pm N_2$ (type V: methane-carbonic-rich),

In terms of spatial association, it appears that not all of the five fluid inclusion types occur in the same place, as some of the fluid types do not occur at some sampling locations; the observations in this regard are summarized in Table 4.1. Different types of inclusions are present at different locations along the shear zone from southwest to northeast. The spatial

distribution of the fluid inclusions have been noted as follows: The aqueous (Type I) and the carbonic (type III) fluid inclusions occur almost throughout the sampled extent of the shear zone, type II and V occur only in the central and NE parts, respectively, as minor constituents, methane (Type IV) fluid inclusions occur in the SW and NE parts only and are dominant where they occur (Fig. 4.13, Table 4.1). Type III fluid inclusions are more prevalent towards the NE of the shear zone whereas the type I fluid inclusions are more prevalent towards the SW (Fig. 4.13, Table 4.1). Further observations are that type I fluid inclusions were found to be absent in the area just to the NE of the central area and appear again in the far NE end, whereas type III fluid inclusions are dominant in the NE area and disappear entirely towards the far NE end (Fig. 4.13).

The distribution of the fluid inclusions in the shear zone is summarized in a schematic diagram in Fig. 4.13. The aqueous (Type I) fluid inclusions, which occur almost throughout the entire shear zone, and the methane (Type IV) fluid inclusions occurring in the SW and NE, are both primary and synchronous (Figs. 4.13 & 4.14). The carbonic (type III) fluid inclusions that are dominant in the NE, also occurring in the central area and to the SW are primary (Figs. 4.13 & 4.17). Figs 4.15 and 4.16B indicate that the carbonic (type III) and the aqueous (Type I) fluid inclusions are contemporaneous. The minor methane-carbonic (Type V) fluid inclusions in the NE are primary, so are the minor aqueous-carbonic (type II) inclusions in the central part (Figs. 4. 13). The type II and type III fluid inclusions are synchronous (Fig. 4.16A). The aforementioned observations indicate that types I and IV coexist as primary fluid inclusions in both the SW and NE parts of the shear zone, whereas types II and III also coexist as primary fluid inclusions in the central part. It further indicates that types III and V, the only fluid inclusion types observed in the immediate NE area, coexist as primary fluid inclusions.

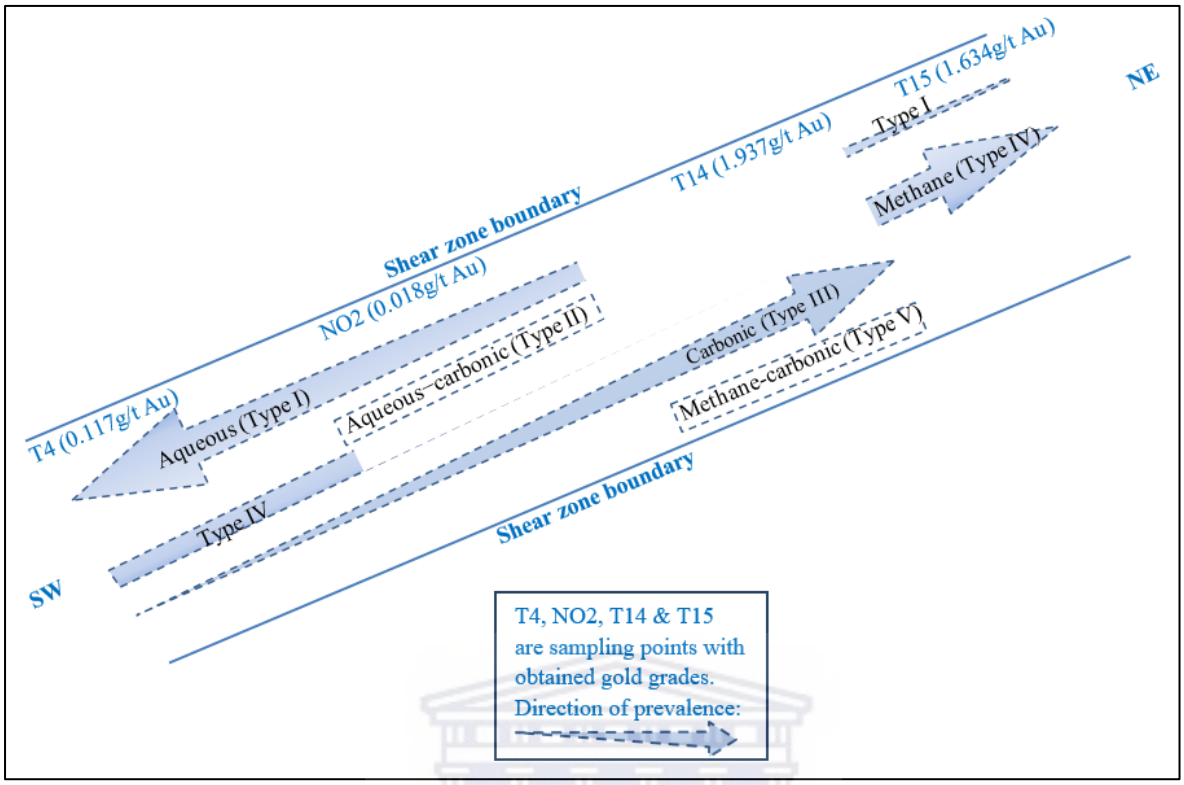

Fig. 4.13. Schematic diagram, showing spatial distribution of fluid inclusions at the Sandamap prospect. The occurrence of the aqueous (Type I) fluid inclusions is as follows: dominant towards the SW part of the shear zone, present in the central parts, absent in the NE and minor amounts observed in the far NE end. Type IV fluid inclusions are present in the SW and the far NE end where they are more prevalent, but absent in the central and the NE parts. With reference to the sequence of formation all encountered type I and type IV fluid inclusions are primary. The type III fluid inclusions dominate in the NE, decrease in abundance towards the SW and are absent in the far NE end of the shear zone. In terms of timing, type III fluid inclusions in the NE, the central and the SW are all primary. The other two fluid inclusion types; the aqueous−carbonic (Type II) and the methane-carbonic (Type V) only occur in the central and NE parts of the shear zone respectively. These two fluid inclusion types are also the least prevalent in the shear zone. With reference to timing, both type Vand type II fluid inclusions are primary.

Table 4.1 Chronological classification of the fluid types, their spatial associations and proportions at different sampling localities

Sampling locality	Present fluid types	Fluid composition	Chronological classification
Trench 4	Type I (Aqueous−rich)	$H_2O±CH_4±N_2$	Primary
	Type IV (Methane−rich)	$CH_4±H_2O±N_2$	Primary
	Type III (carbonic−rich)	$CO_2±CH_4±N_2$	Primary
NO2	Type I (Aqueous−rich)	$H_2O±CH_4±N_2$	Primary
	Type III (carbonic−rich)	$CO_2±CH_4±N_2$	Primary
	Type II (Aqueous−carbonic)	$H_2O−CO_2±CH_4±N_2$	Primary
Trench 14	Type III (carbonic−rich)	$CO_2±CH_4±N_2$	Primary
	Type V (methane−carbonic−rich)	$CH_4−CO_2±N_2$	Primary
Trench 15 &15N	Type IV (Methane−rich)	$CH_4±H_2O±N_2$	Primary
	Type I (Aqueous−rich)	$H_2O±CH_4±N_2$	Primary

At trench 4, both aqueous−rich and Methane−rich fluid inclusions appear to occur in trails (Fig. 4.14E & G) along mineral growth zones (Fig. 4.14A & D) and a few aqueous−rich ones occur as isolated inclusions (i.e. Fig. 4.14C) indicating that both types are primary fluid inclusions and the occurrence of aqueous−rich and Methane−rich fluid inclusions in the same trails (Fig. 4.14E & G) support the notion that they formed at the same time. The Carbonic−rich fluid inclusions and aqueous-rich fluid inclusions also occur in the same trails suggesting that they are of the same age (Fig. 4.15).

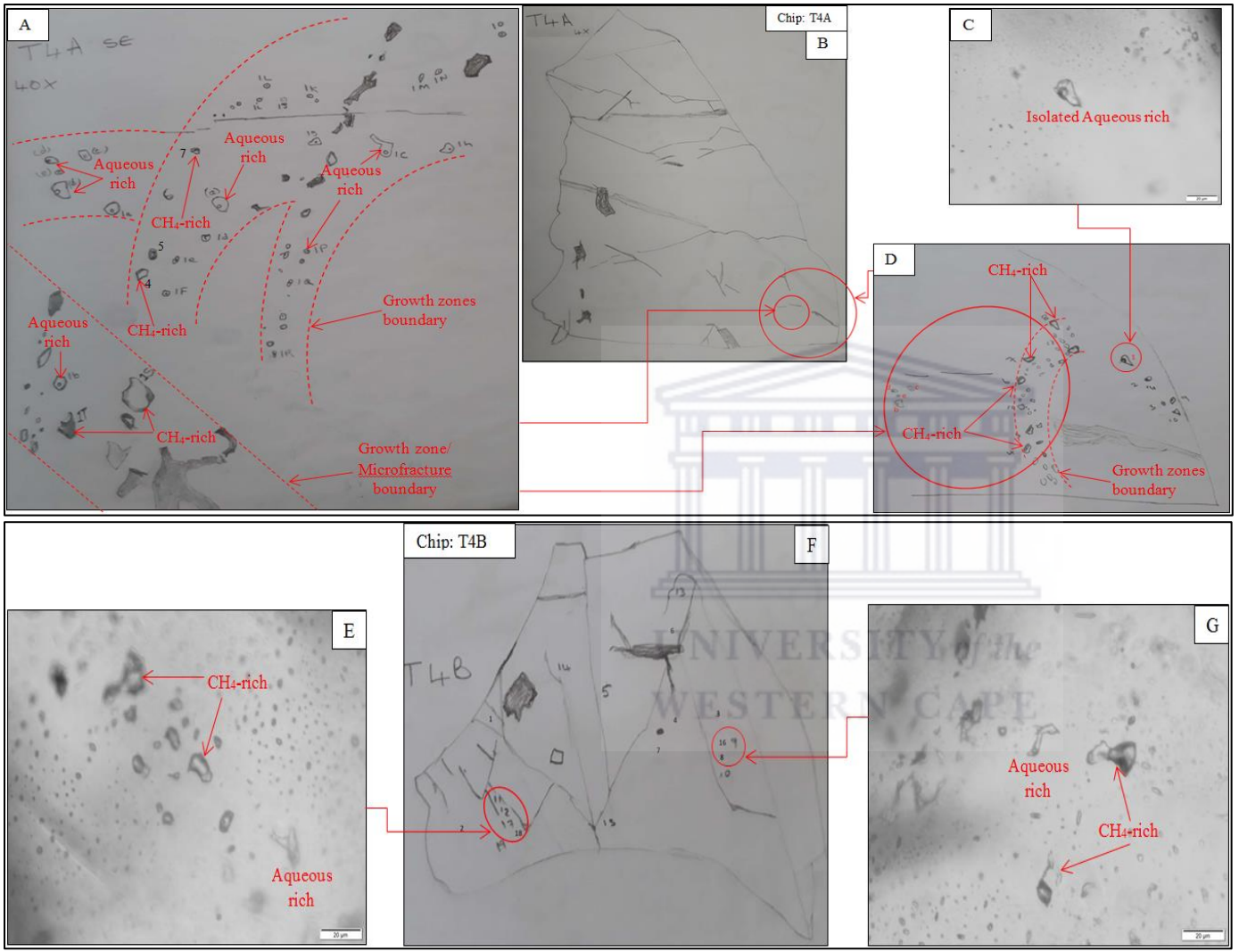

Fig. 4.14. The relationship between the two fluid inclusion types occurring at trench 4. A. Sketches of both aqueous-rich and CH_4-rich fluid inclusions depicting their occurrence along growth zones, B. A sketch of chip T4A broken from doubly polished wafer T4 from trench 4, C. A photomicrograph of an isolated aqueous-rich fluid inclusion, D. Sketches of CH_4-rich fluid inclusions occurring along a growth zone, E. A photomicrograph of both fluid inclusion types in the same trail, F. A sketch of chip T4B broken from the same doubly polished wafer T4 from trench 4, G. A Photomicrograph of both types of fluid inclusion types depicting their occurrence in one trail.

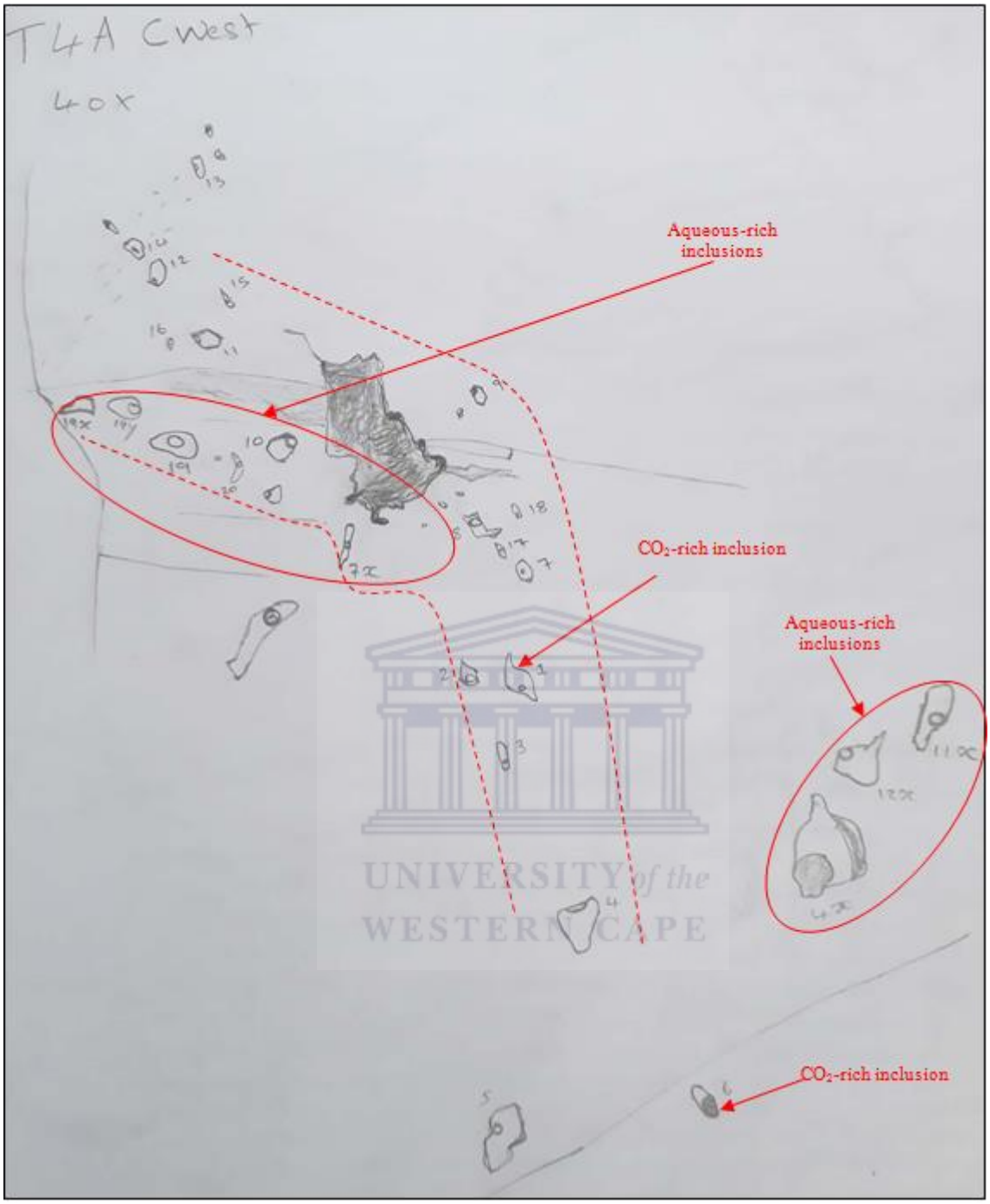

Fig. 4.15. Sketch of CO_2-rich and aqueous-rich fluid inclusions located in the central western part of chip T4A from trench 4. The two fluid inclusion types (type I aqueous-rich and type III CO_2-rich) occur in same trail and are seemingly synchronous.

At sampling point NO2 (located 130 m NE of trench 4) where three fluid inclusion types were observed, some CO_2-rich and aqueous-rich fluid inclusions occur in the same trail or growth zone suggesting that the two are contemporaneous (Fig. 4.16B). Type II (H_2O−CO_2-rich) and type III (CO_2-rich) fluid inclusions occur in the same trails (Fig. 4.16A) suggesting that they are also synchronous. This implies that the aqueous-rich (type I), H_2O−CO_2-rich (type II) and CO_2-rich (type III) are contemporaneous.

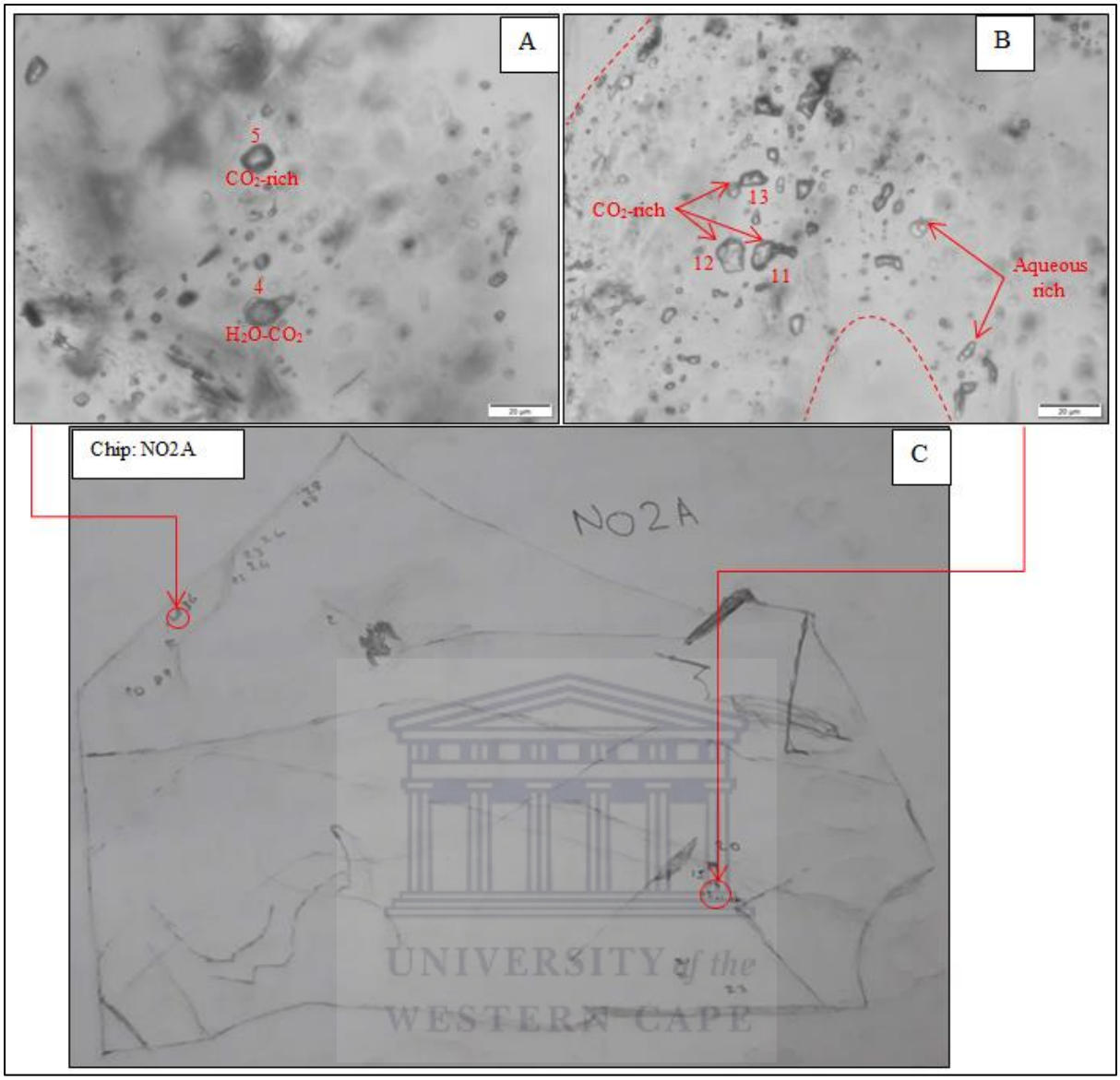

Fig. 4.16. The relationship between the three fluid inclusion types occurring at sampling point NO2. A. A photomicrograph of the H_2O-CO_2-rich (type II) and CO_2-rich (type III) fluid inclusions indicating that the two are synchronous, B. A photomicrograph showing CO_2-rich (type III) and aqueous-rich (type I) fluid inclusions occuring in the same trail or growth zone indicating that the two types are contemporaneous. This means that H_2O-CO_2-rich, aqueous-rch and CO_2-rich fluid inclusions are synchronous and are primary, C. A sketch of chip NO2A broken from a doubly polished wafer NO2 from the sampling point of the same name.

At trench 14, located approximately 300 m NE of NO2, two fluid inclusion types were observed; the major CO_2-rich fluid and the minor CH_4-CO_2-rich type. Samples from this locality also yielded the highest gold content (Chapter 3, Table 3.2). The majority of the CO_2-rich fluid inclusions occur in trails along growth zones (Fig. 4.17B & C) and a few have been observed to occur as isolated inclusions (Fig. 4.17D & E), suggesting a syngenetic relationship with the hosting quartz veins. The chronological relationship between the CO_2-rich and the CH_4-CO_2-rich inclusions could not be established due to the smaller abundance of the latter. It is, however, thought that the CH_4-CO_2-rich inclusions may have resulted from

the modification of the CO_2-rich fluid inclusions, because their compositions are not very different (they are both composed of CH_4, CO_2 and N_2). This, however, is the only evidence established to this effect.

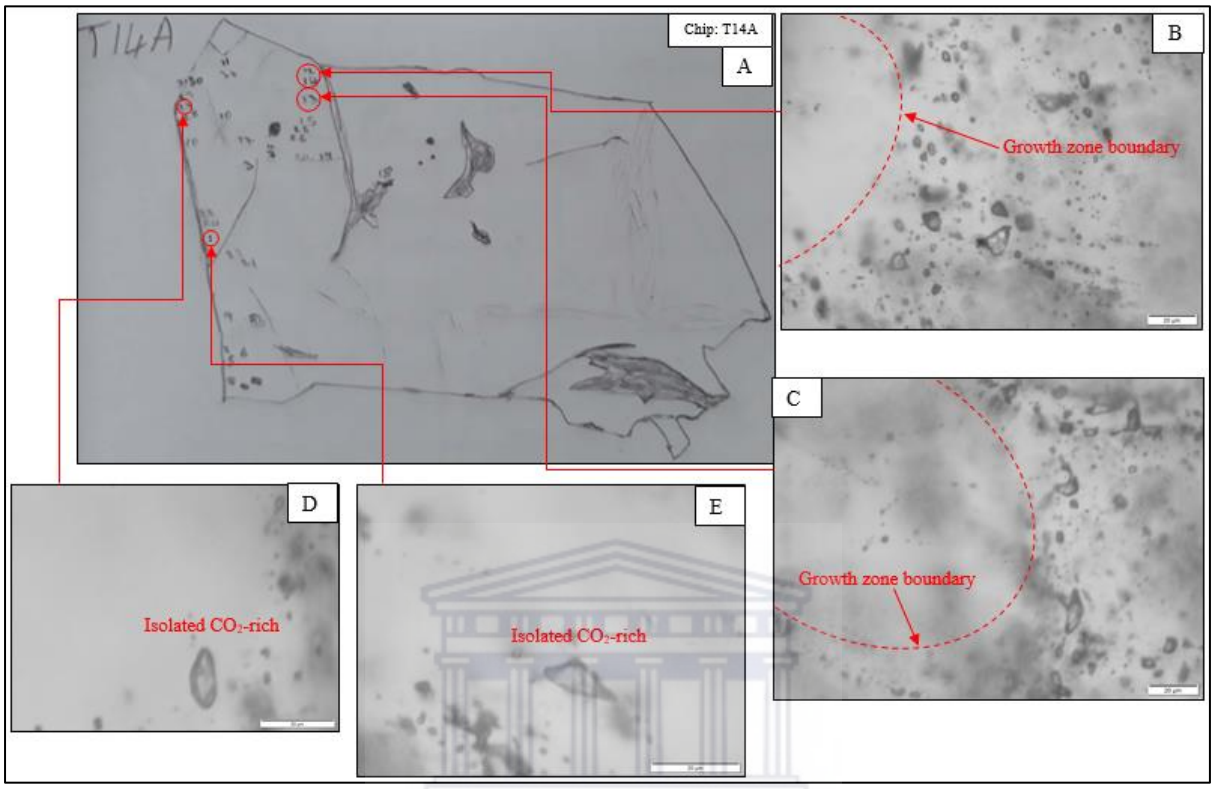

Fig. 4.17. Occurrence of the major fluid inclusions at trench 14. A. Sketch of chip T14A broken from a doubly polished wafer T14 from trench 14, B & C. The majority of the CO_2-rich fluid inclusions occur in trails along growth zones, D & E. Some CO_2-rich fluid inclusions occur as isolated inclusions indicating that they are primary.

At trench 15 and trench 15N located approximately 20 m NE of trench 14, two fluid inclusion types occur, the major CH_4-rich type and the minor aqueous-rich type. The major fluid inclusion type occur in trails along growth zones (Fig. 4.18C & D, Fig. 4.19B) and with a few occurring as isolated inclusions (Fig. 4.19C & D) suggesting that they are primary inclusions. Some of the minor fluid inclusions also occur as isolated inclusions (Fig. 4.18A) suggesting coexistence of the two fluid types although this could not be further substantiated (e.g. the coexistence of the two types in the same trails where two or more microfractures cross or join are absent).

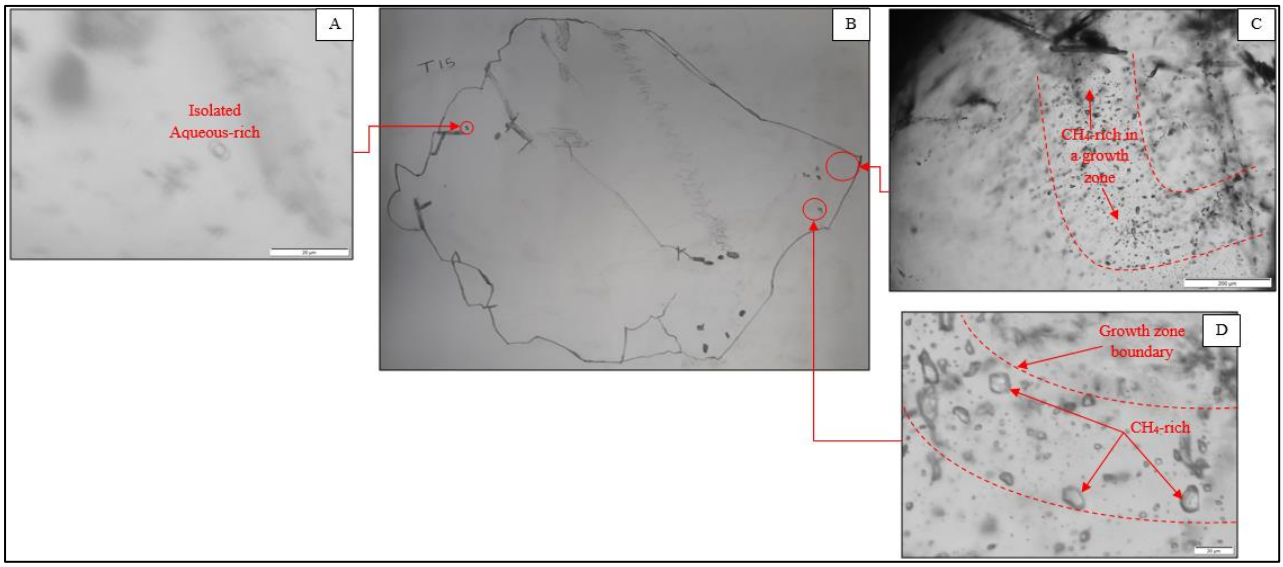

Fig. 4.18. Occurrence of fluid inclusions at trench 15. A. Photomicrograph showing an isolated aqueous-rich fluid inclusion, B. Sketch of chip T15A broken from a doubly polished wafer T15 from trench 15, C & D. Most of the major (CH_4-rich) fluid inclusions occur in trails along growth zones.

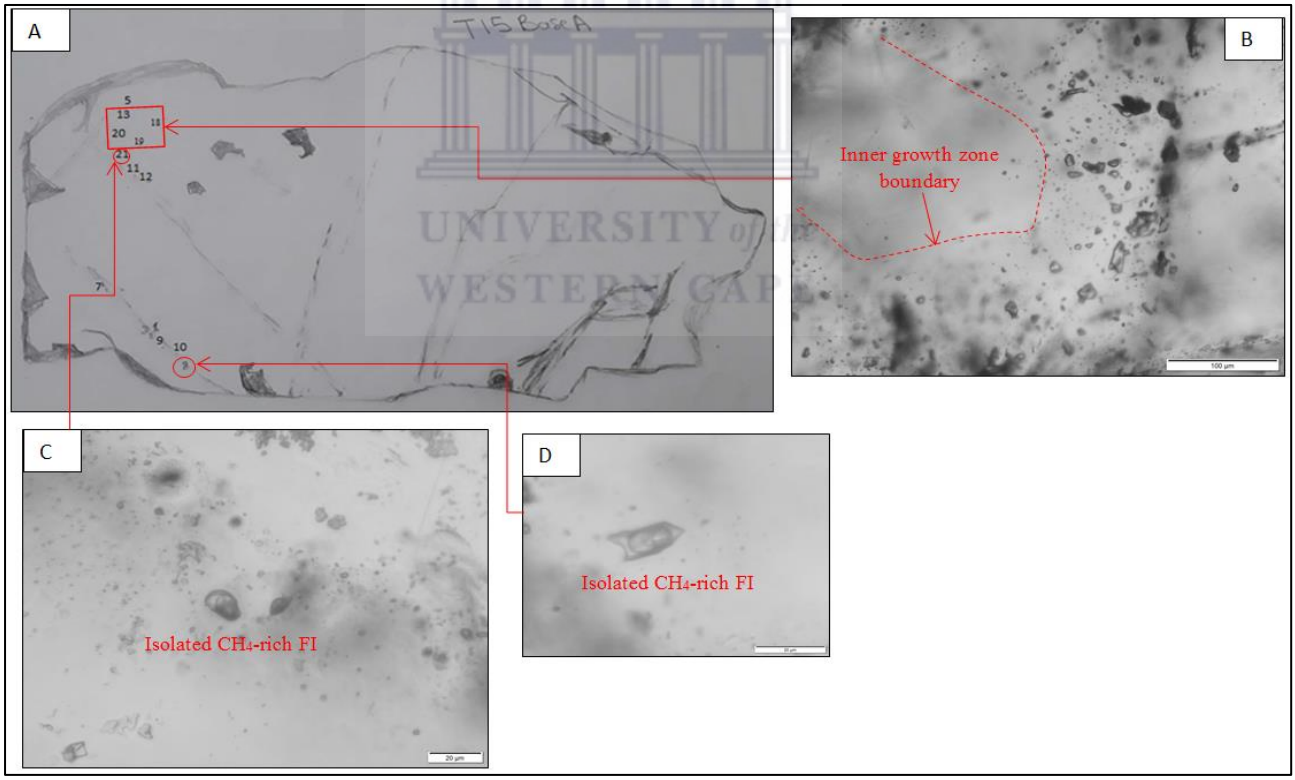

Fig. 4.19. Occurrence of the major fluid inclusions at trench 15N. A. Sketch of chip T15Base A broken from a doubly polished wafer T15N Base from trench 15N, B. The majority of the CH_4-rich fluid inclusions occur in trails along growth zones, C & D. Some CH_4-rich fluid inclusions occur as isolated inclusions.

4.4 MICROTHERMOMETRY RESULTS

Petrographic observations revealed that the overall fluid inclusion population is dominated by relatively large mono-phase carbonic / gaseous fluid inclusions (CO_2- and CH_4-rich) with a small abundance of relatively small sized aqueous-rich bi-phase fluid inclusions and a minor aqueous carbonic population. Five types of fluid inclusions were identified by microthermometry and transmitted light petrographic observations (Table 4.2).

Table 4.2. Five types of fluid inclusions were identified by microthermometry and transmitted light petrographic observations

Fluid inclusion type	**Locality**
H_2O±CH_4±N_2 (Type I)	T4, NO2, T15 & T15N
H_2O−CO_2±CH_4±N_2 (Type II)	NO2
CO_2±CH_4±N_2 (Type III)	T4, NO2 & T14
CH_4±H_2O±N_2 (type IV	T4, T15 & T15N
CH_4−CO_2±N_2 (type V	T14

4.4.1 MICROTHERMOMETRY DATA OF EACH FLUID INCLUSION TYPE

Type I: H_2O±CH_4±N_2 fluid inclusions

The aqueous (Type I) fluid inclusions have an ice melting temperature ($T_{m(ice)}$) ranging from -22.4 to -1.6 °C (Tables 4.3 & F2). Melting temperatures of the clathrates $T_{m(CL)}$, which are likely CO_2 or CH_4, range from 1.5 to 10.5°C (Table 4.4). These inclusions have temperatures of total homogenization (T_h), to liquid, occurring from 152 to 329°C (Fig. 4.26). The Type I fluid inclusions are bi-phase at room temperature (Fig. 4.20 & Fig. B28).

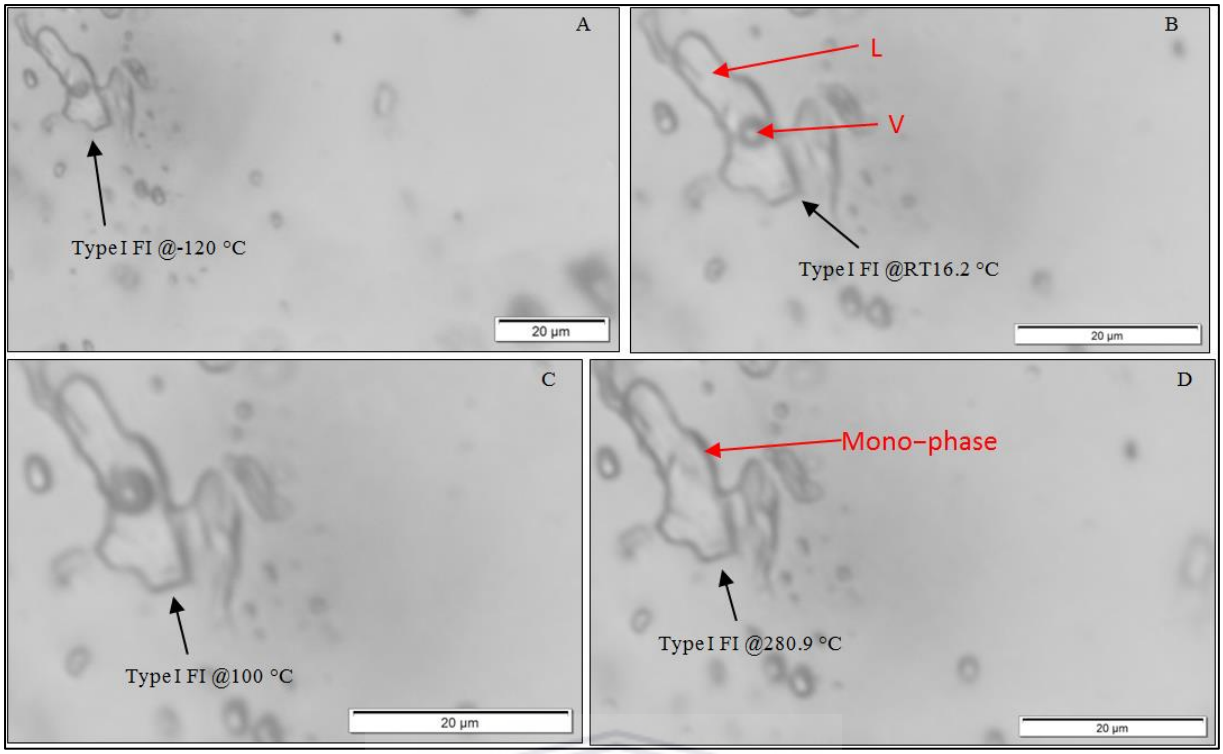

Fig. 4.20. Photomicrographs of a fluid inclusion from Chip T4ASE showing a type I fluid inclusion at various temperatures. The images depict a mono-phase inclusion at its homogenization temperature (280.9°C) and 2 phase inclusions at lower temperatures. (FI: Fluid inclusion).

Type II: H_2O-CO_2±CH_4±N_2 fluid inclusions

The aqueous-carbonic (type II) fluid inclusions have melting temperature of the carbonic phase ($T_{m(CO2)}$) ranging from −57.7 to −57.2 °C (Tables 4.3 & F3, Fig. 4.27), indicating the presence of other minor volatiles besides CO_2. The homogenization temperature of CO_2 obtained is 15.3°C (Tables 4.3 & F3, Fig. 4.28). These inclusions are very rare and only six (6) fluid inclusions were noted and from these only three (3) $T_{m(CO2)}$ and one (1) $T_{h(CO2)}$ measurements were obtained. During the heating run, some of the aqueous-carbonic fluid inclusions decrepitated between 346 and 350°C, prior to final homogenization. The homogenization temperatures of this type of fluid inclusion could not be determined from the non-decrepitated ones due to their lack of abundance. The Type II fluid inclusions are composed of 3-phases (Fig. 4.21 & Fig. B30).

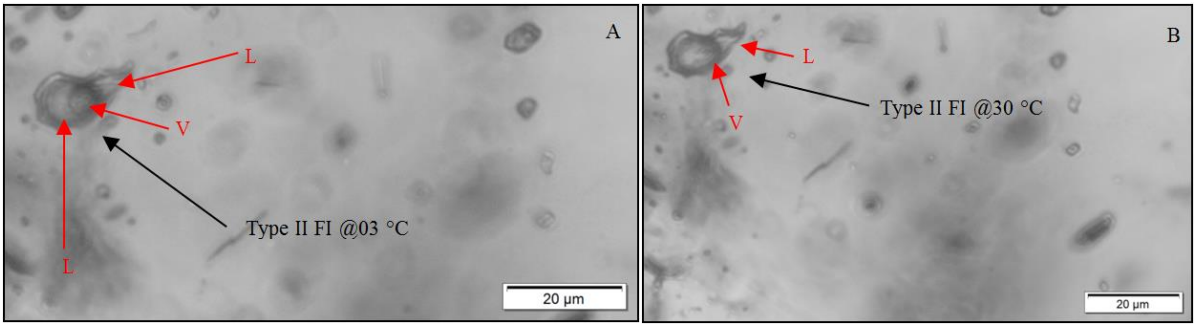

Fig. 4.21. Photomicrographs of a fluid inclusion from Chip NO2A showing type II (aqueous−carbonic) fluid inclusions at different temperatures. The images depict 3−phases at a lower temperature (3°C) and as being bi-phase at 30°C.

Type III: CO_2±CH_4±N_2 fluid inclusions

The carbonic (type III) fluid inclusions have melting temperatures of the carbonic phase ($T_{m(CO2)}$) ranging from -58.4 to -56.3 °C (Tables 4.3 and F4, Fig. 4.27). During the cooling run of some of the carbon dioxide-rich fluid inclusions, the CO_2 phase melted at temperatures as low as -58.4°C indicating the presence of variable, but minor amounts of other volatiles that may probably be CH_4 and / or CH_4 and N_2. Final CO_2 homogenization temperatures ($T_{h(CO2)}$), occurred from -8.3 to 29.2°C (Fig. 4.28). Overall, of the type III fluid inclusions, 94.1% homogenized to liquid and the remainder homogenized to vapour (Tables 4.3 & F4, Fig. 4.28). This is also reflected by extreme variations (0 – 100%) in the percentage (%) of vapour (Tables 4.3 & F4, Fig. 4.27). The Type III fluid inclusions are either mono-phase or bi-phase (Figs. 4.22, Fig. B3).

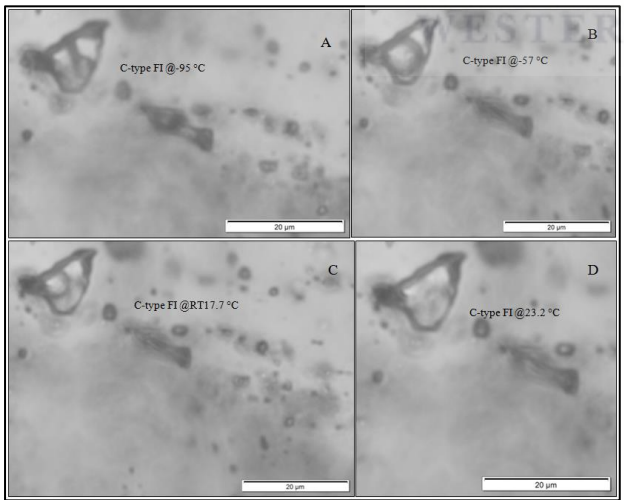

Fig. 4.22. Photomicrographs of a fluid inclusion from Chip T14A showing type III (CO_2-rich) fluid inclusion at various temperatures. B and C. The inclusion is bi-phase at -57°C and 17.7°C, D. The inclusion is mono-phase after homogenization at 23.2°C.

Type IV: $CH_4 \pm H_2O \pm N_2$ fluid inclusions

The CH_4-rich fluid inclusions have final homogenization temperatures (T_h) to the vapour phase occurring from -130 to -71.4°C with a mean of -103.5°C (Tables 4.3 & F5, Fig. 4.28). These inclusions did not freeze during the cooling run to -196°C because the triple points of the gases comprising these fluid inclusions (triple points of pure CH_4 and pure N_2 are -182.5°C and -210°C respectively) or their mixture is below the -190°C stage limit. The Type IV fluid inclusions are mono-phase at higher temperatures and bi-phase (liquid vapour) at lower temperatures (Figs. 4.23, Fig. B9).

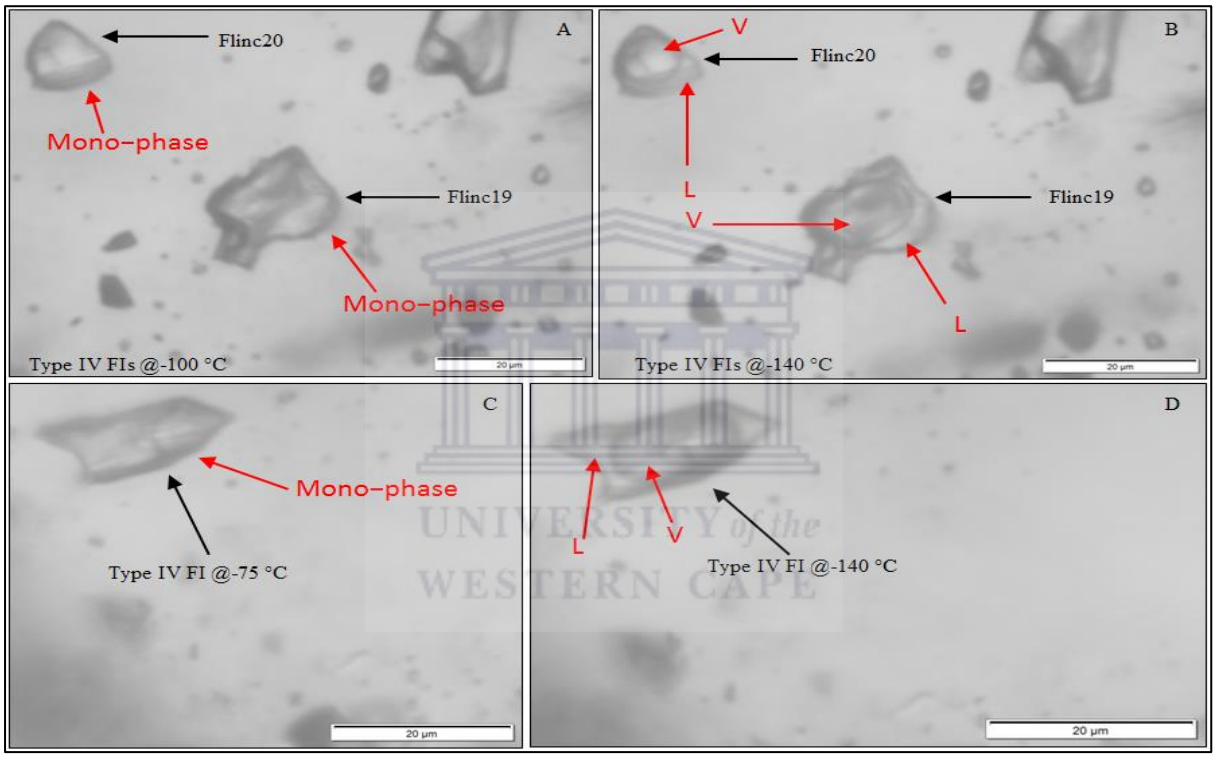

Fig. 4.23. Photomicrographs from Chip T15N Lower vein showing type IV (CH_4-rich) fluid inclusions at various temperatures. The images depict mono-phase inclusions above their homogenization temperatures and bi-phases at lower temperature (-140 °C).

Type V: $CH_4 - CO_2 \pm N_2$ fluid inclusions

The CH_4-CO_2-rich fluid inclusions have melting temperatures of the carbonic phase ($T_{m(CO2)}$) ranging from -64.8 to -62.1°C (Tables 4.3 & F6, Fig. 4.27) and their final homogenization temperatures (T_h) to liquid occurring from -31.4 to -22.1°C with a mean of -25.3°C (Tables 4.3 & F6, Fig. 4.28). These inclusions, like the aqueous−carbonic type (Type II), are not very common and only a few were observed. The Type V fluid inclusions are mono-phase at room temperature (Figs. 4.24, Fig. B31).

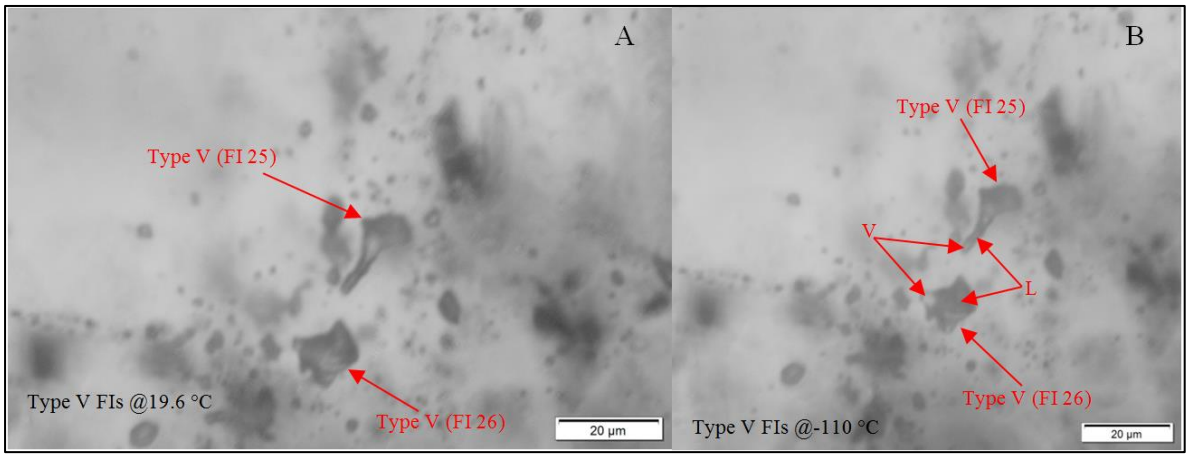

Fig. 4.24. Photomicrographs from Chip T14A showing type V fluid inclusions at different temperatures. A. Mono-phase inclusions at 19.6°C, and B. Vapour present in the fluid inclusions at -110 °C.

The data given in Table 4.3 gives a summary of the cooling and heating experiments. It is a synopsis of the data collected from microthermometry and classification of the fluid inclusions into the given types was accomplished using an indirect method based on the interpretation of the microthermometry data and petrographic descriptions. The table gives minimum and maximum measurements: carbon dioxide melting ($T_{m(CO2)}$) and homogenization temperatures ($T_{h(CO2)}$), clathrate melting temperatures ($T_{m(CL)}$), CH_4-rich homogenization temperatures ($T_{h(Methane-rich}$) and total homogenization temperatures of aqueous fluids (T_h). The L and V indicate the phase to which the fluid inclusions homogenized, which was either liquid (L) or vapour (V), respectively. N is the number of fluid inclusions analysed.

Table 4.3 A summary of microthermometry data. The detailed raw analytical data is given in Tables F2 to F6. (N: number of fluid inclusions)

FI type	Range	Size (µm)	Vapour (%)	$T_{m(CO2)}$ (°C)	$T_{m(CL)}$ (°C)	$T_{h(CO2)(L)}$ (°C)	$T_{h(CO2)(V)}$ (°C)	$T_{h(L)}$ (°C)	$T_{h(V)}$ (°C)	$T_{h\ tot(L)}$ (°C)
TYPE I (H_2O±CH_4±N_2)	Min	4	10	–	1.5	–	–	–	–	152
	Max	32	50	–	10.5	–	–	–	–	329
	Mean	11	10	–	7.5	–	–	–	–	242.9
	N	51	51	–	8	–	–	–	–	39

Table 4.3 continues

FI type	Range	Size (µm)	Vapour (%)	$T_{m(CO2)}$ (°C)	$T_{m(cla)}$ (°C)	$T_{h(CO2)(L)}$ (°C)	$T_{h(CO2)(V)}$ (°C)	$T_{h(L)}$ (°C)	$T_{h(V)}$ (°C)	$T_{h\ tot(L)}$ (°C)
TYPE II (H_2O-CO_2±CH_4±N_2)	Min	7	20	−57.7	–	15.3	–	–	–	–
	Max	25	50	−57.2	–	15.3	–	–	–	–
	Mean	15	38	−57.4	–	15.3	–	–	–	–
	N	6	6	3	–	1	–	–	–	–
TYPE III (CO_2±CH_4±N_2)	Min	7	0	−58.4	–	−8.3	16.5	–	–	–
	Max	29	100	−56.3	–	29.2	17.1	–	–	–
	Mean	15	10	−57.3	–	19.0	16.8	–	–	–
	N	44	44	44	–	32	2	–	–	–
TYPE IV (CH_4±H_2O±N_2)	Min	8	100	–	–	–	–	–	−130.0	–
	Max	42	100	–	–	–	–	–	−71.4	–
	Mean	17	100	–	–	–	–	–	−103.5	–
	N	61	61	–	–	–	–	–	53	–
TYPE V (CH_4−CO_2±N_2)	Min	13	0	−64.8	–	–	–	−31.4	–	–
	Max	27	0	−62.1	–	–	–	−22.1	–	–
	Mean	18	0	−63.5	–	–	–	−25.3	–	–
	N	5	5	5	–	–	–	3	–	–

4.5 CALCULATIONS FOR BULK DENSITY

Bulk density for the type III (CO_2-rich) fluid inclusions was calculated by using $T_{h(CO2)}$ and compositions for CO_2 and CH_4 in the FLUIDS package of computer Program 1: BULK, version 01/03 developed by Bakker (2003) and using the equation by Thiéry et al. (1994). The relative concentration of CO_2-CH_4 was determined by plotting $Tm_{(CO2)}$ and $Th_{(CO2)}$ on one of the *v*X diagrams calculated for the CO_2–CH_4 system from Thiéry et al. (1994) (Fig. 4.25). The molar volume range of the inclusions, read from the *v*X diagram, are from 48.4 to 88.9 cm^3/mol. CO_2 and CH_4 compositions ranged from 0.9208 – 0.9875 and 0.0125 – 0.0792 respectively. The presence of CO_2 and CH_4 has also been confirmed by the Raman analytical results.

The bulk density for the type IV (CH_4-rich) fluid inclusions was done by using the homogenization temperature of the methane-rich ($T_{h(CH4\text{-}rich)}$) fluid inclusions and compositions for CH_4, H_2O and N_2 following procedures given in Bakker and Brown (2003). The bulk density for the Type I (aqueous–rich) fluid inclusions, was calculated by using ice melting temperature and $Th_{(tot)}$ into the FLUIDS, package of computer Program 1: BULK and using the equation by Bodnar (1993).

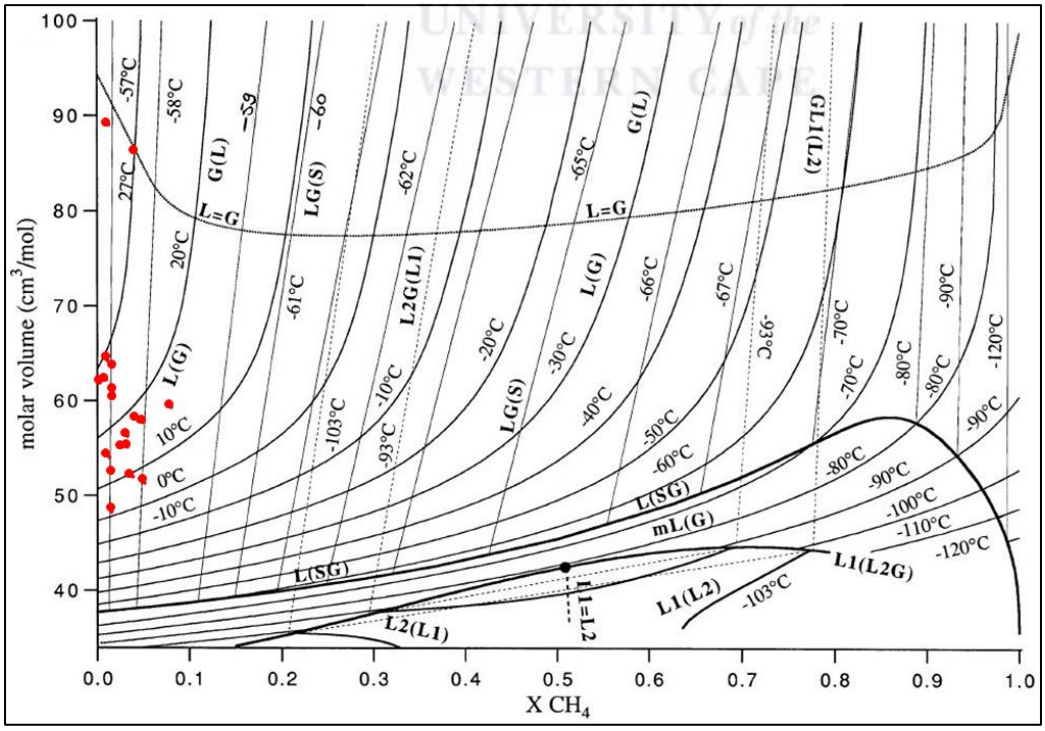

Fig. 4.25. *v*X diagrams calculated for the CO_2–CH_4 system. The red dots are the $Tm_{(CO2)}$ and $Th_{(CO2)}$ points which were used to determine the composition of CH_4 (the diagram is after Thiéry et al., 1994). Raman spectroscopy analysis also confirmed the presence of CO_2 and CH_4.

4.6 DATA ANALYSIS

4.6.1 HISTOGRAMS

Histograms of temperatures of homogenization ($T_{h(CO2)}$ and $T_{h(CH4)}$ (Fig. 4.28), $T_{h(tot)}$ (Fig. 4.26)) and CO_2 melting temperatures (Fig. 4.27) were constructed to depict the distribution of temperatures and also to show which inclusions are dominant either as isolated inclusions or those occurring in trails. Due to small number of clathrates recorded a characterization table was rather drawn (Table 4.4). Overall, fluid inclusions occurring in trails show dominance at the Sandamap prospect (Figs. 4.26 – 4.28).

The dominant type III (carbonic) fluid inclusions are primary (Figs. 4.27, 4.28) and occur in trails. The majority of the type III (carbonic) fluid inclusions, all primary and all from sampling point T14, have their CO_2 melting temperatures between -58.5 and -56.5 °C (Fig. 4.27). The type II (aqueous-carbonic) inclusions, all primary and all from sampling point NO2 also have their CO_2 melting temperatures between -58.0 and -57.5 °C (Fig. 4.27). The type V (methane-carbonic) fluid inclusions, all primary, occurring in trails, have CO_2 melting temperatures between -65 and -62.5 °C (Fig. 4.27).

A type II (aqueous-carbonic) inclusion from sampling point NO2 gave a CO_2 homogenization temperature of 15.3 °C (Fig. 4.28). The majority of the type III (carbonic) fluid inclusions, all primary and all from sampling point T14, also have their CO_2 homogenization temperatures around or above 10 °C (Fig. 4.28), and the type V (methane-carbonic) fluid inclusions, all primary, have CO_2 homogenization temperatures between -32 and -24 °C (Fig. 4.28).

All type I (aqueous-rich) inclusions are primary (Figs. 4.26, Table 4.4) and dominantly occur in trails. The dominating total homogenization temperatures of the type I fluid inclusions are around 180 to 310 °C (Fig. 4.26). Type IV (methane-rich) fluid inclusions are all primary (Fig. 4.28) and dominantly occur in trails. The homogenization temperatures of the type IV fluid inclusions (CH_4-rich) range from around -130 to -72 °C with a dominance at around -110 °C (Fig. 4.28). Melting temperatures of the clathrates ($T_{m(CL)}$) obtained from type I fluid inclusions range from 1.5 to 11 °C and are likely CO_2 or CH_4 clathrate (Table 4.4).

Table 4.4 Characterization table of clathrate melting of type I fluid inclusions from sampling point NO2.

Temperature (°C)	Number of fluid inclusions				Fluid inclusion type
	Trail	Isolated	Primary	Secondary	
0 - 2	1	0	1	0	Type I
>2 – 4	1	0	1	0	Type I
>4 – 6	0	0	0	0	Type I
>6 – 8	1	1	2	0	Type I
>8 – 10	0	1	1	0	Type I
>10 – 12	1	2	3	0	Type I
Total	**4**	**4**	**8**	**0**	

Note:The clathrate melting temperatures are between 0 and 11 °C suggesting them to be due to either CO_2 or CH_4.

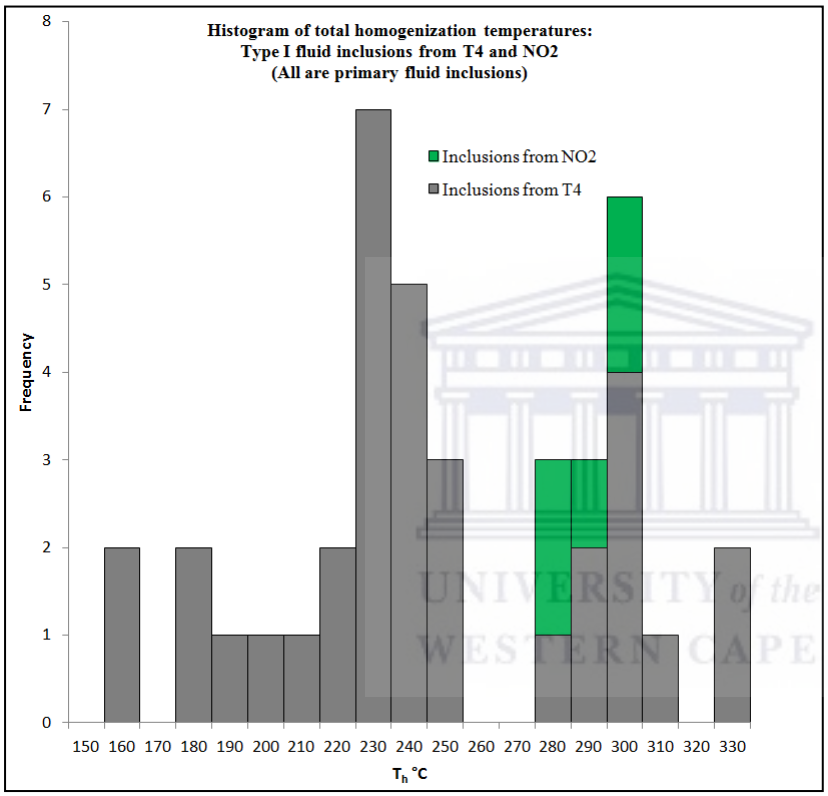

Fig. 4.26. Histogram of temperatures of total homogenization obtained from type I fluid inclusions from sampling points T4 and NO2.

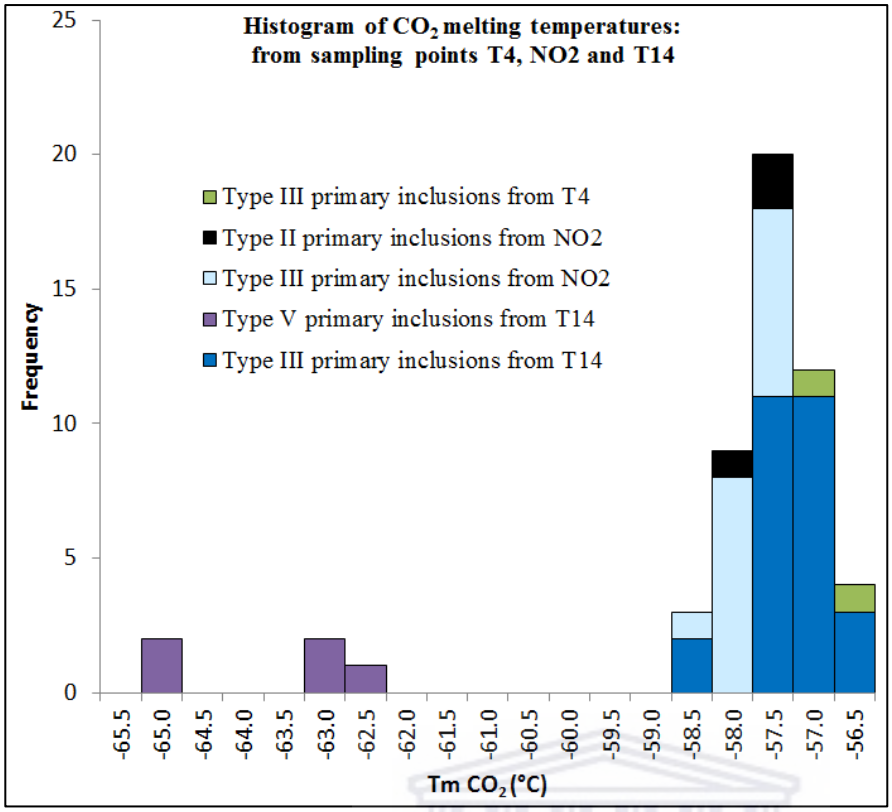

Fig. 4.27. Histograms of CO_2 melting temperatures of different fluid inclusion types from sampling points T4, NO2 and T14.

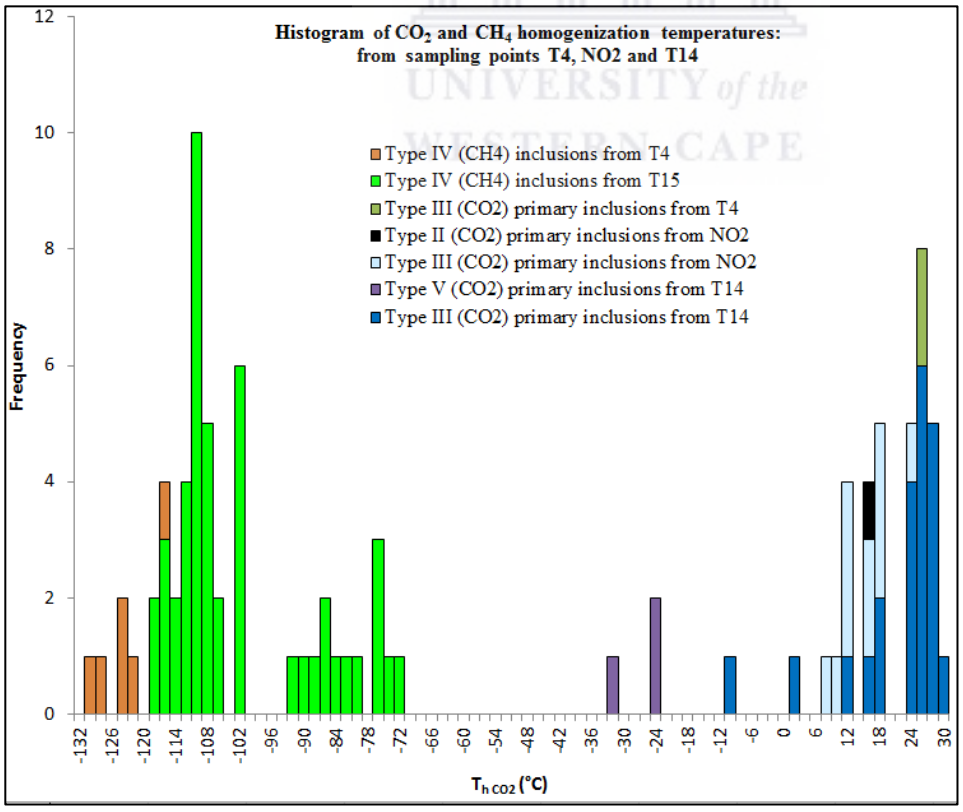

Fig. 4.28. Histograms of the homogenization temperatures of CO_2 and CH_4 of fluid inclusions from sampling points T4, NO2, T14 and T15.

Low to moderate temperatures (152 – 329 °C, average 242.9 °C) and dominant carbonic / gaseous fluid inclusions supports a metamorphic fluid source but this, however, does not rule out a magmatic origin (Wilkinson, 2001; Yardley et al., 2015).

4.6.2 ISOCHORES

Isochores for the type III (CO_2-rich) and the type IV (CH_4-rich) fluid inclusions were calculated by inserting bulk density and fluid composition into the FLUIDS package of computer Program 1: ISOC, version 01/03 developed by Bakker (2003). The equation used is that of Holloway (1977).

Pressure−temperature conditions and depth of entrapment

The depth of formation was calculated by using the equation:

$P = pgz$,

where P is the pressure of entrapment, p is the rock density (2600 kg/m^3 for metamorphic rocks), g is the gravitational acceleration (9.8 m/s^2), and z is the depth of formation.

The trapping P-T conditions can be determined using the following (Roedder and Bodnar, 1980; Shepherd et al., 1985): (i) dissolution temperatures of daughter minerals, (ii) intersecting isochores of co-existing fluids, (iii) vapour pressure at T_h, (iv) crystallisation temperatures determined using independent geothermometers (e.g. stable isotope geothermometry).

The type I and type III fluids are contemporaneous and the intersections of their isochores represent P-T conditions at trapping (Roedder and Bodnar, 1980) (Fig. 4.29). Based on the total homogenization temperatures of the aqueous fluid inclusions, two temperature groups were identified from the aqueous fluids: (1) the lower temperature group (150 – 250 °C), and (2) the higher temperature group (270 – 330 °C) (Fig. 4.26). Both temperature groups are present at trench 4 and at locality NO2 only the high temperature group is present (Fig. 4.26). The minimum and maximum P-T conditions of trapping of the two groups are defined by

isochore intersections of the CO_2 and aqueous fluids that were trapped at three different locations (T4, NO2 and T14) at the same time (Fig. 4.29).

Two sets of P-T estimations were carried out (1) using fluids from T4 and NO2, and (2) using fluids from T4 and T14. In each set, minimum and maximum P-T conditions were estimated for the two aqueous temperature groups, giving a total of eight P-T estimations for each set (these are the min. and max. temperatures and pressures for each temperature group) and their corresponding depths (Fig. 4.29, Tables 4.5 and 4.6). Also shown in Fig. 4.29 is the possible maximum trapping P-T conditions represented by a grey-shaded area. The possible maximum trapping P-T conditions is based on the postulation by Steven (1993), stating that since the abundant sillimanite-bearing assemblages in the central zone (CZ) seem to have originated from essentially isobaric heating, it is deemed unlikely for the peak metamorphic pressures at any stage in the evolution of the CZ to have exceeded the Al_2SiO_5 triple-point value of 3.76±0.3 kbar (Holdayway, 1971).

The Sandamap mineralization placed at 472 ± 3 Ma (this study - chapter 6), was deposited during retrograde metamorphism and this is supported by (i) the WR-biotite, K-Ar biotite and Rb-Sr biotite ages from 501 – 459 Ma that record cooling through 300 °C in the northern central zone (nCZ) (Jung et al., 1998; Haack and Hoffer, 1976; Haack et al., 1980) (Miller, 2008) (Fig. 4.29), and (ii) the $^{39}Ar/^{40}Ar$ hornblende ages (486 and 478 Ma) that record cooling through 525 °C towards the northern boundary of nCZ (Hawkesworth et al., 1983 as given in Miller, 2008) (Fig. 4.29).

T4 AND NO2 P-T ESTIMATIONS

Lower temperature group: data (Section 4.3.2, Figs. 4.15 & 4.16B, Table 4.5) shows that T4 type I and NO2 type III fluids are synchronous and that the minimum and maximum P-T ranges are 290 – 378 °C and 1.24 – 2.02 kbars corresponding to 5 – 8 km (Fig. 4.29, Table 4.5).

Higher temperature group: data (Section 4.3.2, Figs. 4.15 & 4.16B, Table 4.5) shows that T4 type I and NO2 type III fluids are synchronous and that the minimum and maximum P-T ranges are 448 – 520 °C and 1.78 – 2.58 kbars corresponding to 7 – 11 km (Fig. 4.29, Table 4.5).

T4 AND T14 P-T ESTIMATIONS

Lower temperature group: data (Section 4.3.2, Figs. 4.15 & 4.16B, Table 4.6) show that T4 type I and T14 type III fluids are synchronous and that the minimum and maximum P-T ranges are 187 – 424 °C and 0.95 – 2.64 kbars corresponding to 4 – 11 km (Fig. 4.29, Table 4.6).

Higher temperature group: data (Section 4.3.2, Figs. 4.15 & 4.16B, Table 4.6) shows that T4 type I and T14 type III fluids are synchronous and that the minimum and maximum P-T ranges are 293 (mean for a range of 270 – 330 ^{o}C) – 594 °C and 1.16 – 3.42 kbars corresponding to 5 – 14 km (Fig. 4.29, Table 4.6). The aqueous isochores for this group intersect with that of CO_2 below the hydrostatic gradient (Fig. 4.29) and as such, 293 °C (mean of the high temperature group for a range of 270 – 330 ^{o}C) was used as the minimum temperature at trapping.

GEOTHERMOMETERS

Temperatures from geothermometry on arsenopyrite and sphalerite from Navachab gold mineralization (494 ±8 Ma) (Jacob et al., 2000), located 40km to the east of Sandamap gold (472 ± 3 Ma) yielded 575 °C and 590 °C respectively (Nörtemann et al., 2000). Obtained pressures and depths from these geothermometers fall within the range determined from fluid inclusions. Navachab is 11 million years older than Sandamap and formed at the time when the subducting plate detached and hot mantle rose from below the nCZ. The implication is that the geotherms must have been likely higher than at the time when Sandamap formed, supporting this assertion is the fact that this is a period when nCZ underwent cooling through 525 and 300 °C. P-T intersections of arsenopyrite gave 3.2 kbars corresponding to 13 km and that of sphalerite gave 3.4 kbars corresponding to 14 km (Fig. 4.29, Table 4.5).

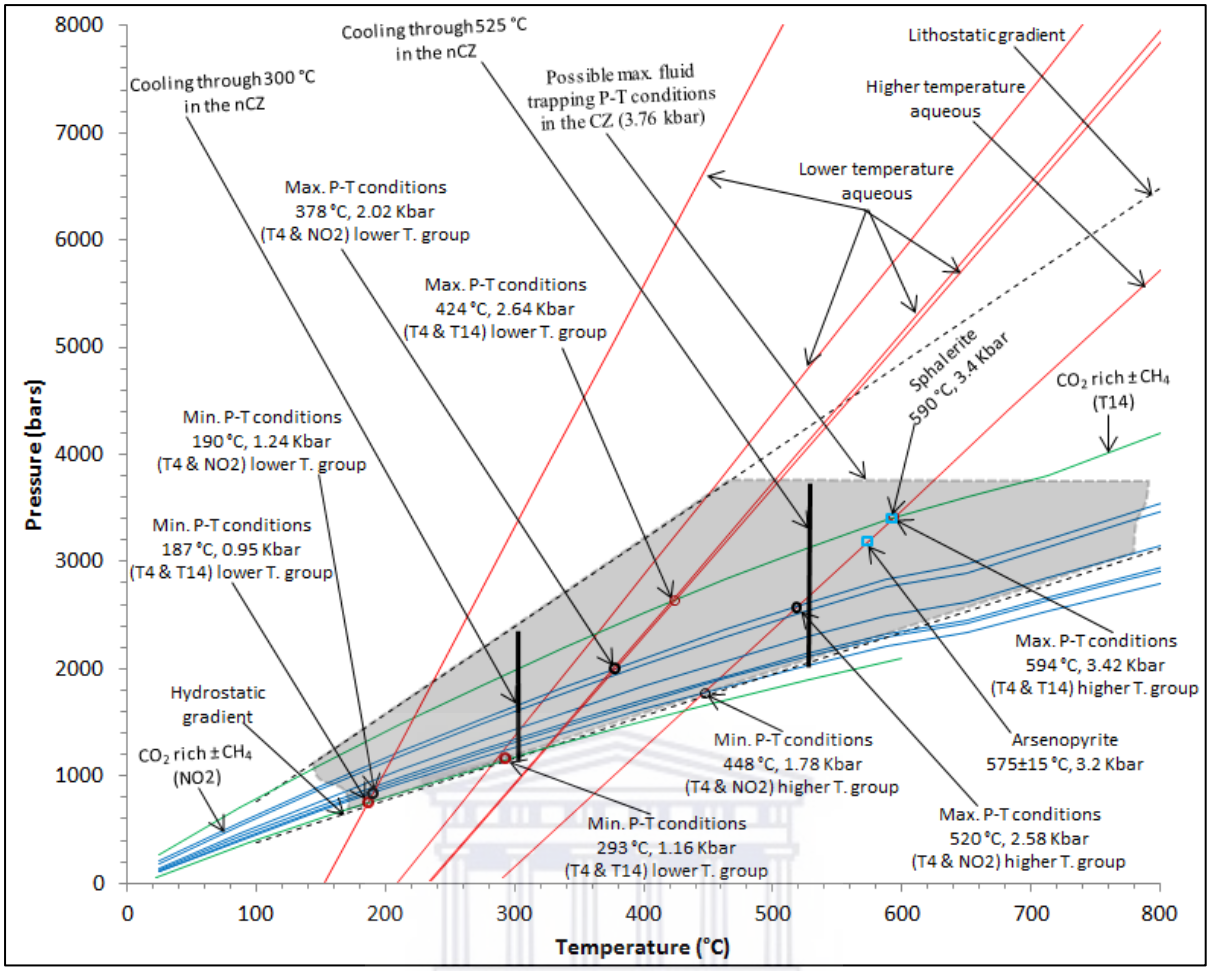

Fig. 4.29. Isochores for fluid inclusions from trench 4 and NO2, Sandamap gold prospect. The red lines represent aqueous fluid inclusions, the blue lines represent CO_2 rich $\pm CH_4$ fluid inclusions from NO2 and the green lines represent CO_2 rich $\pm CH_4$ fluid inclusions from T14. The aqueous and CO_2 rich $\pm CH_4$ fluid inclusions are contemporaneous; their intersections represent P-T conditions at trapping. The minimum and maximum conditions at trapping for the two aqueous fluid temperature groups identified in Fig 4.26 are shown. The possible maximum trapping P-T conditions represented by the grey shaded area is based on the postulation by Steven (1993), that it was unlikely for the peak metamorphic pressures at any stage in the evolution of the CZ to have exceeded the Al_2SiO_5 triple-point value of 3.76±0.3 kbar. Ore fluids were trapped during retrograde metamorphism indicated by cooling through 525 and 300 °C. Geothermometry on arsenopyrite and sphalerite from Navachab gold mineralization (494 ±8 Ma) (Jacob et al., 2000), located 40km to the east of Sandamap gold (472 ± 3 Ma) yielded 575 ±15 °C and 590 °C respectively (Nörtemann et al., 2000).

In a summary, the estimated P-T conditions using isochore intersections between fluids from the three different locations point roughly to the depth range of entrapment of 4 – 14 km. The Sandamap fluids seem to have formed at a wide range of depth mirroring a wide range of temperatures and pressures.

Table 4.5 Common pressure-temperature (P-T) conditions at trapping, estimated from contemporaneous CO_2 and aqueous fluids shown in Fig. 4.29 from trench 4 and NO2, Sandamap prospect.

LOCALITIES T4 AND NO2		T (°C)	P (bars)	Depth (m)	Depth (km)
Lower temperature group	Minimum	190	1,240.0	5,073.6	5
	Maximum	378	2,020.0	8,265.1	8
Higher temperature group	Minimum	448	1,780.0	7,283.1	7
	Maximum	520	2,580.0	10,556.5	11
Higher temperature group	Arsenopyrite	575	3,200.0	13,093.3	13
	Sphalerite	590	3,400.0	13,911.6	14

Table 4.6 Common pressure-temperature (P-T) conditions at trapping, estimated from contemporaneous CO_2 and aqueous fluids shown in Fig. 4.29 from trench 4 and 14, Sandamap prospect.

LOCALITIES T4 AND T14		T (°C)	P (bars)	Depth (m)	Depth (km)
Lower temperature group	Minimum	187	950.0	3,887.1	4
	Maximum	424	2,2640.0	10,802.0	11
Higher temperature group	Minimum	293	1160.0	4,746.3	5
	Maximum	594	3,420.0	13,993.5	14

Trapping conditions given in Tables 4.5 and 4.6 from three localities (T4, NO2 and T14) fall within a temperature range of 187 – 594 °C, pressure of 0.95 – 3.42 kbars corresponding to a depth range of 4 to 14 km. This depth range of entrapment covers the lower portion of the epizonal zone to the lower portion of the hypozonal zone (Fig 7.3).

4.7 RAMAN SPECTROSCOPY

Fluid inclusions contained in five doubly polished vein quartz chips described under "Samples for Raman spectroscopy" (Section 4.7.1) were analysed by Raman spectroscopy. Quantitative assessments were not carried out on the inclusions but relative terms such as weak and strong are used where the signal is weak or strong due to the volume fraction in the focal area of the beam. Raman spectra acquisition was also done on the hosting quartz matrix not covered by fluid inclusions and these were used as tests to unmask peaks resulting from the hosting quartz.

4.7.1 SAMPLES FOR RAMAN SPECTROSCOPY

Some representative fluid inclusions from each sampling point were analysed by Raman spectroscopy to carry out a qualitative assessment on the fluid inclusions present and also to confirm fluid compositions established through microthermometry. A total of 25 fluid inclusions were analysed: 4 from chip T4A (Fig. 4.30), 4 from chip T4B, 8 from chip T14A, 5 from chip T15BaseA and 4 from chip NO2B. Photomicrographs and sketches of analysed fluid inclusions are given in this section. A total of 19 fluid inclusions (T4A (1, b, c and d), T4B (1 and 8), T14 (8, 11, 15, 21, 22, 25, 26 and 29), T15 (1, 7, 13, 18 and 20)) which were analyzed by Raman spectroscopy have microthermometry data and the remaining six (T4B (7 and 18), NO2 (1, 2, 3 and 4)) do not.

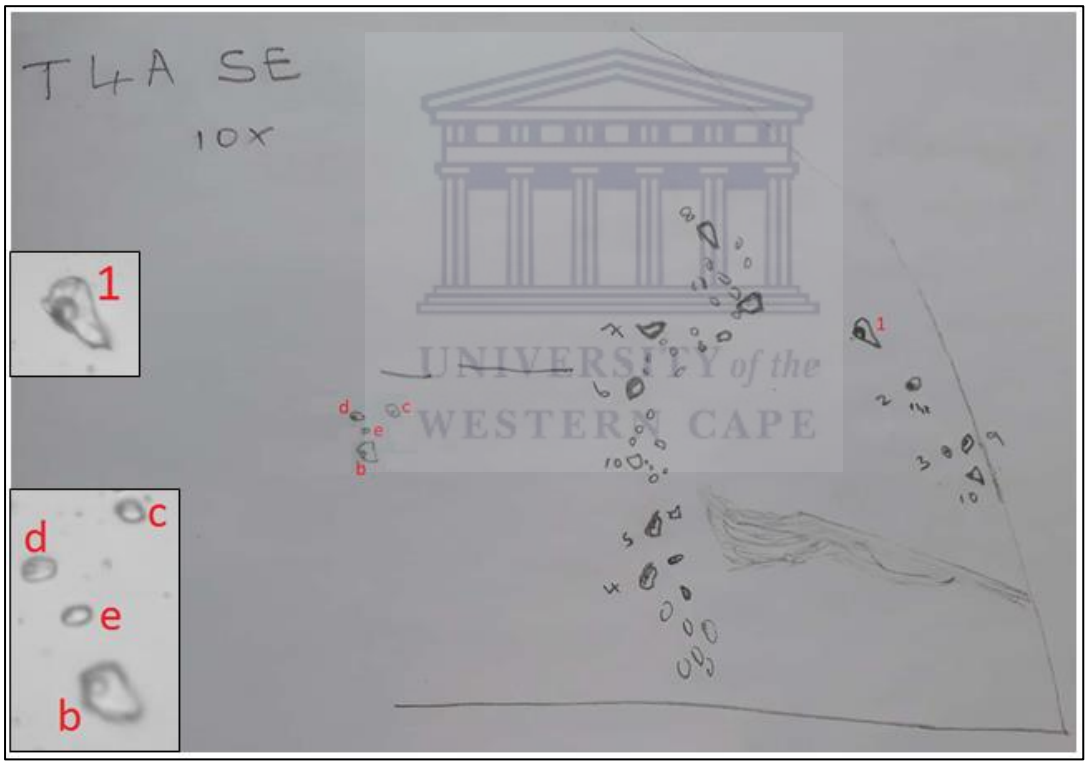

Fig. 4.30. Fluid inclusions analysed by Raman spectroscopy: A sketch of the left bottom corner of a double polished vein quartz wafer chip (T4A), (Fig. 4.7B) indicating positions of fluid inclusions and photomicrographs of the fluid inclusions marked in the sketch (1, b, c & d) that were analysed by Raman Spectroscopy.

At sampling point NO2 the focus was put on the analysis of fluid inclusions which were identified as H_2O-CO_2-rich (aqueous−carbonic) by microthermometry. These fluid inclusions were observed only at this locality, are occurring in trails, and a total of four fluid inclusions were analysed (Fig. 4.31).

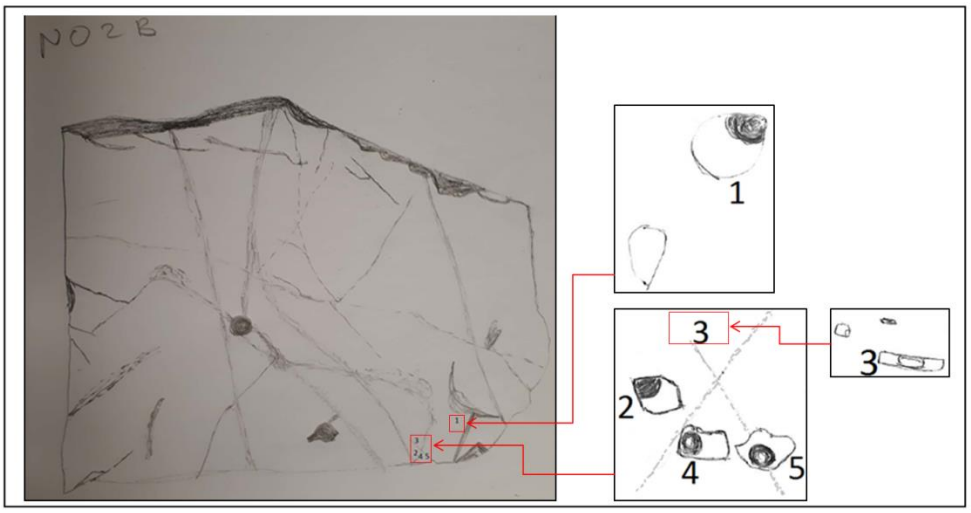

Fig. 4.31. Fluid inclusions analysed by Raman spectroscopy: Sketch of a double polished vein quartz wafer chip (NO2B) indicating positions of fluid inclusions in the chip and the sketches marked 1 to 4 are the fluid inclusions analysed by Raman spectroscopy.

A total of eight fluid inclusions (marked 8, 11, 15, 21, 22, 25, 26 and 29 in Fig. 4.32), all occurring in trails, were analysed from trench 14, with two of these (8 and 29) being bi-phase inclusions while the remainder are mono-phase inclusions. Fluid inclusions 15, 25 and 26 occur in the same trail. A total of five mono-phase fluid inclusions (marked 1, 7, 13, 18 and 20) from different trails were analysed at trench 15N and these are shown in Fig. 4.33.

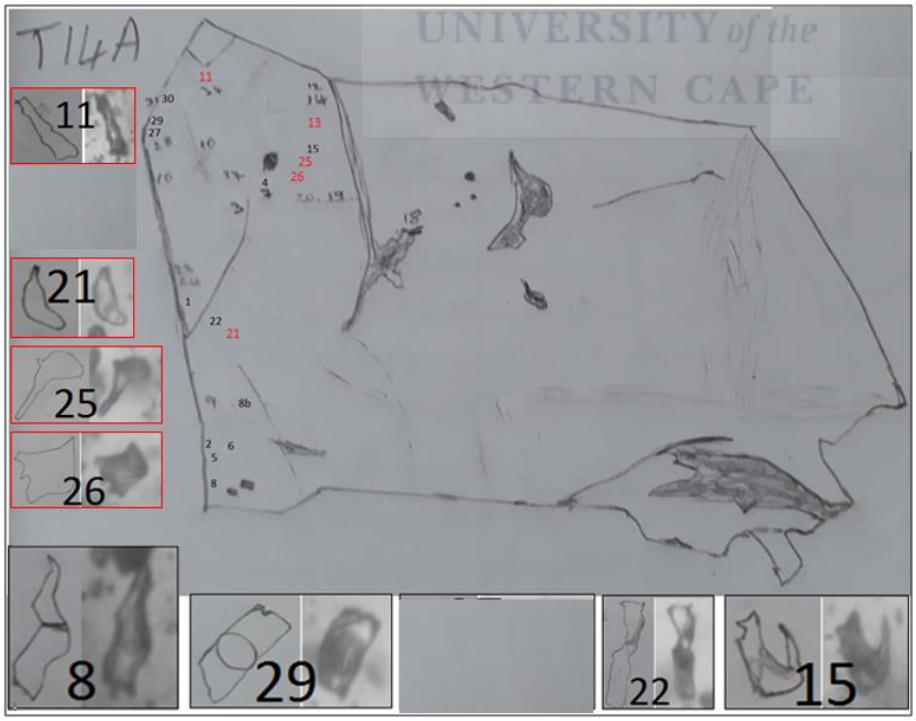

Fig. 4.32. Fluid inclusions analysed by Raman spectroscopy and their sampling locations: Sketch of a double polished vein quartz wafer chip (T14A) indicating positions of fluid inclusions; insert images are photomicrographs and sketches of the fluid inclusions marked in the chip (8, 11, 15, 21, 22, 25, 26 and 29) that were analysed by Raman spectroscopy.

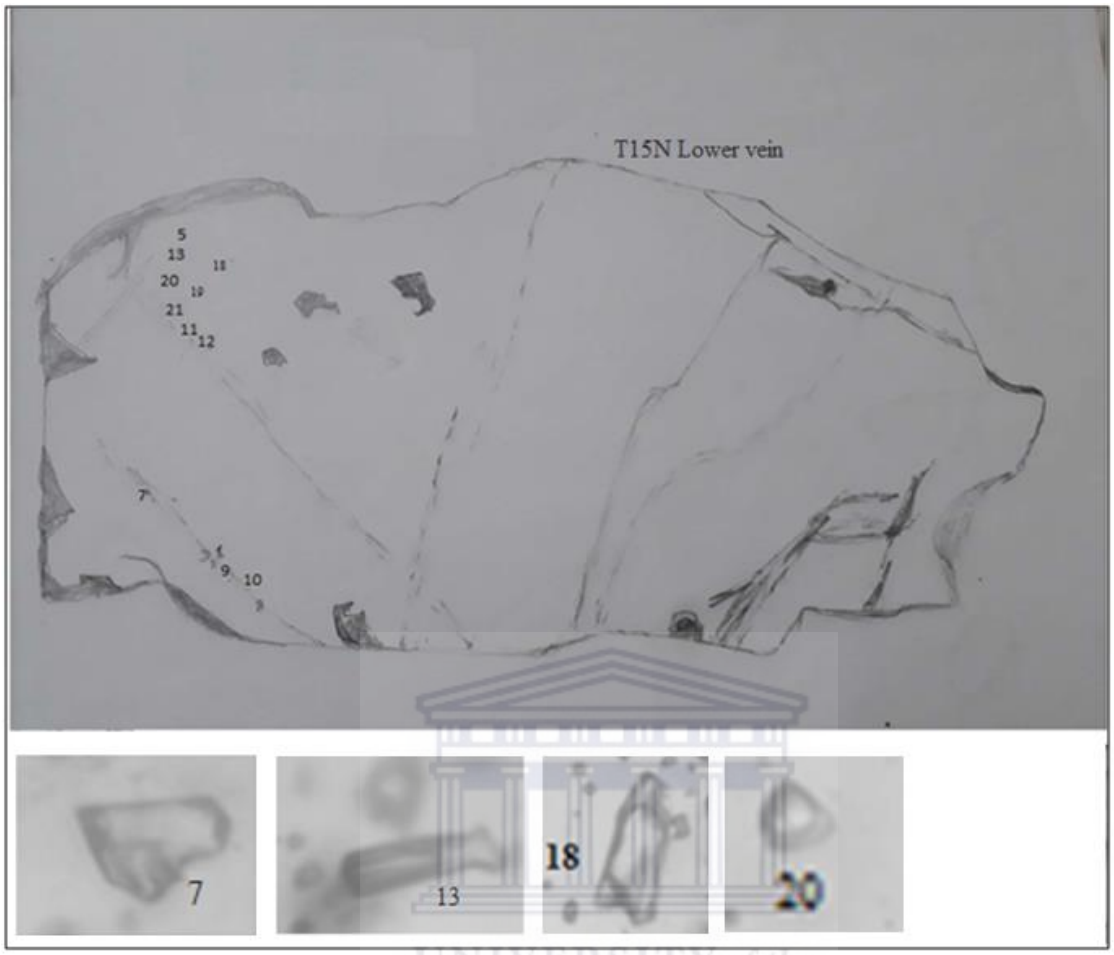

Fig. 4.33. Fluid inclusions analysed by Raman spectroscopy: Sketch of a doubly polished vein quartz wafer chip (T15N Lower vein) indicating positions of fluid inclusions; insert images are photomicrographs of the fluid inclusions marked in the chip (7, 13, 18 and 20) that were analysed by Raman spectroscopy.

4.7.2 RAMAN SPECTROSCOPY RESULTS

Results obtained from Raman spectroscopy are in agreement with the microthermometric data. At trench 4 the four analysed bi-phase fluid inclusions in chip T4A were found to contain type I fluid inclusions ($H_2O \pm CH_4 \pm N_2$ (Figs. 4.34A, B, C, D, Fig. M2A and B). Fluid inclusions marked as c and d (Fig. M2A and B) were too small for the laser beam diameter for the vapour and liquid portions to be measured separately, and, as such, these were analysed together.

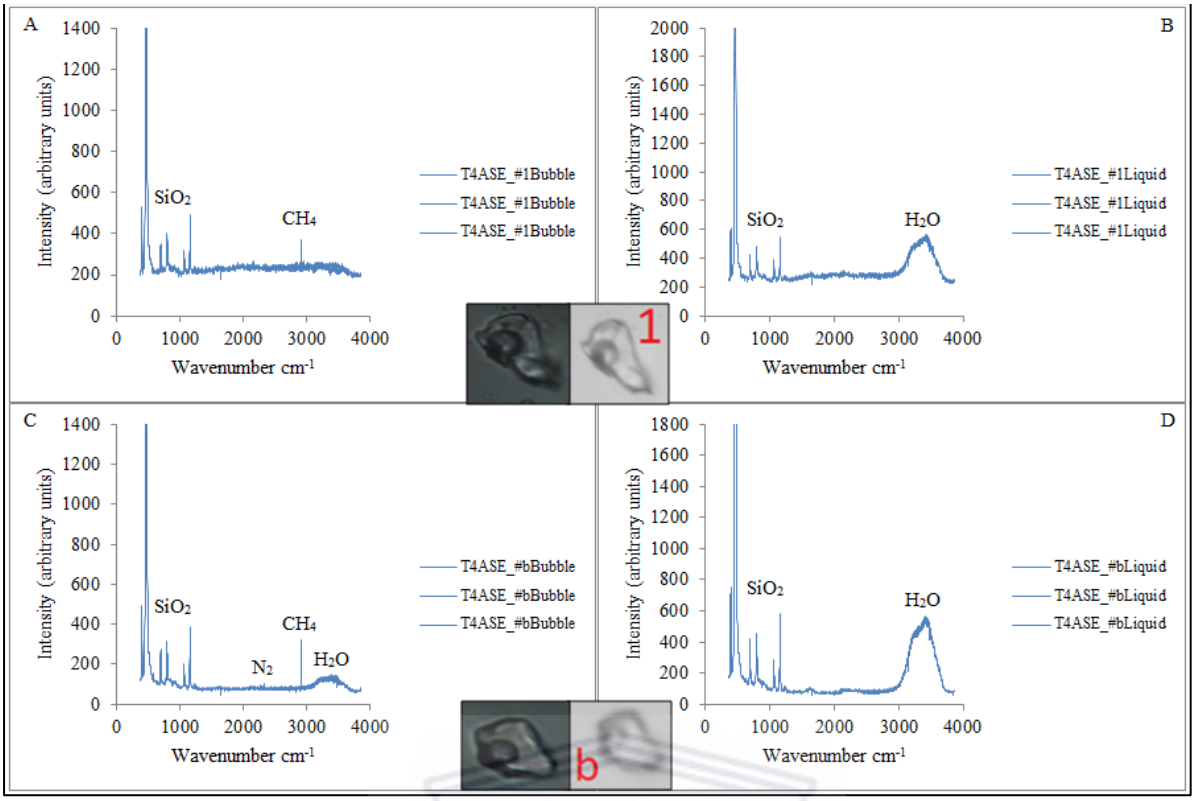

Fig. 4.34. Raman spectra for fluid inclusions 1 and b in chip T4A from trench 4. The insert images are Photomicrographs of the analysed fluid inclusions. A. Bubble spectrum showing the presence of CH_4, B. Liquid spectrum depicting the presence of H_2O, C. Bubble spectrum showing the presence of CH_4, H_2O and minor N_2, D. Liquid spectrum depicting the presence of H_2O. Other peaks are as a result of the host rock matrix (quartz).

The other bi-phase fluid inclusions from trench 4 chip T4B contain H_2O (Fig. M2C and D, Fig. M3A and B), and the mono-phase inclusion yielded $CH_4 \pm N_2$ (Fig. M3C).

Fluid inclusions from sampling point NO2 which were found to be composed of $H_2O-CO_2 \pm CH_4 \pm N_2$ by using microthermometry were confirmed by Raman spectroscopy to be as such (aqueous−carbonic fluid inclusions) and these are depicted in Fig. 4.35 and Fig. M4).

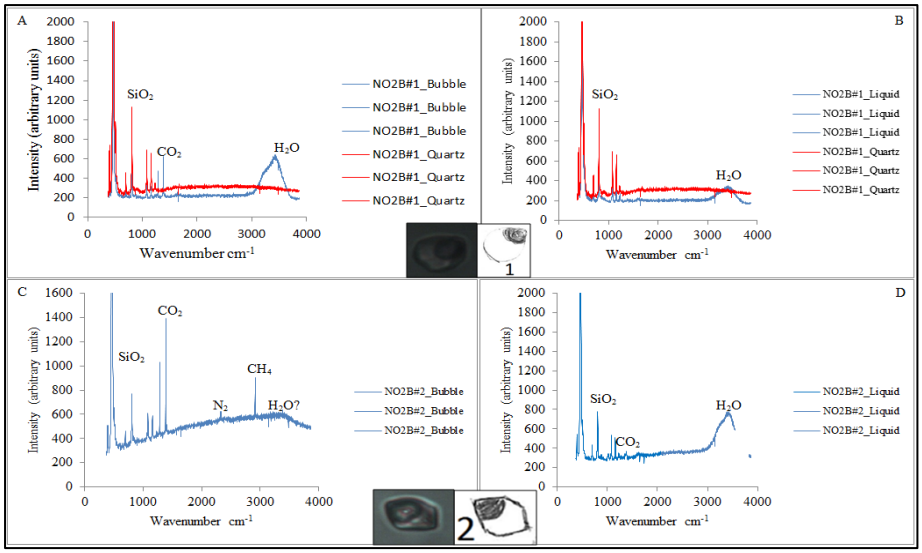

Fig. 4.35. Raman spectra for fluid inclusions 1 and 2 in chip NO2B from sampling point NO2. The insert images are photomicrographs of the analysed fluid inclusions. A. Spectra showing the presence of SiO_2, CO_2, and H_2O, B. Spectra showing the presence of H_2O and SiO_2, C. Spectrum showing the presence of CO_2, CH_4, N_2 and H_2O, D. Spectrum showing the presence of H_2O and CO_2. Red spectra in A and B are for quartz, the blue spectra in A and C are for bubbles, the blue spectra in B and D are for liquid.

At trench 14 two fluid inclusion types were obtained: CO_2±CH_4±N_2 and CH_4-CO_2±N_2. Fluid inclusions 8 and 29 yielded CO_2±CH_4±N_2 (Fig. 4.36A and Fig. M6), while inclusions 15, 25 and 26 gave CH_4-CO_2±N_2 (Fig. 4.36C, Fig. M5B and C). Fluid inclusions 11, 21 and 22 proved to be empty (Fig. 4.36B and D, Fig. M5A), probably due to leakage during microthermometry before Raman spectrocopy.

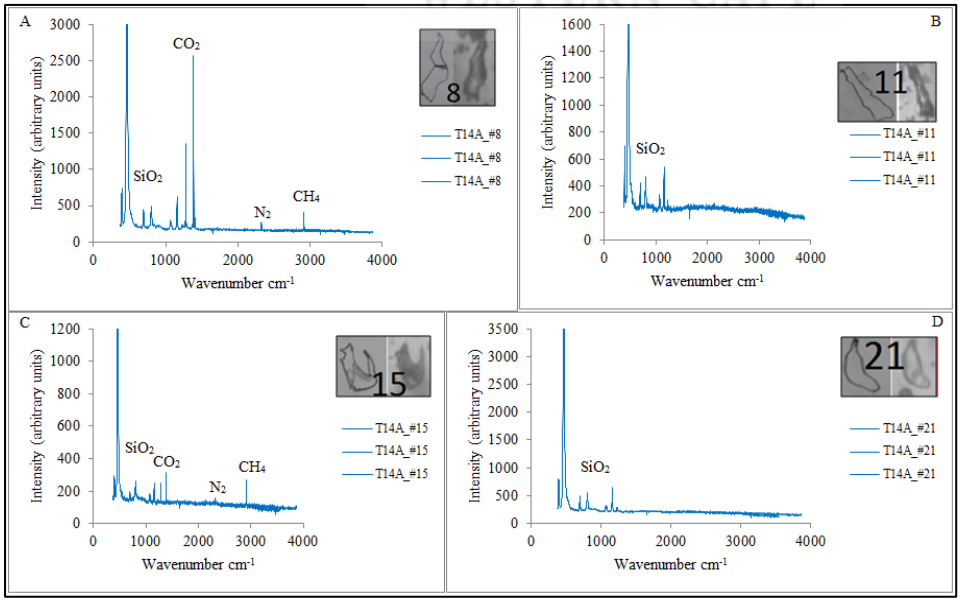

Fig. 4.36. Raman spectra for fluid inclusions 8, 11, 15 and 21 in chip T14A from trench 14. The inset images are photomicrographs and sketches of the analysed fluid inclusions. A. Spectrum showing the presence of CO_2, CH_4, and N_2, B. Inclusion 11 gave no gas peaks, C. Spectrum showing the presence of CO_2, CH_4, and N_2, D. Inclusion 21 gave no gas peaks.

Fluid inclusions 7, 13, 18 and 20 (Fig. 4.37) from the trench 15N showed the presence of $CH_4 \pm N_2$. The broad central feature depicted by the spectra in Fig. 4.37 is due to fluorescence likely from epoxy in fracture and cracks. If there was any H_2O in these inclusions it was probably concealed by the broad fluorescence spectra. Generally fluorescence occurs as a very broad background at many times greater intensity than Raman scattering and it may be due to the mounting or polishing epoxy, a matrix mineral e.g. fluorite, plagioclase feldspar or even quartz, or fluid inclusions containing fluorescent daughter minerals or aromatic hydrocarbons (Frezzotti *et al.*, 2012; Burke, 2001). Fluorescence can mask weak Raman features (Frezzotti *et al.*, 2012).

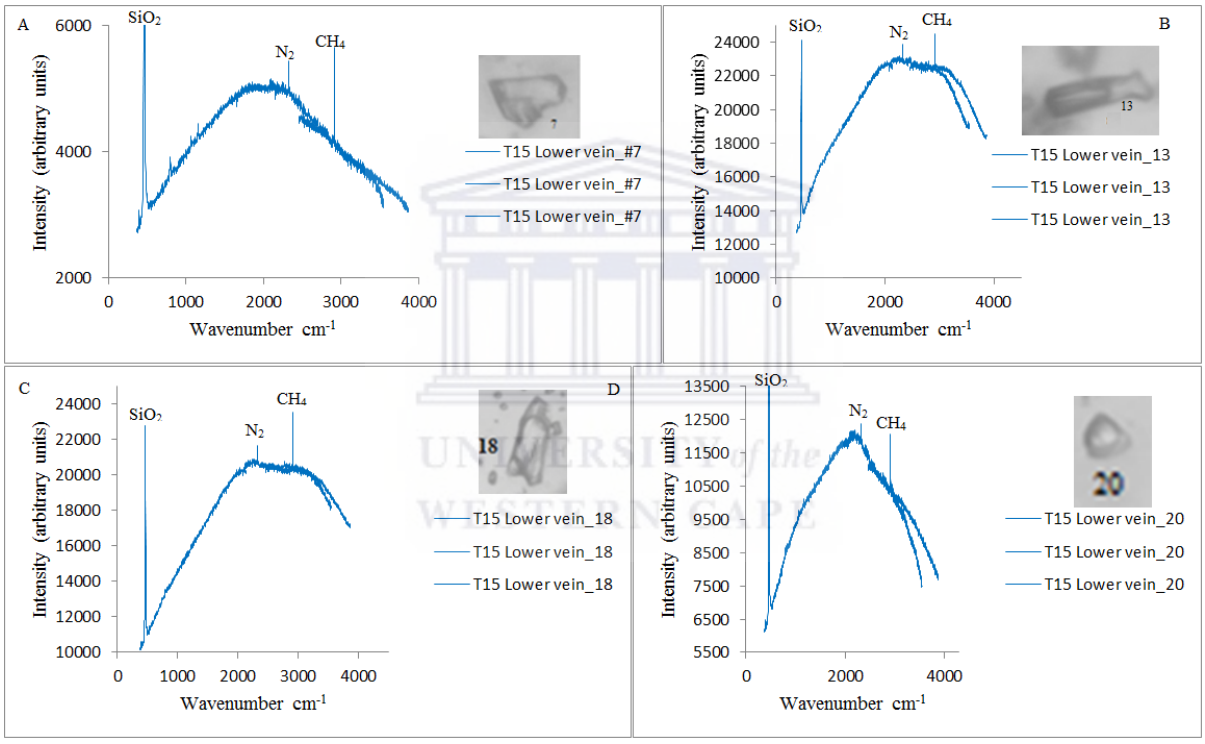

Fig. 4.37. Raman spectra for fluid inclusions 7, 13, 18 and 20 in chip T15 Lower vein from trench 15N. The insert images are photomicrographs of the analysed fluid inclusions. A.− D. Spectra showing the presence of N_2 and CH_4. The broad central feature depicted by the spectra is due to fluorescence likely due to epoxy in fractures and cracks.

In summary, the fluid inclusion types established by microthermometry have also been confirmed by Raman spectroscopy and these are given in Table 4.7.

Table 4.7 A summary of fluid inclusions identified by Raman spectroscopy

Fluid inclusion ID	**Fluid incluision type**	**Location**
T4A#1, b, c, d; T4B#1, 7, 8 and 18	Type I (H_2O±CH_4±N_2)	Trench 4
1, 2, 3 and 5	Type II (H_2O-CO_2±CH_4±N_2)	NO2
8 and 29	Type III (CO_2±CH_4±N_2)	Trench 14
7, 13, 18 and 20	Type IV (CH_4±H_2O±N_2)	Trench 15N
15, 25 and 26	Type V (CH_4-CO_2±N_2)	Trench 14

4.8 INTERPRETATIONS

Melting temperatures of the CO_2 (Tm_{CO2}) phase in the fluids and homogenization temperatures of the gaseous fluids

The CO_2 melting temperature (Tm_{CO2}) histogram (Fig. 4.27) depicts two distinctive compositions of CO_2-containing fluids: (1) fluids consisting of almost pure CO_2 with Tm_{CO2} in the vicinity of -56.6 °C and these are type II and III fluids from trench 4, NO2 and trench 14 and, (2) fluids with a CO_2 phase which melted at low temperatures ranging from -65.5 to -62.5 °C indicating that it is a mixed CH_4-CO_2±N_2 fluid (type V from trench 14) as per raman spectroscopy results. The CH_4-rich fluids homogenized at lower temperatures (ranging from -132 to -118 °C) at T4 in the SW than those in the NE at T15 that homogenized at a temperature range -120 to -72 °C (Fig. 4.38). CO_2 homogenized at variable temperatures ranging from -34 to 30 °C depicting no trend, but noteworthy is that the lowest temperatures (-34 to -24 °C) were obtained from the mixed CH_4-CO_2 fluid at T14 (Fig. 4.38).

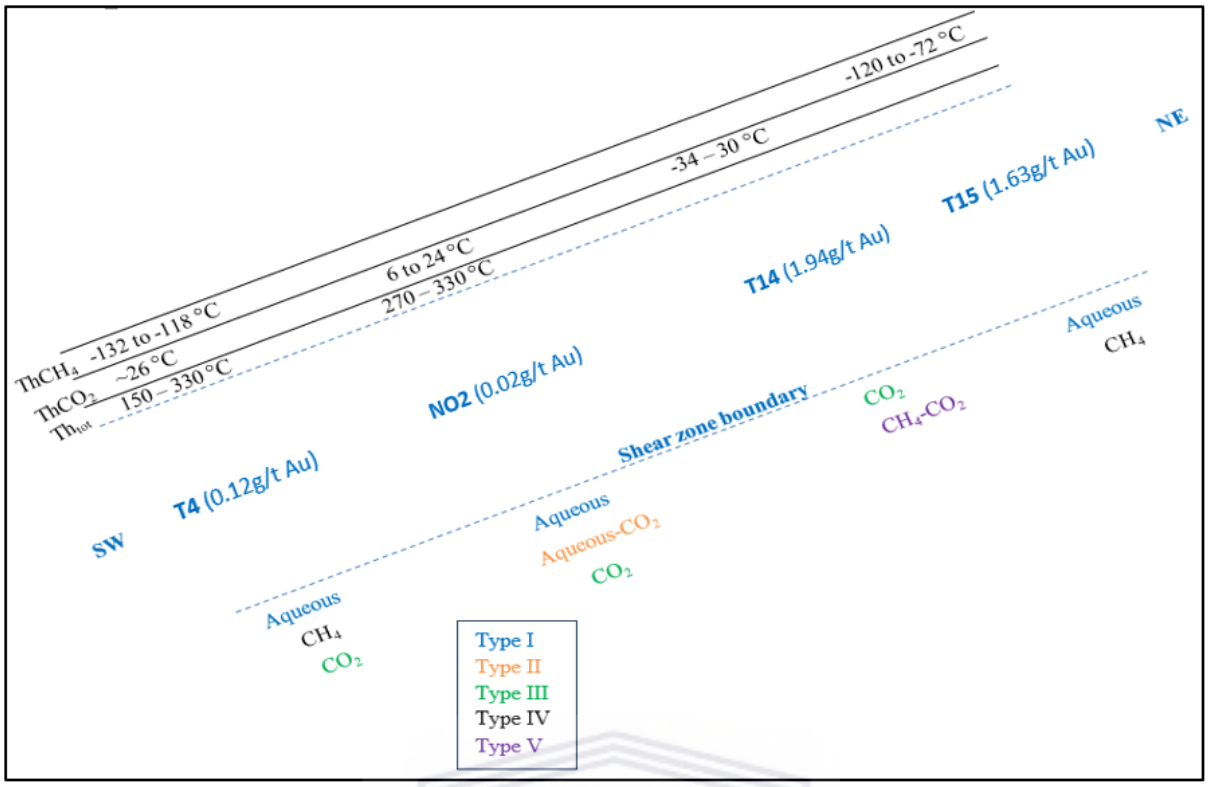

Fig.4.38 Homogenization temperature trends. Total homogenization temperatures obtained from aqueous fluid inclusions show two temperature groups; the lower temperature group (150 – 250 °C) at T4 and the higher temperature group (250 – 330 °C) at T4 and NO2 indicating a temperature increase towards the NE. Noteworthy is the association of the "rare" mixed CH_4-CO_2 fluid with highest Au grade recorded in this study (1.937 g/t Au).

Groups identified from temperatures of total homogenization

Two temperature groups: (1) the lower temperature group (150 – 250 °C), and (2) the higher temperature group (270 – 330 °C) were identified from the histogram of total homogenization temperatures (Figs. 4.26 and 4.38). The occurrence of lower and higher temperature type I fluid inclusion groups within the same quartz vein (Figs. 4.7) suggests fracturing and healing though fluid pressure build-up (Fault-valve model). The higher temperature group occurs at trench 4 and NO2, while lower temperature group occurs only at T4. After P-T corrections using synchronous fluid inclusion types I and III, the conditions at trapping were estimated as follows: the lower temperature group was trapped at temperatures ranging from 190 – 378 °C, pressures from 1.24 – 2.02 kbar (Fig. 4.29) and depths of 5 – 8 km (Tables 4.5); and the higher temperature group was trapped at temperatures ranging from 448 – 520 °C, pressures from 1.78 – 2.58 kbar (Fig. 4.29) and depths of 7 – 11 km (Table 4.5).

The observation is that the two temperature groups at T4 occur in the same quartz vein sample (Fig. 4.7, Table F2). As can be seen above, the higher temperature fluids were trapped at relatively higher pressures and greater depths. The occurrence of fluid inclusions with different pressures in a single quartz vein sample could be linked to the fault-valve model which is a process of repeated cycles of progressive fluid pressure build-up that leads to hydraulic fracturing at the ductile-brittle transition zone (Sibson et al., 1988; Robert and Kelly, 1987; Cox et al., 2001; Bodnar et al., 2014). The pressure regime can instantaneously change at the ductile-brittle transition which takes place at temperatures around 400 °C from lithostatic where deformation is ductile to hydrostatic where fluid pressure surpasses the brittle failure strength of the rock resulting in rock fracturing (Bodnar et al., 2014) (Fig. 4.39). This process can be repeated many times over and as a result fractures get healed through precipitation of quartz (Bodnar et al., 2014). The lower and higher temperature fluids were likely brought together through pressure build-up, fracturing followed by healing of fractures (Fig. 4.39).

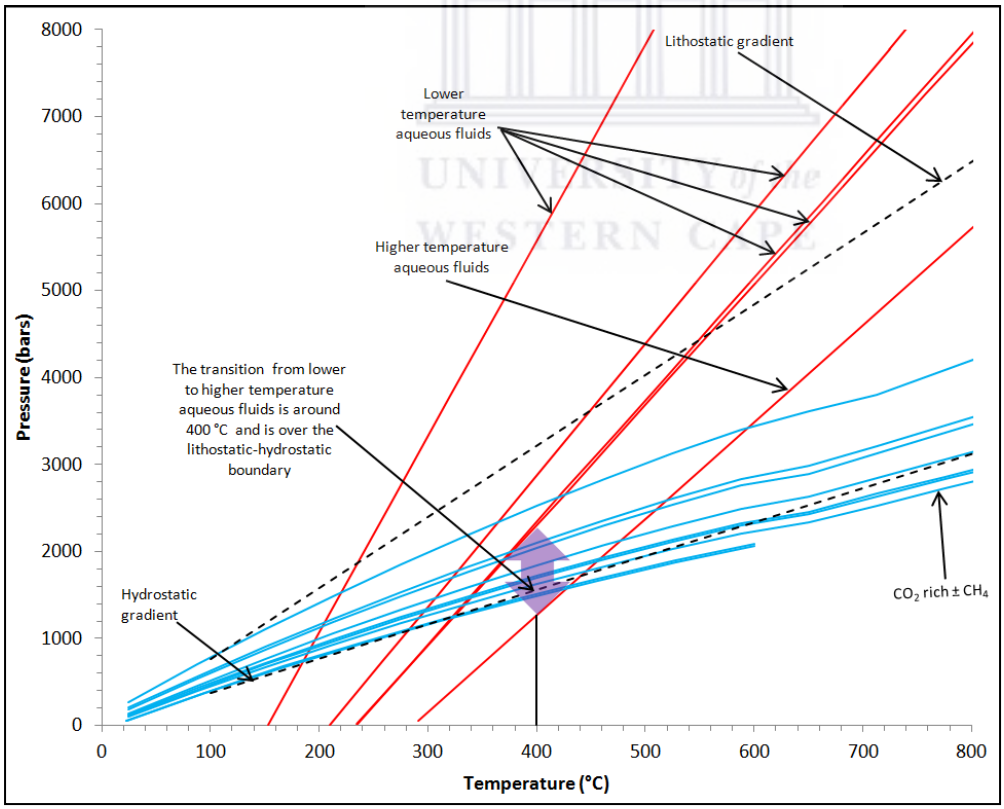

Fig. 4.39 The transition from lower to higher temperature aqueous fluids is around 400 °C and is over the lithostatic-hydrostatic boundary. This shows that it is likely that the lower and higher temperature fluids were brought together through pressure build-up, fracturing followed by healing of the fractures.

Gold deposit type

The trapping conditions stated above favour orogenic gold deposits as the deposit type for Sandamap. These commonly form at crustal depths ranging from 2 to 20 km, temperatures of 200 to 650 °C and pressures of 1 to 5 kbar (Groves et al., 1998, Goldfarb and Groves, 2015, Groves and Santosh, 2015). There are some deposits where conditions of formation have been found to be as low as 0.5 kb and 150 °C. Temperatures as high as 700 °C and pressures as high as 4-5 kb have, however, been reported for some deposits at deeper crustal levels (Groves, 1993; Groves et al., 1998; Groves et al., 2000). Further to that, the dominant CO_2-rich and CH_4-rich fluids observed at Sandamap do not contradict this interpretation. A magmatic source was a possibility but data gathered in this study weighs heavily towards a metamorphic source.

Fluids associated with higher Au grades

The highest gold grade of 1.94 g/t Au was recorded at trench 14 and it has been noted that type V (CH_4-CO_2±N_2) was only encountered at this locality in the entire study, bringing forth the assumption that this fluid type or a combination of the fluids encountered at this location (types III and V) may be associated with higher gold grades (Fig. 4.38). The second highest recorded grade of 1.63 g/t Au was recorded 20 m towards the northeast but the fluid types at trench 14 are absent.

4.9 REFERENCES

Bakker, R. J. (2003). Package FLUIDS 1. Computer programs for analysis of fluid inclusion data and for modelling bulk fluid properties. *Chemical Geology*, *194*(1−3), 3−23.

Bakker, R. J., Brown, P. E. (2003). Computer modelling in fluid inclusion research. In: Samson, I., Anderson, A. and Marshall, D. (eds), *Fluid inclusions – analysis and interpretation. Mineralogical Association of Canada, Short Course Series*, v. 32, p. 175−212).

Beane, R. E. (1983). The magmatic−meteoric transition. *Geothermal Resources Council Special Report, 13,* 245−253.

Bodnar, R. J. (1993). Revised equation and table for determining the freezing point depression of H_2O−NaCl solutions. *Geochimica et Cosmochimica Acta, 57*(3), 683−684.

Bodnar, R.J. (2003). Reequilibration of fluid inclusions. In: Samson, I., Anderson, A. and Marshall, D. (eds), *Fluid inclusions – analysis and interpretation. Mineralogical Association of Canada, Short Course Series,* v. 32, p.213−231.

Bodnar, R. J., Lecumberri−Sanchez, P., Moncada, D., Steele−MacInnis, M. (2014). 13.5—Fluid inclusions in hydrothermal ore deposits. *Treatise on Geochemistry, Second Edition. Elsevier, Oxford,* pp. 119−142.

Bodnar, R. J., Vityk, M. O. (1994). Interpretation of microthermometric data for H_2O−NaCl fluid inclusions. In. De Vivo b., Frezzotti M. L. (eds) *Fluid inclusions in minerals: methods and applications,* short course of the working group (IMA), International Mineralogical Association, Pontignano, 117−130.

Burke, E. A. (2001). Raman microspectrometry of fluid inclusions. *Lithos, 55*(1−4), 139−158.

Chi, G. X., Lu, H. Z. (2008). Validation and representation of fluid inclusion microthermometric data using the fluid inclusion assemblage (FIA) concept. *Acta Petrologica Sinica, 24*(9), 1945−1953.

Cox, S., Knackstedt, M., Braun, J. (2001). Principles of structural control on permeability and fluid flow in hydrothermal systems. *Reviews in Economic Geology 14,* 1–24.

Frezzotti, M. L., Tecce, F., Casagli, A. (2012). Raman spectroscopy for fluid inclusion analysis. *Journal of Geochemical Exploration, 112,* 1−20.

Goldstein, H. R., Reynold, T. J. (1994). Systematics of fluid inclusions in diagenetic minerals. *SEPM short course, 31, Society for Sedimentary Geology,* 199.

Goldfarb, R.J., and Groves, D.I. (2015). Orogenic gold: Common or evolving fluid and metal sources through time. *Lithos, 233,* 2-26.

Groves, D.I. (1993). The crustal continuum model for late-Archaean lode gold deposits of the Yilgarn block, Western Australia. *Mineralium Deposita 28,* 366-374.

Groves, D.I., Goldfarb, R.J., Knox-Robinson, C.M., Ojala, J., Gardoll, S., Yun, G.Y., and Holyland, P. (2000). Late-kinematic timing of orogenic gold deposits and significance for computer-based exploration techniques with emphasis on the Yilgarn Block, Western Australia. *Ore Geology Reviews, 17*(1-2), 1-38.

Groves, D.I., Goldfarb, R.J., Gebre-Mariam, M., Hagemann, S.G., and Robert, F. (1998). Orogenic gold deposits: a proposed classification in the context of their crustal distribution and relationship to other gold deposit types. *Ore Geology Reviews, 13*(1-5), 7-27.

Groves, D.I., and Santosh, M. (2015). Province-scale commonalities of some world-class gold deposits: implications for mineral exploration. *Geoscience Frontiers* 6, 389-399.

Haack, U. and Hoffer, E. (1976). K/Ar ages of biotites from the Damara-Orogen, South West Africa. *Trans. geol. Soc. S. Afr*., 79, 213-216.

Haack, U., Gohn, E. and Klein, J.A. (1980). Rb/Sr ages of granitic rocks along the middle reaches of the Omaruru River and the timing of orogenetic events in the Damara Belt (Namibia). *Contrib. Miner. Petrol*., 74, 349-360.

Hawkesworth, C.J., Gledhill, A.R., Roddick, J.C., Miller, R.McG. and Kröner, A. (1983). Rb-Sr and 40Ar/39Ar studies bearing on models for the thermal evolution of the Damara Belt, Namibia, 323-338. *In*: Miller, R.McG. (Ed.) *Evolution of the Damara Orogen of South West Africa/Namibia*. Spec. Publ. geol. Soc. S. Afr., 11, 515 pp.

Holdaway, M.J. (1971). Stability of andalusite and the aluminium silicate phase diagrams. *American Journal of Science*, **271**, 97-131.

Holloway, J. R. (1977). Fugacity and activity of molecular species in supercritical fluids. In: Fraser, D. (ed), *Thermodynamics in geology*. Reidel, Boston, p. 161−181.

Jacob, R.E., Moore, J.M. and Armstrong, R.A. (2000). Zircon and titanite age determination from igneous rocks in the Karibib District, Namibia: implications for

Navachab vein-style gold mineralization, *Communications of the geological of Survey of Namibia*, **12**, 157-166.

Jung, S., Mezger, K. and Hoernes, S. (1998). Petrology and geochemistry of syn- to post-collisional metaluminous A-type granites - a major and trace element and Nd – Sr - Pb - O isotope study from the Proterozoic Damara Belt, Namibia. *Lithos*, 45, 147-175.

Kokh, M. A., Akinfiev, N. N., Pokrovski, G. S., Salvi, S., and Guillaume, D. (2017). The role of carbon dioxide in the transport and fractionation of metals by geological fluids. *Geochimica et Cosmochimica Acta*, *197*, 433-466.

Mei, W., Lü, X., Cao, X., Liu, Z., Zhao, Y., Ai, Z., Tang, R., Abfaua, M. M. (2015). Ore genesis and hydrothermal evolution of the Huanggang skarn iron–tin polymetallic deposit, southern Great Xing'an Range: Evidence from fluid inclusions and isotope analyses. *Ore Geology Reviews*, *64*, 239−252.

Miller, R.M. (2008). Neoproterozoic and early Palaeozoic rocks of the Damara Orogen. In: Miller, R.M. (Ed.), The Geology of Namibia. Geological Survey of Namibia, Windhoek vol. 2, pp. 13-1–13-410.

Nörtemann, M. F. J., Mücke, A., Weber, K., & Meinert, L. D. (2000). Mineralogy of the Navachab skarn deposit, Namibia: an unusual Au-bearing skarn in high-grade metamorphic rocks. *Communications of the Geological Survey of Namibia*, *12*, 149-156.

Ray, J. S. (2009). Carbon isotopic variations in fluid-deposited graphite: evidence for multicomponent Rayleigh isotopic fractionation. *International Geology Review*, *51*(1), 45-57.

Robert, F., Kelly, W. C. (1987). Ore−forming fluids in Archean gold−bearing quartz veins at the Sigma Mine, Abitibi greenstone belt, Quebec, Canada. *Economic Geology*, *82*(6), 1464−1482.

Roedder E., Bodnar R.J. (1980). Geological pressure determinations from fluid inclusion studies. *Annual Reviews of Earth and Planetary Sciences*, 8(1), 263-301.

Roedder, E., Bodnar, R. J. (1997). Fluid inclusion studies of hydrothermal ore deposits. In: Barnes H. L. (ed), *Geochemistry of hydrothermal ore deposits*. Wiley, New York, pp. 657–697.

Shepherd, T. J., Rankin, A. H., Alderton, D. H. (1985). A practical guide to fluid inclusion studies. Blackie. Glasgow, p.239.

Sibson, R. H., Robert, F., Poulsen, K. H. (1988). High-angle reverse faults, fluid-pressure cycling, and mesothermal gold-quartz deposits. *Geology*, *16*(6), 551−555.

Steven, N.M. (1993). A study of epigenetic mineralization in the Central Zone of the Damara Orogen, Namibia with special reference to gold, tungsten, tin and rare earth elements. *Memoir of the Geological Survey of Namibia*, **16**, 166 pp.

Thiery, R., Van Den Kerkhof, A. M., Dubessy, J. (1994). vX properties of CH_4−CO_2 and CO_2−N_2 fluid inclusions: modelling for T< 31^{o}C and P < 400 bars. *European Journal of Mineralogy*, *6(6)*, 753−771.

Wilkinson, J. J. (2001). Fluid inclusions in hydrothermal ore deposits. *Lithos*, *55*(1−4), 229−272.

Yardley, B.W., Cleverly J.S. (2015). The role of metamorphic fluids in the formation of ore deposits. *Geological Society, London, Special publications,* 393(1), 117–134.

CHAPTER 5

STABLE ISOTOPE STUDIES

5.1 RESEARCH EQUIPMENT

Oxygen and carbon gaseous extracts were prepared from pulverized vein quartz and carbonate samples and analyzed for delta values of oxygen-18 ($\delta^{18}O$) and carbon-13 ($\delta^{13}C$). A Finnigan Delta XP dual inlet Gas Source Mass Spectrometer was used to measure isotopic ratios of oxygen and carbon at the Department of Geological Sciences, University of Cape Town (UCT).

5.2 SAMPLE PREPARATION AND ANALYSIS

Sample preparation for the analysis of oxygen in vein quartz samples was carried out using a conventional silicate line. Approximately 10 mg of sample was reacted with ClF_3, and the liberated O_2 was converted to CO_2 using a hot platinized carbon rod. Oxygen isotope ratios were measured offline using a Finnigan Delta XP mass spectrometer in dual-inlet mode on CO_2 (conventional). The results are given in delta notation (δ) where $\delta^{18}O = (R_{sample}/R_{standard} - 1) \times 1000$, where R = the measured $^{18}O/^{16}O$ ratio. For the whole-rock data (whole rock mill of quartz vein), duplicate splits of the quartz standard (NBS28) were run with each batch of samples and were used to convert the raw data to the Standard Mean Ocean Water (SMOW) scale using the $\delta^{18}O$ value of 9.64‰ for NBS28 following recommendations by Coplen et al. (1983). The long-term statistical variability in replicate analyses of NBS28 suggests a 2σ error of 0.16‰ (Harris *et al.*, 2015).

Sample preparation for the analysis of carbon utilized a carbonate line for the extraction of CO_2 in carbonate samples using phosphoric acid. The carbonate samples were reacted with '103%' phosphoric acid overnight at 50°C and the data as such represents the total carbonate (calcite + dolomite) present. An internal standard calibrated against NBS-19 ($\delta^{18}O$ = 28.64‰, $\delta^{13}C$ = 1.95‰) was used to normalise the carbonate data to Pee Dee Belemnite (PDB) and SMOW. The results are reported in δ notation, where $\delta = (R_{sample}/R_{standard} -1) \times 1000$, and R = the measured ratio (i.e. $^{13}C/^{12}C$). A total of 8 samples were submitted for analysis of both O

and C isotopes; from these seven yielded O isotopes values and only two contained calcite giving only two C isotope values (Table 5.1).

Samples (1-2 g) of vein quartz fragments of <3 mm were heated at temperatures >800°C and inclusion fluids (H_2O, CO_2) were liberated by decrepitation of fluid inclusions. The quartz fragments were degassed at 200°C for two hours and at 200°C under vacuum for 30 minutes. The water obtained was trapped cryogenically and analysed for hydrogen isotopes following the Zn reduction method by Vennemann and O'Neil (1993). Any CO_2 produced from the inclusions was also trapped, but the amount of gas was too small for analysis. The D/H ratios were analysed using a Finnigan Delta XP mass spectrometer and results are given in the delta notation, normalized to the SMOW scale. Standardisation was carried out relative to two in-house water standards of broadly differing δD value (-7.4 and -131.4‰) and these values were used to correct for scale compression.

5.3 RESULTS

5.3.1 $\delta^{18}O$ and $\delta^{13}C$ of quartz, calcite and fluids

The analytical data on oxygen and carbon isotopes of vein quartz, calcite and the calculated $\delta^{18}O_{water}$ values of ore-fluids are listed in Table 5.1. The $\delta^{18}O_{SMOW}$ analytical values from quartz vary from 13.7 to 18.4‰. $\delta^{18}O_{SMOW}$ analytical values for quartz from SW to NE are given as follows: T4 yielded 13.7‰, NO2 gave 16.9‰, T14 gave 16.0‰ and 3 quartz veins were analysed at T15 , these yeleded 14.0 ‰, 17.8‰ and 18.4‰ and a vein 2m further north at T15N gave 16.7‰. In a summary it is noted that there is no trend observed in the data. Only two $\delta^{18}O_{SMOW}$ analytical values were determined from calcite; 24.07‰ and 24.14‰ from T6 and T15NB respectively and accordingly, only two $\delta^{13}C_{PDB}$ values were determined from calcite and these are -5.82 from T6 and -4.22‰ from T15NB. The $\delta^{18}O_{water}$ values were calculated from the $\delta^{18}O$ values for quartz and the mean homogenization temperature obtained from fluid inclusions, using an equation for quartz–water isotopic equilibrium (Clayton et al., 1972). The homogenization temperatures of aqueous fluid inclusions were assumed to be the estimated minimum trapping temperatures and these varied from 152 to 329°C; a total of 39 measurements (Tables 4.3; Appendix F). Two temperature groups have been identified from the homogenization temperatures of the aqueous fluid inclusions; (1) the lower temperature group (150 – 250 °C), and (2) the higher temperature group (270 – 330 °C)

(Fig. 4.26, Section 4.6.2). The averages of these groups (217.7 °C and 293.4 °C) were used to calculate $\delta^{18}O_{water}$ values of ore-fluids. The results show that the calculated $\delta^{18}O_{water}$ values of the ore-fluids of the lower temperature group range from +3.1 to +7.8‰, with an average of +5.6‰ and those of the higher temperature group range from +6.6 to +11.3‰, with an average of +9.1‰ (Table 5.1).

Table 5.1 Stable isotope results

Sample ID	$\delta^{18}O_{SMOW}$ (‰; quartz)	$\delta^{13}C_{PDB}$ (‰; calcite)	$\delta^{18}O_{SMOW}$ (‰; calcite)	$\delta^{18}O_{water}$ (‰) (217.7°C)	$\delta^{18}O_{water}$ (‰) (293.4°C)	δD_{water} (‰)	wt.% water	wt.% carb
NO2	16.9			6.3	9.8	-45	0.034	
NO2a						-49	0.022	
T4	13.7			3.1	6.6	-43	0.098	
T4a						-35	0.016	
T6		-5.82	24.07					46
T14	16.0			5.4	8.9			
T15 3d	17.8	no gas		7.2	10.7			<1%
T15 IZ	18.4			7.8	11.3			
T15 NB	16.7	-4.22	24.14	6.1	9.6			8
T15	14.0			3.4	6.9			

Notes: $\delta^{18}O_{water}$ (‰) in equilibrium with quartz is calculated according the equation: $1000\ln\alpha_{quartz\text{-}water} = 3.38 \times 10^6\ T^{-2} - 3.40$ (Clayton et al., 1972); mean homogenization temperatures of 217.7 °C and 293.4 °C of the two temperature groups were used as the equilibrium temperatures.

5.4 DATA ANALYSIS

According to Goldfarb & Groves (2015) it is difficult, but not impossible, to determine whether carbon in the ore-forming fluids, and ultimately in the hydrothermal carbonates, is derived from carbonates, organic material in the crust, or magmas. The universal observation is that the majority of orogenic deposits show consistency in having slightly negative carbon isotope compositions whether calculated from measurements on carbonates or measured directly on CO_2 extracted from fluid inclusions (Goldfarb & Groves, 2015).

5.4.1 Ore fluid equation

The equation used to determine the $\delta^{18}O$ water values of the ore fluids is:

$1000\ln\alpha_{quartz\text{-}water} = 3.38 \times 10^6\ T^{-2} - 3.40$ by Clayton et al. (1972)

The calculated $\delta^{18}O_{water}$ values of the ore-fluids of the higher temperature group (+6.6 to +11.3‰) fall in the range of metamorphic fluids which themselves can be indicative of an orogenic gold deposit (+7 to +13‰) (Goldfarb & Groves, 2015) typically derived from metamorphic fluids. The calculated $\delta^{18}O_{water}$ values of the ore-fluids of the lower temperature group (+3.1 to +7.8‰) are indicative of a mixed meteoric and metamorphic fluid source. However, the observed trapping pressure variations between the lower and higher temperature fluid inclusions groups within the same quartz vein samples (Fig. 4.7) and the transition from lower to higher isochores along the lithostatic-hydrostatic boundary at around 400 °C suggest different deposition episodes of fluid inclusions linked to fault-valve model (Sibson et al., 1988) (Fig. 4.7, Section 4.8-Fig. 4.39).

The fault-valve model can be defined as repetitious hydraulic fracturing of the rock at the brittle–ductile transition resulting from pressure buildup and fracture healing by quartz precipitation (Sibson *et al.*, 1988). The fault-valve behaviour causes abrupt fluid pressure fluctuations from pre-failure lithostatic to post-failure hydrostatic levels, linked to the earthquake cycle (Sibson, 1990). Fault-valve behaviour may occur at any level within over-pressured portions of seismically active crust, wherever an active fault transect a suprahydrostatic fluid pressure gradient, or wherever an active fault cuts an impermeable barrier (Sibson, 1990).

Faults act as impermeable seals prior to post-failure, when they become highly permeable channel-ways for fluid discharge (Sibson, 1990). Fault-valve behaviour is likely to be associated with high-angle reverse faults. The fracturing likely occurs along zones of weaknesses which in the case of a shear zone would be along shear fabric. This process can repeat itself many times over resulting in layered quartz veins or thin quartz veinlets (Bodnar et al., 2014; Sibson et al., 1988).

Features of fault-valve behaviour are:

(i) Cross-cutting relationships between pre-failure extension veins and post-failure discharge veins lying within the fault zones or subhorizontal quartz vein perpendicular to subvertical shear zones (Sibson, 1990; Chi, and Guha, 2011).

(ii) Post-failure discharge quartz veins indicating incremental deposition alternating with episodes of fault slip (Sibson, 1990).

(iii) Lenticular fault veins of quartz subparallel to the shear-zone schistosity or mylonitic foliation (Sibson, 1990).

Fluid inclusions in quartz from the Sandamap deposit have δD values from −35‰ to −49‰ (Table 5.1). In a plot of δD vs. $\delta^{18}O_{H2O}$ (Fig. 5.1), quartz samples from the Sandamap deposit plot in the metamorphic field with some plotting in the overlap region between the metamorphic and magmatic fields.

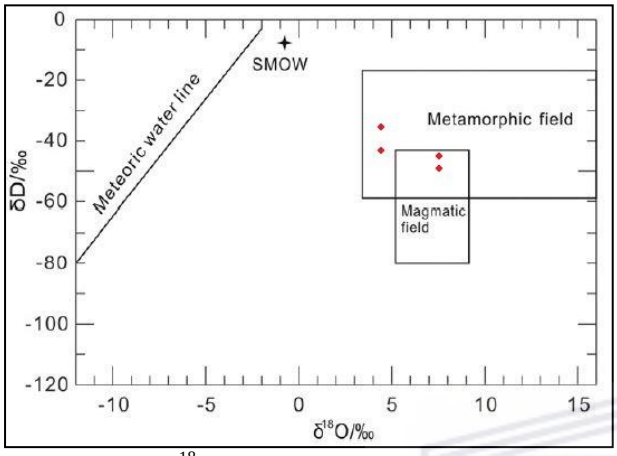

Fig. 5.1 δD vs. $\delta^{18}O_{H2O}$ diagram of fluids from ore vein quartz. Data plot in the metamorphic field with some plotting in the overlap between the metamorphic and magmatic fields (after Shen et al., 2016).

5.5 REFERENCES

Bodnar, R.J., Lecumberri-Sanchez, P., Moncada, D. and Steele-MacInnis, M., 2014. Fluid inclusions in hydrothermal ore deposits. In: H.D. Holland and K.K. Turekian (Editors), Treatise on Geochemistry, Second Edition. Elsevier, Oxford, 13: 119-142.

Chi, G., & Guha, J. (2011). Microstructural analysis of a subhorizontal gold-quartz vein deposit at Donalda, Abitibi greenstone belt, Canada: Implications for hydrodynamic regime and fluid-structural relationship. *Geoscience Frontiers*, *2*(4), 529-538.

Clayton, R. N., O'Neil, J. R., & Mayeda, T. K. (1972). Oxygen isotope exchange between quartz and water. *Journal of Geophysical Research*, *77*(17), 3057-3067.

Deines, P., Langmuir, D., & Harmon, R. S. (1974). Stable carbon isotope ratios and the existence of a gas phase in the evolution of carbonate ground waters. *Geochimica et Cosmochimica Acta*, *38*(7), 1147-1164.

Goldfarb, R. J., & Groves, D. I. (2015). Orogenic gold: common or evolving fluid and metal sources through time. *Lithos*, *233*, 2-26.

Harris, C., Le Roux, P., Cochrane, R., Martin, L., Duncan, A. R., Marsh, J. S., Le Roex A. P., & Class, C. (2015). The oxygen isotope composition of Karoo and Etendeka picrites: high $\delta^{18}O$ mantle or crustal contamination? *Contributions to Mineralogy and Petrology*, *170*, 1-24.

Shen, P., Pan, H., & Zhu, H. (2016). Two fluid sources and genetic implications for the Hatu gold deposit, Xinjiang, China. *Ore Geology Reviews*, *73*, 298-312.

Sibson, R. H. (1990). Conditions for fault-valve behaviour. *Geological Society, London, Special Publications*, *54*(1), 15-28.

Sibson, R. H., Robert, F., Poulsen, K. H. (1988). High-angle reverse faults, fluid-pressure cycling, and mesothermal gold-quartz deposits. *Geology*, *16*(6), 551−555.

Vennemann, T. W., & O'Neil, J. R. (1993). A simple and inexpensive method of hydrogen isotope and water analyses of minerals and rocks based on zinc reagent. *Chemical Geology*, *103*(1-4), 227-234.

CHAPTER 6

GEOCHRONOLOGICAL STUDIES

6.1 INTRODUCTION

Argon 40-Argon 39 radiometric dating was carried on hydrothermal micas in vein quartz samples in order to determine the age of the mineralizing event. A total of three rock samples were submitted for $^{40}Ar/^{39}Ar$ isotope dating at the University of Johannesburg. U-Pb isotope dating of zircons from intrusive bodies (foliated granite and non-foliated granite) was done at the Central Analytical Facilities (CAF), Stellenbosch University to assess the age relationship with the mineralizing event.

6.1.1 U-Pb DATING, SAMPLE PREPARATION AND ANALYSIS

Five (5) kg of each the three plutonic rock samples (foliated granite, non-foliated granite and dolerite dyke) were crushed and seived at the Geological Survey of Namibia. Equipments were thoughly cleaned with a brush, compressed air and ethanol after every sample to avoid cross-contamination.

The McClure Mountain hornblende (MMhb, with an age of 523.1 ± 1 Ma, Renne et al., 1998) was utilized as a fluence monitor. Despite the fact that MMhb has been described to give a variety of values (Baksi et al., 1996; Renne et al., 1998), the analyzing lab (University of Johannesburg) found that this monitor yields consistent J-values and in particular Ca/K and Cl/K factors. A J value of 0.008714 ± 0.000024 is reported. Blank measurements were dispersed in succession of every three or four analyses. The value of the total decay constant used is $5.554 \pm 0.014 \times 10^{-10}$ yr^{-1} (Kossert and Günther, 2004; Renne et al., 2010). Run regressions, corrections and age calculations were achieved using in-house developed software, which encompasses full error propagation (incorporating uncertainties of the decay constant and J-values) utilizing Monte Carlo simulations. The data is presented at the 95% confidence level.

6.2 RESULTS

6.2.1 ARGON-ARGON DATING RESULTS

Three vein quartz samples from trenches 14 and 15, and from sampling point NO 2 were sent to the lab analysed by $^{40}Ar/^{39}Ar$ dating at the University of Johannesburg (UJ). Only flakes

separated from NO 2 produced micas suitable for dating; those from trenches 14 and 15 though seemed fresh to a naked eye proved too weathered to be suitable for the purpose. Two muscovite grains were analysed from sample NO 2 and these are referred to herein as NO 2 grain 1 and 2. The individual step ages, weighted ages and inverse isochron ages are given in Tables 6.1 and 6.2 and the detailed measurements given as Appendix G. Their corresponding plateau age plots are in Figs. 6.1 and 6.2. The muscovite separate from NO 2 Grain 1 yielded an $^{40}Ar/^{39}Ar$ age of 2977 ± 18 Ma determined by ~88.7% ^{39}Ar released gas from the 2897th to 2900th heating steps (Table 6.1, Fig. 6.1). The muscovite separate NO 2 Grain 2 yielded a $^{40}Ar/^{39}Ar$ age of 472 ± 3Ma determined by ~98.8% ^{39}Ar released gas from the 2910th to 2923rd heating steps (Table 6.2, Fig. 6.2).

A robust age should be represented by a plateau, which is defined by Fleck et al. (1977) as that part of an age-spectrum diagram composed of a set of three or more consecutive steps with statistically indistinguishable ages that together represent more than 50% of the total ^{39}Ar released from the sample. Statistically indistinguishable ages means that there should be no two ages in the plateau that vary by more than a critical value *CV*, where $CV = 1.96 (\sigma_1^2 + \sigma^2_2)^{½}$, with σ1 and σ2 representing the uncertainty in the individual ages (Swindle and Weirch, 2017).

The $^{40}Ar/^{39}Ar$ age-spectrum (i.e., Figs. 6.1 and 6.2) is an analytical tool for assessing the validity of the obtained ages. For an undisturbed sample, i.e., a sample that behaved as a closed system with respect to K and Ar, the age measured at each step will be the same, within analytical uncertainty and this would mean that the measured age is the true formation age of the sample (Taylor and Aitken, 1997). An example of this is given in Fig. 6.2 and this is also referred to as a plateau, as defined by Fleck et al. (1977). If a sample has however been disturbed, then the release spectra will be discordant (Taylor and Aitken, 1997), as it is for Fig. 6.1. The age spectra of sample NO 2, grain 2 satisfy the definition of a plateau (Fig. 6.2); eleven (11) consecutive steps gave a plateau with statistically indistinguishable ages that together represent 98.8% of total ^{39}Ar released from the sample, at a confidence level of 95%.

Table 6.1 $^{40}Ar/^{39}Ar$ ages of individual steps for sample NO2 grain 1

Step name	$\%^{39}Ar$	Age (Ma)	+/-95%	Steps included in the weighted age average calculation (1:included / 0:not included)
2892_No-2 _h-p_16_1_10.36A	0.008209	0	8172.709	0
2894_No-2_ h-p_16_1_10.76A	0.318868	2076.068	464.4601	0
2895_No-2_ h-p_16_1_11.00A	7.053636	2208.785	33.92647	0
2896_No-2_ h-p_16_1_11.24A	0.275178	3242.483	444.3673	0
2897_No-2_ h-p_16_1_11.48A	39.775	2977.952	23.22875	1
2899_No-2_ h-p_16_1_11.72A	14.1809	2921.546	30.11971	1
2900_No-2_ h-p_16_1_11.96A	34.72533	2997.757	21.15622	1
2901_No-2_ h-p_16_1_12.20A	2.693726	2307.760	59.90501	0
2902_No-2_ h-p_16_1_12.44A	0.969149	3245.403	130.7563	0

Weighted average of included steps

$\%^{39}Ar$ sum	Age (Ma)	+/-95%
88.68123	2976.891	18.14525

Inverse isochron calculation results

$^{40}Ar/^{39}Ar(I)$	Sigma (σ)	$^{40}Ar/^{36}Ar$	Sigma (σ)	app. age (Ma)	+/-95%
438.801	1203.9	-19248.9	38227.23	2839.546	4618.754

Shown for each step is the uncertainty, % 39 Ar released, and a column indicating steps included in the weighted average. Below the individual steps data are the weighted average and inverse isochron ages.

Table 6.2 $^{40}Ar/^{39}Ar$ ages of individual steps for sample NO2 grain 2

Step name	$\%^{39}Ar$	Age (Ma)	+/-95%	Steps included in the weighted age average calculation (1:included / 0:not included)
2907_No-2_ h-p_60_2_9.80A	0.19985	230.0614	15.71847	0
2908_No-2_ h-p_60_2_10.05A	0.312391	371.4874	9.37891	0
2909_No-2_ h-p_60_2_10.29A	0.663398	454.2791	7.886798	0
2910_No-2_ h-p_60_2_10.54A	2.783224	470.3122	4.613563	1
2912_No-2_ h-p_60_2_10.78A	7.092899	470.2773	3.267521	1
2913_No-2_ h-p_60_2_11.03A	8.989212	472.8597	3.41126	1
2914_No-2_ h-p_60_2_11.28A	14.62664	474.0104	3.393105	1
2915_No-2_ h-p_60_2_11.52A	17.92401	473.9056	3.175777	1
2917_No-2_ h-p_60_2_11.77A	7.953578	473.0401	3.348292	1
2918_No-2_ h-p_60_2_12.02A	11.6609	470.6112	3.370836	1
2919_No-2_ h-p_60_2_12.26A	10.69083	467.7527	3.268522	1
2920_No-2_ h-p_60_2_12.51A	12.07464	470.3454	3.346795	1
2922_No-2_ h-p_60_2_12.75A	2.014129	469.2803	3.933005	1
2923_No-2_ h-p_60_2_13A	3.014297	472.8644	3.933897	1

Table 6.2 continues

Weighted average of included steps

$\%^{39}Ar$ sum	Age (Ma)	+/-95%
98.82436	471.7808	3.252454

Inverse isochron calculation results

$^{40}Ar/^{39}Ar(I)$	Sigma (σ)	$^{40}Ar/^{36}Ar$	Sigma (σ)	app. age	+/-95%
34.50644	8.154657	613.1623	415.1751	474.4366	194.8292

Shown for each step is the uncertainty, % 39 Ar released, and a column indicating steps included in the weighted average. Below the individual steps data are the weighted average and inverse isochron ages.

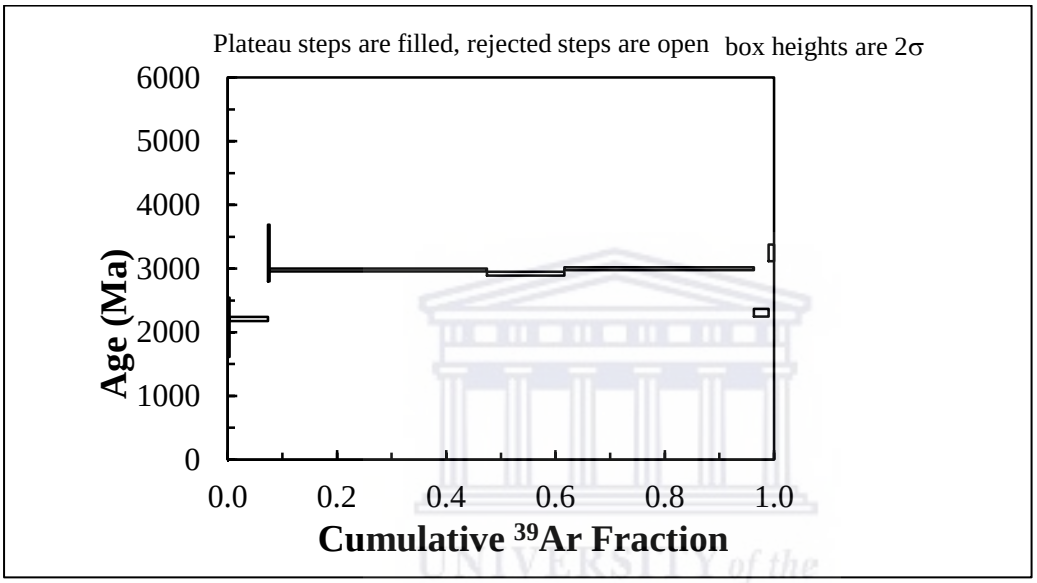

Fig. 6.1. Plots of the age spectra of sample NO 2, grain 1 depicting no meaningful plateau age. NO 2 grain 1 appears to be a detrital grain.

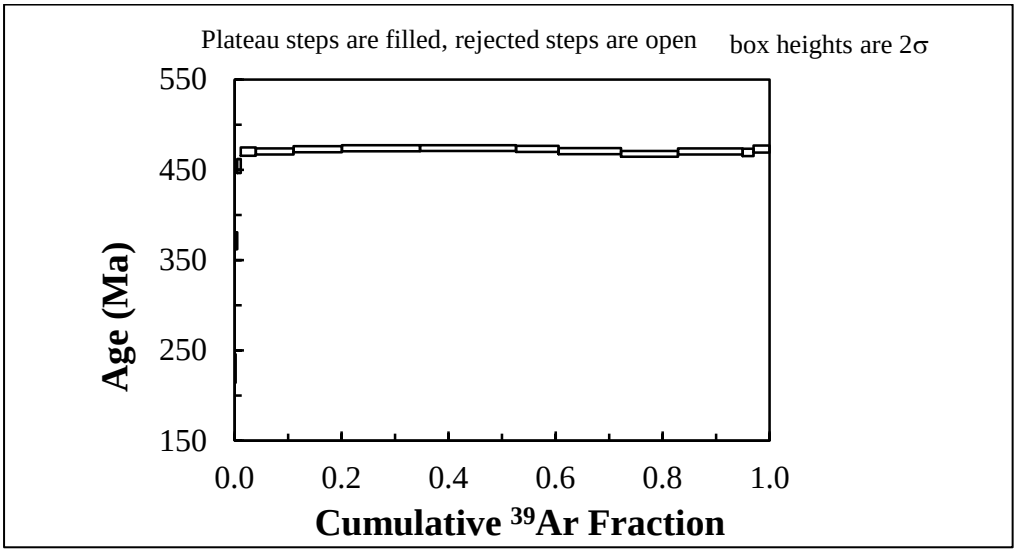

Fig. 6.2. Plots of the age spectra of sample NO 2, grain 2 depicting a good plateau age of 472 ± 3 Ma which is a good approximation for the timing of hydrothermal fluid flow.

6.2.2 U-Pb DATING RESULTS

In an attempt to constrain the age of the plutonic rocks in the vicinity of the Sandamap gold prospect zircons were extracted from the proximal three plutonic bodies (the foliated granite, and the non-foliated granite) and dated by LA-ICP-MS U-Pb analysis. Representative Cathodoluminescent (CL) images of the analysed zircons are shown in Figs. 6.3 - 6.5 together with concordia diagrams. All analyses from granitic plutons show varying degrees of discordance and only the dolerite dyke gave concordant ages. The discordance is due to Pb loss that may be attributed to metamictization marked by disruption of zonation pattern in the CL images of the zircons.

Zircons from the foliated granite sample (FG) are light brown to brown with prismatic crystal shapes varying in length from 58 to 434 µm (Fig. 6.3b). A total of 32 spots from 31 zircons were analyzed, with the analyzed spots yielding uranium contents ranging from 1250 to 15570 ppm and (Th/U) varying from 0.003 to 0.061. The high uranium concentration points towards metamictisation and the observed high degree of discordance in the analytical results (Fig. 6.3a). The discordance can be seen on the concordia diagram (Fig. 6.3a) and the calculated $^{206}Pb/^{238}U$ dates vary from 108 to 350 Ma (Table 6.3).

Zircons from the foliated granite sample in trench 9 (GT) are light brown to brown with prismatic crystal shapes varying in length from 81 to 446 µm (Fig. 6.4b). A total of 15 spots from 14 zircons were analyzed, with the analyzed spots yielding uranium contents ranging from 629 to 24170 ppm and Th/U varying from 0.03 to 0.92. Again, the high uranium concentration points towards metamictisation and the observed high degree of discordance in the analytical results (Fig. 6.4a). The discordance can be seen on the concordia diagram (Fig. 6.4a) and the calculated $^{206}Pb/^{238}U$ dates vary from 39 to 832 Ma (Table 6.4).

Zircons from the non-foliated granite sample (UG) are light brown to brown with prismatic crystal shapes varying in length from 76 to 506 µm (Fig. 6.5b). A total of 21 spots from 20 zircons were analyzed with the analyzed spots yielding uranium contents ranging from 2790 to 14850 ppm and Th/U varying from 0.01 to 0.51. The same applies to this sample as well, with the high uranium concentration pointing towards metamictisation and the observed high degree of discordance in the analytical results (Fig. 6.5a). The discordance can be seen on the concordia diagram (Fig. 6.5a), and the calculated $^{206}Pb/^{238}U$ dates vary from 59 to 406 Ma (Table 6.5).

Table 6.3 LA-ICP MS analytical results from U/Pb dating of the foliated granite sample (sample FG)

Spot number	^{206}Pb (CPS)	U (ppm)	Th/U	Data for Tera-Wasserburg plot [a]		Data for Wetherill plot [a]		Dates (Ma)			Concordance [b]
				$^{238}U/^{206}Pb$	$^{207}Pb/^{206}Pb$	$^{207}Pb/^{235}U$	$^{206}Pb/^{238}U$	$^{207}Pb/^{206}Pb$	$^{206}Pb/^{238}U$	$^{207}Pb/^{235}U$	%
FG – 3	753000	4190	0.02	24.81	0.1048	0.5814	0.0403	1708	255	465	55
FG – 5	1175000	15570	0.03	59.38	0.2326	0.5386	0.0168	3066	108	437	25
FG – 6	250000	1250	0.06	23.50	0.1088	0.6360	0.0426	1762	269	499	54
FG – 7	844000	5330	0.02	27.13	0.0992	0.5050	0.0369	1608	233	415	56
FG – 8	869000	5170	0.01	26.39	0.0827	0.4312	0.0379	1255	240	364	66
FG – 9	1147000	13420	0.01	51.44	0.2646	0.7079	0.0194	3268	124	543	23
FG – 10	748400	4092	0.00	24.08	0.0713	0.4069	0.0415	964	262	347	76
FG – 11	450000	1890	0.03	20.61	0.1160	0.7730	0.0485	1888	305	581	53
FG – 12	1165000	9020	0.01	36.08	0.1692	0.6430	0.0277	2522	176	502	35
FG – 13	725000	4520	0.02	27.56	0.1005	0.5026	0.0363	1626	230	413	56
FG – 14	775000	3600	0.06	21.04	0.0814	0.5314	0.0475	1220	299	432	69
FG – 15	795000	3822	0.03	21.27	0.0810	0.5251	0.0470	1218	296	428	69
FG – 16	370000	1403	0.02	18.76	0.0764	0.5615	0.0533	1104	335	452	74
FG – 17	579000	2121	0.01	17.91	0.0982	0.7550	0.0559	1583	350	571	61
FG – 18	635000	3810	0.02	27.34	0.0772	0.3897	0.0366	1122	232	334	69
FG – 19	643000	3630	0.01	27.79	0.1376	0.6840	0.0360	2185	228	527	43
FG – 20	648000	3080	0.01	21.59	0.0832	0.5287	0.0463	1268	292	431	68
FG – 21	492000	3060	0.02	31.42	0.1345	0.5900	0.0318	2151	202	470	43
FG – 22	788000	3915	0.00	22.29	0.0689	0.4263	0.0449	894	283	360	78
FG – 23	982000	8310	0.01	37.81	0.1379	0.5046	0.0265	2196	168	415	41
FG – 26	999600	7860	0.02	34.98	0.1069	0.4224	0.0286	1745	182	358	51
FG - 27	928000	6630	0.01	35.04	0.2171	0.8536	0.0285	2956	181	626	29
FG - 28	882000	6270	0.01	32.62	0.1315	0.5557	0.0307	2110	195	448	43
FG - 30	1028000	11470	0.01	49.78	0.2543	0.7080	0.0201	3202	128	542	24
FG - 31	1482000	12600	0.00	36.98	0.1970	0.7380	0.0270	2799	172	561	31
FG - 33	664000	4480	0.00	29.42	0.0697	0.3268	0.0340	911	216	288	75
FG - 34	590000	3310	0.01	27.32	0.1035	0.5197	0.0366	1682	232	425	55

Table 6.3 continues				Data for Tera-Wasserburg plot [a]		Data for Wetherill plot [a]		Dates (Ma)			Concordance [b]
Spot number	^{206}Pb (CPS)	U (ppm)	Th/U	$^{238}U/^{206}Pb$	$^{207}Pb/^{206}Pb$	$^{207}Pb/^{235}U$	$^{206}Pb/^{238}U$	$^{207}Pb/^{206}Pb$	$^{206}Pb/^{238}U$	$^{207}Pb/^{235}U$	%
FG - 35	1007000	8850	0.01	39.71	0.1621	0.5624	0.0252	2476	160	453	35
FG - 37	567000	3600	0.00	29.99	0.0635	0.2927	0.0333	719	211	261	81
FG - 38	830000	8050	0.01	41.79	0.1390	0.4559	0.0239	2205	152	381	40
FG - 39	837000	4920	0.01	26.69	0.1402	0.7250	0.0375	2209	237	552	43
FG - 40	544000	3850	0.02	35.64	0.1295	0.5014	0.0281	2087	178	412	43

Uncertainties quoted without components related to systematic error unless otherwise stated. Total systematic uncertainties (s sys): $^{206}Pb/^{238}U$ = 1.8 %; $^{207}Pb/^{206}Pb$ = 0.5 (2s).

[a] Data not corrected for common Pb

[b] Concordance calculated as: ($^{206}Pb^{238}U$ date/$^{207}Pb^{235}U$ date)*100

^{204}Pb radiation measurements and $^{206}Pb/^{204}Pb$ ratios were below detection limit

CPS: counts per second

Table 6.4 LA-ICP MS analytical results from U/Pb dating of the foliated granite sample (trench 9) (sample GT)

Spot number	^{206}Pb (CPS)	U (ppm)	Th/U	Data for Tera-Wasserburg plot [a]		Data for Wetherill plot [a]		Dates (Ma)			Concordance [b]
				$^{238}U/^{206}Pb$	$^{207}Pb/^{206}Pb$	$^{207}Pb/^{235}U$	$^{206}Pb/^{238}U$	$^{207}Pb/^{206}Pb$	$^{206}Pb/^{238}U$	$^{207}Pb/^{235}U$	%
GT - 3	843000	21170	0.04	105.75	0.3570	0.4657	0.0095	3734	61	388	16
GT - 4	493000	1145	0.15	9.92	0.0988	1.3720	0.1008	1599	619	876	71
GT - 5	392000	629	0.45	7.26	0.0938	1.7800	0.1378	1493	832	1035	80
GT - 6	838000	15230	0.40	77.04	0.3026	0.5389	0.0130	3480	83	438	19
GT - 11	921000	20030	0.05	94.38	0.3379	0.4921	0.0106	3651	68	406	17
GT - 12	407000	1212	0.21	12.93	0.0624	0.6625	0.0773	678	480	516	93
GT - 14	727000	20400	0.20	115.21	0.3556	0.4250	0.0087	3728	56	360	15
GT - 16	628000	24170	0.16	165.40	0.3938	0.3280	0.0060	3883	39	288	14
GT - 19	754700	18470	0.07	99.50	0.4050	0.5615	0.0101	3925	64	452	14
GT - 20	943000	18900	0.34	82.03	0.3638	0.6117	0.0122	3766	78	484	16
GT - 22	561000	5170	0.07	38.31	0.1405	0.5045	0.0261	2229	166	414	40
GT - 26	615100	3088	0.92	20.81	0.1465	0.9700	0.0481	2303	303	687	44
GT - 27	829000	12640	0.04	64.98	0.2668	0.5635	0.0154	3279	98	453	22
GT - 29	810000	4870	0.05	24.60	0.0806	0.4504	0.0407	1209	257	377	68
GT - 30	720000	4790	0.03	26.88	0.1438	0.7330	0.0372	2262	236	557	42

Uncertainties quoted without components related to systematic error unless otherwise stated. Total systematic uncertainties (s sys): $^{206}Pb/^{238}U$ = 1.8 %; $^{207}Pb/^{206}Pb$ = 0.5 (2s).

[a] Data not corrected for common Pb

[b] Concordance calculated as: ($^{206}Pb^{238}U$ date/$^{207}Pb^{235}U$ date)*100

^{204}Pb radiation measurements and $^{206}Pb/^{204}Pb$ ratios were below detection limit

CPS: counts per second

Table 6.5 LA-ICP MS analytical results from U/Pb dating of the non-foliated granite sample (sample UG)

Spot number	^{206}Pb (CPS)	U (ppm)	Th/U	Data for Tera-Wasserburg plot [a]		Data for Wetherill plot [a]		Dates (Ma)			Concordance [b]
				$^{238}U/^{206}Pb$	$^{207}Pb/^{206}Pb$	$^{207}Pb/^{235}U$	$^{206}Pb/^{238}U$	$^{207}Pb/^{206}Pb$	$^{206}Pb/^{238}U$	$^{207}Pb/^{235}U$	%
UG - 5	537000	4330	0.01	34.03	0.0675	0.2750	0.0294	849	187	247	76
UG - 7	684000	8450	0.42	54.47	0.2174	0.5514	0.0184	2959	117	446	26
UG - 8	946000	11590	0.18	54.56	0.2219	0.5621	0.0183	2992	117	453	26
UG - 9	892000	10010	0.17	49.83	0.1605	0.4450	0.0201	2460	128	374	34
UG - 10	596600	8160	0.23	59.49	0.1503	0.3496	0.0168	2344	108	304	35
UG - 12	879000	3040	0.01	15.37	0.0585	0.5266	0.0651	542	406	429	95
UG - 13	805000	14850	0.19	77.76	0.1653	0.2938	0.0129	2508	83	262	32
UG - 14	973000	12570	0.04	54.23	0.1653	0.4209	0.0184	2507	118	357	33
UG - 15	957000	7500	0.02	33.40	0.0736	0.3055	0.0299	1026	190	271	70
UG - 16	554400	8210	0.07	65.75	0.2060	0.4327	0.0152	2870	97	365	27
UG - 17	813000	14850	0.07	78.19	0.1716	0.3025	0.0128	2570	82	269	30
UG - 18	729000	6510	0.03	40.55	0.1109	0.3767	0.0247	1811	157	325	48
UG - 22	602200	8170	0.05	59.31	0.1731	0.4019	0.0169	2584	108	343	31
UG - 24	479000	3040	0.12	30.61	0.0698	0.3148	0.0327	911	207	278	75
UG - 26	1024000	7840	0.02	31.88	0.0661	0.2859	0.0314	803	199	255	78
UG - 27	470000	11540	0.51	108.84	0.1941	0.2453	0.0092	2771	59	223	26
UG - 29	506000	2790	0.05	24.39	0.0675	0.3811	0.0410	841	259	328	79
UG - 32	783300	8755	0.14	52.14	0.2076	0.5478	0.0192	2882	122	443	28
UG - 33	564000	7240	0.22	60.10	0.1420	0.3246	0.0166	2243	106	285	37
UG - 34	621000	4310	0.14	30.64	0.0739	0.3320	0.0326	1030	207	291	71
UG - 35	658100	4960	0.16	31.65	0.0725	0.3157	0.0316	994	201	278	72

Uncertainties quoted without components related to systematic error unless otherwise stated. Total systematic uncertainties (s sys): $^{206}Pb/^{238}U$ = 1.8 %; $^{207}Pb/^{206}Pb$ = 0.5 (2s).

[a] Data not corrected for common Pb

[b] Concordance calculated as: ($^{206}Pb^{238}U$ date/$^{207}Pb^{235}U$ date)*100

^{204}Pb radiation measurements and $^{206}Pb/^{204}Pb$ ratios were below detection limit

CPS: counts per second

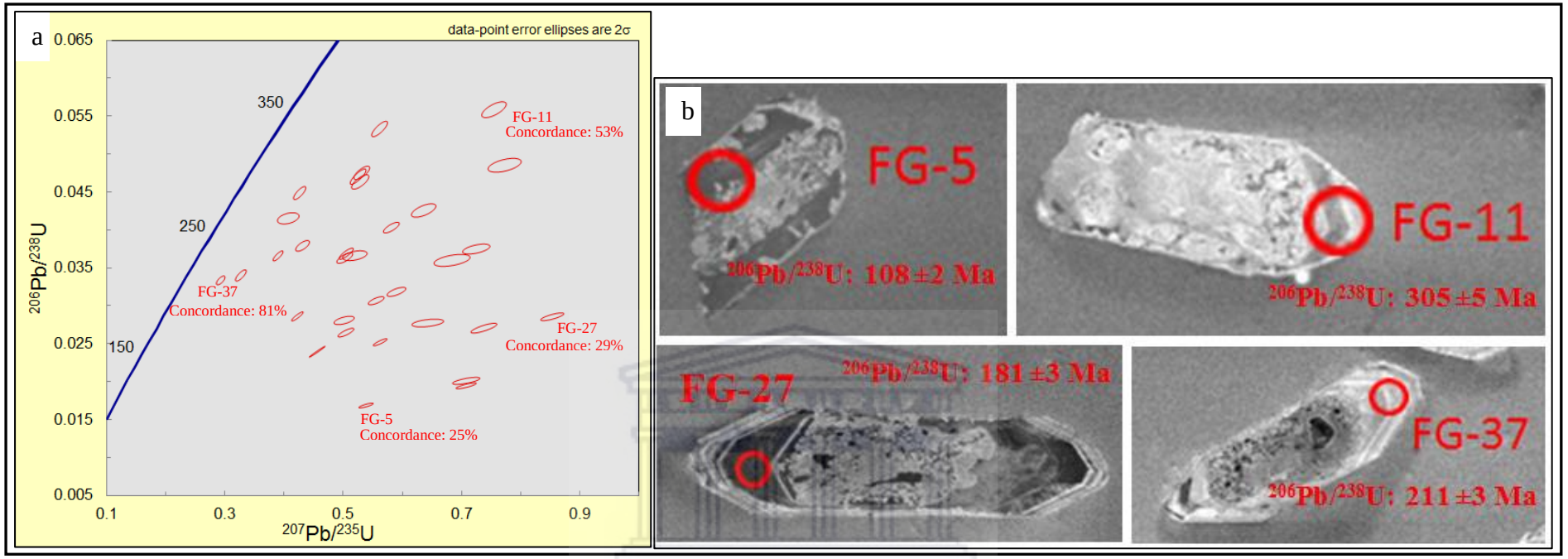

Fig. 6.3. (a) Discordance is clearly evident in the concordia diagram of zircons from the foliated granite sample (sample FG). (b) Representative cathodoluminescence (CL) images of zircon grains indicated in (a), displaying ablated spots and $^{206}Pb/^{238}U$ dates. Red spot sizes (25µm) reflect the size of the spots ablated during analysis. The dates range from 108 - 305 Ma.

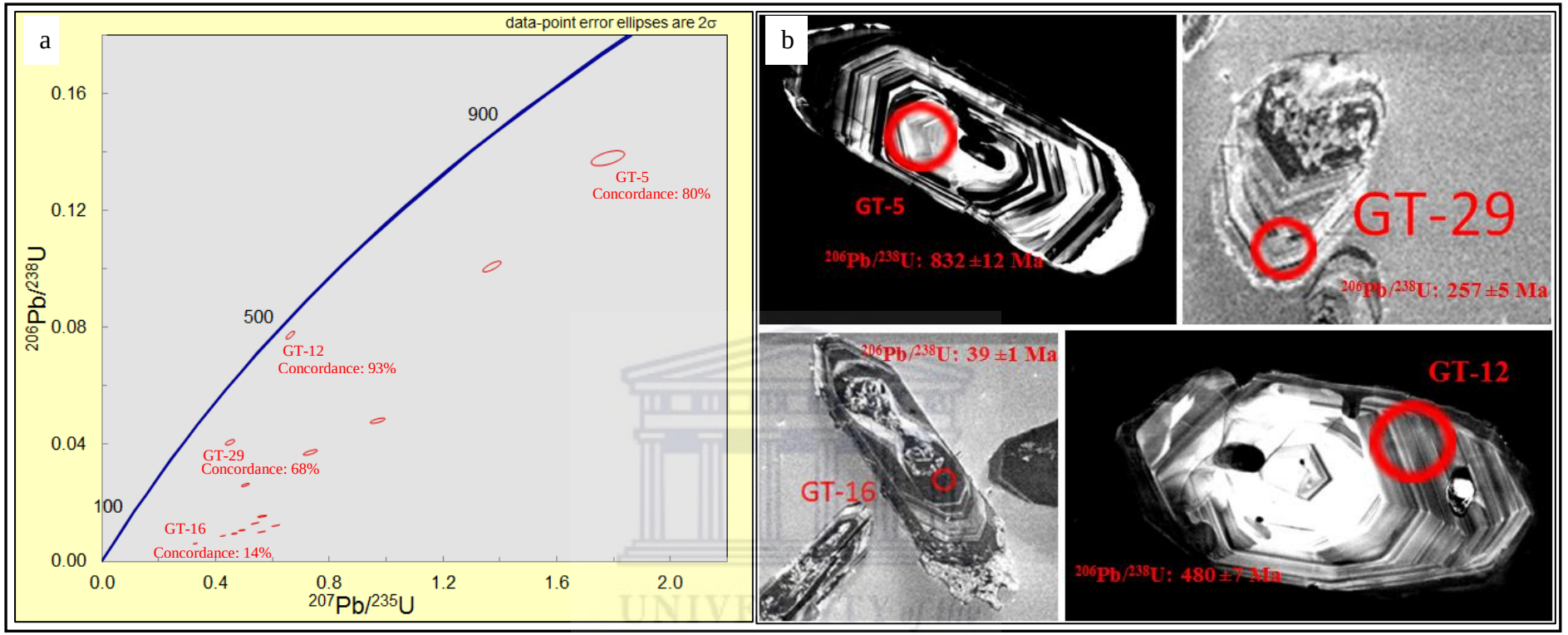

Fig. 6.4. (a) Discordance is clearly evident in the concordia diagram of zircons from the foliated granite in trench 9 (sample GT). (b) Representative cathodoluminescence (CL) images of zircon grains indicated in (a), displaying ablated spots and $^{206}Pb/^{238}U$ dates. Red spot sizes (25µm) reflect the size of the spots ablated during analysis. The dates range from 39 - 832 Ma.

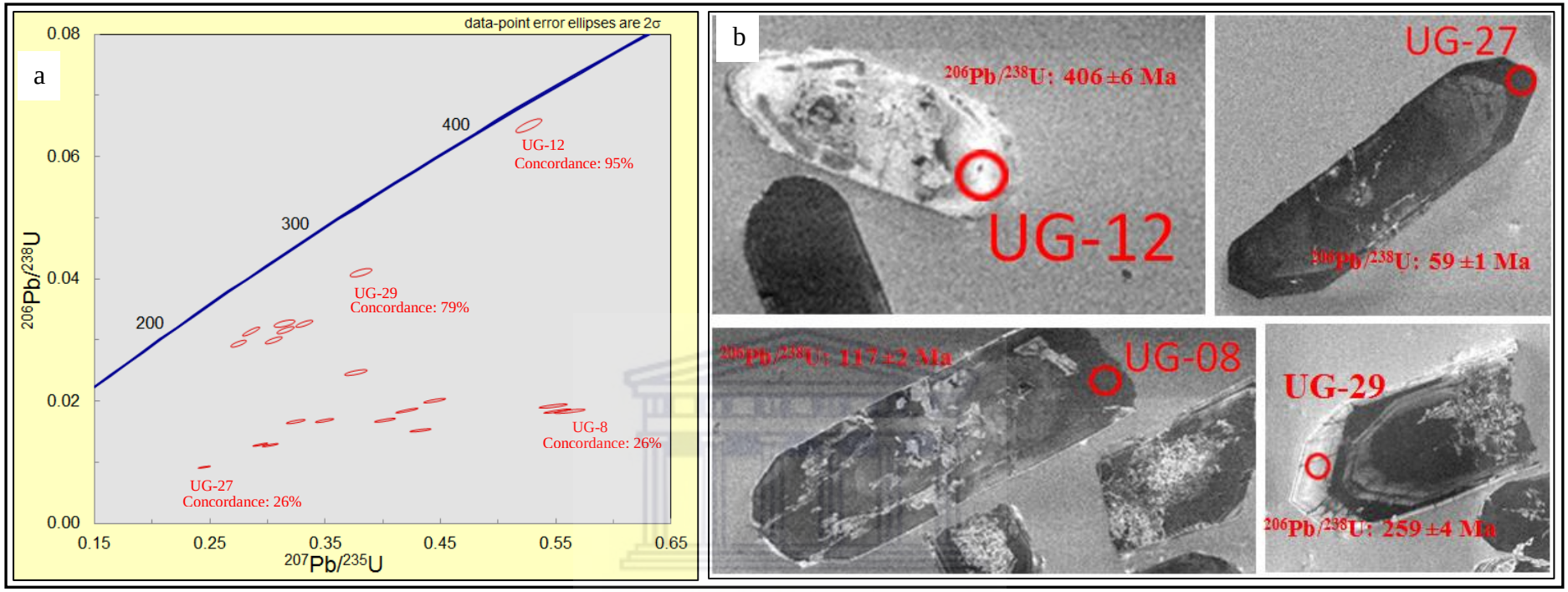

Fig. 6.5. (a) Discordance is clearly evident in the concordia diagram of zircons from the non-foliated granite sample (sample UG), (b) Representative cathodoluminescence (CL) images of zircon grains indicated in (a), displaying ablated spots and $^{206}Pb/^{238}U$ dates. Red spot sizes (25µm) reflect the size of the spots ablated during analysis. The dates range from 59 - 406 Ma. Zircon with UG-12 show a high degree of metamictization. The dark portions in the rims without oscillatory/ concentric zoning suggest that they did not grow in a magma and could be interpreted as an overgrowth suggesting a possible metamorphic event.

Representative U-Pb analysis data of zircons, given in Tables P1 – P3, show that the higher the uranium concentration in zircons and the lower the concordance percentage, i.e., there is correlation between the uranium concentration and discordance. Concordance was calculated using the formula ($^{206}Pb^{238}U$ date/$^{207}Pb^{235}U$ date)*100 whereas discordance is calculated using [1-($^{206}Pb^{238}U$ date/$^{207}Pb^{235}U$ date)]*100 (Spencer et al., 2016).

The general observation from Tables 6.3 – 6.5 is that the $^{207}Pb/^{206}Pb$ dates are much older than the $^{206}Pb/^{238}U$ dates which are more close to the true given the fact that the Damara belt is younger than 1.2 Ga (Spencer et al., 2016). The $^{207}Pb/^{206}Pb$ ages may offer a more correct age for discordant data if recent Pb-loss has occurred, because recent lead loss does not have an effect on the $^{207}Pb/^{206}Pb$ ratio (Spencer et al., 2016). However, this is a more assumptive approach in comparison to filtering data for a more robust measure of concordance (Spencer et al., 2016). Observation of tabulated data from this study show that concordance between the $^{207}Pb/^{206}Pb$ and the other dates ($^{206}Pb/^{238}U$ and $^{207}Pb/^{235}U$) would be very low and in any case $^{207}Pb/^{206}Pb$ ages would give a high disconcordance since they are suitable for zircons much older than the zircons under question (Spencer et al., 2016).

Based on inferences deduced from the regional geologic evolution of the area under question, as given by Miller (2008), and geochronological data by Steven (1993), the ages of the analyzed plutonic rocks (FG, UG & GT) are expected to be younger than 550 Ma. Since the expected ages are younger than ~ 1.2 Ga, $^{206}Pb/^{238}U$ would give more acurate dates if it was not for the observed discordance, as opposed to $^{207}Pb/^{206}Pb$ dates that would be suitable for ages older than ~1.2 Ga (Spencer et al., 2016).

The age of the gold mineralization obtained by $^{40}Ar/^{39}Ar$ dating (single determination) of muscovite associated with gold hosting quartz vein is interpreted to have occurred at 472 ± 3Ma (Section 6.2.1). This is expected to be older than the non-foliated granite (GT) which hosts a mineralized xenolith, but the obtained $^{206}Pb/^{238}U$, $^{207}Pb/^{235}U$ and $^{207}Pb/^{206}Pb$ dates of the granitic samples are either much older or much younger than the mineralization (Tables 6.3 and 6.5) due to Pb loss attributed to metamictization. This renders $^{206}Pb/^{238}U$, $^{207}Pb/^{235}U$ and $^{207}Pb/^{206}Pb$ dates (Tables 6.3 and 6.5) invalid. Parts of the pegmatitic granite from where sample GT and UG were collected extend into the shear zone where mineralization is concentrated and during the intrusion it sampled parts of the shear zone hence the presence of a mineralized xenolith. The locality of the xenolith is within the shear zone and is sheared. The conformal relationship between the quartz veins and shear zone fabric brings about the

assumption that the mineralising fluid flow was along shear zone, which was pre-existent, and that shearing must have occurred subsequent to the foliated leucogranite emplacement and uplift of the carbonate dome.

The Rb-Sr whole-rock dates of the foliated granite (FG) (512± 19 Ma) and non-foliated granite (UG and GT) (473±23 Ma) are within error and are as such interpreted as the same. The foliation in the foliated granite which Steven (1993) interpreted as metamorphic banding suggest that the two Rb-Sr whole-rock dates records a metamorphic event. No cross-cutting relationship between the foliated granite and non-foliated granite has been observed in the field therefore the discussion on the relative ages of these two plutonic bodies remains open. It should however be pointed out that the presence of metamorphic banding in the foliated granite and its absence in the non-foliated granite suggests that the non-foliated granite may be younger than the foliated one. Additionally, it should be noted that Rb and Sr are more mobile elements, particularly if a fluid phase is involved such as the migration fluids in the Damara belt following tectonism and deformation events. With this in mind the ages obtained from these elements has to be interpreted and quoted with caution.

Inference from the above given information in conjunction with the regional geologic evolution of the area given by Miller (2008), Rb-Sr geochronology data by Steven (1993) and the argon-argon data (Section 6.2), indicate that the U–Pb dates for samples FG, GT and UG are invalid due to discordance attributed to metamictization resulting from high uranium content (629 - 24170 ppm). It appears that Pb-loss lowered the $^{206}Pb/^{238}U$ and $^{207}Pb/^{235}U$ dates of the foliated and non-foliated granites in zircon spots FG-37 and 22 (Table P1), UG-12 and 29 (Table P1). This discordance is also observed on concordia diagrams given in Figs. 6.3 to 6.5.

6.2.3 ZIRCON MORPHOLOGY AND GENESIS

Introduction

Assessment of internal and external morphology of zircon crystals can play a role in the determination of magma source, chemical composition and temperature of the melt as well as metamorphic and recrystallization processes that modified the zircon (Daneshvar et al., 2018 and references therein). Pupin (1980) classified zircon crystals on the alkalinity index (IA)-temperature index (IT) typology diagram (Fig.6.6) using relative growth of crystal faces. The

classification is based on the relative growth of {100} to {110} prisms and {211} to {101} pyramids (Fig. 6.7). Based on the morphology of zircons, granites can be classified into three groups: (1) granites of mainly crustal origin, (2) hybrid granites (crustal and mantle origin) and (3) granites of mainly mantle origin (Fig. 6.8) (Pupin, 1980).

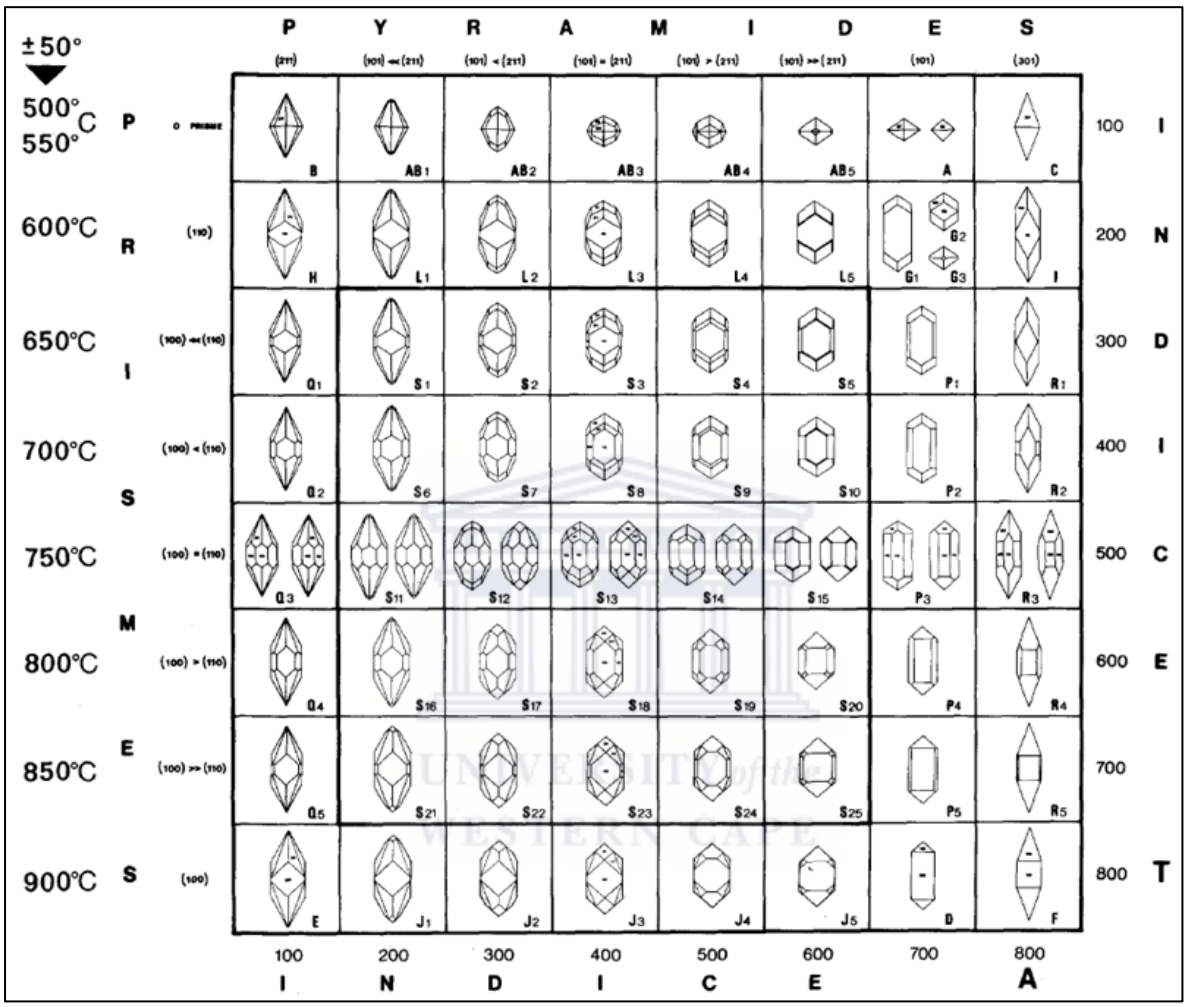

Fig. 6.6. Typological classification diagram of zircons and corresponding geothermometric scale. (after Pupin, 1980)

Chemical composition has an effect on the relative growth of zircon pyramids, for instance zircons from hyperaluminous or hypoalkaline media are dominantly characterised by {211} pyramids, while zircons from hyperalkaline or hypoaluminous media are characterised by {101} pyramids and zircons from a potassium-rich alkaline media are characterised by {301} pyramids (Pupin, 1980; Köksal et al., 2008). Accordingly, I-type granites are characterized by mainly zircon crystals with flat {101} pyramids, whereas the S-type, mainly have zircon crystals with steep {211} pyramids (Daneshvar et al., 2018 and references therein). Morphological features of zircon crystals can be used as geothermometers and accordingly, zircon crystals from high temperature melts are dominated by {100} prisms,

while those from low temperature melts are dominated by {110} prisms (Daneshvar et al., 2018).

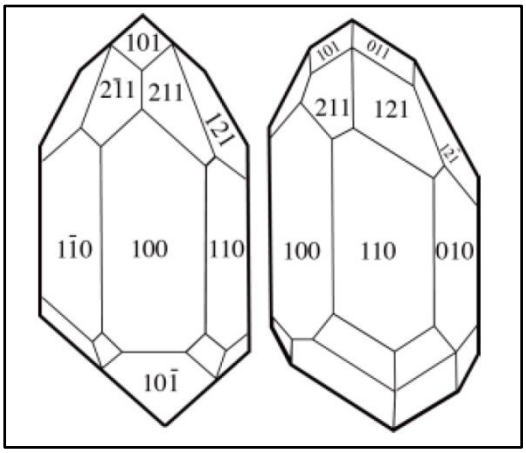

Fig. 6.7. Sketch models of zircon crystals faces (modified after Ohira, 1994).

6.2.4 SAMPLES GT, UG & FG

External morphology of zircon

Zircon crystals are euhedral and translucent with the majority exhibiting long prismatic shapes with a few stubby shapes. The crystals are characterised by well-developed {110} prisms, {121} and {211} pyramidal crystalline faces on the basis of the zircon typology by Pupin (1980). On the typology classification diagram, zircons from these samples exhibit low to intermediate alkalinity index (200 - 400) with low temperature index (200 - 300) and suggest $L_{1–2}$, $S_{1–2–3–4–6–8}$ morphological sub-types (Fig. 6.6). Based on the morphology of the zircon crystals from samples GT, UG and FG, the minimum crystallization temperatures are 600 to 700 °C (Fig. 6.6). The morphological assessment of the zircons is summarised in Table 6.6.

Table 6.6 Summary of the morphology and genesis of the zircons

Sample ID		**FG**	**UG**	**GT**
Crystal faces	**Prisms**	{110}	{110}	{110}
	pyramids	{211}	{211}	{211}
Morphological subtypes		$L_{1–2}$, $S_{1–2–3–4–6–8}$	$L_{1–2}$, $S_{1–2–3–4–6–8}$	$L_{1–2}$, $S_{1–2–3–4–6–8}$
Alkalinity index (IA)		200 – 400 (low to moderate)	200 – 400 (low to moderate)	200 – 400 (low to moderate)
Temperature index (IT)		200 – 300 (low)	200 – 300 (low)	200 – 300 (low)
Temperature of melt (Based on zircon morphology)		600 – 700°C	600 – 700°C	600 – 700°C
Magma source		Crustal	Crustal	Crustal
Granite type		S-type (polyphased anatectic granite)	S-type (polyphased anatectic granite)	S-type (polyphased anatectic granite)

Internal morphology of zircon

The majority of the crystals exhibit dark or bright unzoned cores and if these were originally zoned, they have been disrupted and what remain are irregular unzoned patches of varying luminosity indicating that they have been subjected to metamictization (Figs. 6.10- 6.12). A few exhibit overgrowth and zoning in {211} pyramidal faces suggesting polyphased anatexis during a long basement evolution (Figs. 6.10 – 6.12 e.g. spots FG8, 11, 17, 20, 33 & 37, UG 5, 18, 24, 26 & 34, GT 12, 26, 29 & 30, given in Table 6.7). Granites that contain zircons exhibiting zoning in {211} pyramidal faces are thought to have been formed by crustal reactivation (Pupin, 1980 and references therein). Zircons from Sandamap granites are dominantly characterized by {211} pyramids and {110} prisms suggesting that they are from aluminous granites (S-type granites) (Fig.6.8) (Pupin, 1980; Köksal et al., 2008; Daneshvar et al., 2018). Since the Sandamap granites are from S-type granites, the plausible explanation for the zoning in the {211} pyramids likely resulted from variations in temperature and/or pressure during anatexis or peak conditions of a metamorphic P-T path (Roberts and Finger, 1997). Additionally, the absence of oscillatory zoning, presence of sector zoning and the dominance of unzoned zircon domains in zircons suggest that these zircons are of metamorphic origin. (Hoskin and Black, 2000; Wu and Zheng, 2004).

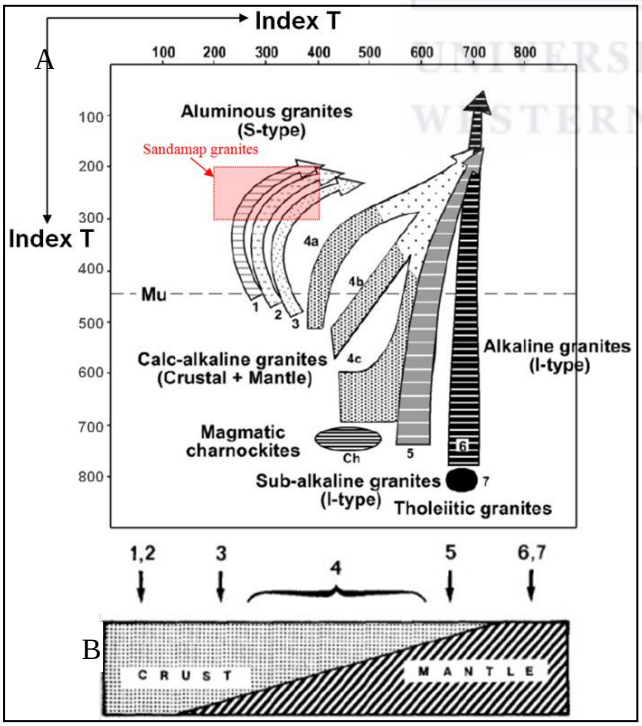

Fig.6.8. (A) Zircon populations in the petrogenetic classification proposed by Pupin (1980): 1, 2 & 3 are granites of crustal or mainly crustal origin; 4 & 5 are granites of crustal + mantle origin (hybrid granites); 6 & 7 are granites of mantle or mainly mantle origin. Granitoids from Sandamap are S-type granites represented in the diagram a red shaded rectangle. (B) Schematic diagram summarizing origin of material that produced the different granites numbered 1 to 7. Mu= limit of muscovite granites (temperature <725°C) (after Pupin, 1980).

One zircon crystal from the non-foliated granite (sample GT) portrays oscillatory zoning in its core and unzoned overgrowth in its rim (Fig. 6.12-spots GT4 & 5). Both the rim and core dates can be described as outliers in that they are more than 100 million years older than the oldest date obtained from the cluster of dates in the sample (the rim GT4 (619 Ma) is more than 120 million years older and the core GT5 (832 Ma) is more than 320 million years older). The large age gap between the core (832 Ma) and rim (619 Ma), the oscillatory zoning in the core, the high Th/U ratio in the core (0.45), the low Th/U ratio in the rim and the dark unzoned rim, all suggest that the core is inherited (and possibly magmatic) and the rim is a metamorphic rim/overgrowth (Wu and Zheng, 2004; Manzotti et al., 2015; Aysal et al., 2012). Generally, the majority of the zircons from the three granites exhibit low Th/U ratios ranging from 0.00 – 0.06, 0.03 – 0.92 and 0.01 – 0.51 for FG, GT and UG respectively (Appendix I – K), suggesting a metamorphic source (Th/U <0.1) (Fig. 6.9) (Manzotti et al., 2015; Aysal et al., 2012). From all the three granite samples, only rims were sampled in exception of one grain (spot GT5) which seemed distinct in the sense that the core has oscillatory zoning that are well preserved, whereas the majority of the samples had no zoning in the core. Overgrowth in the {211} prisms of the zircon crystals are bright and zoned and/or dark and unzoned (Table 6.7). The dark colour, the absence of zonation and the low Th/U ratio suggest that the outermost dark domains are possibly metamorphic rims/overgrowth.

All rims from the foliated granite (FG) have Th/U ratios of < 0.1, indicating consistence with a metamorphic source (Fig. 6.9) (Manzotti et al., 2015; Aysal et al., 2012). Forty eighty (48) percent of the rims from foliated granite (UG) plot under metamorphic source while 43% plot under intermediate zone (metamorphic-igneous) and 10% plot under igneous source (Fig. 6.9). Samples from foliated granite (GT): 47% plot under metamorphic source while both the intermediate zone and the igneous source have 27% each (Fig. 6.9). Overall, 72% of all the grains plot under metamorphic source whereas those that plotted in the intermediate zone and the igneous source are 19% and 9% respectively (Fig. 6.9). From the samples plotting under magmatic source one is an inherited core with an age of 832 Ma and the other is metamict characterized by a high Th/U ratio, with bright-irregular patches defining its internal structure (this is likely an inherited grain that has undergone severe metamictization resulting in Pb loss and a younger age) (Fig. 6.9).

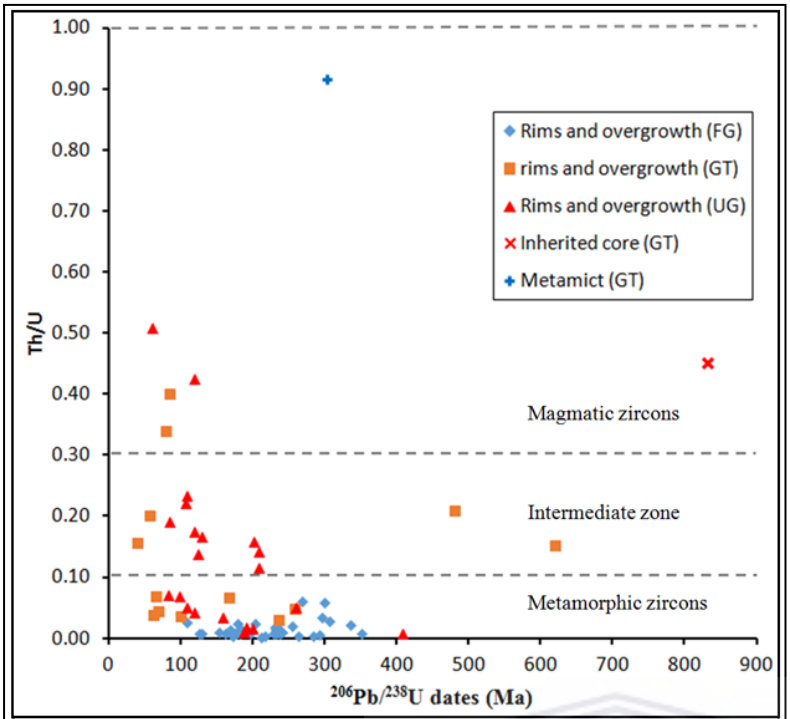

Summary of the zircon Th/U ratio vs. age plot

Sample ID		FG	UG	GT	Overall
Zircon source	Metamorphic zircons	100%	48%	47%	**72%**
	Intermediate Zone	0%	43%	27%	**19%**
	Igneous zircons	0%	10%	27%	**9%**

Fig. 6.9. Zircon Th/U ratio vs. age plot for samples from Sandamap granites. From a total of 68 ablated zircon spots, the majority (49) of the ablated zircon spots representing 72% plot under metamorphic sources, 13 ablated zircon spots representing 19% plot under intermediate and 6 ablated zircon spots representing 9% plot under magmatic sources. From those plotting in magmatic sources: one is metamict with a relatively high Th/U ratio (0.92) and the other an inherited core which yielded a relatively high age (832 Ma). Below the plot is the assessment of the plotted data indicating the percentage plotting under each source. Zircon sources as proposed by Teipel et al. (2004) and Linnemann et al. (2011) (after Manzotti et al., 2015; Aysal et al., 2012).

Zircon topology and initial $^{87}Sr/^{86}Sr$ ratio

The initial $^{87}Sr/^{86}Sr$ ratios from the non-foliated (0.7153) and foliated (0.7267) granites from Sandamap, indicating a crustal source are consistent with the genetic data from zircon typological studies as shown by Pupin, (1980). The typology of the zircon crystals from the Sandamap granites suggest that they are of crustal origin and with a possibility of polyphased anatexis.

Comparison of U/Pb dates from different zircon segments.

Zircon $^{206}Pb/^{238}U$ dates from different segments of the zircons were compared to see if any correlations exist between the three granites samples (Figs. 6.10 – 6.12, Table 6.7). The observation is that correlation exists in dates from zircon rims: it is observed that the dark unzoned rims in all three samples yielded younger dates (all 202 ±2 Ma and less) than the bright zoned and unzoned rims (Table 6.7). Noteworthy is that dark unzoned rims of zircons from the non-foliated granite-sample GT yielded the lowest dates (all <98 ±2 Ma) and zircons from the foliated granite yielded dates as high as 200 ±3 Ma (Table 6.7). Dates from bright unzoned and zoned rims of zircons overlap and fall within a range of 211 ±3 to 350 ±5 Ma for the foliated granite-sample FG (Table 6.7). Bright unzoned rims yielded dates older than those from bright zoned rims in zircons from the non-foliated granite (sample UG) (Table 6.7). Bright unzoned rims that are well defined and large enough for ablation were not identified on zircons from non-foliated granite-sample GT and as such no dates are available for comparison. In a summary Table 6.7 reveals that dark unzoned rims are the youngest and these are possibly metamorphic rims/growth. The bright unzoned rims are the oldest and the significance of these dates remains debatable; however their brightness and presence of fractures and irregular structures in some suggest that these domains have undergone metamictization. Their dates may therefore be possibly recording times when metamictization and Pb loss occurred.

Two zircons with spot IDs GT5, and GT12 have different internal structures; both their cores and rims are zoned and additionally, their dates are much older and thus not comparable with the dates obtained from the rest of the zircons. The obtained $^{206}Pb/^{238}U$ dates from rims of GT5 and GT12 are 619 ± 2 Ma and 480 ± 7 Ma respectively (Fig. 6.12) and these zircons are thought to have been inherited. The zoned core of GT5 yielded a date of 832 ± 12 Ma. A very interesting observation is one noted from spots FG 27 and 28, where the outermost (bright and zoned) segment which genetically came later yielded a date 14 million years older than the inner segment (dark unzoned) (Fig. 6.10). The inner domain is a dark unzoned domain between the bright core and the bright zoned rim. Both domains in question yielded low Th/U ratios of 0.1 each suggesting metamorphic sources (Manzotti et al., 2015; Aysal et al., 2012). This would possibly mean that the dark unzoned domains are metamorphic overgrowth. This

could explain the observation behind the younger dates obtained from them. Equipped with this information one can argue that the relationship between the dates obtained from the dark unzoned rims of the samples may have a genetic implication. The assessment of the dates shows that FG rims (124 - 202 Ma) yielded older dates in comparison to the other two samples (GT: 61 - 98 Ma, UG: 57 - 128 Ma) (Table 6.7). This suggests that the foliated granite (FG) is possibly the oldest and the unfoliated granite (GT) possibly the youngest. This assumption is consistent with the inference brought forth in Section 7.1.2 from the initial strontium ratios which also suggest that the foliated granite (FG) is older than the unfoliated granites (GT & UG). In some cases ablation spots overlapped different zircon domains e.g. FG26, yielding a mixed date and rendering the obtained date meaningless.

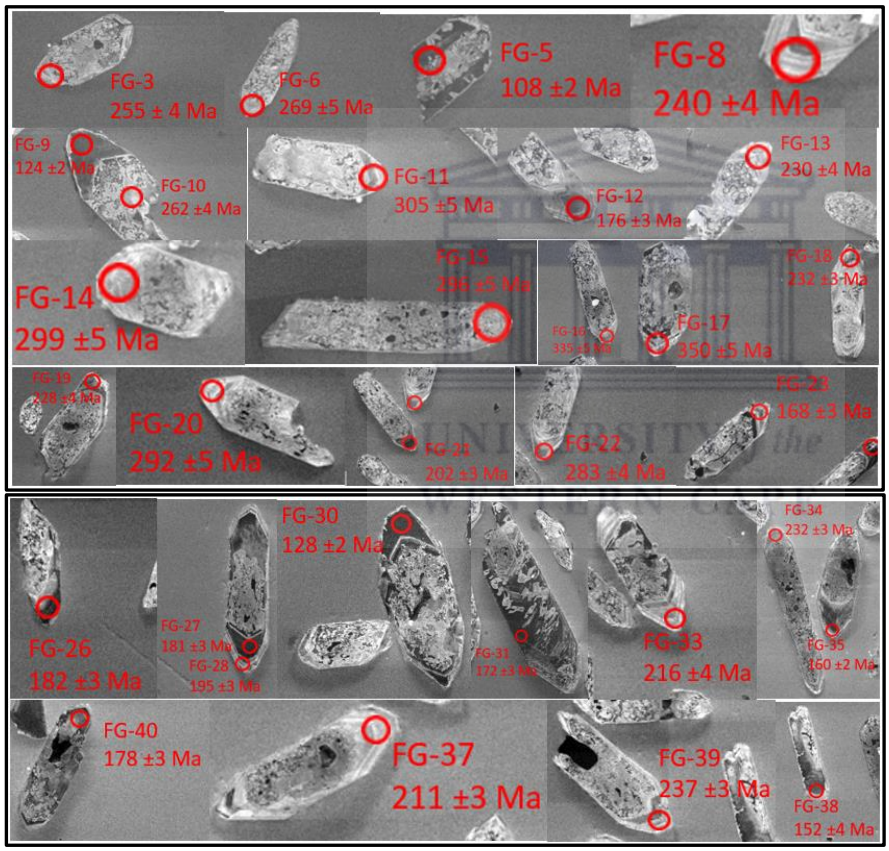

Fig. 6.10. Cathodoluminescence images of zircons from the foliated granite (sample FG). Red spot sizes (25µm) reflect the size of the spots ablated during analysis. The sample ID and the obtained $^{206}Pb/^{238}U$ dates reported at 2s are given.

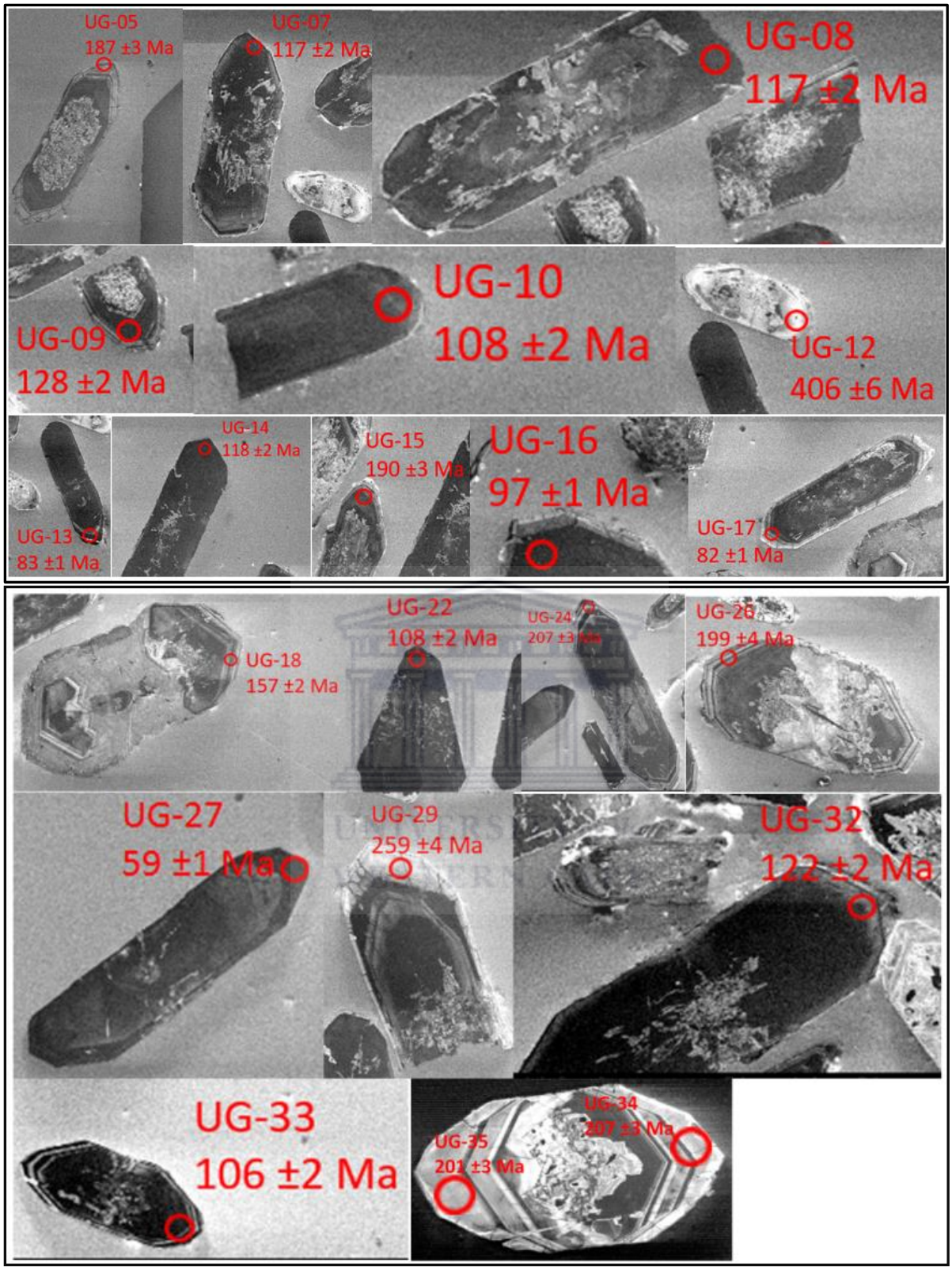

Fig. 6.11. Cathodoluminescence images of zircons from the non-foliated granite (sample UG). Red spot sizes (25μm) reflect the size of the spots ablated during analysis. The sample ID and the obtained $^{206}Pb/^{238}U$ dates reported at 2s are given.

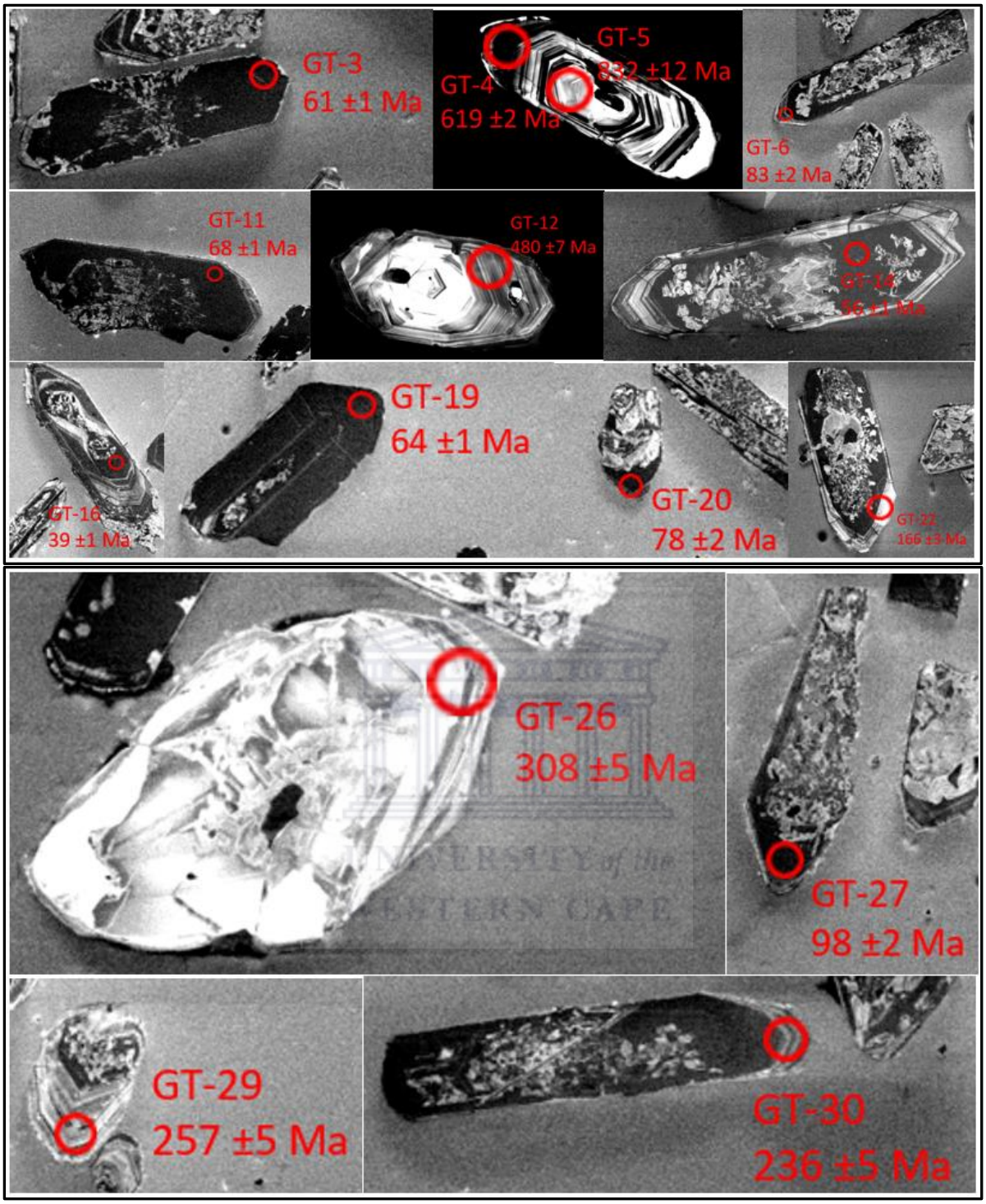

Fig. 6.12. Cathodoluminescence images of zircons from the non-foliated granite (sample GT). Red spot sizes (25μm) reflect the size of the spots ablated during analysis. The sample ID and the obtained $^{206}Pb/^{238}U$ dates reported at 2s are given.

Table 6.7. Comparison of $^{206}Pb/^{238}U$ dates from different segments of zircons

Sample ID	Zircon Segment	FG		UG		GT	
		Spot ID	$^{206}Pb/^{238}U$ dates (Ma)	Spot ID	$^{206}Pb/^{238}U$ dates (Ma)	Spot ID	$^{206}Pb/^{238}U$ dates (Ma)
Zircon rim	**Dark-unzoned**	9, 12, 21, 27, 30, 40	124, 176, 202, 195, 128, 178	7, 8, 9, 10, 14, 27	117, 117, 128, 108, 118, 57	3, 11, 19, 20, 27	61, 68, 64, 78, 98
	Bright-zoned	8, 11, 17, 20, 33, 37	240, 305, 350, 292, 216, 211	5, 18, 24, 26, 34	187, 157, 207, 199, 207	12, 26, 29, 30	480, 308, 257, 236
	Bright-unzoned	3, 6, 13, 14, 15	255, 269, 230, 299, 296	12, 29	406, 259		
Zircon core	**Dark-zoned**						
	Dark-unzoned					14, 16	56, 39
	Bright-zoned					5	832
Observed trends		BZ, BUZ dates > DUZ dates		BUZ dates > BZ dates > DUZ dates		BZ dates > DUZ dates	

Note: DUZ: BZ: Bright zoned, BUZ: Bright unzoned, Dark unzoned. Errors not included in the given dates (These are given in the CL image dates- Figs. 6.10 – 6.12).

Discordance may be caused by low temperature Pb loss due to metamictization of old and U-rich grains, assimilation of ^{204}Pb in minute inclusions or along cracks or along fractures and, dissolution/reprecipitation, such as when metamorphic rims overgrow inherited cores of a range of different ages (Villa and Hanchar, 2017). Radioactive elements such as U and Th are incorporated in zircons during crystallization, as proposed by Silver and Deutsch (1963). The growth of zircon crystals begin early in the history of the magmatic melt and continue growing over most of the crystallization history (Silver and Deutsch 1963; Villa and Hanchar, 2017). The residual melt is enriched in incompatible elements, including U and Th, and as a result late crystallizing zircon (i.e., either whole magmatic zircon crystals or magmatic rims of inherited cores) would be enriched in those elements and thus be more affected by the effects of metamictization (i.e., ^{204}Pb incorporation or Pb loss) caused by radioactive decay of U and Th (Silver and Deutsch 1963; Villa and Hanchar, 2017).

Proterozoic and Archean zircons were found to have relatively accumulated high radiation damage in comparison to Paleozoic, Mesozoic and younger zircons (Krogh and Davis, 1975) and are more susceptible to cracking and would thus be prone to infiltration of ^{204}Pb carried by external fluids (Villa and Hanchar, 2017). In the same vein the outer layers of zircon crystals are weaker due to high U contents resulting in accumulation of radiation damage and the subsequent metamictization (Villa and Hanchar, 2017). The interaction of radiation damaged regions of the zircon or damaged crystal with low temperature fluids leads to Pb loss (Villa and Hanchar, 2017).

The discordance observed in samples GT, UG and FG is likely due to recent low-temperature Pb loss from metamict crystals. Fluids that were flowing in the Damara region belt as a result of tectonism and deformation events interacted with zircons or regions of zircons that has accumulated radiation damage, resulting in metamicts which consequently led to Pb loss.

6.3 REFERENCES

Aysal, N., Öngen, S., Peytcheva, I., & Keskin, M. (2012). Origin and evolution of the Havran Unit, Western Sakarya basement (NW Turkey): new LA-ICP-MS U-Pb dating of the metasedimentary-metagranitic rocks and possible affiliation to Avalonian microcontinent. *Geodinamica Acta*, *25*(3-4), 226-247.

Baksi, A.K., Archibald, D.A., & Farrar, E. (1996). Intercalibration of $^{40}Ar/^{39}Ar$ dating standards. *Chemical Geology*, 129, 307-324.

Chisholm, E. K. I., Sircombe, K. N., & DiBugnara, D. L. (2014). *Handbook of Geochronology Mineral Separation Laboratory Techniques*. Geoscience Australia.

Daneshvar, N., Maanijou, M., Azizi, H., & Asahara, Y. (2018). Study of the zircon morphology and internal structures as a tool for constraining magma source: example from granitoid bodies in the northern Sanandaj Sirjan zone (SW Saqqez). *Geopersia*, *8*(2), 245-259.

Fleck, R. J., Sutter, J. F., & Elliot, D. H. (1977). Interpretation of discordant $^{40}Ar/^{39}Ar$ age-spectra of Mesozoic tholeiites from Antarctica. *Geochimica et Cosmochimica Acta*, *41*(1), 15-32.

Gopalan, K. (2002). Direct correction for mass fractionation of spiked isotopic ratios from dynamic multicollector measurements. *Geochemical journal*, *36*(1), 83-89.

Horstwood, M.S., Košler, J., Gehrels, G., Jackson, S.E., McLean, N.M., Paton, C., Pearson, N.J., Sircombe, K., Sylvester, P., Vermeesch, P., & Bowring, J.F., (2016). Community-derived standards for LA-ICP-MS U-(Th-) Pb geochronology–Uncertainty propagation, age interpretation and data reporting. *Geostandards and Geoanalytical Research*, *40*(3), 311-332.

Hoskin, P. W. O., & Black, L. P. (2000). Metamorphic zircon formation by solid-state recrystallization of protolith igneous zircon. *Journal of metamorphic Geology*, *18*(4), 423-439.

Jackson, S. E., Pearson, N. J., Griffin, W. L., & Belousova, E. A. (2004). The application of laser ablation-inductively coupled plasma-mass spectrometry to in situ U–Pb zircon geochronology. *Chemical Geology*, *211*(1-2), 47-69.

Köksal, S., Göncüoglu, M. C., Toksoy-Köksal, F., Möller, A., & Kemnitz, H. (2008). Zircon typologies and internal structures as petrogenetic indicators in contrasting granitoid types from central Anatolia, Turkey. *Mineralogy and Petrology*, *93*(3-4), 185-211.

Kossert, K., & Günther, E. (2004). LSC measurements of the half-life of ^{40}K. *Applied Radiation and Isotopes*, 60, 459-464.

Krogh, T. E., and Davis, D. (1975). Alteration in zircons and differential dissolution of altered and metamict zircon. Carnegie Institution of Washington Yearbook, 74, 619-623.

Lee, J-Y., Marti, K., Severinghaus, J.P., Kawamura, K., Yoo, H-S., Lee, J-B., & Kim, J-S. (2006). A redetermination of the isotopic abundances of atmospheric Ar. *Geochimica et Cosmochimica Acta*, 70, 4507–4512.

Linnemann, U., Ouzegane, K., Drareni, A., Hofmann, M., Becker, S., Gärtner, A., & Sagawe, A. (2011). Sands of West Gondwana: an archive of secular magmatism and plate interactions—a case study from the Cambro-Ordovician section of the Tassili Ouan Ahaggar (Algerian Sahara) using U–Pb–LA-ICP-MS detrital zircon ages. *Lithos*, *123*(1-4), 188-203.

Manzotti, P., Poujol, M., & Ballèvre, M. (2015). Detrital zircon geochronology in blueschist-facies meta-conglomerates from the Western Alps: implications for the late Carboniferous to early Permian palaeogeography. *International Journal of Earth Sciences*, *104*(3), 703-731.

Ohira H., (1994). Inference of parent rocks by means of zircon crystal morphology and major element composition of host rocks - An example of granitic mylonites within the Tanakura Shear Zone -. *Journal of the Geological Society of Japan*, 100, 495-504.

Paton, C., Hellstrom, J., Paul, B., Woodhead, J., & Hergt, J. (2011). Iolite: Freeware for the visualisation and processing of mass spectrometric data. *Journal of Analytical Atomic Spectrometry*, *26*(12), 2508-2518.

Petrus, J. A., & Kamber, B. S. (2012). VizualAge: A novel approach to laser ablation ICP-MS U-Pb geochronology data reduction. *Geostandards and Geoanalytical Research*, *36*(3), 247-270.

Ranen, M. C., & Jacobsen, S. B. (2008). Fractionation corrections for high-precision multi-collector thermal ionization mass spectrometry. *Lunar and Planetary Science Conference* (Vol. 39, p. 1966).

Reiners, P. W., Carlson, R. W., Renne, P. R., Cooper, K. M., Granger, D. E., McLean, N. M., & Schoene, B. (2017). *Geochronology and thermochronology*. John Wiley & Sons.

Renne, P. R., Swisher C. C., Deino A. L., Karner D. B., Owens T., & DePaolo D. J. (1998) Intercalibration of standards, absolute ages and uncertainties in $^{40}Ar/^{39}Ar$ dating. *Chemical Geology (Isotope Geoscience Section)*, 145, 117–152.

Renne, P.R., Mundil, R., Balco, G., Min, K., & Ludwig, K.R. (2010). Joint determination of ^{40}K decay constants and $^{40}Ar^*/^{40}K$ for the Fish Canyon sanidine standard, and improved accuracy for $^{40}Ar/^{39}Ar$ geochronology. *Geochimica et Cosmochimica Acta*, 74, 5349–5367.

Roberts, M. P., & Finger, F. (1997). Do U-Pb zircon ages from granulites reflect peak metamorphic conditions?. *Geology*, *25*(4), 319-322.

Silver, L.T., and Deutsch, S. (1963). Uranium-lead isotopic variations in zircon: a case study. *Journal of Geology*, 71, 721-758.

Sláma, J., Kosler, J., Condon, D.J., Crowley, J.L., Gerdes, A., Hanchar, J.M., Horstwood, M.S.A., Morris, G.A., Nasdala, L., Norberg, N., Schaltegger, U., Schoene, B., Tubrett, M.N., & Whitehouse, M.J. (2008). Plešovice zircon—a new natural reference material for U–Pb and Hf isotopic microanalysis. *Chemical Geology*, *249*(1-2), 1-35.

Spencer, C. J., Kirkland, C. L., & Taylor, R. J. (2016). Strategies towards statistically robust interpretations of in situ U–Pb zircon geochronology. *Geoscience Frontiers*, *7*(4), 581-589.

Swindle, T. D., and Weirch, J. R. (2017). The effect of partial thermal resetting on ^{40}Ar-^{39}Ar "Plateaus". "In Proceedings of the 48th Lunar and Planetary Science Conference, The Woodlands, TX, USA, Abstract#1265

Taylor, R. E., and Aitken, M. J. (Eds.). (1997). Chronometric Dating in Archaeology (Vol. 2). Springer Science & Business Media.

Teipel, U., Eichhorn, R., Loth, G., Rohrmüller, J., Höll, R., & Kennedy, A. (2004). U-Pb SHRIMP and Nd isotopic data from the western Bohemian Massif (Bayerischer Wald, Germany): implications for upper Vendian and lower Ordovician magmatism. *International Journal of Earth Sciences*, *93*(5), 782-801.

Villa, I. M., & Hanchar, J. M. (2017). Age discordance and mineralogy. *American mineralogist*, *102*(12), 2422-2439.

Wang, W. (2018). *Archean-Mesoproterozoic Crustal Evolution and Crust-Mantle Geodynamics of Western Liaoning-Northeastern Hebei Provinces, North China Craton*. *Springer*, Singapore, 305.

Wu, Y., & Zheng, Y. (2004). Genesis of zircon and its constraints on interpretation of U-Pb age. *Chinese Science Bulletin*, *49*(15), 1554-1569.

Young, E. D., Galy, A., & Nagahara, H. (2002). Kinetic and equilibrium mass-dependent isotope fractionation laws in nature and their geochemical and cosmochemical significance. *Geochimica et Cosmochimica Acta*, *66*(6), 1095-1104.

CHAPTER 7

DISCUSSION, CONCLUSIONS AND RECOMMENDATIONS

7.1 DISCUSSION

7.1.1 Stable isotopes

The calculated $\delta^{13}C_{CO2}$ value of the ore-fluids (-5.1‰) falls within the range of -11 to -2‰ observed in typical orogenic gold deposits and, as such, points towards an orogenic source (Goldfarb and Groves, 2015). All calculated $\delta^{18}O_{water}$ values of the high temperature group (+6.6 to +11.3‰) and some of the low temperature group (+3.1 to +7.8‰) (Table 5.1) from the Sandamap mineralization fall within the range observed in typical orogenic gold deposits found in Phanerozoic terrains (+7 to +13‰) (Goldfarb and Groves, 2015).

Fluid inclusions in vein quartz from the Sandamap prospect have δD values from -35‰ to -49‰ (Table 5.1). These values falls within the range of most published data for typical orogenic gold deposits which varies from -20 to -80‰ (Kerrich et al., 2000; Shen et al., 2016). In a plot of δD vs. $\delta^{18}O_{H2O}$ (Fig. 5.1), 50% of the quartz samples data from the Sandamap deposit plot in the metamorphic field and the other 50% plot in the overlap region between the metamorphic and magmatic fields. This is also indicative of a dominant metamorphic fluid source, or basically a metamorphic fluid source since the overlap region cannot be used confidently to make a source discrimination.

According to Goldfarb and Groves (2015), evidence for the fluid source in orogenic deposits is circumstantial and long fluid flow paths make interpretations of data from fluid inclusions and isotopic studies equivocal. Even though a scenario where orogenic gold fluids are sourced from granitoids emplaced into the upper and middle crust is permissible due to abundant geochemical data that are open to interpretation, geological and geochronological data are not in support of a magmatic-hydrothermal model in the upper to middle crust (Goldfarb and Groves, 2015). Goldfarb and Groves (2015) further state that there is no universal temporal association between orogenic gold and magmatism, and go on to say that where an age overlap has been established, no specific type of magmatism has been found to be consistently associated with gold formation. A metamorphic model for fluid and metal sources, on the other hand, has been found to be very consistent with geological, geochronological, and geochemical data (Goldfarb and Groves, 2015). At Sandamap, the δD

values, and calculated $\delta^{18}O_{water}$ values of the ore-fluids, along with the δD vs. $\delta^{18}O_{H2O}$ plot, are all consistent with a metamorphic fluid source.

7.1.2 Age of mineralization vs. age of proximal igneous bodies

Two grains from a muscovite sample associated with the hydrothermal quartz veins at Sandamap yielded two plateau $^{40}Ar/^{39}Ar$ ages. The Sample NO2, grain 1 produced a plateau age of 2977 ± 18 Ma (Fig. 6.1), however, the obtained age is improbable, geologically meaningless and therefore unacceptable because this date was obtained from rocks that form part of the Neoproterozoic Damara orogenic belt which is not older than 900 Ma (Miller, 2008). This makes the obtained date more than 2000 Ma older. The 2977 ± 18 Ma date cannot be explained by argon loss because it is too old and not the other way because Pb loss would unlikely result in a date higher than the expected, neither can it be explained by excess argon because the other grain (NO2, grain 1) would have also been affected, nor can it be explained by contamination because the two grains were in the same batch during irradiation. Contamination may be a possible explanation but why would it only affect NO2, grain 1 but not NO2, grain 2 since they were in the same batch during irradiation? A plausible explanation for the spectrum in Fig. 6.1 is that sample No 2, grain 1 is most likely a detrital mica grain (Verdel et al., 2012; Neubauer and Bojar, 2013). Sample NO2 Grain 2 yielded a plateau age of 472 ± 3 Ma (Fig. 6.2) and this is interpreted as the true age of mineralization because it is consistent with local geological processes of the region, which are full development of the nCZ as a back arc (490 – 460 Ma), where Sandamap is located and with the timing of D_3 doming (480 – 460 Ma) which is interpreted to have produced the shear zone which served as the conduit for the mineralizing fluids of the Sandamap deposit.

An attempt to constrain the age of the plutonic rocks in the vicinity of the Sandamap gold mineralization using LA-ICP-MS U-Pb zircon dating did not, unfortunately, yield much success (Section 6.2.2). Analyses were carried out on zircon samples from three proximal plutonic bodies (the foliated granite and the non-foliated granite). All analytical results from the granitic bodies show variable discordance (Figs. 6.3 – 6.5). The discordance of the zircons in the granitoid bodies is due to Pb loss, which may be attributed to metamictization which is clearly noticeable as disrupted zonation patterns in cathodoluminescence (CL) images of the zircons (Figs. 6.3 – 6.5). The metamictization and Pb loss is likely attributed to extensive deformation, metamorphism and fluid flow in the region and along the shear zone.

The relatively high uranium contents in the zircons, that range from 629 to 24,170 ppm (Appendix I - K), are a cause of the metamictization.

Data from disturbed U-Pb systems will form quasi-linear arrays on Wetherill plots and where the discordia intercepts with concordia indicate the time at which the mineral began to accumulate radiogenic daughter products and the time at which the disturbance occurred (Marfunin, 1995). If the data are not very disturbed the upper intercept will approach the formation age (Marfunin, 1995). In this study's Wetherill plots the linear arrays do not intercept the concordia and thus no meaningful interpretation can made from them (Figs. 6.3 – 6.5).

Steven (1993) linked the age of the Sandamap Au fluids to stanniferous pegmatite (Stanniferous leucogranite in this study) with a Rb-Sr whole rock date of 468 ± 14 Ma (Fig. 7.1), and Steven et al. (1994) reported Pb-Pb model ages of 469 – 464 Ma from galena collected from the mineralized zone. The age of 475 – 469 Ma (472 ± 3 Ma) obtained in this study partially overlaps with Steven et al. (1994)'s Pb-Pb model ages. The geospatial relationship of the foliated leucogranite and non-foliated leucogranite with Rb-Sr whole-rock ages of 512 ± 19 Ma and 473 ± 23 Ma respectively (Steven, 1993) is depicted in Fig. 7.1.

Initial strontium ratios of the plutonic bodies at Sandamap

The high initial $^{87}Sr/^{86}Sr$ ratios of the leucogranites (0.7153) and pegmatites (0.7267) at Sandamap indicate that they are products of partial crustal melting. The metamorphic fabric (Steven, 1993) in the foliated granite suggests a recrystallization event. The geospatial relationship (Fig. 7.1) and the whole rock Rb/Sr dates obtained from the foliated (512 ± 19 Ma) and the non-foliated (473 ±23 Ma) granites cannot be used to discriminate the ages of these plutonic bodies. However, considering their geospatial relationship (Fig. 7.1), their textures and their differences in initial strontium ratios brings forth an argument that they may be possible products of the same melt. The spatial relationship and relative texture of these plutonic bodies are consistent with the fact that residual melt is likely to produce a more pegmatitic pluton with a higher initial strontium ratio due to incompatibility of Rb, however, a more in-depth study would be required to have this confirmed. Due to its incompatibility, during crystallization rubidium is concentrated in residual melt (Simmons and Webber,

2008), resulting in relatively higher Rb/Sr ratios in later crystallizing rocks and consequently an increase in ^{87}Rb's radiogenic daughter (^{87}Sr). The non-foliated granite is more pegmatitic than the foliated one (hence termed pegmatites in some literatures (e.g. Steven, 1993) and has a higher initial ^{87}Sr/^{86}Sr ratio.

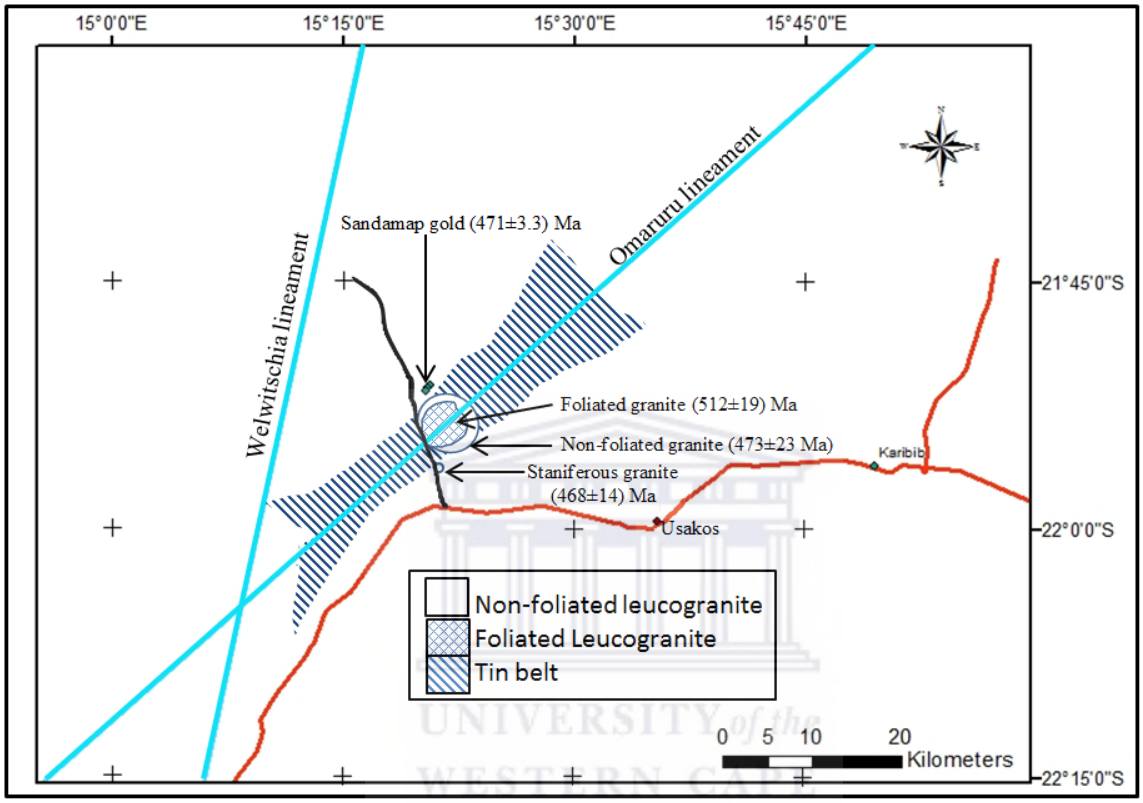

Fig. 7.1 Location of granitic intrusions on Sandamap. (modified after Steven, 1993)

According to Steven, (1993), the significance of the non-foliated granite (UG, GT) date (473 ± 23 Ma) is unclear due to sampling problems and these are however not further described. Additionally, since Rb and Sr are mobile elements, particularly in regions that have experienced high-grade metamorphism and considerable fluid flow, an age obtained from Rb and Sr data may likely not reflect the age of intrusion, crystallisation or emplacement of an intrusion and can, as such, not be solely relied upon.

While acknowledging the limitations of the Rb-Sr dating method and uncertainty regarding the meaning of the Rb-Sr whole-rock dates obtained from the intrusions at Sandamap, Steven (1993) noted two features. The first is the close agreement of the emplacement ages for specific granite and pegmatite types obtained by different workers (Fig. N1 & Table N1) and

the other being the consistency of ages and $(^{87}Sr/^{86}Sr)_I$ ratios for specific types of intrusion (pegmatites and leucogranites) in the central zone (CZ) over an area of approximately 12500 km^2 (Table N1) (Steven, 1993). Isotopically four types of intrusions were identified in the area: (i) undeformed post-D_1 Salem granitoids with low $(^{87}Sr/^{86}Sr)_I$ ratios intruded at 560-540 Ma, (ii) the peraluminous leucogranites intruded along major structural breaks during D_2 at the peak of regional metamorphism (~520 Ma) (includes the foliated leucogranite in this study), (iii) the syn-D_3 leucogranites with ages of ~500-475 Ma which are responsible for the northeast-trending elliptical outcrop pattern of the CZ and, (iv) the late-/post-tectonic pegmatites (includes the non-foliated leucogranites in this study) concentrated near deep-seated crustal fractures such as the Welwitschia lineament zone or found in the tin belts (Fig. N1) (Steven, 1993).

7.1.3 Correlation between fluid trapping temperatures and cooling histories from literature

Blocking and annealing temperatures of a diverse number of isotopic systems and fission tracks in minerals divulged cooling histories across various parts of the Damara belt (Miller, 2008). K/Ar and Rb/Sr ages of biotite record cooling through 300°C between 495 and 440 Ma across the Damara Belt from the NZ to the SMZ (Miller, 2008). Below 300°C, garnet fission track ages of 496 − 455 Ma in the SZ, 360 Ma in the sCZ and 315 Ma in the nCZ record cooling through approximately 280°C (Miller, 2008). The $^{40}Ar/^{39}Ar$ hornblende ages (486 and 478 Ma) record cooling through 525 °C towards the northern boundary of nCZ (Hawkesworth et al., 1983 as given in Miller, 2008) (Fig. 4.29). $^{40}Ar/^{39}Ar$ dating gave an age of 472 ± 3 Ma as the age at which the fluids were trapped (this study - chapter 6), with this age falling within the period that the Damara orogenic belt was undergoing a cooling process, and thus records the closure temperature of mica in the quartz. The calculated fluid trapping temperatures of 283 – 594 °C from the Sandamap prospect, along with the $^{40}Ar/^{39}Ar$ age of 472± 3 Ma, corresponds to the time between 495 and 440 Ma, recorded by K/Ar and Rb/Sr biotite ages, during which the Damara belt cooled below 300°C, as well as cooling of the Damara belt through 525 °C obtained from $^{40}Ar/^{39}Ar$ hornblende ages between 486 and 478 Ma. This also indicates that mineralization was likely deposited during retrograde metamorphism.

7.1.4 Fault-valve behaviour features

Fault-valve behaviour features have been observed at the Sandamap gold prospect. Lenticular fault quartz veins were observed at trench 14 and vein quartz samples collected from this locality are lenticular shaped (Fig. 2.31), a feature suggesting fault valve action within post-failure discharge zones (Sibson, 1990). Cross-cutting relationships between pre-failure extension veins and post-failure discharge veins, a common fault-valve behaviour feature (Sibson, 1990; Chi, and Guha, 2011), was observed at trench 15, where subhorizontal quartz veinlets are lying perpendicular to the subvertical shear zone foliation and quartz veins that lie parallel to shear zone foliation (Fig.2.32). The coexistence of different temperature groups within the same quartz sample (Fig. 4.7) is indicative of different episodes of deposition at contrasting pressures and temperatures through pressure fracturing and healing of quartz veins. Varying pressures within the same sample are consistent with fault-valve behavior.

7.1.5 Epithermal mineralization vs. post-hydrothermal weathering of sulfides

Kaolinite, dickite and alunite were observed within the mineralized zone at the Sandamap deposit. These minerals may be found in association with pyrophyllite and diaspore and are common in high sulfidation epithermal deposits (Reyes, 1990; White and Hedenquist, 1995). Kaolinite and alunite do not occur in low sulfidation epithermal deposits, except as an overprint of near-surface origin unrelated directly to ore mineralization (Vikre, 1985; White and Hedenquist, 1995). Quartz, adularia and sericite are indicative of low sulfidation mineralization, as opposed to quartz, kaolinite and alunite that occur in high sulfidation epithermal deposits (Groves et al., 1998; White & Hedenquist, 1995).

The presence of kaolinite and alunite does not, however, necessarily indicate a high sulfidation epithermal system, owing to the fact that these minerals can result from alteration caused by near-surface steam-heated waters in low sulfidation systems (White & Hedenquist, 1995). The steam-heated acid-sulfate waters form at temperatures near 100°C but may be heated if they flow downwards along fractures (Reyes, 1990) resulting in overprinting the ore, and, where jarosite occurs together with kaolinite and alunite, would be an alteration indicating post-hydrothermal weathering of sulfide minerals (White and Hedenquist, 1995). A combination of these three minerals (kaolinite, alunite and jarosite) occurs at Sandamap suggesting possible alteration caused by post-hydrothermal weathering of sulfides.

Jarosite possibly formed at temperatures below 200 °C (Frost et al., 2005) (Fig. 7.2) during post-hydrothermal weathering of sulfides (White and Hedenquist, 1995) (Fig.7.3). Dickite is commonly of hydrothermal origin formed partly from the alteration of aluminosilicate minerals (i.e. kaolinite) and, as such, is an important alteration indicator in hydrothermal systems (Handbook of Mineralogy, 2001). Hydronium jarosite is stable up to temperatures of around 200 °C where decomposition commences and involves the loss of hydroxyl units (Frost et al., 2005). The likely scenario at Sandamap is that the hydrothermal mineralization is likely of orogenic origin (based on stable isotope analysis, temperature of formation and depth of entrapment), followed by post-hydrothermal weathering of sulphides, as evidenced by the occurrence of kaolinite, alunite and jarosite.

With respect to tectonism, the age of mineralization at Sandamap, which is placed at 472 ± 3 Ma (Section 6.2.1), or 469 – 464 Ma (Steven et al., 1994), occurred during the post-tectonic period (490-460 Ma) characterized by, amongst others: 1) the full development of the nCZ as a back-arc region, 2) D_3 doming and the intrusion of numerous syn- to post-tectonic D_3 granites in the nCZ, and 3) the pop-up of the nCZ on the Omaruru Lineament (OML), the Waterberg Thrust (WT), and the Autseib Fault and Otjohorongo Thrust (AFOT) (Miller, 2008) while the reactivation of the abovementioned lineament, fault and thrusts are younger than the gold mineralization (Miller, 2008).

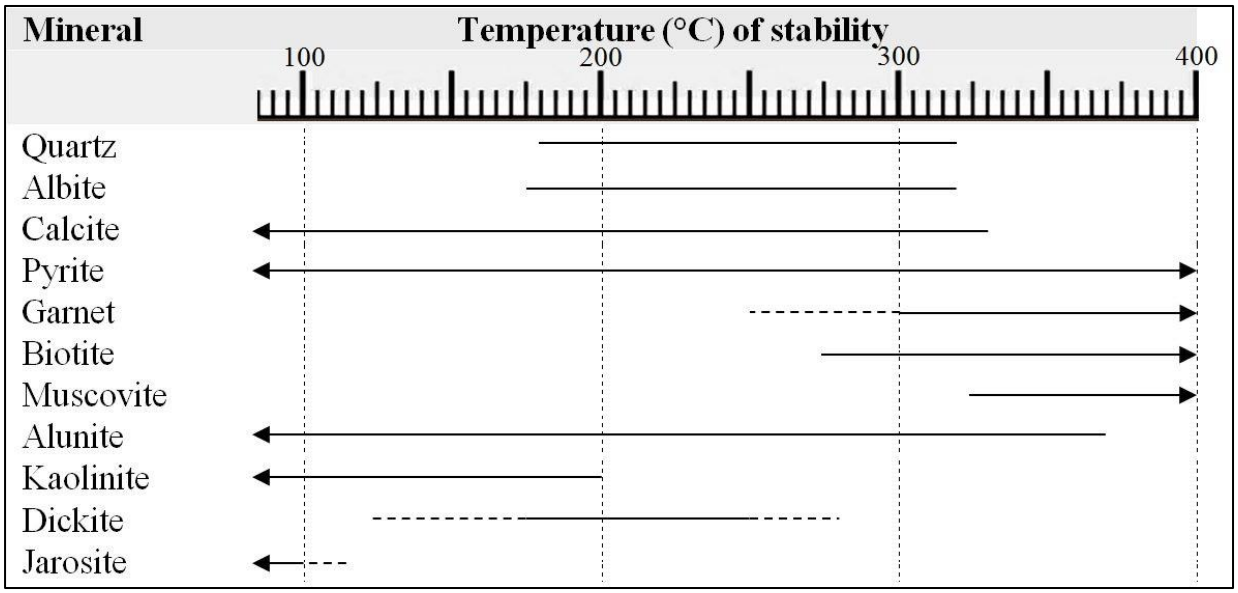

Fig.7.2. Temperature stability ranges at which hydrothermal alteration minerals form. Temperatures outside normal stability ranges are represented by dashed lines (From Reyes, 1990; Reyes et al., 1993; White and Hedenquist, 1995; John, 2007)

Therefore in terms of timing, the Sandamap deposit satisfies the timing relationship that other orogenic deposits have with respect to tectonism of their immediate host rocks. According to Groves et al. (1998) orogenic deposits are either syn- or post-tectonic and the latter is described as simultaneously syn-orogenic with respect to ongoing deep-crustal, subduction-related thermal processes.

7.1.6 Epithermal gold vs. orogenic gold

Epithermal ore deposits form at shallow depths (near surface to 2 km deep) and over the temperature range of 100°C to ~300°C (White and Hedenquist, 1995; Groves et al., 1998). High sulfidation fluids are characterised by moderate to low salinity (Hedenquist and Lowenstern, 1994), pH of <2, with kaolinite and alunite as distinctive alteration minerals (White and Hedenquist, 1995). Low sulfidation fluids, on the other hand, are characterized by low salinity (Hedenquist and Lowenstern, 1994), near neutral pH (Giggenbach, 1992) and an association with alteration minerals such as adularia, calcite, illite and sericite (White and Hedenquist, 1995). The oxygen ($\delta^{18}O$) and hydrogen (δD) isotopes of hydrothermal fluids from low sulfidation deposits indicate a dominantly meteoric water origin, with some deposits containing water and reactive gases of magmatic origin (Hedenquist and Lowenstern, 1994), whereas high sulfidation deposits are characterised by waters of magmatic origin mixed with meteoric water (Hedenquist and Lowenstern, 1994).

The alteration consists of carbonation, sericitization and sulfidation (Groves et al., 1998) while mineralizing fluids are characterised by near-neutral pH (5.5) and low-salinity (3–7 wt.% NaCl equiv.) (Goldfarb and Groves, 2015; Groves et al., 1998). Fluid compositions of orogenic gold deposits are identified by the following ranges in stable isotopes: (a) most published δD values for typical orogenic gold deposits vary from -20 to -80‰ (Kerrich et al., 2000; Shen et al., 2016); (b) $\delta^{18}O$ values for Precambrian ores range from +6 to +11‰, and from +7 to +13‰ for Phanerozoic ores, and (c) $\delta^{13}C$ values that range from -11 to -2‰ (Goldfarb and Groves, 2015). The vein system may continue vertically for up to 2 km with little or no change in gold grade or mineralogy (Groves et al., 1998).

Characterization of the deposit based on the following data aided the discrimination between epithermal and orogenic gold deposits: oxygen ($\delta^{18}O$) and hydrogen (δD) isotope values of the ore fluids, calculated depth of entrapment of mineralization, and the temperature of

formation. Data used for discrimination is tabulated in Fig. 7.3 and this data negate the possibility of the Sandamap prospect being an epithermal gold deposit while making the argument favouring an orogenic deposit more admissible.

The depth of entrapment of fluids has a range of 4 to 14 km (Fig.7.3) using isochore intersections of contemporaneous aqueous (type I) and CO_2 (type III) fluids. This depth range of entrapment covers the lower portion of the epizonal zone to upper portion of the hypozonal zone (Fig 7.3).

7.1.7 Source of gold

A review by Tomkins (2013) indicate that the source of gold in orogenic gold deposits remain under discussion. Magmatic, metamorphic and sedimentary sources have been suggested by various workers (Tomkins, 2013 and references therein). At the Sandamap gold prospect, the schist hosting the mineralized shear zone has a gold content of 0.05 ppm Au and would represent a possible source candidate. The extraction of gold from the schist would deplete the schist of its gold content or leave the lithology below mineralization concentration levels and the presence of altered schist suggests that leaching has taken place. However, this could not be established due to the non-availability of samples from such depth. The shear zone acted as a conduit for ore-fluid migration and provided enough surface area for fluid-rock interaction permitting easier extraction of the gold from the rocks. Chloride (Cl^-) and hydrogen sulphide (HS^-) are possible complexing agents during the transportation of gold (Gaboury, 2019). The extraction of gold from the source rock and its transportation require the availability of appropriate ligands, and hydrogen sulphide (HS^-) is the most suitable ligand in orogenic gold deposits, as proposed by Phillips and Powell (2010) (Gaboury, 2019).

The interpretation of gold transfers across the lithosphere has been based on the fundamental assumption that only hydrogen sulfide (HS^-) and chloride (Cl^-) can form stable complexes ($Au(HS)_2^-$ and $AuCl_2^-$) with the main gold oxidation state (Au^+), in hydrothermal fluids (Pokrovski et al., 2015). This assumption follows the knowledge that hydrothermal fluids systematically contain sulfur and chloride compounds that are known to favour gold dissolution in aqueous solution (Pokrovski et al., 2015).

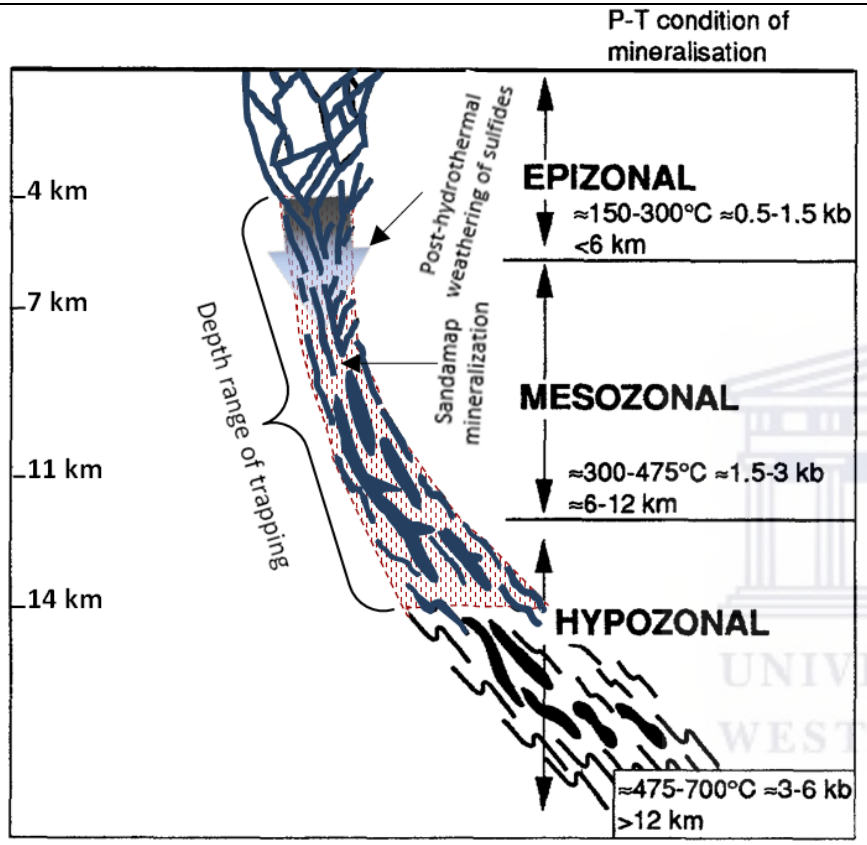

Conditions of entrapment	Epithermal mineralisation	Orogenic mineralisation	Sandamap gold
Depth	up to 2 km	2 to 20 km	4 to 14 km
Temperature	100°C to ~ 300°C [c]	150 to ~ 700°C [d]	187 – 594 °C
Pressure	<100 bars [f]	1 to 5 kbars	0.95 – 3.42 kbars
$\delta^{18}O_{water}$ values: (Phanerozoic terrains)	-17 to +10‰[g]	+7 to +13‰[a]	+6.6 to +11.3‰
δD values	-140 to -20‰[g]	-80 to -20‰[b]	-49‰ to -35‰
Origin of fluids ($\delta^{18}O_{water}$ vs. $\delta^{18}O_{water}$)	Magmatic & meteoric[e]	Metamorphic[a]	Metamorphic

Fig. 7.3. Crustal level of fluid entrapment of the Sandamap gold mineralization. The depth range of fluid entrapment is from 5 to 11 km. This depth range was calculated using isochore intersections of contemporaneous aqueous (type I) and CO_2-rich (type III) fluids. Also indicated is the post-hydrothermal weathering, decreasing with depth (vertical extent was not determined). Tabulated data indicate condition of entrapment for different hydrothermal sysytems. (Diagram modified after Gebre-Mariam et al., 1995; Goldfarb and Groves, 2015[a, d]; Kerrich et al., 2000[b]; Shen et al., 2016[b]; Hayba et al. 1985[c]; White and Hedenquist, 1995[c]; Groves et al., 1998[c]; Groves, 1993[d]; Groves et al., 1998[d]; Groves et al., 2000[d]; Groves and Santosh, 2015[d]; Hedenquist and Lowenstern, 1994[e]; Hao et al., 2016 and references therein[f]; Li et al., 2018[g]).

However, Pokrovski et al., (2015) demonstrated that sulfur radical species, such as the trisulfur ion (S_3^-) form very stable and soluble complexes with Au^+ in aqueous solution at elevated temperatures (>250 °C) and pressures (>100 bar). Pokrovski et al., 2015 further showed that the S_3^- ion greatly increases the fluid capacity to extract Au from magma or rocks and to transport it to ore deposition sites and, as a consequence, it plays an important control role in the concentration, and distribution of gold in economic deposits. Very rapid breakdown of S_3^- to sulfate and sulfide in aqueous solution upon cooling accounts for its exclusion in most known models of hydrothermal fluids and this, as a result, prohibits its detection in experimental and natural fluid samples (Pokrovski et al., 2015).

Ore fluids at Sandamap are rich in iron (Chapter 3) and the trapping temperature of the ore fluids has been established as 187 – 594 °C. Two mechanisms of deposition were possibly at play: (i) the presence of iron-rich fluids at temperatures below 500 °C would exhibit decreased solubility of pyrite and possibly sulfidation (from rock-fluid interaction), causing S_3^- and $Au(HS)S_3^-$ to breakdown resulting in decreased solubility of Au and consequent deposition (Pokrovski et al., 2015), and (ii) the elevated amount of CO_2 (i.e. such as at trench 14 where CO_2-rich fluid inclusions are dominant) led to a sharp decrease in the amount of $Au(HS)_2^-$ and $Au(HS)S_3^-$ ions, causing decreased gold solubility and its subsequent deposition (Kokh et al., 2017). The elevated concentrations of CO_2 caused the break down/ destabilization of $Au(HS)_2^-$ and $Au(HS)S_3^-$ ions, leading to their decreased content in the fluids and the subsequent deposition of gold.

The analyzed $\delta^{13}C_{PDB}$ value of calcite (-4.22‰), the calculated $\delta^{18}O_{water}$ values of the ore-fluids of the higher temperature group (+6.6 to +11.3‰), δD values from −35‰ to −49‰ and a plot of δD vs. $\delta^{18}O_{H2O}$ (Fig. 5.1) are indicative of a metamorphic fluid source. Therefore H_2O, CO_2 and CH_4 were mobilized from sediments during metamorphism.

7.2 CONCLUSION

Orogenic gold deposits and epithermal gold deposits are not uncommon in post-orogenic extensional environments such as back-arc settings (White and Hedenquist, 1995; Groves et al., 2000) i.e. that in which the Sandamap deposit formed. The occurrence of kaolinite and alunite would suggest a high sulphidation epithermal deposit. However this is ruled out by

the presence of jarosite which indicates post-hydrothermal weathering of sulphides nullifying the existence of a high sulfidation epithermal deposit. Various sources of data from this study, giving rise to a depth range of entrapment (4 to 14 km), temperature of entrapment of fluids (187 – 594 °C), pressures of entrapment of fluids (0.95 – 3.42 kbars), stable isotope data ($\delta^{18}O$), δD values and δD vs. $\delta^{18}O_{H2O}$ diagram are all in favour of an orogenic gold deposit. Additionally, the dominant CO_2-rich and CH_4-rich fluids observed at Sandamap do not contradict this interpretation.

Analysis of microthermometry and hydrothermal alteration data from Sandamap resulted in the schematic model shown in Fig. 7.3. This depth range of entrapment covers the lower portion of the epizonal zone to upper portion of the hypozone (Fig 7.3) (Gebre-Mariam et al., 1995; Groves et al., 2000). Mineralization is currently at surface level implying that, if the depth of entrapment of the mineralization is 4 km, then 4 km or more of overburden has been eroded; however, the level of erosion and depth of post-hydrothermal weathering could not be established (no subsurface samples were available). The schist hosting the mineralized shear zone with a gold content of 0.05 ppm Au or its higher grade equivalent at depth, is a possible gold source candidate.

The age of Sandamap gold mineralization is placed at 472 ± 3 Ma. The mineralization is younger than shear zone, which acted as a conduit for ore-fluid migration and it has no age relationship with proximal plutonic bodies. It is younger than the foliated granite (512 ± 19 Ma) which exhibits metamorphic fabric in the form of mineral segregation, but older than the non-foliated granite (473 ± 23 Ma) which hosts a mineralized xenolith. Although the age of mineralization (472 ± 3 Ma) and that of the non-foliated granite (473 ± 23 Ma) are within error, the mineralized xenolith point towards a younger age for the latter.

7.3 RECOMMENDATIONS FOR FUTURE STUDIES

Studies to delineate and characterize the extent of mineralization along strike towards the northeast following the shear zone, where it is almost entirely under sand cover, would be beneficial for mineral exploration purposes. The portion covered by this thesis indicates that the gold content is higher towards the northeast, hence a recommendation for characterization in that direction. Characterizing the orebody at depth, where geophysics may play a vital role

if sulphides are present, the depth extent of post-hydrothermal weathering as well as an assessment of possible supergene enrichment, and the relationship between Au and gangue minerals will assist in better understanding the ore body. Characterization of the ore deposit in terms of mineralogy and metallurgy are vital components in further understanding the deposit. Future studies may also consider looking at the age relationship between the shear zone, marble and granite domes as well as their relationship with other deformational features in the area. Characterization of the Au transporting ligands, complexes or species will be vital in assessing the further potential of the deposit.

7.4 REFERENCES

Chi, G., & Guha, J. (2011). Microstructural analysis of a subhorizontal gold-quartz vein deposit at Donalda, Abitibi greenstone belt, Canada: Implications for hydrodynamic regime and fluid-structural relationship. *Geoscience Frontiers, 2*(4), 529-538.

Frost, R., Wills, R., Kloprogge, J., and Martens, W. (2005). Thermal decomposition of hydronium jarosite $(H_3O)Fe_3(SO_4)_2(OH)_6$. *Journal of Thermal Analysis and Calorimetry, 83*(1), 213-218.

Gebre-Mariam, M., Hagemann, S.G., and Groves, D.I. (1995). A classification scheme for epigenetic Archaean lode-gold deposits. *Mineralium Deposita, 30*(5), 408-410.

Gehrig, M., Lentz, H., and Franck, E.U. (1979). Thermodynamic properties of water–carbon dioxide–sodium chloride mixtures at high temperatures and pressures. In: Timmerhaus, K.D., Barber, M.S. (Eds.), High Pressure Science and Technology. *Physical Properties and Material Synthesis, vol. 1,* pp. 539–542.

Giggenbach, W.F. (1992). Magma degassing and mineral deposition in hydrothermal systems along convergent plate boundaries. *Economic Geology, 87,* 1927-1944.

Goldfarb, R.J., and Groves, D.I. (2015). Orogenic gold: Common or evolving fluid and metal sources through time. *Lithos, 233,* 2-26.

Groves, D.I. (1993). The crustal continuum model for late-Archaean lode gold deposits of the Yilgarn block, Western Australia. *Mineralium Deposita 28,* 366-374.

Groves, D.I., Goldfarb, R.J., Knox-Robinson, C.M., Ojala, J., Gardoll, S., Yun, G.Y., and Holyland, P. (2000). Late-kinematic timing of orogenic gold deposits and significance for computer-based exploration techniques with emphasis on the Yilgarn Block, Western Australia. *Ore Geology Reviews, 17*(1-2), 1-38.

Groves, D.I., Goldfarb, R.J., Gebre-Mariam, M., Hagemann, S.G., and Robert, F. (1998). Orogenic gold deposits: a proposed classification in the context of their crustal distribution and relationship to other gold deposit types. *Ore Geology Reviews, 13*(1-5), 7-27.

Groves, D.I., and Santosh, M. (2015). Province-scale commonalities of some world-class gold deposits: implications for mineral exploration. *Geoscience Frontiers* 6, 389-399.

Handbook of Mineralogy. (2001). *Mineral Data Publishing (version 1.2)* [PDF file]. Retrieved from http://rruff.info/doclib/hom/

Hao, B., Deng, J., Bagas, L., Ge, L., Nie, F., Turner, S., & Qing, M. (2016). The Gaosongshan epithermal gold deposit in the Lesser Hinggan Range of the Heilongjiang Province, NE China: implications for Early Cretaceous mineralization. *Ore Geology Reviews*, *73*, 179-197.

Hawkesworth, C.J., Gledhill, A.R., Roddick, J.C., Miller, R.McG. and Kröner, A. (1983). Rb-Sr and 40Ar/39Ar studies bearing on models for the thermal evolution of the Damara Belt, Namibia, 323-338. *In*: Miller, R.McG. (Ed.) *Evolution of the Damara Orogen of South West Africa/Namibia*. Spec. Publ. geol. Soc. S. Afr., 11, 515 pp.

Hedenquist, J.W., and Lowenstern, J.B. (1994). The role of magmas in the formation of hydrothermal ore deposits. *Nature, 370*(6490), 519.

John, L. (2007). Hydrothermal alteration mineralogy in geothermal fields with case examples from Olkaria Domes geothermal field, Kenya. Report, United Nations University-Geothermal Training Programme, 26.

Kerrich, R., Goldfarb, R., Groves, D., and Garvin, S., 2000. The geodynamics of world-class gold deposits—characteristics, space–time distribution, and origins. *Reviews in Economic Geology 13*, 501–544.

Kokh, M. A., Akinfiev, N. N., Pokrovski, G. S., Salvi, S., and Guillaume, D. (2017). The role of carbon dioxide in the transport and fractionation of metals by geological fluids. *Geochimica et Cosmochimica Acta*, *197*, 433-466.

Li, S.N., Ni, P., Bao, T., Li, C.Z., Xiang, H.L., Wang, G.G., Huang, B., Chi, Z., Dai, B.Z. and Ding, J.Y. (2018). Geology, fluid inclusion, and stable isotope systematics of the Dongyang epithermal gold deposit, Fujian Province, southeast China: implications for ore genesis and mineral exploration. *Journal of Geochemical Exploration*, *195*, 16-30.

Marfunin, A.S. (1995): Advanced mineralogy: methods and instrumentation (results and recent developments). Vol. 2. SpringerVerlag, Berlin-Heidelberg-New York, 441 p

Miller, R.M., 2008. Neoproterozoic and early Palaeozoic rocks of the Damara Orogen. In: Miller, R.M. (Ed.). The Geology of Namibia. Geological Survey of Namibia, Windhoek vol. 2, pp. 13-1–13-410.

Neubauer, F., & Bojar, A. V. (2013). Origin of sediments during Cretaceous continent—continent collision in the Romanian Southern Carpathians: preliminary constraints from 40Ar/39Ar single-grain dating of detrital white mica. *Geologica Carpathica*, *64*(5), 375-382.

Phillips G.N., and Powell, R. 2010. Formation of gold deposits: a metamorphic devolatilization model. *Journal of Metamorphic geology, 28(6),* 689–718.

Pokrovski, G.S., Kokh, M.A., Guillaume, D., Borisova, A.Y., Gisquet, P., Hazemann, J.-L., Lahera, E., Del Net, W., Proux, O., Testemale, D., Haigis, V., Jonchière, R., Seitsonen, A.P., Ferlat, G., Vuilleumier, R., Saitta, A.M., Boiron, M.-C., and Dubessy J. (2015) Sulfur radical species form gold deposits on Earth. *Proceedings of the National Academy of Sciences, 112*(44), 13484-13489.

Reyes, A.G. (1990). Petrology of Philippine geothermal systems and the application of alteration mineralogy to their assessment. *Journal of Volcanology and Geothermal Research*, *43*(1-4), 279-309.

Reyes, A.G., Giggenbach, W.F., Saleras, J.R., Salonga, N.D., and Vergara, M.C. (1993). Petrology and geochemistry of Alto Peak, a vapor-cored hydrothermal system, Leyte Province, Philippines. *Geothermics*, *22*(5-6), 479-519.

Roedder, E., 1984. Fluid inclusions. Mineralogical Society of America. *Reviews in Mineralogy, vol. 12,* 644 pp.

Shen, P., Pan, H., and Zhu, H. (2016). Two fluid sources and genetic implications for the Hatu gold deposit, Xinjiang, China. *Ore Geology Reviews, 73,* 298-312.

Simmons, W. B. S., and Webber, K. L. (2008). Pegmatite genesis: state of the art. *European Journal of Mineralogy*, *20*(4), 421-438.

Skinner, B.J., 1997. Hydrothermal mineral deposits: what we do and don't know. In: Barnes, H.L. (Ed.), *Geochemistry of Hydrothermal Ore Deposits.* 3rd edn. Wiley, New York, pp. 1–29.

Steven, N.M. 1993. A study of epigenetic mineralization in the Central Zone of the Damara Orogen, Namibia with special reference to gold, tungsten, tin and rare earth elements. *Memoir of the Geological Survey of Namibia*, 16, 166 pp.

Steven, N.M., Badenhorst, F.P., and Petzel, V.F.W. (1994). A review of gold occurrences in the northern and central zones of the Damara Orogen and the underlying mid-

Proterozoic basement, central Namibia. *Communications of the Geological Survey of Namibia, 9,* 63-77.

Tomkins, A.G. (2013). On the source of orogenic gold. *Geology, 41(12),* 1255–1256.

Trigub, A. L., Tagirov, B. R., Kvashnina, K. O., Lafuerza, S., Filimonova, O. N., and Nickolsky, M. S. (2017). Experimental determination of gold speciation in sulfide-rich hydrothermal fluids under a wide range of redox conditions. *Chemical Geology*, *471*, 52-64.

Verdel, C., van der Pluijm, B. A., & Niemi, N. (2012). Variation of illite/muscovite 40 Ar/39 Ar age spectra during progressive low-grade metamorphism: an example from the US Cordillera. *Contributions to Mineralogy and Petrology*, *164*(3), 521-536.

Vikre, P.G. (1985). Precious metal vein systems in the National district, Humboldt County, Nevada. *Economic Geology*, *80*(2), 360-393.

White, N.C., and Hedenquist, J.W. (1995). Epithermal gold deposits: styles, characteristics and exploration. *Society of Economic Geologists newsletter*, *23*(1), 9-13.

Wilkinson, J.J. (2001). Fluid inclusions in hydrothermal ore deposits. *Lithos, 55*(1−4), 229−272.

Appendix A: Some mineral's definition and occurrence

Albite: a plagioclase feldspar mineral having less than 10% anorthite content ($NaAlSi_3O_8$). It occurs in granite and pegmatite masses and pegmatite bodies and in some hydrothermal vein deposits (Handbook of Mineralogy, 2001).

Almandine: a garnet ($Fe_3Al_2(SiO_4)_3$) The most common garnet, in mica schists and gneisses (Handbook of Mineralogy, 2001).

Alunite: a hydrated aluminium potassium sulfate mineral, ($KAl_3(SO_4)_2(OH)_6$). Alunite is an analog of jarosite, where aluminium replaces Fe^{3+}. The mineral forms at temperatures between 15°C and 400°C by action of sulfate or solfataric action on aluminous rocks (Handbook of Mineralogy, 2001).

Calcite: a calcium carbonate mineral ($CaCO_3$) which may occur as gangue in hydrothermal veins (Handbook of Mineralogy, 2001).

Cummingtonite: a metamorphic amphibole. A magnesium iron silicate hydroxide ($(Mg,Fe^{2+})_2(Mg,Fe^{2+})_5Si_8O_{22}(OH)_2$) which commonly occurs in metamorphosed magnesium−rich rocks and in amphibolites (Handbook of Mineralogy, 2001). There are also reports of the mineral's occurrence in hydrothermal deposits e.g. Benkó *et al.* (2015).

Dickite: a phyllosilicate clay mineral ($Al_2Si_2O_5(OH)_4$). Commonly of hydrothermal origin formed partly from the alteration of aluminosilicate minerals and as such an important alteration indicator in hydrothermal systems (Handbook of Mineralogy, 2001).

Dolomite: a hydrous carbonate mineral composed of calcium magnesium carbonate, ($CaMg(CO_3)_2$) (Handbook of Mineralogy, 2001).

Haematite: the mineral form of iron (III) oxide (Fe_2O_3). The mineral can crystallize during the differentiation of magma or precipitate from mobile hydrothermal fluids seeping through a rock unit (Handbook of Mineralogy, 2001).

Hydroniumjarosite: a Trigonal member of the alunite group with a chemical formula: ($(H_3O)Fe^{3+}{}_3(SO_4)_2(OH)_6$) The mineral occur in oxidized zone of rapidly weathering sulfide−bearing rocks. A relatively rare member of the alunite group because the ubiquitous abundance of alkali ions in surface waters normally precludes its stability. (Handbook of Mineralogy, 2001).

Kaolinite: a clay mineral ($Al_2Si_2O_5(OH)_4$). The mineral forms by replacement of other aluminosilicate minerals during hydrothermal alteration and weathering (Handbook of Mineralogy, 2001).

Muscovite: *a hydrated* phyllosilicate mineral of aluminium and potassium ($KAl_2(AlSi_3O_{10})(FOH)_2$, or $(KF)_2(Al_2O_3)_3(SiO_2)_6(H_2O)$). It is formed from other minerals under hydrothermal conditions; it may be detrital or authigenic (Handbook of Mineralogy, 2001).

Quartz: a mineral composed of silicon and oxygen atoms in a continuous tetrahedra framework of SiO_4, with chemical formula of SiO_2. It forms from magma, and also occurs in hydrothermal veins and in hydrothermal metal deposits (Handbook of Mineralogy, 2001).

Appendix B: Fluid inclusion images

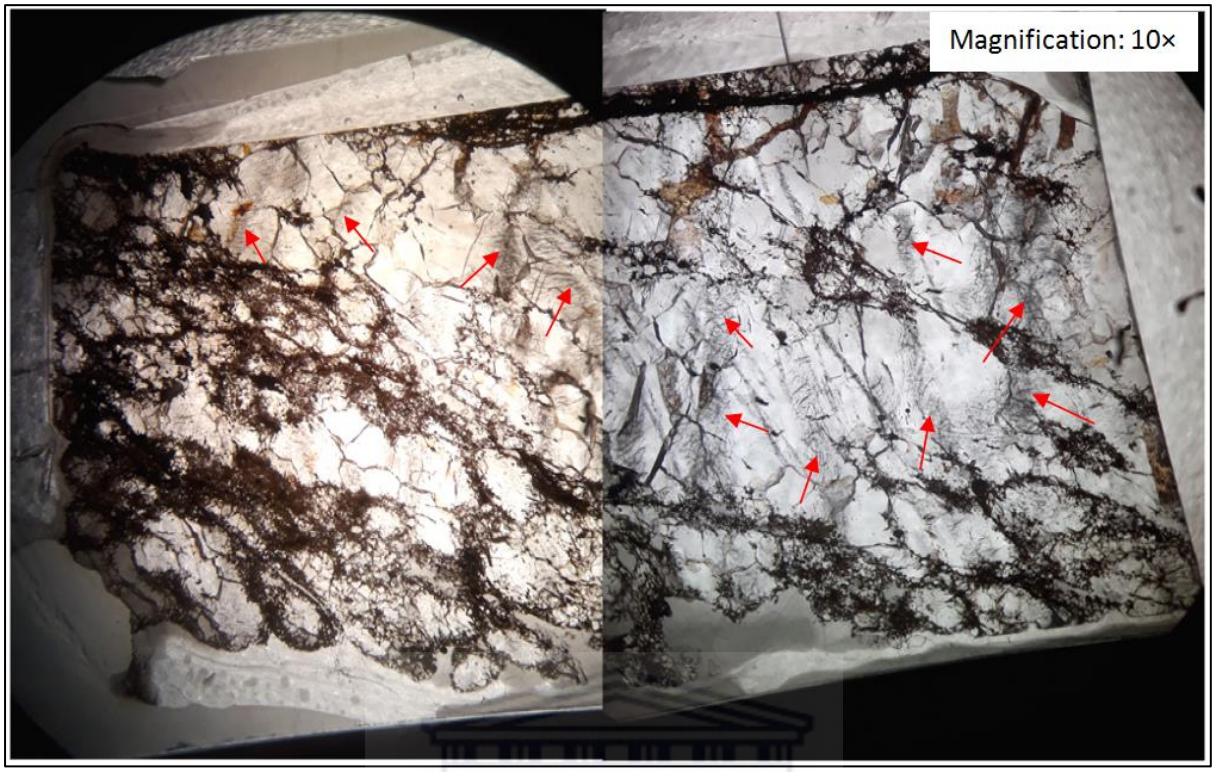

Fig. B1. An image showing an overview of a double polished thin section (T15) depicting trails of fluid inclusions (red arrows) which are dominantly Mono−phase Type IV (Methane−rich) and Type III (Carbonic−rich) fluid inclusions

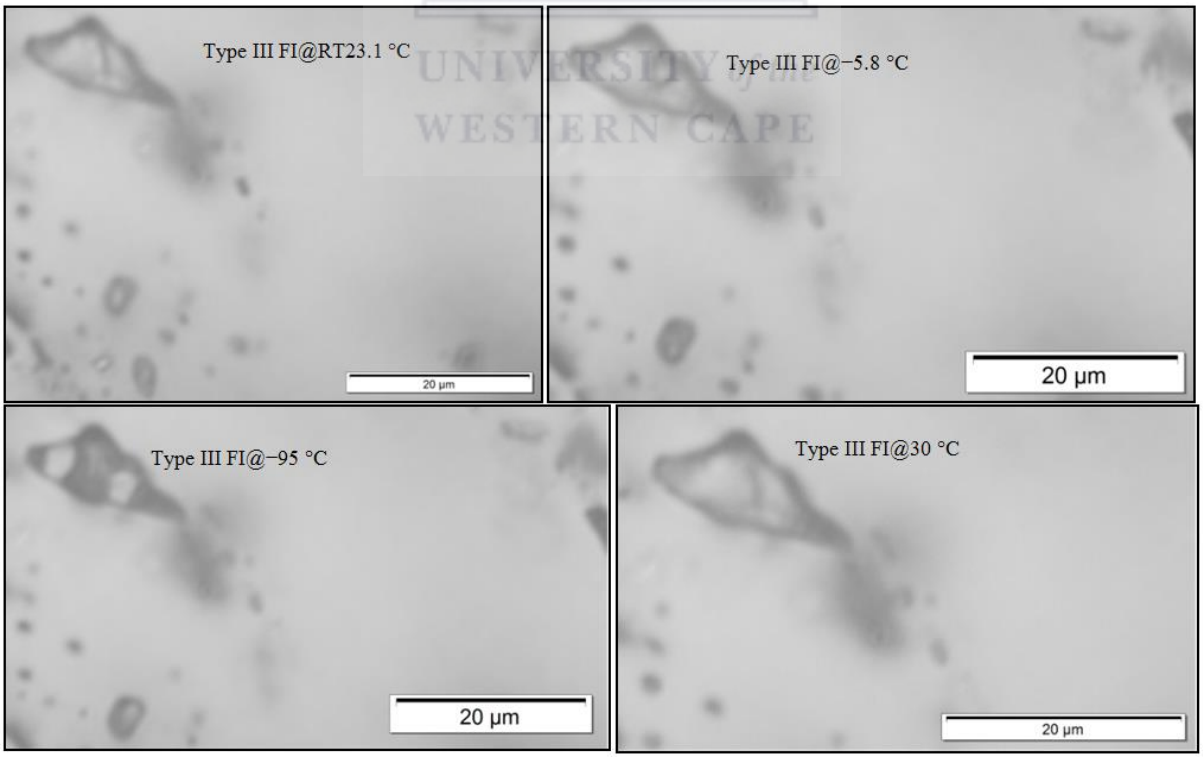

Fig. B2. Chip T14A: Type III (Carbonic−rich) fluid inclusion at various temperatures. Depicting Mono−phase at high temperatures and 2−phases at low temperatures.

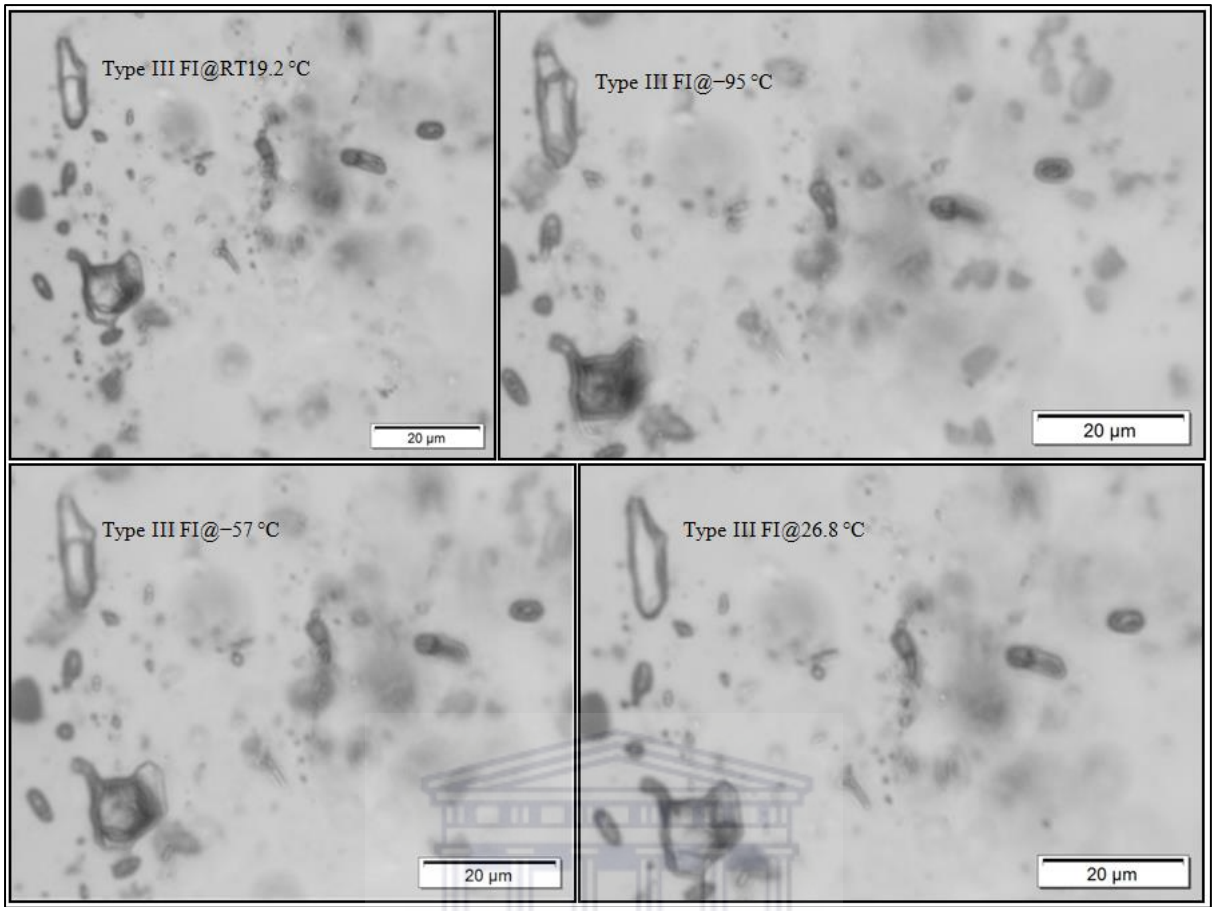

Fig. B3. Chip T14A: Type III (Carbonic−rich) fluid inclusion at various temperatures. Depicting Mono−phase after homogenization at 26.8 °C and 2−phases at room temperature (19.2 °C).

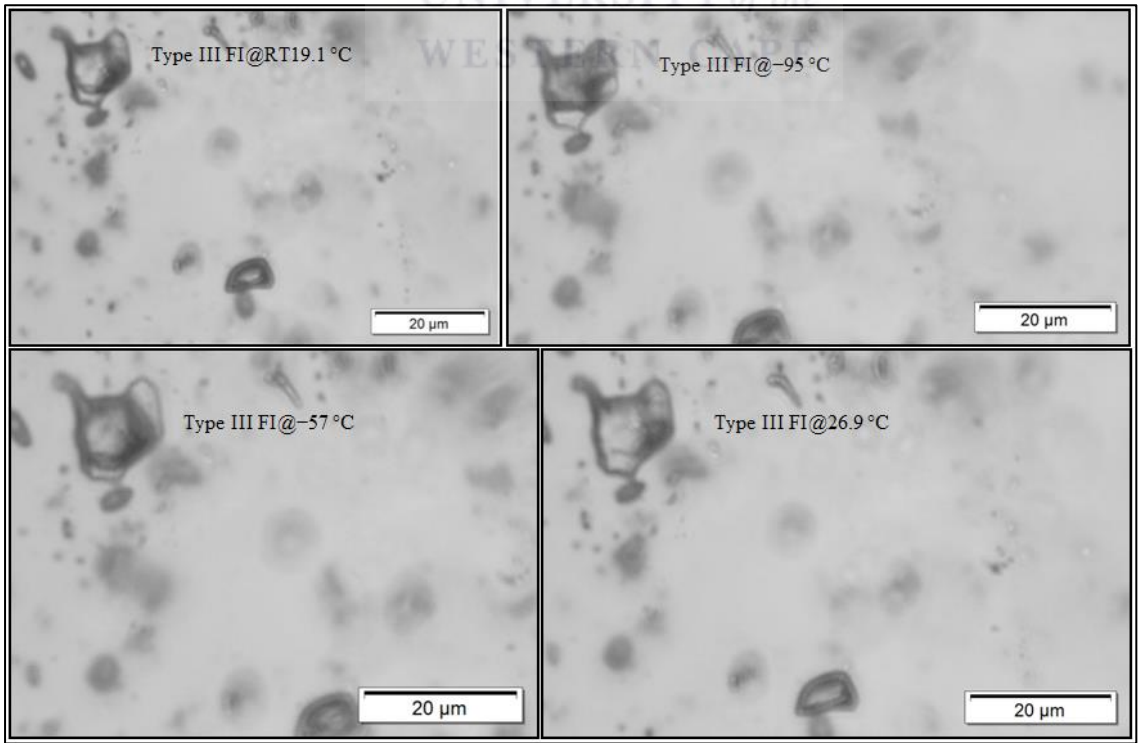

Fig. B4. Chip T14A: Type III (Carbonic−rich) fluid inclusion at various temperatures. Depicting Mono−phase after homogenization at 26.9 °C and 2−phases at room temperature (19.1 °C).

Fig. B5. Chip T14A: Type III (Carbonic−rich) fluid inclusion at various temperatures. Depicting Mono−phase after homogenization at 26.8 °C and 2−phases at room temperature (19.1 °C).

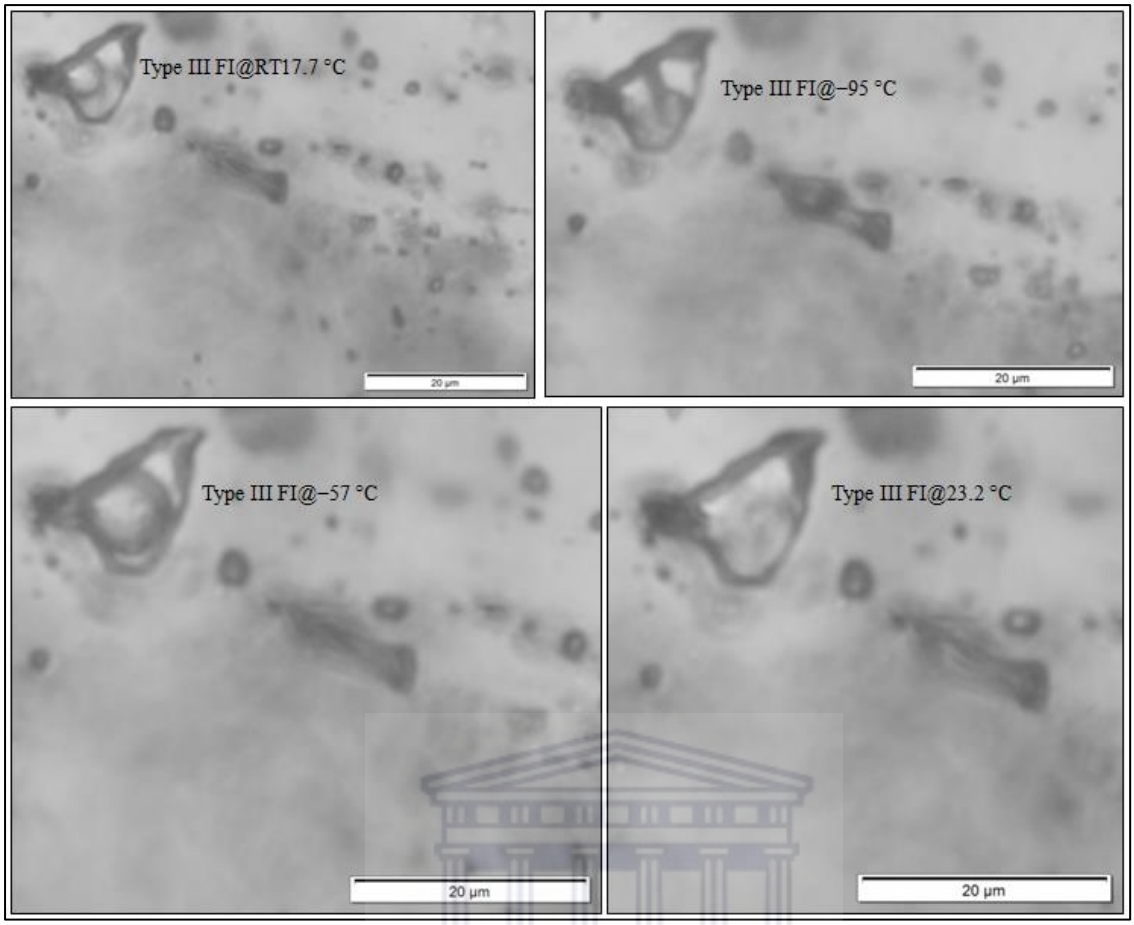

Fig. B6. Chip T14A: Type III (Carbonic−rich) fluid inclusion at various temperatures. Depicting Mono−phase after homogenization at 23.2 °C and 2−phases at room temperature (17.7 °C).

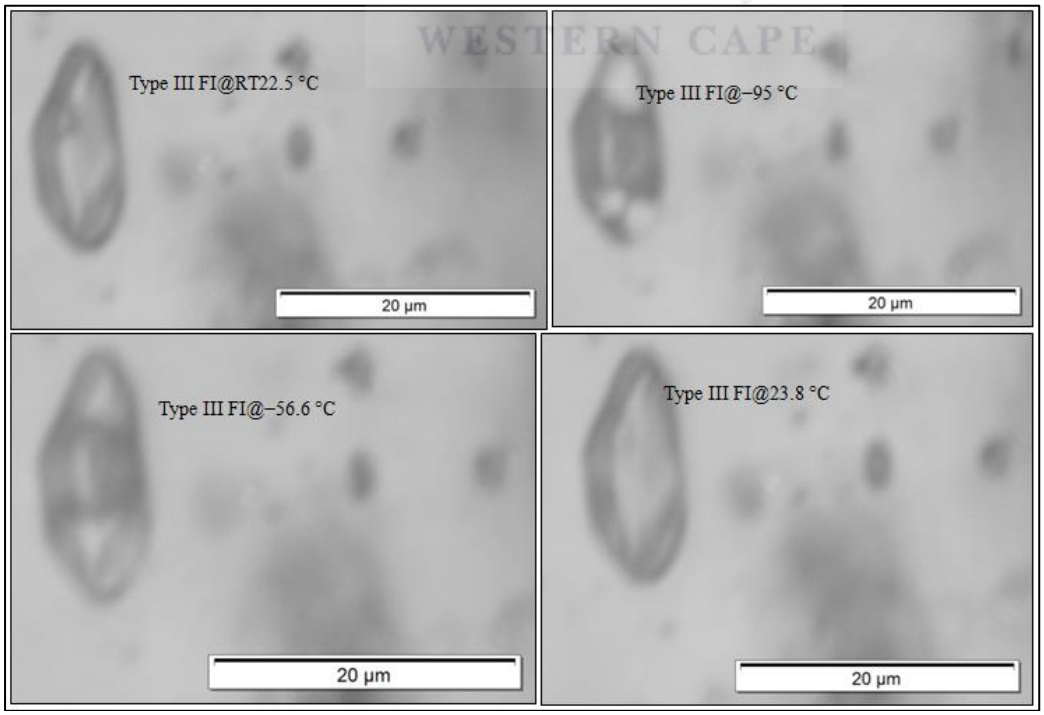

Fig. B7. Chip T14A: Type III (Carbonic−rich) fluid inclusion at various temperatures. Depicting Mono−phase after homogenization at 23.8 °C and 2−phases at room temperature (22.5 °C).

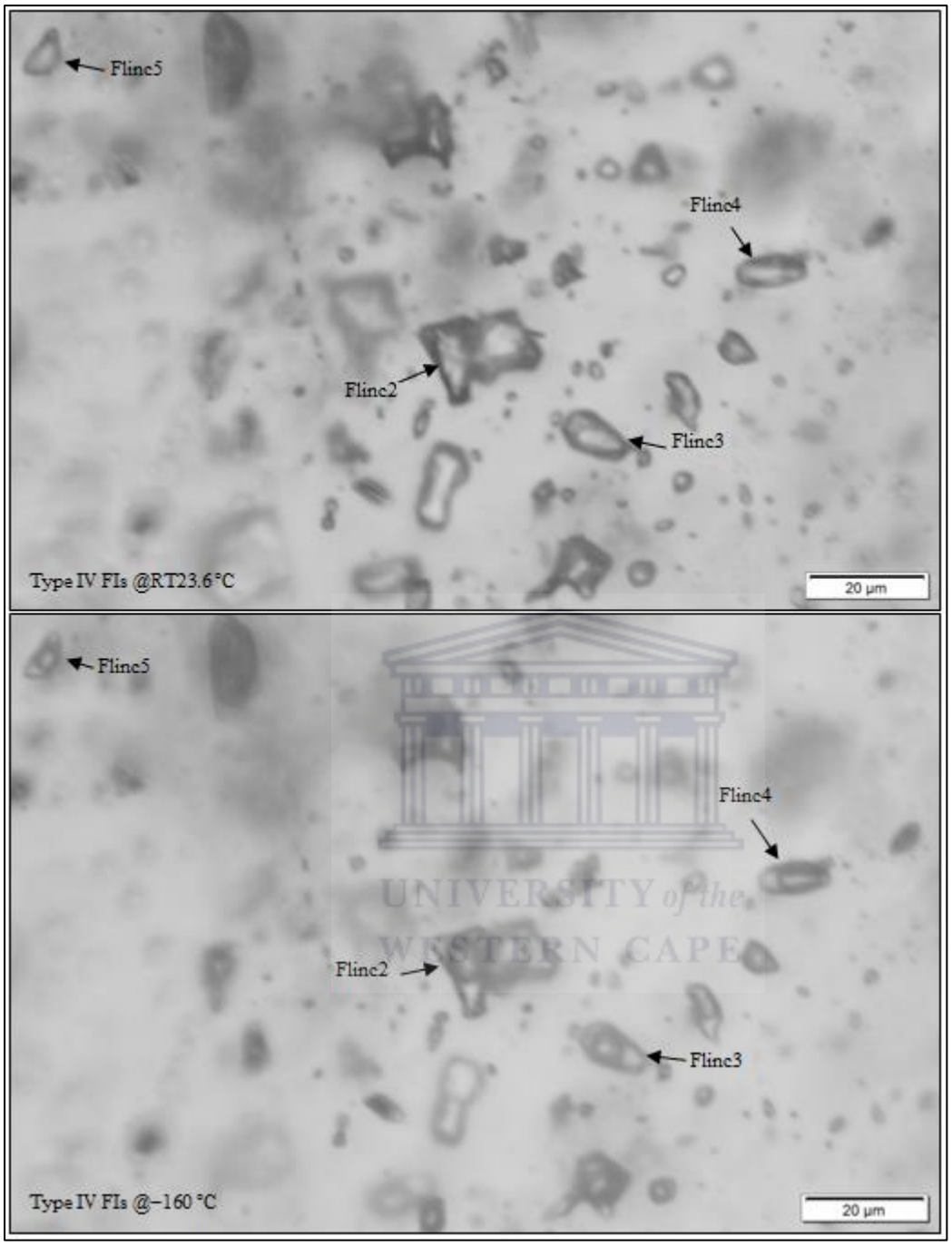

Fig. B8. Chip T15A: Type IV (Methane−rich) fluid inclusions at various temperatures. Depicting Mono−phases at room temperature (23.6 °C) and 2−phases at low temperature (−160 °C).

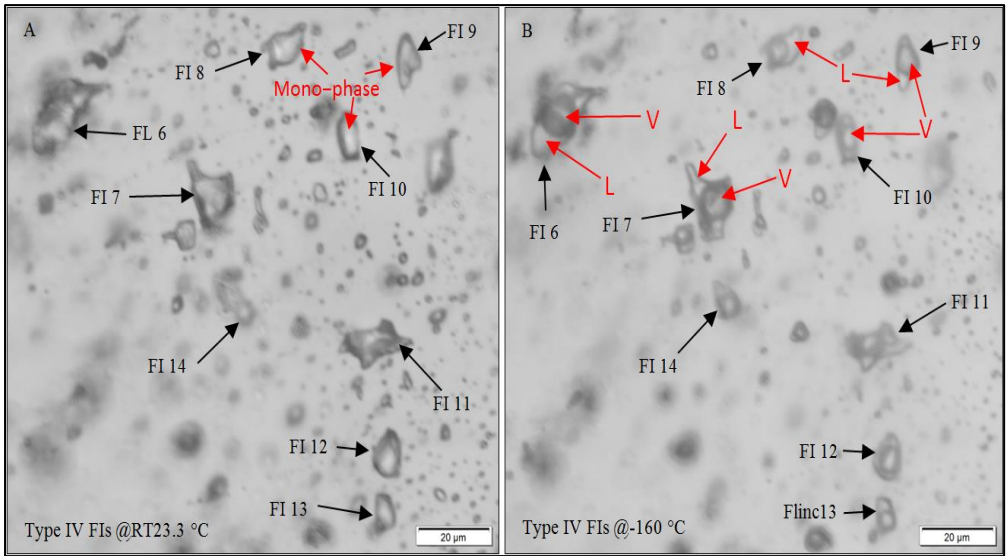

Fig. B9. Photomicrographs from Chip T15BaseA showing type IV (CH_4-rich) fluid inclusions at different temperatures. The inclusions are mono-phase at room temperature (23.3°C) and bi-phase at low temperature (−160°C). Noteworthy is the pervasiveness of the Type IV fluid inclusions.

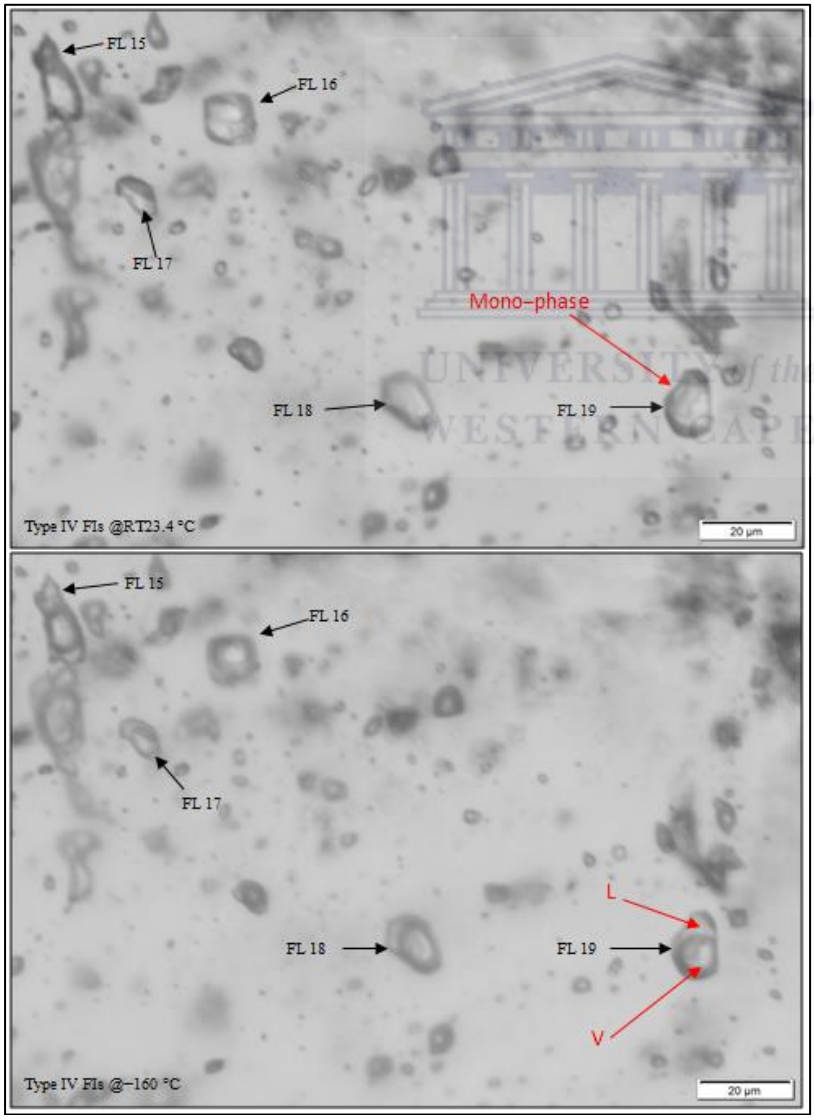

Fig. B10. Chip T15A: Type IV (Methane−rich) fluid inclusions at various temperatures. Depicting Mono−phases at room temperature (23.4 °C) and 2−phases at low temperature (−160 °C).

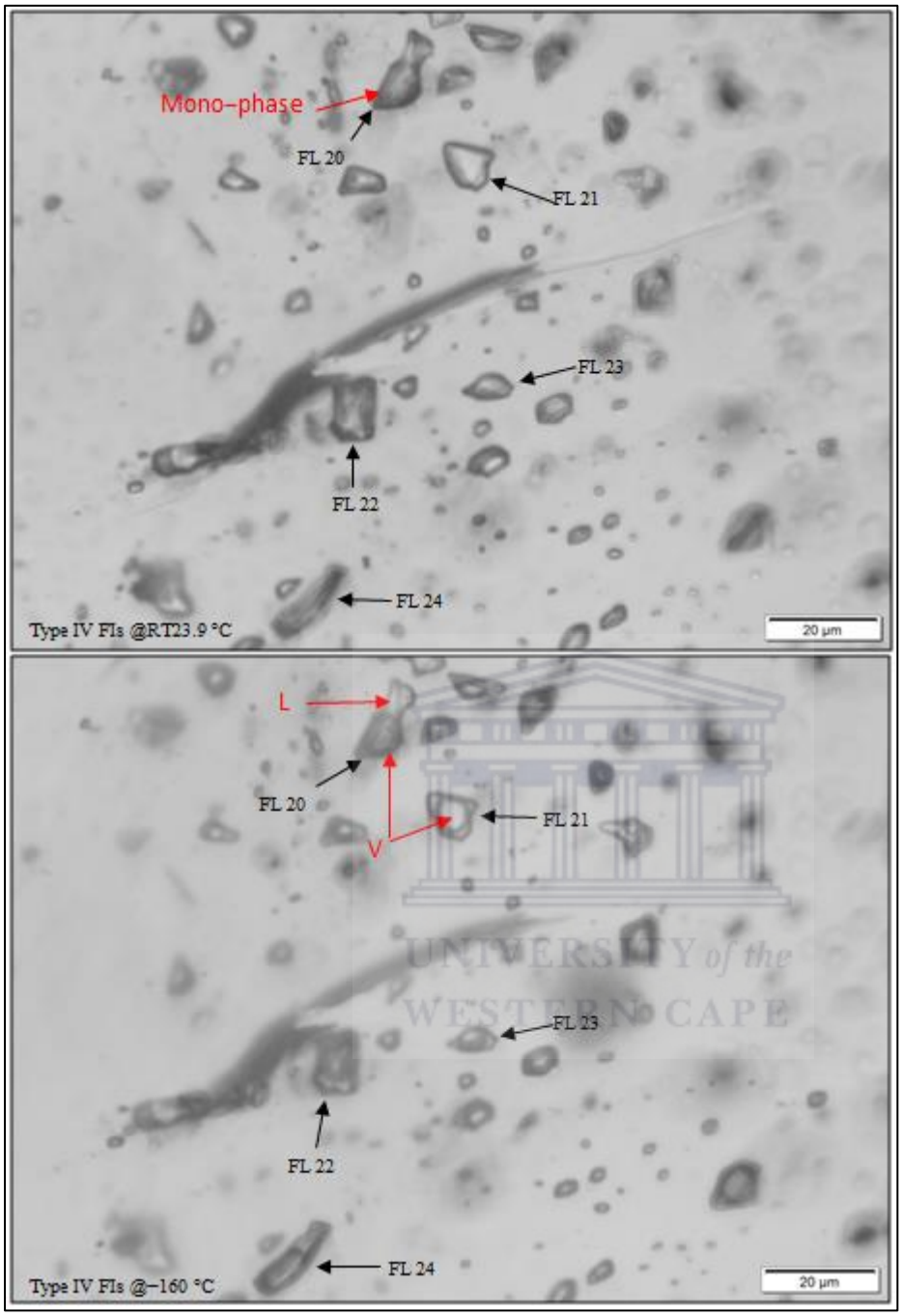

Fig. B11. Chip T15A: Type IV (Methane−rich) fluid inclusions at various temperatures. Depicting Mono−phases at room temperature (23.9 °C) and 2−phases at low temperature (−160 °C).

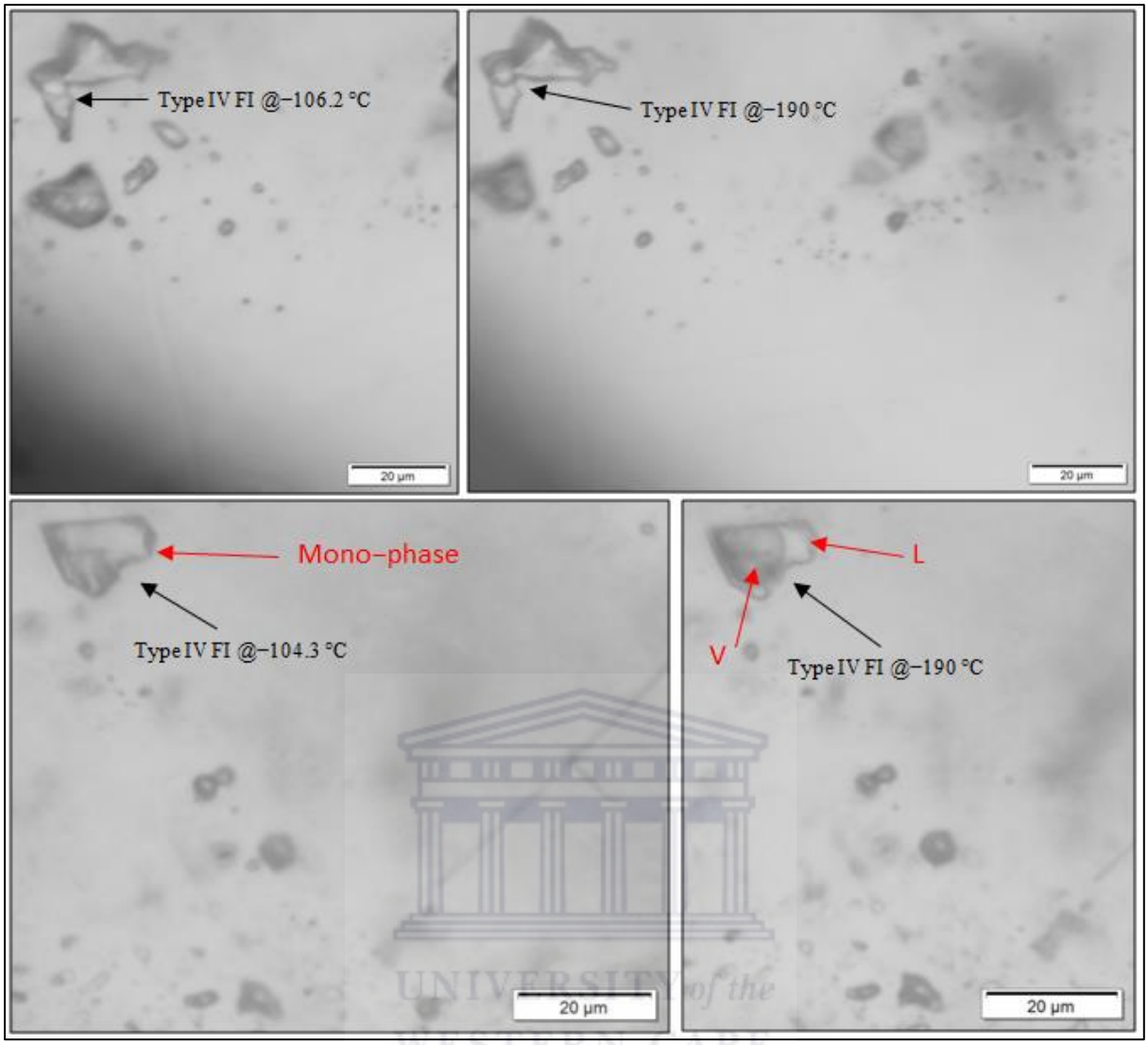

Fig. B12. Chip T15BaseA: Type IV (Methane−rich) fluid inclusions at various temperatures. Depicting Mono−phases at their homogenization temperatures and 2−phases at lower temperature (−190 °C).

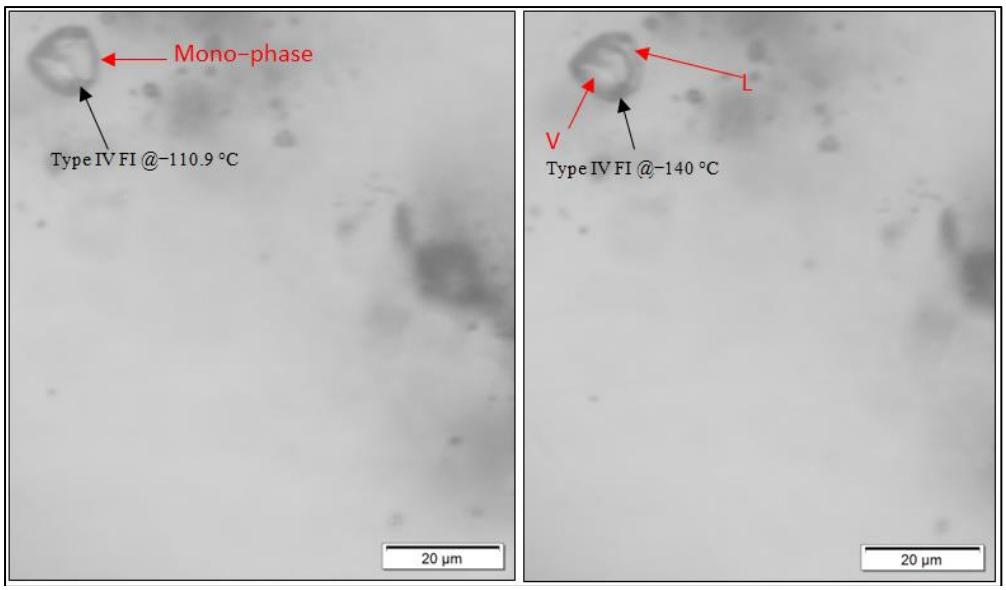

Fig. B13. Chip T15BaseA: Type IV (Methane−rich) fluid inclusions at different temperatures. Depicting Mono−phase at its homogenization temperature (−110.9 °C) and 2−phases at a lower temperature (−140 °C).

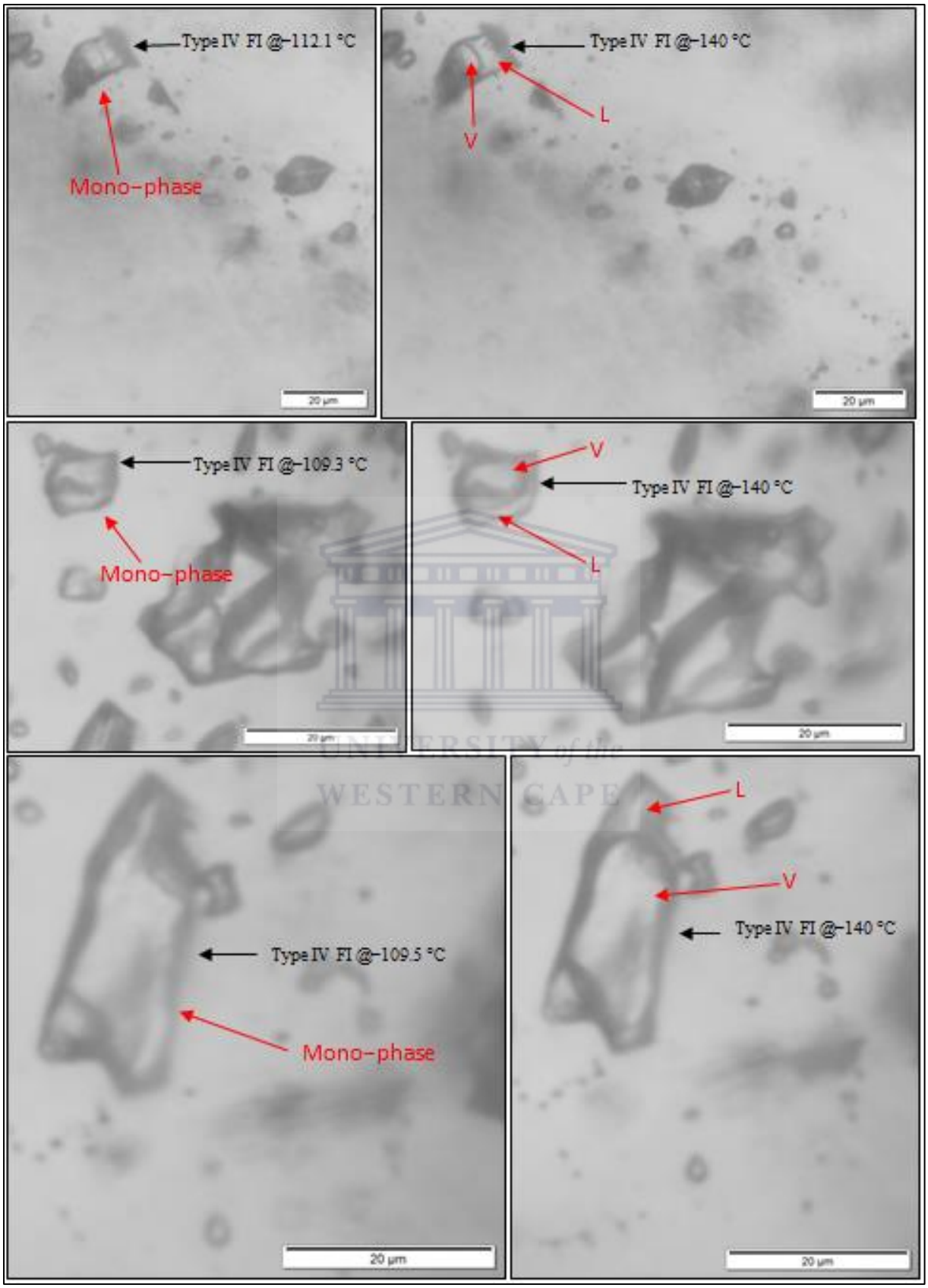

Fig. B14. Chip T15BaseA: Type IV (Methane−rich) fluid inclusions at various temperatures. Depicting Mono−phases at their homogenization temperatures and 2−phases at lower temperature (−140 °C).

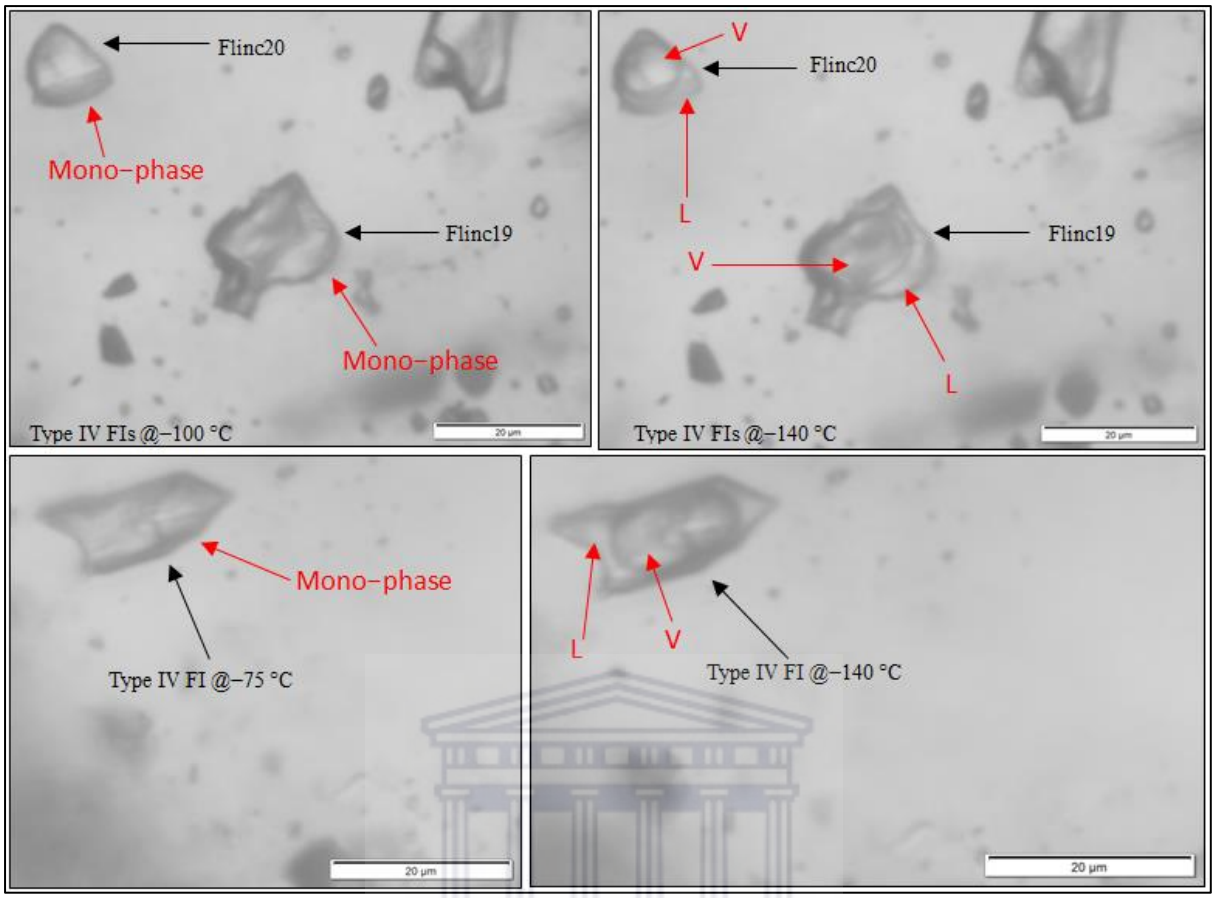

Fig. B15. Chip T15BaseA: Type IV (Methane−rich) fluid inclusions at various temperatures. Depicting Mono−phases above their homogenization temperatures and 2−phases at lower temperature (−140 °C).

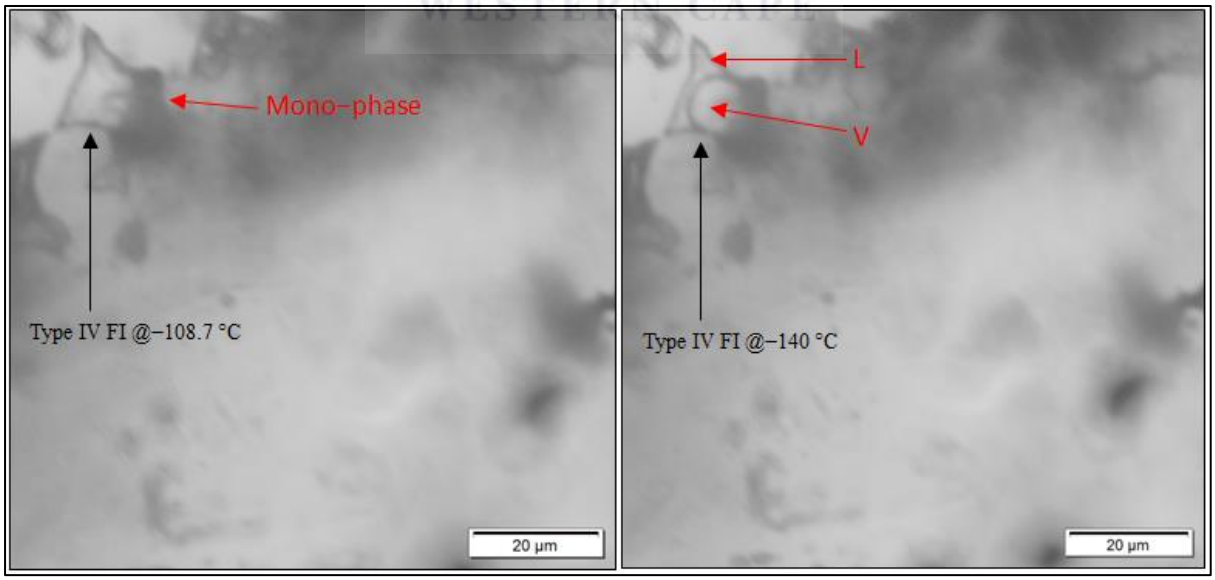

Fig. B16. Chip T15NTA: Type IV (Methane−rich) fluid inclusions at different temperatures. Depicting Mono−phase at the homogenization temperature (−108.7 °C) and 2−phases at lower temperature (−140 °C).

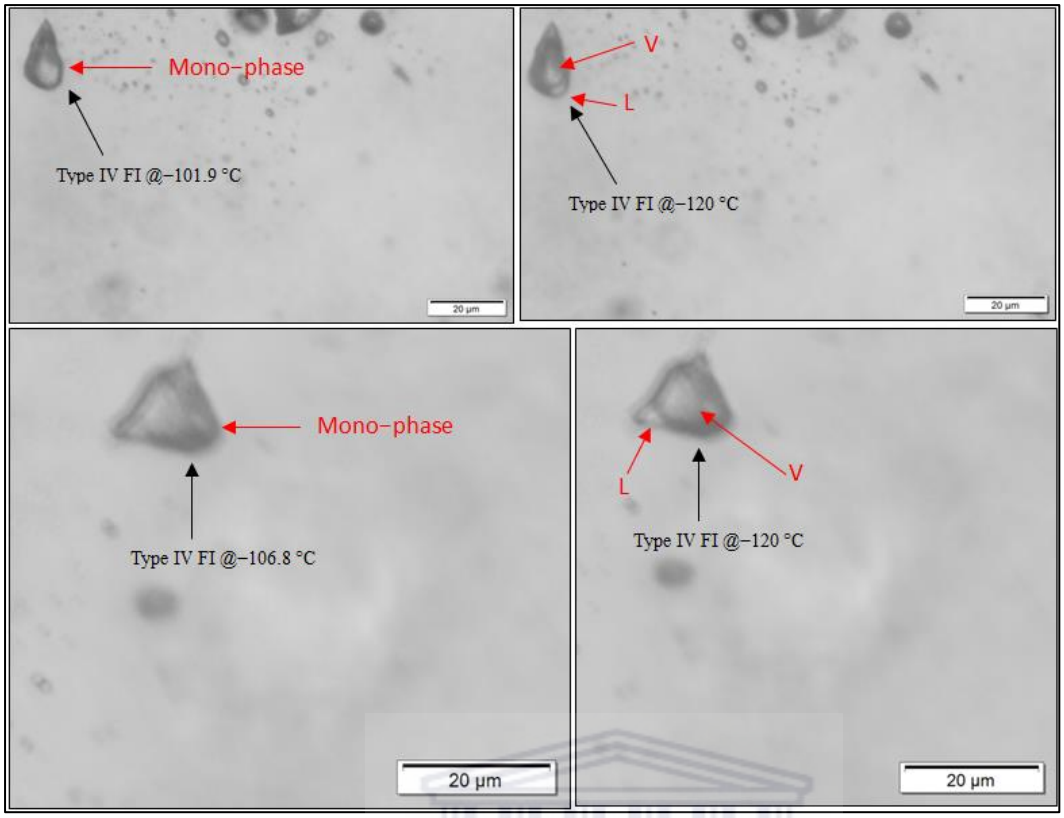

Fig. B17. Chip T15NTA: Type IV (Methane−rich) fluid inclusions at various temperatures. Depicting Mono−phases at their homogenization temperatures and 2−phases at lower temperature (−120 °C).

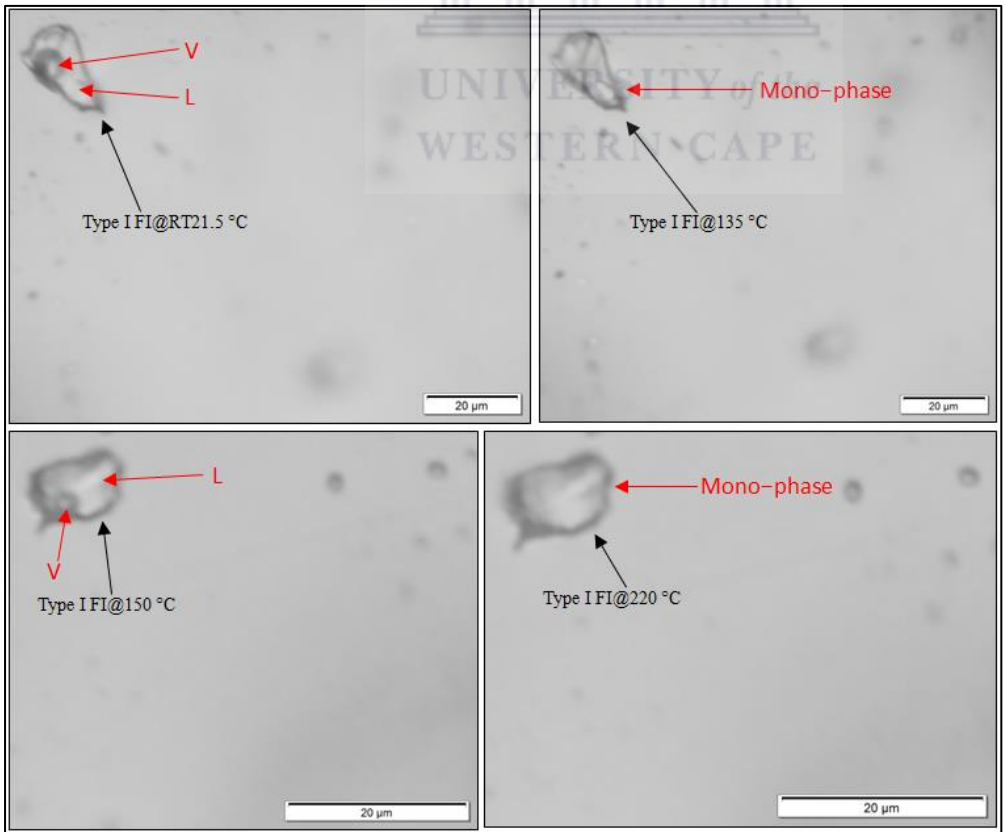

Fig. B18. Chip T4ASE: Type I (aqueous rich) fluid inclusions at various temperatures. Depicting Mono−phases at their homogenization temperatures and 2−phases at lower temperatures.

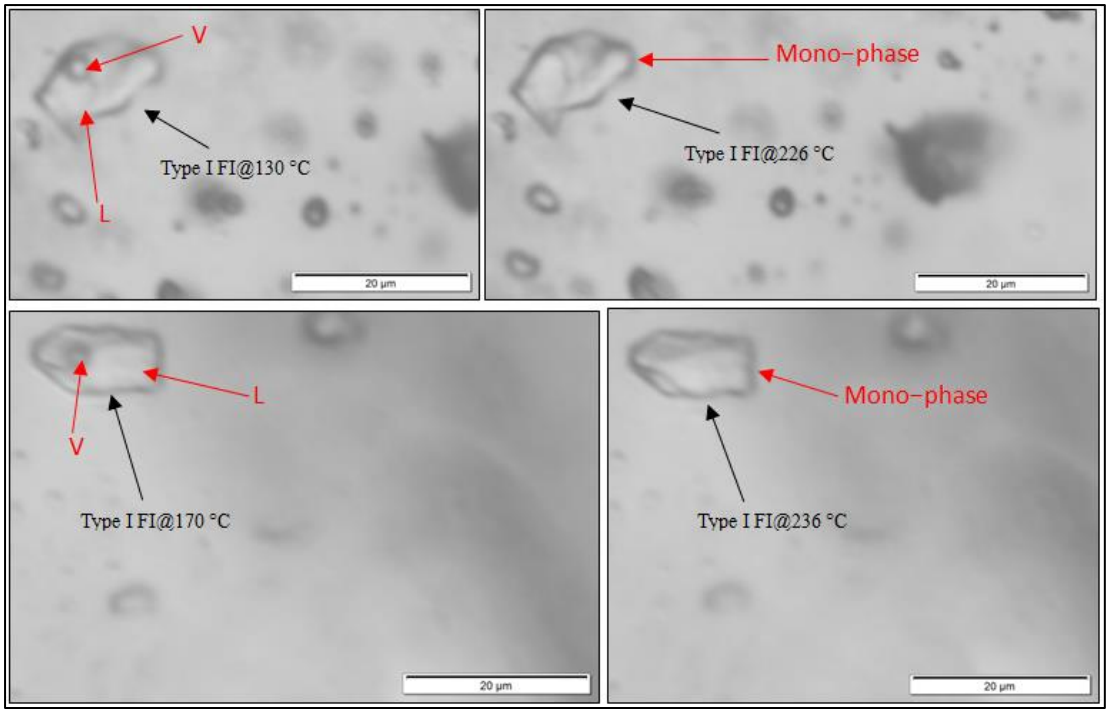

Fig. B19. Chip T4ASE: Type I (aqueous rich) fluid inclusions at various temperatures. Depicting Mono−phases at their homogenization temperatures and 2−phases at lower temperatures.

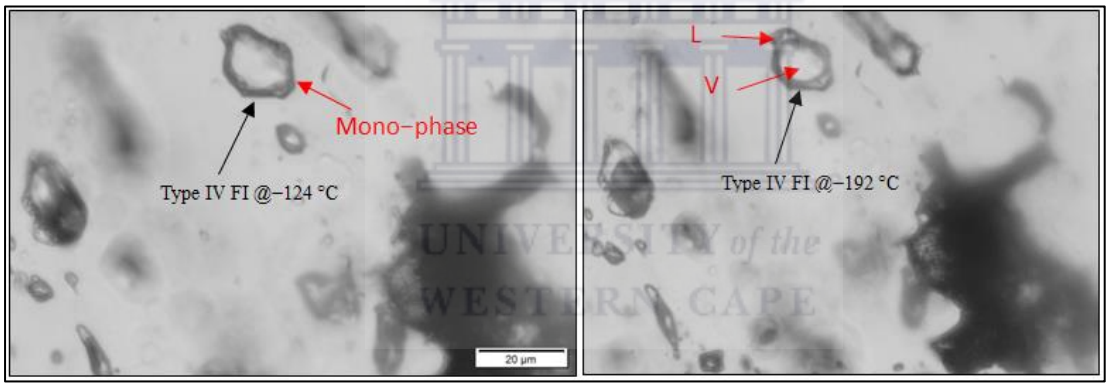

Fig. B20. Chip T4ASE: Type IV (Methane−rich) fluid inclusion at different temperatures. Depicting Mono−phase at its homogenization temperature (−124 °C) and 2−phase at lower temperature (−192 °C).

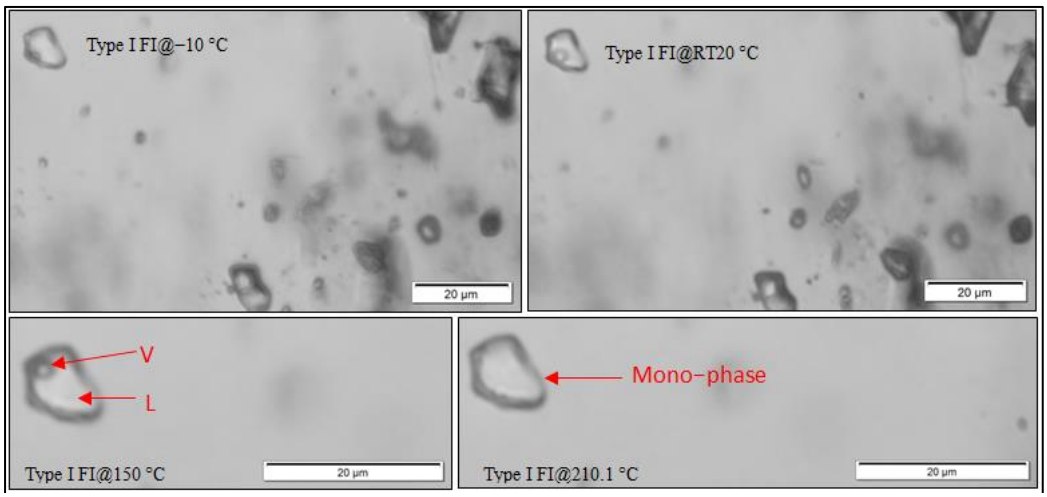

Fig. B21. Chip T4ASE: Type I (aqueous rich) fluid inclusion at various temperatures. Depicting Mono−phase at its homogenization temperature (210.1 °C) and 2−phases at lower temperatures.

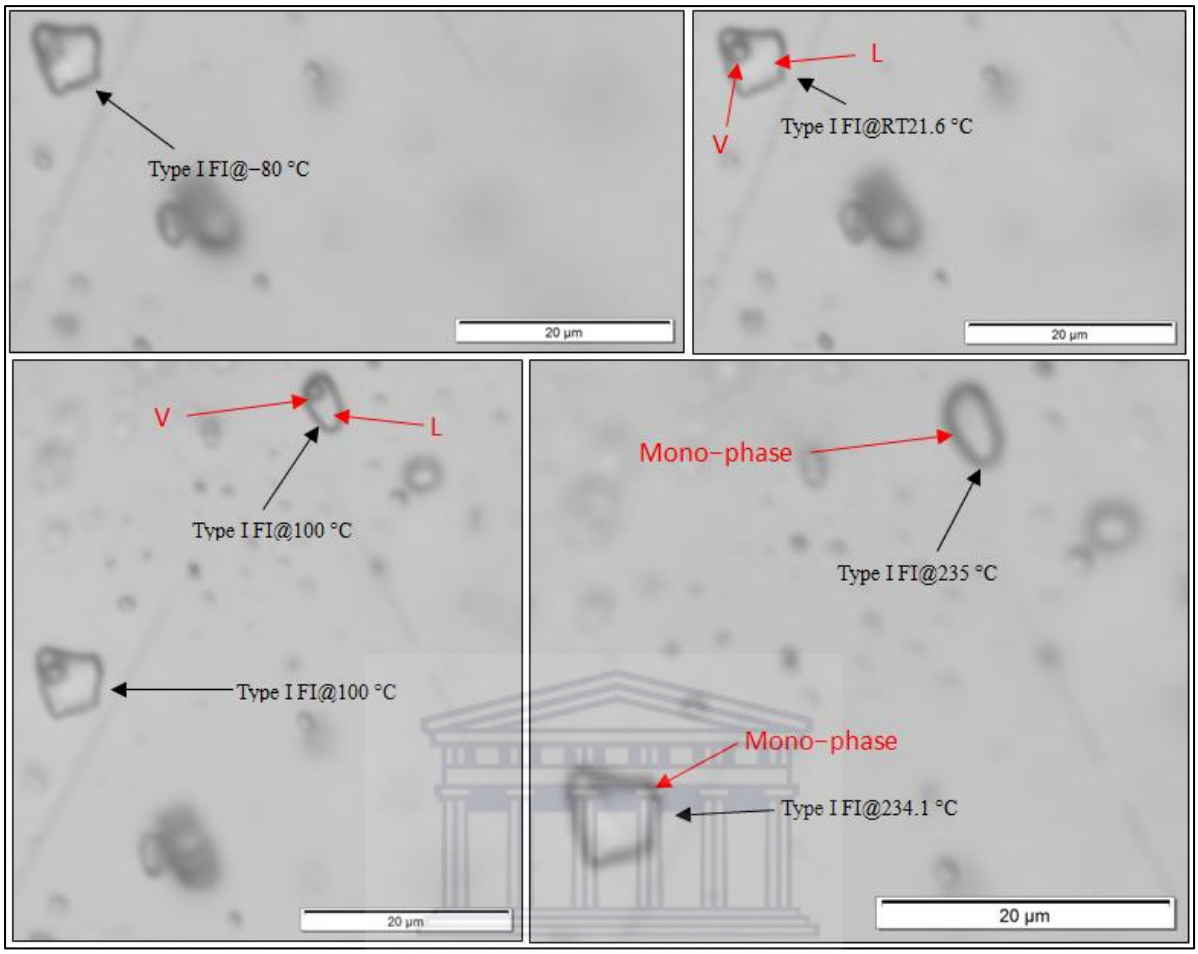

Fig. B22. Chip T4ASE: Type I (aqueous rich) fluid inclusions at various temperatures. Depicting Mono−phases at their homogenization temperatures and 2−phases at lower temperatures.

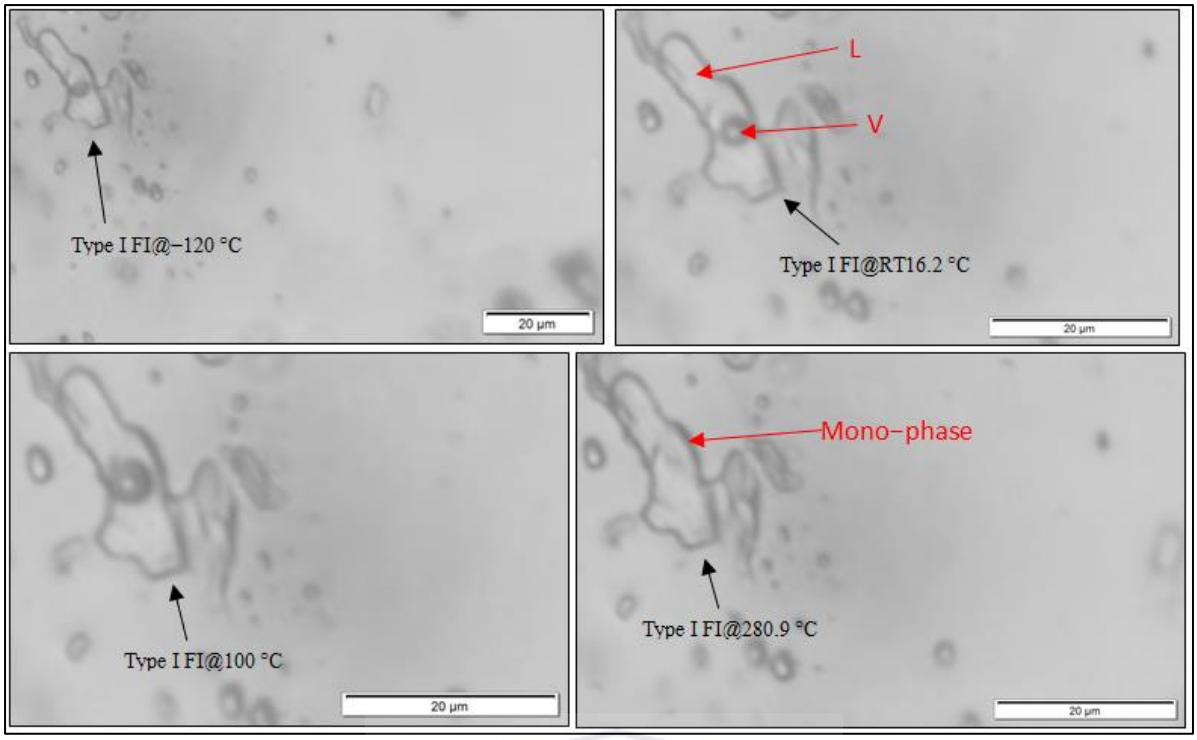

Fig. B23. Chip T4ASE: Type I (aqueous rich) fluid inclusion at various temperatures. Depicting Mono−phase at its homogenization temperature (280.9 °C) and 2−phases at lower temperatures.

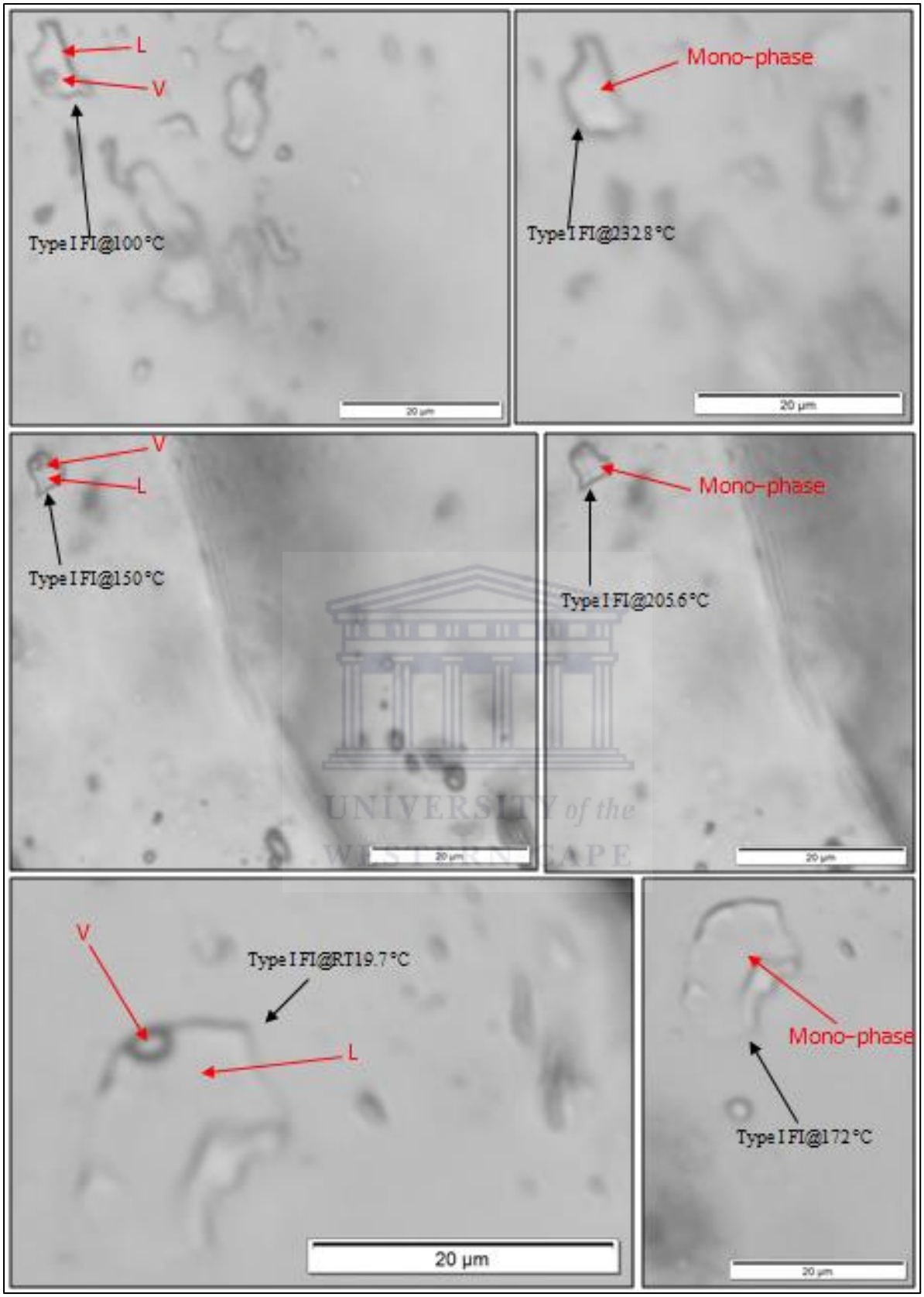

Fig. B24. Chip T4ASE: Type I (aqueous rich) fluid inclusions at various temperatures. Depicting Mono−phases at their homogenization temperatures and 2−phases at lower temperatures.

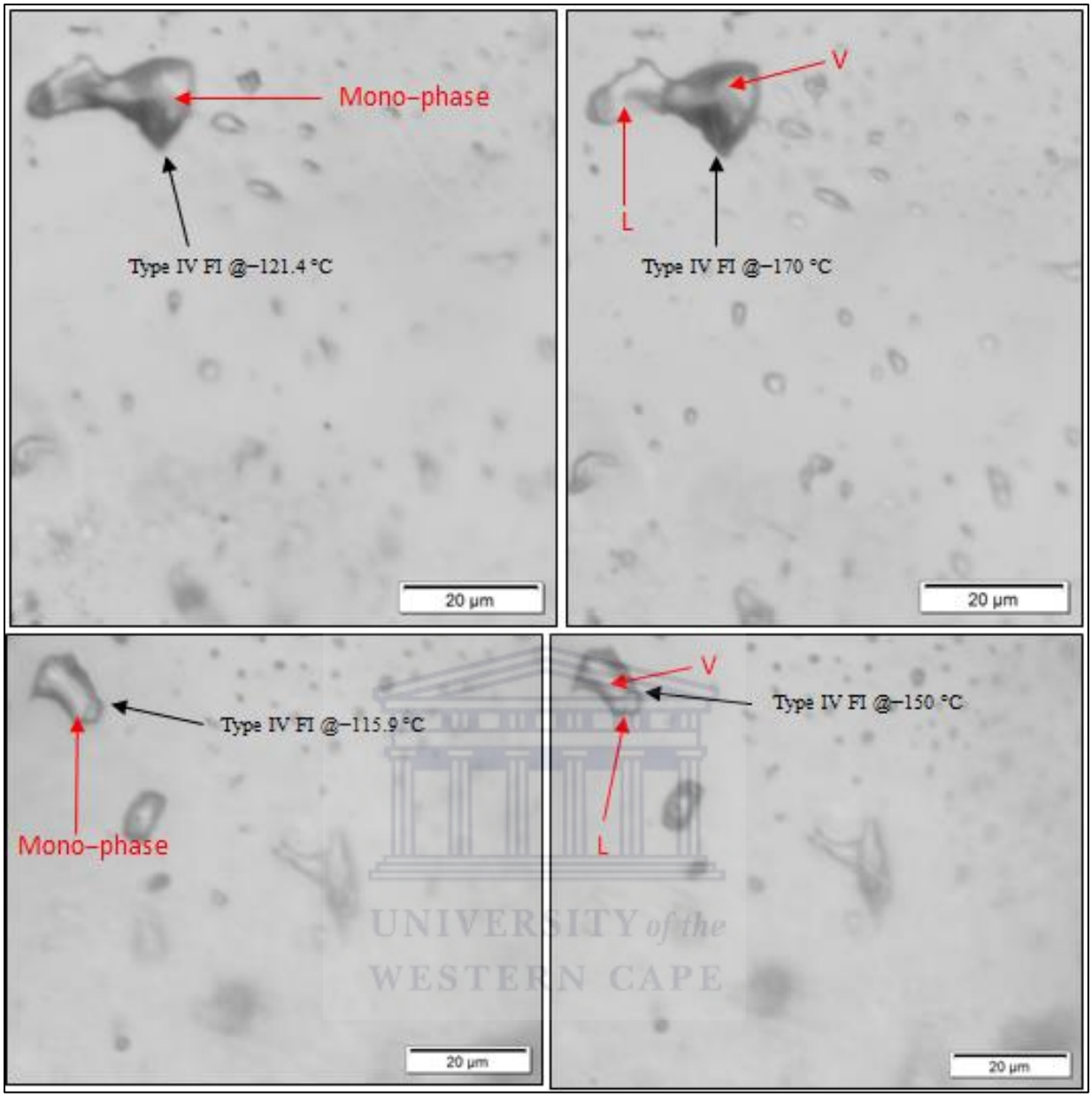

Fig. B25. Chip T4B: Type IV (Methane−rich) fluid inclusions at various temperatures. Depicting Mono−phases at their homogenization temperatures and 2−phases at lower temperatures.

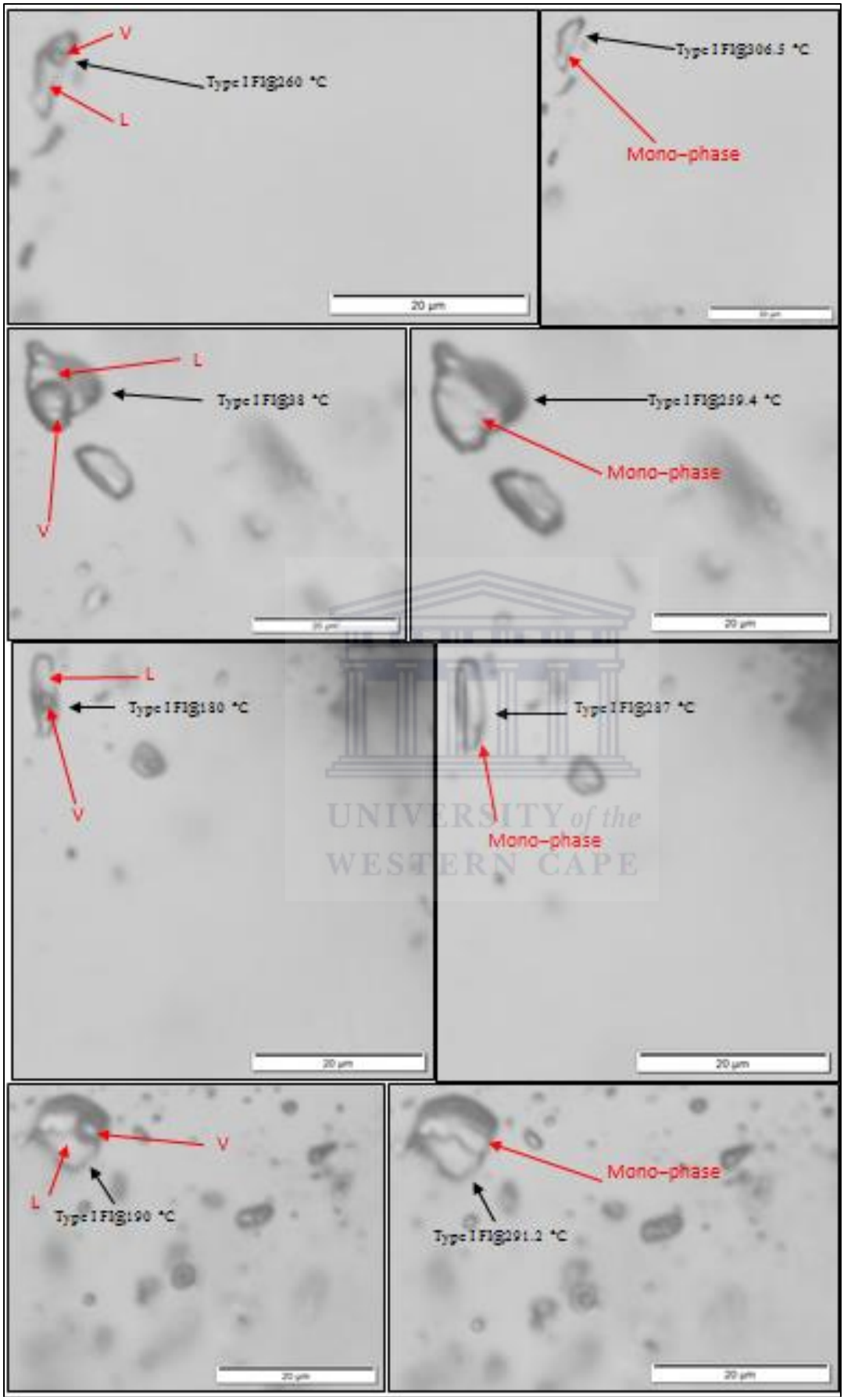

Fig. B26. Chip T4A CWest: Type I (aqueous rich) fluid inclusions at various temperatures. Depicting Mono−phases at their homogenization temperatures and 2−phases at lower temperatures.

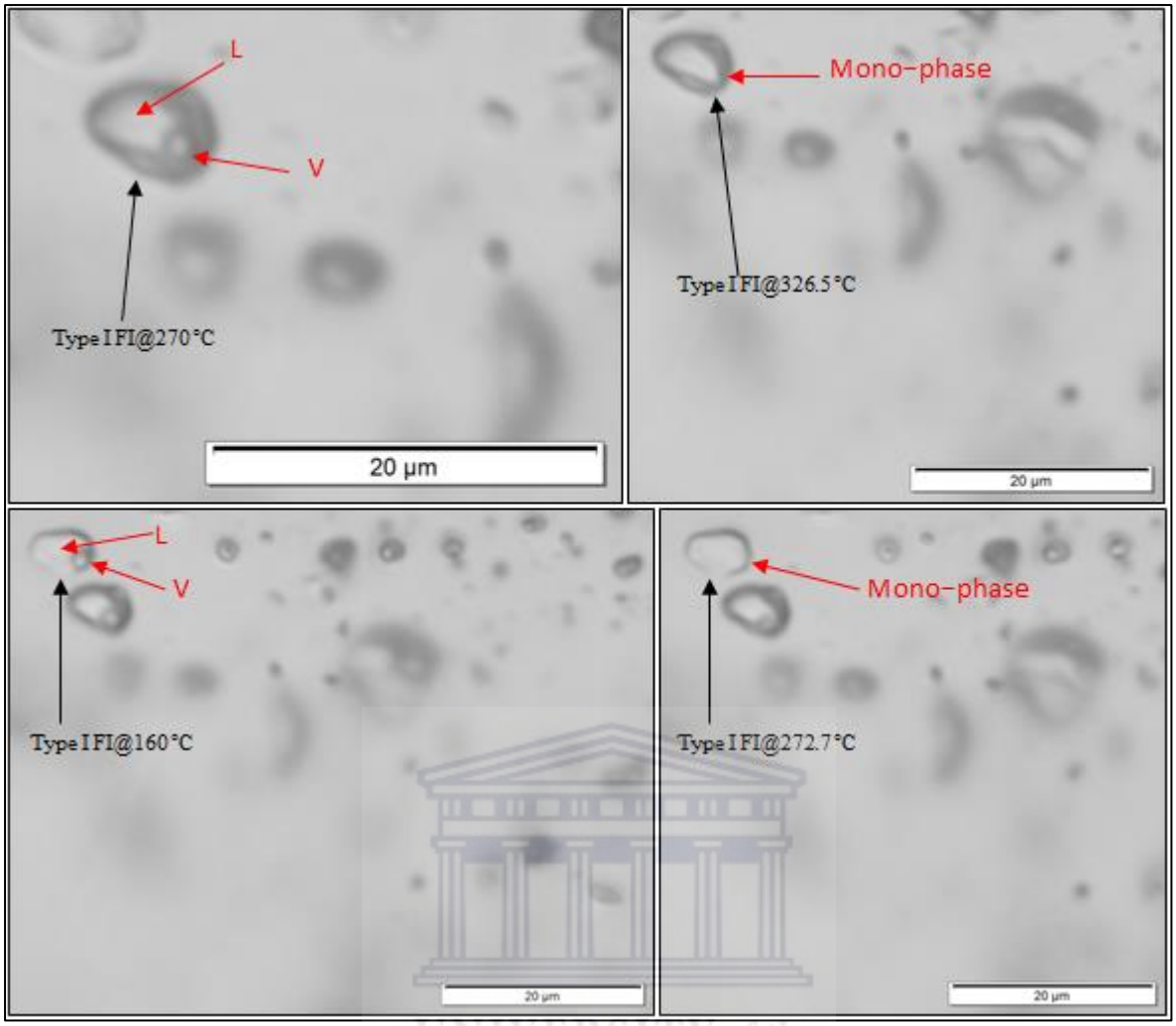

Fig. B27. Chip T4A CWest: Type I (aqueous rich) fluid inclusions at various temperatures. Depicting Mono−phases at their homogenization temperatures and 2−phases at lower temperatures.

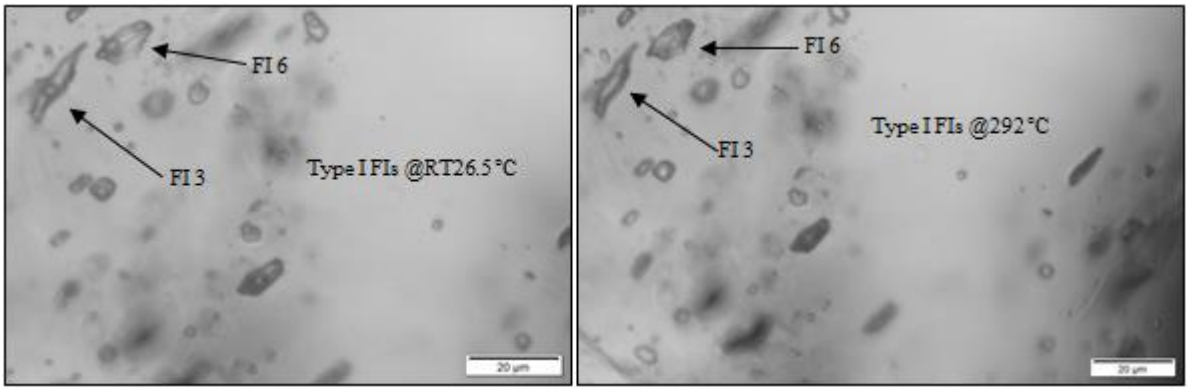

Fig. B28. Chip NO2A: Type I (aqueous rich) fluid inclusions at different temperatures. Depicting Mono−phases at 292 °C which is above their homogenization temperatures and 2−phases at room temperature (26.5 °C).

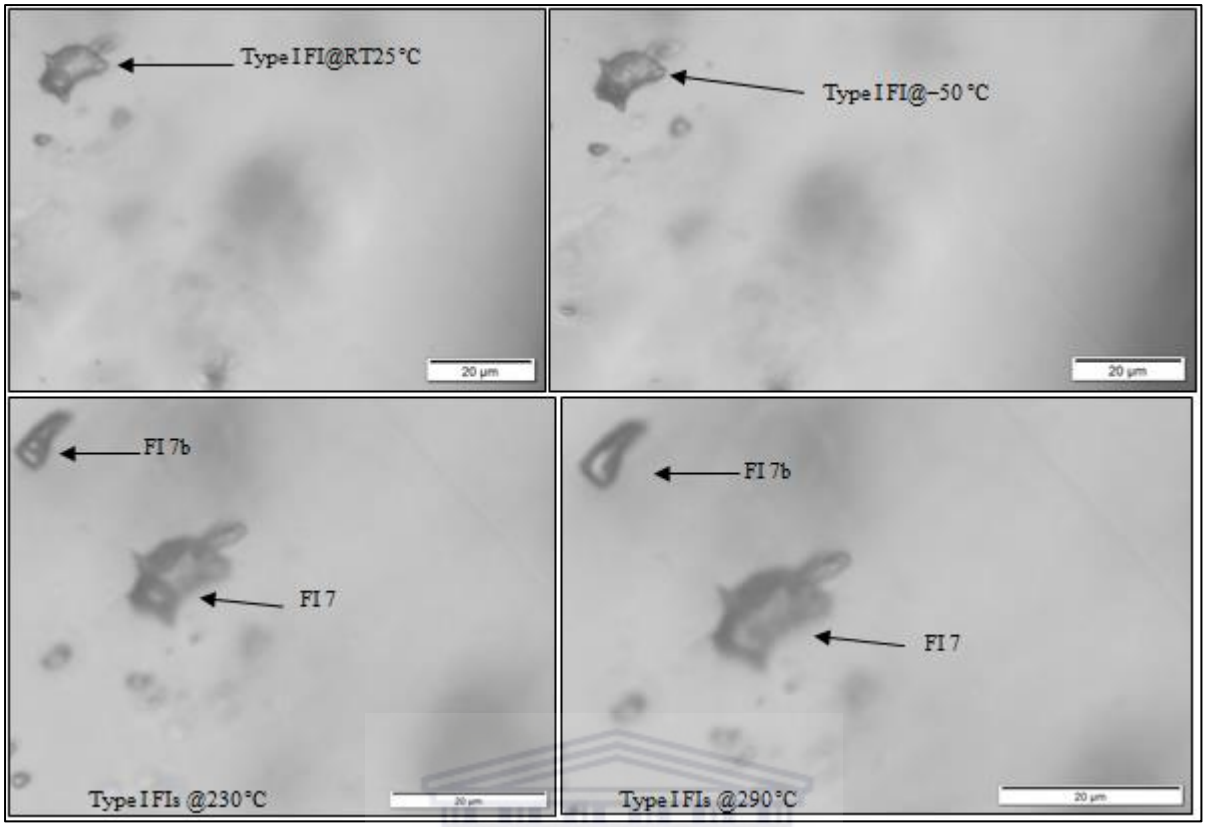

Fig. B29. Chip NO2A: Type I (aqueous rich) fluid inclusions at various temperatures. Depicting Mono−phases at 290 °C which is above their homogenization temperatures and 2−phases at lower temperatures.

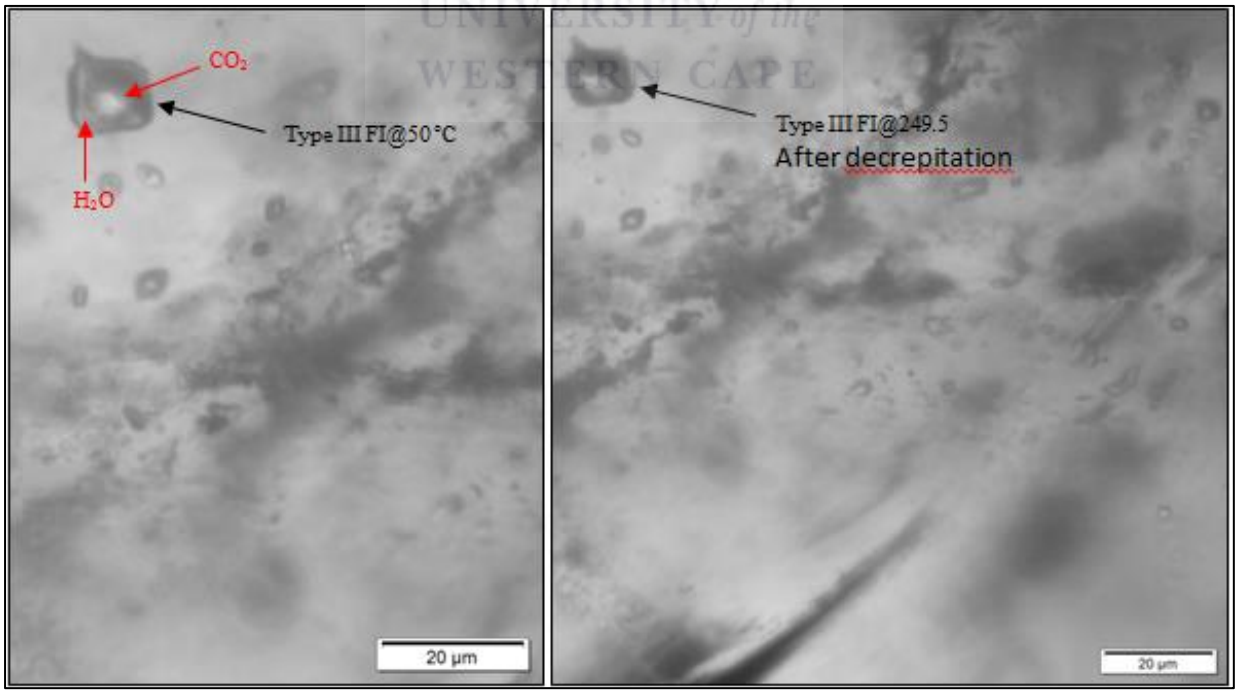

Fig. B30. Chip NO2A: Type III (aqueous−carbonic) fluid inclusion at different temperatures. Depicting 2−phases at a lower temperature at 50 °C and an image after decrepitation at 249.5 °C.

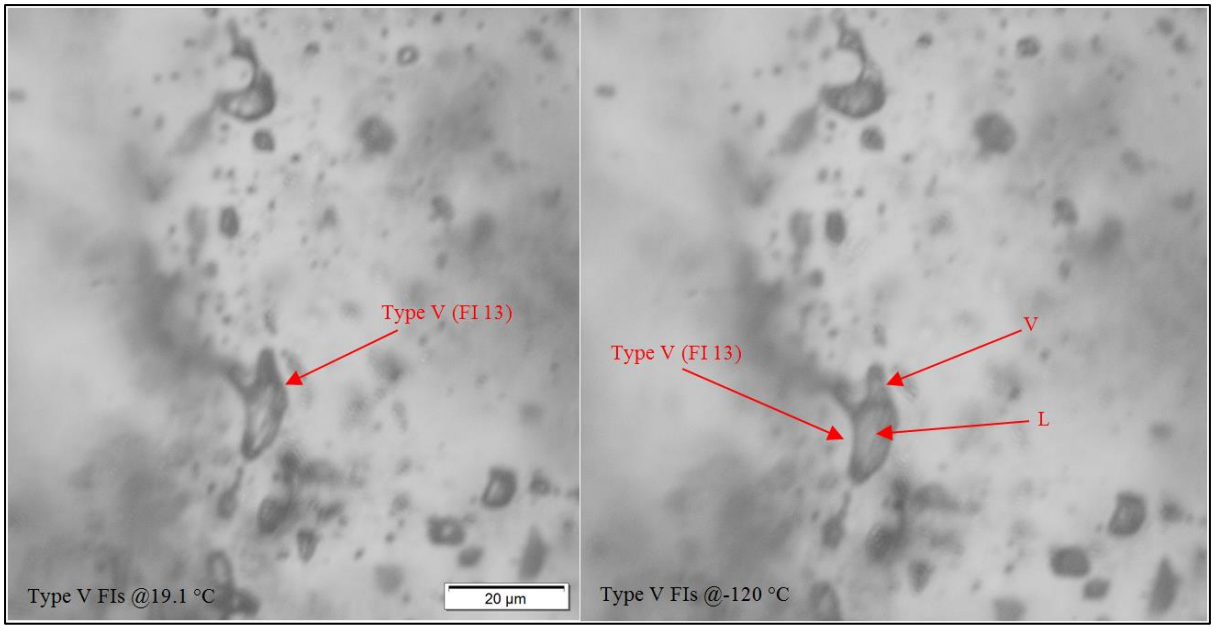

Fig. B31. Photomicrographs from Chip T14A showing type V fluid inclusions at different temperatures. A. Mono-phase inclusions at 19.1°C and B. Vapour present in the fluid inclusion at -120°C.

Appendix C: Fluid inclusion sketches

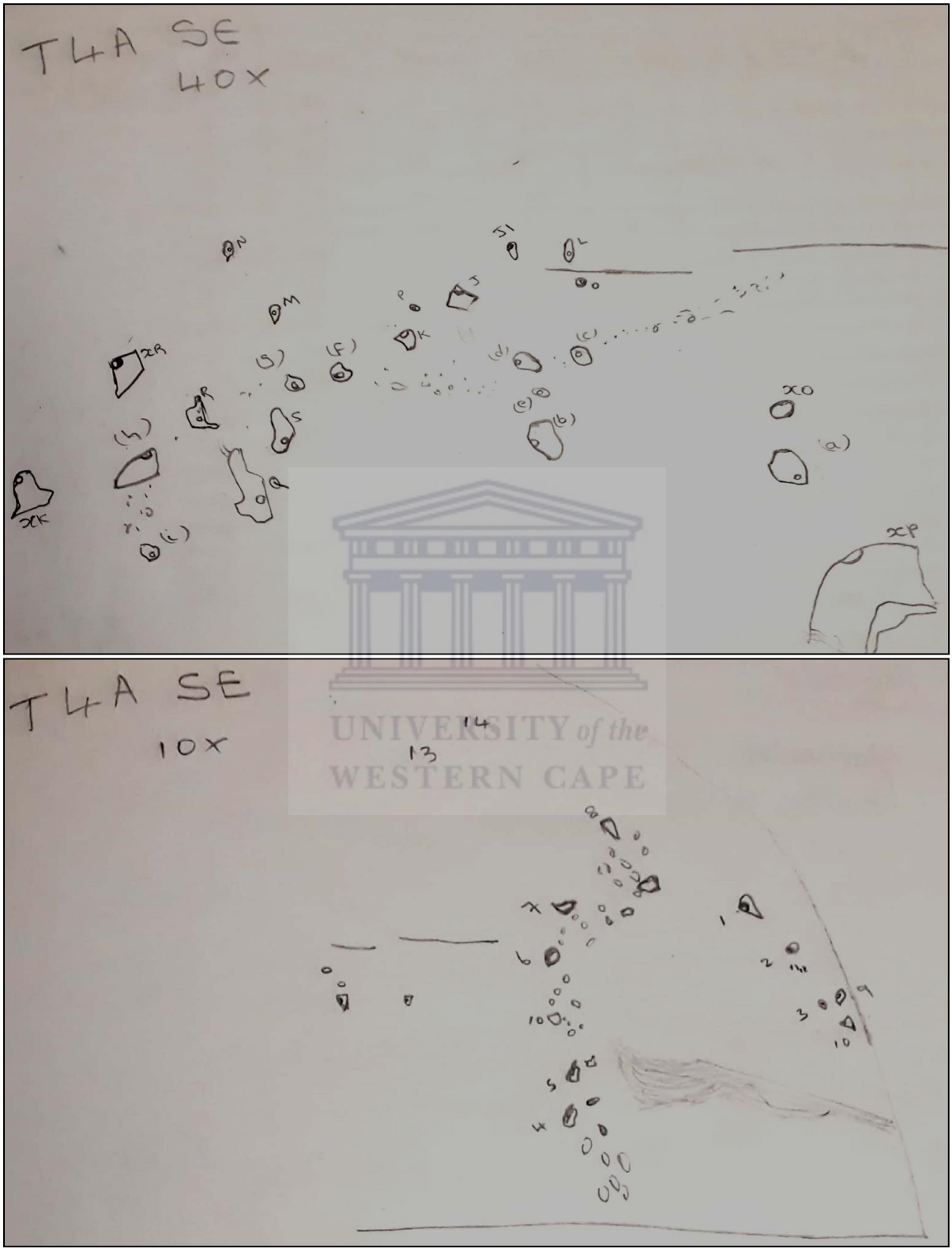

Fig. C1. Chip T4A SE: Parts of chip T4A showing trails of Type I fluid inclusions.

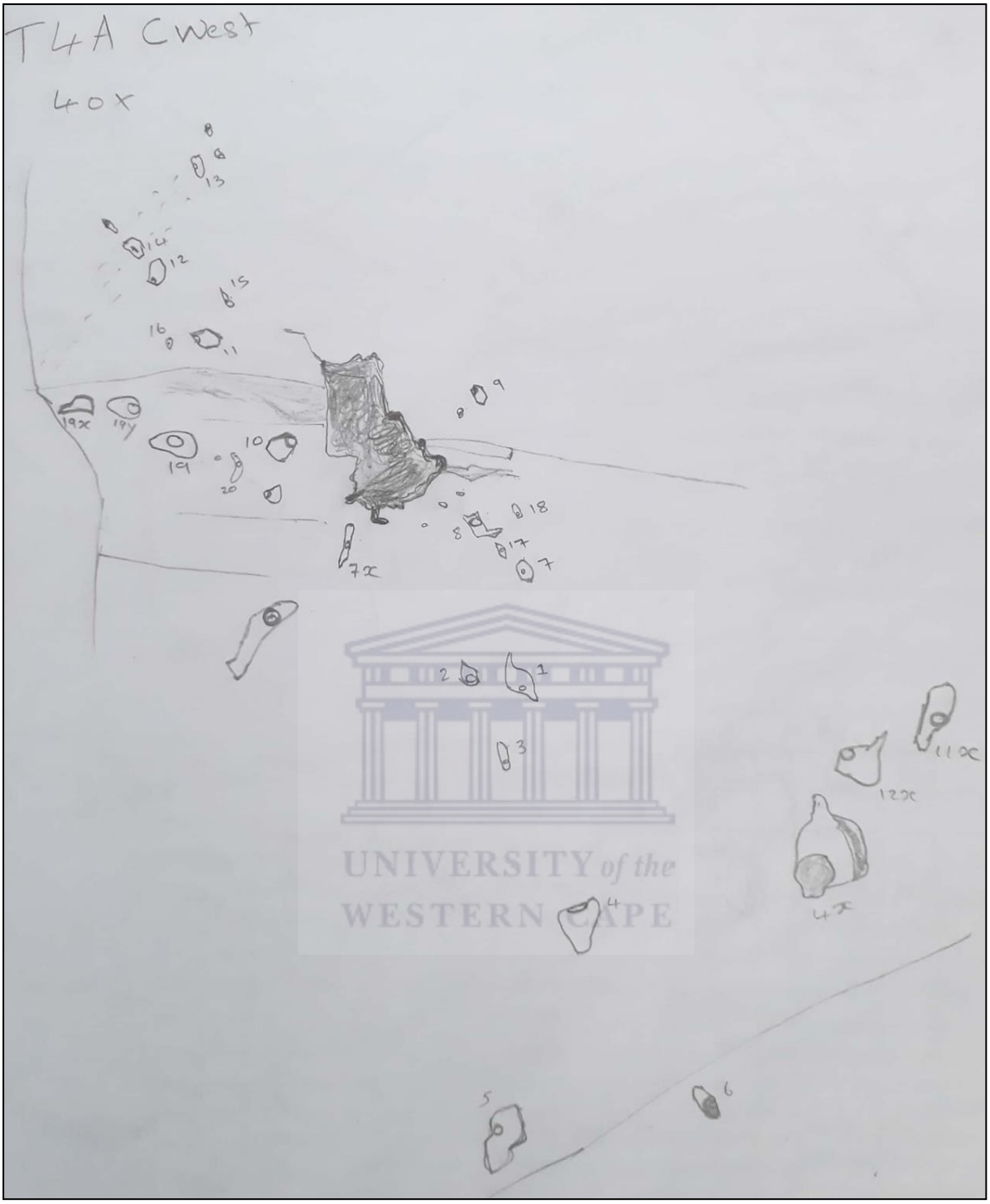

Fig. C2. Chip T4A CWest: Parts of chip T4A showing trails of Type I fluid inclusions (all marked are Type I fluid inclusions in exception of and 6 (type III).

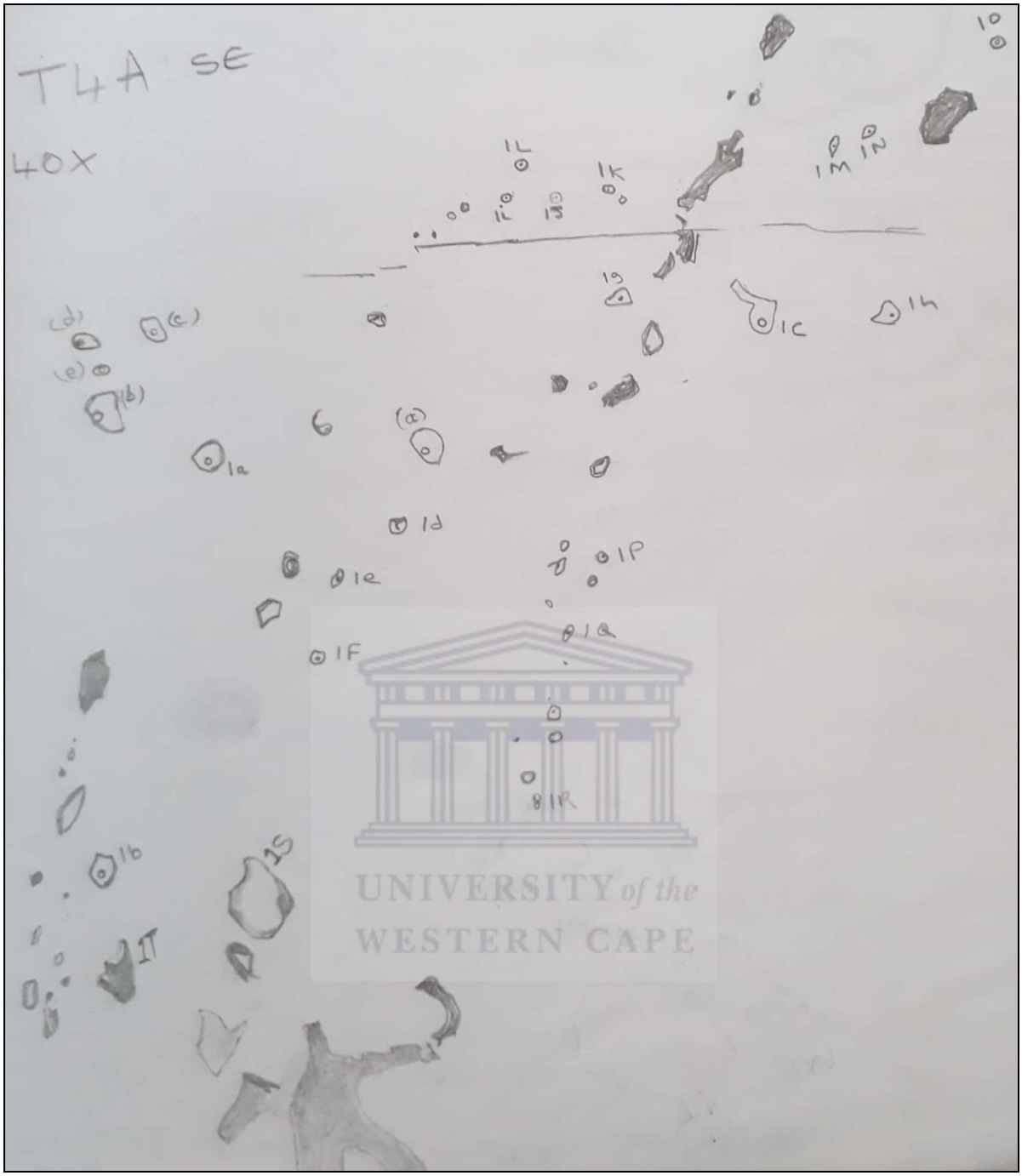

Fig. C3. Chip T4A SE: Part of chip T4A showing trails of Type I fluid inclusions (all marked are Type I fluid inclusions in exception of 1S and 1T (Type IV).

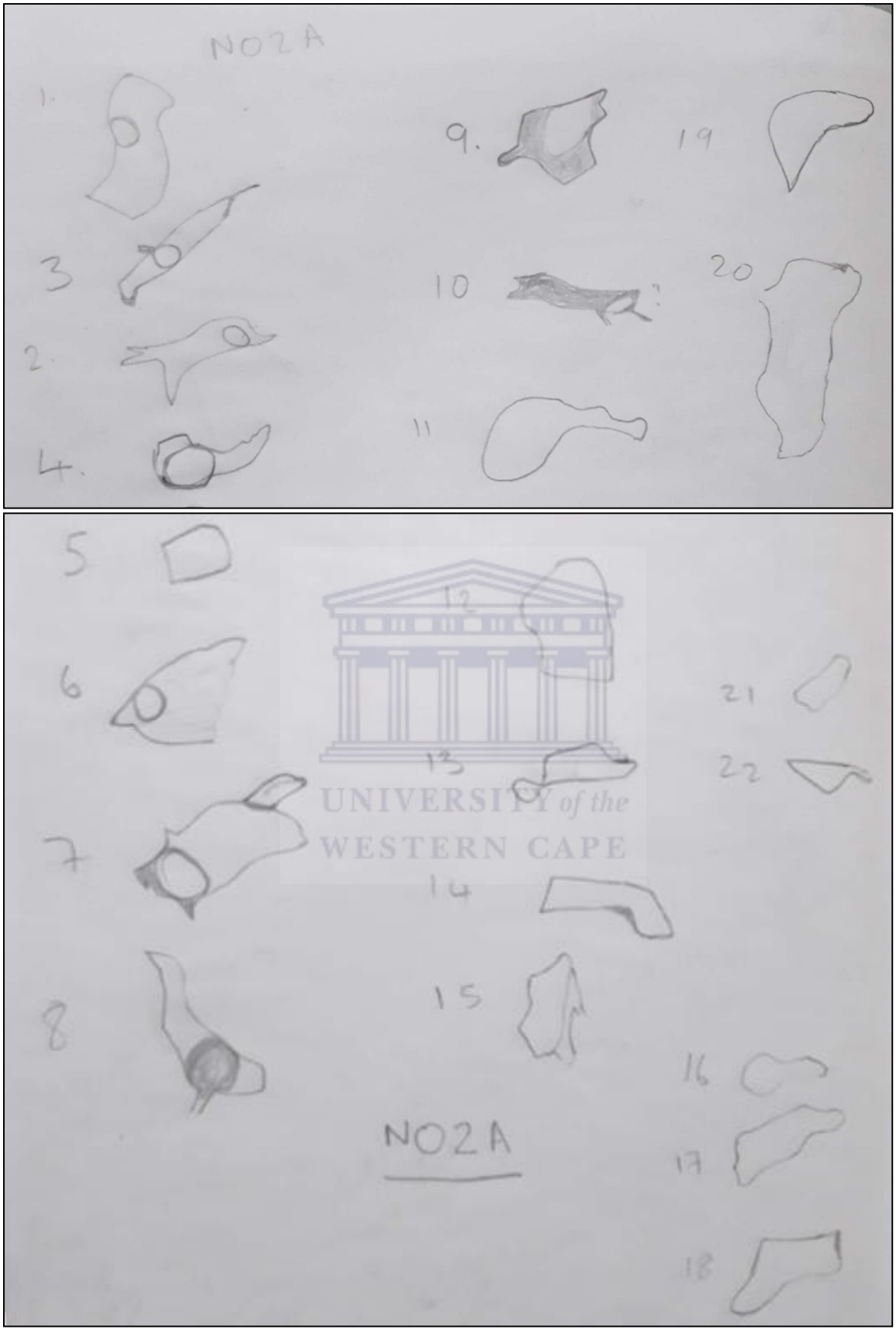

Fig. C4. Chip N02A: Schematic diagrams of 2−phase Type I fluid inclusions (1 − 3, 6 & 7); 2−phase Type III fluid inclusions (4, 8 & 9) and Mono−phase Type III fluid inclusion (5 & 10 − 22).

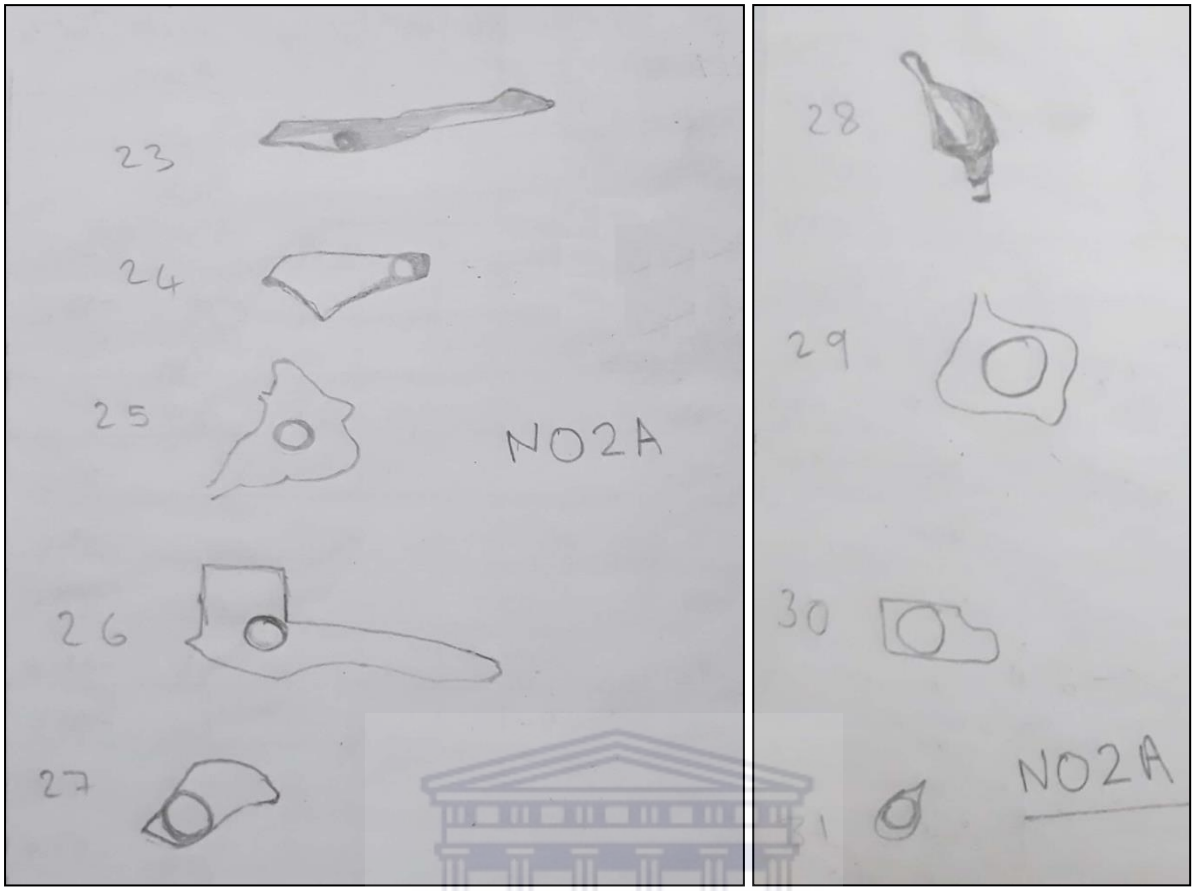

Fig. C5. Chip N02A: Schematic diagrams of 2−phase Type I fluid inclusions (23 – 26); 2−phase Type III fluid inclusion (27); Mono−phase Type III fluid inclusion (28) and 2−phase Type III fluid inclusions (29 – 31).

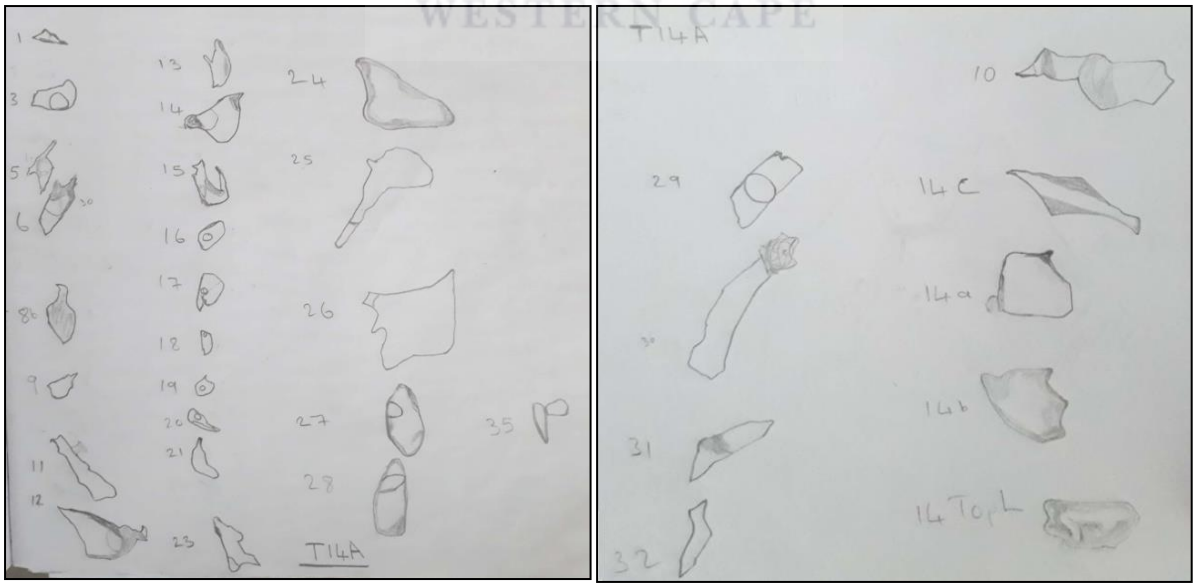

Fig. C6. Chip T14A: Schematic diagrams of Mono−phase type III fluid inclusions (1, 8b, 9, 10, 14c, 14a, 14b, 14TopL, 15, 23, 24, 30, 31, 32 & 35); Mono−phase type V fluid inclusions (11, 13, 25 & 26) and 2−phase Type I fluid inclusions (3, 5, 6, 12, 14, 16 – 20 & 27 – 29).

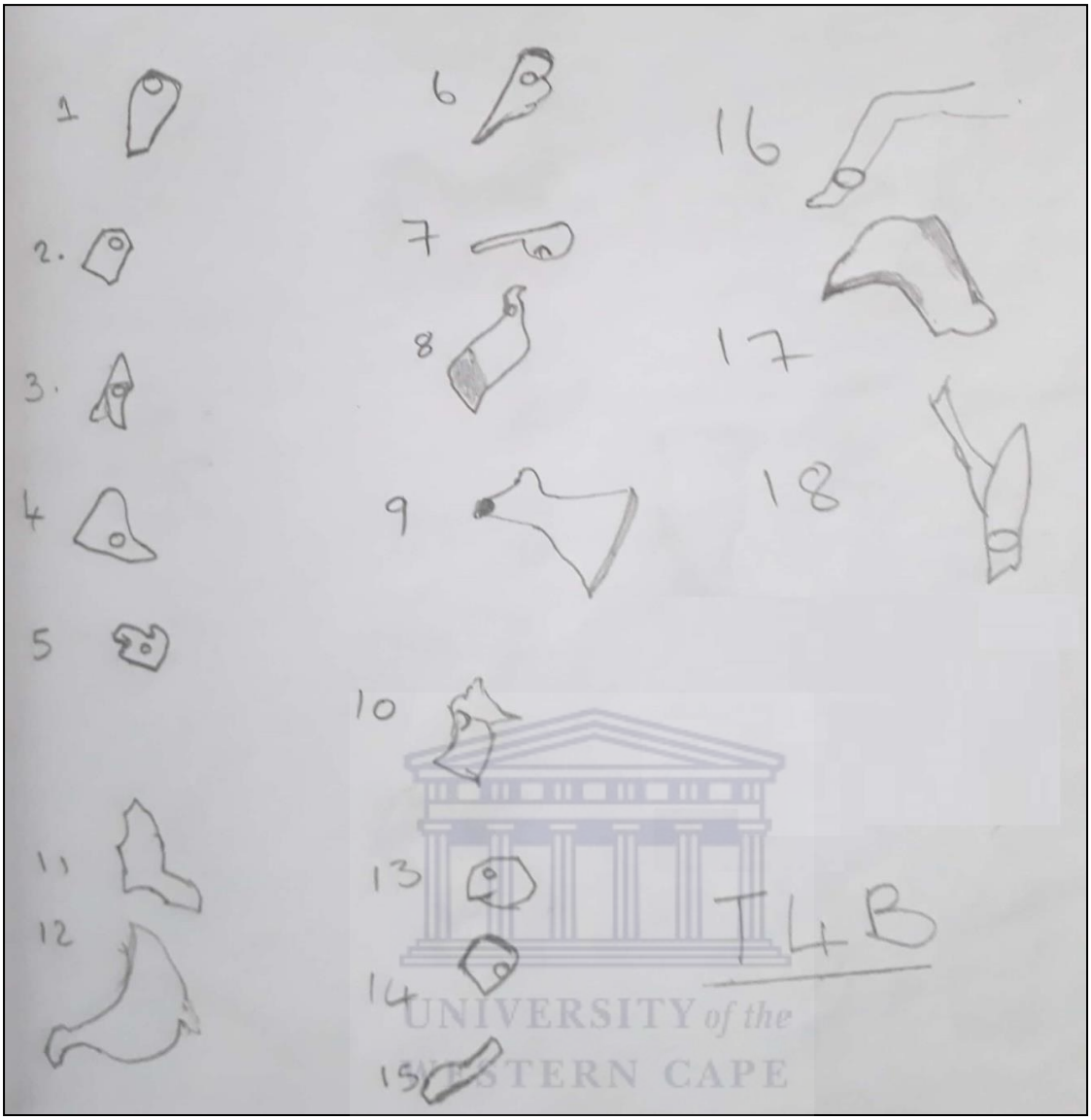

Fig. C7. Chip T4B: Schematic diagrams of Mono−phase Type IV fluid inclusions (9, 11, 12, 15 & 17) and 2−phase Type I fluid inclusions (1 – 8, 10, 13, 14, 16 & 18).

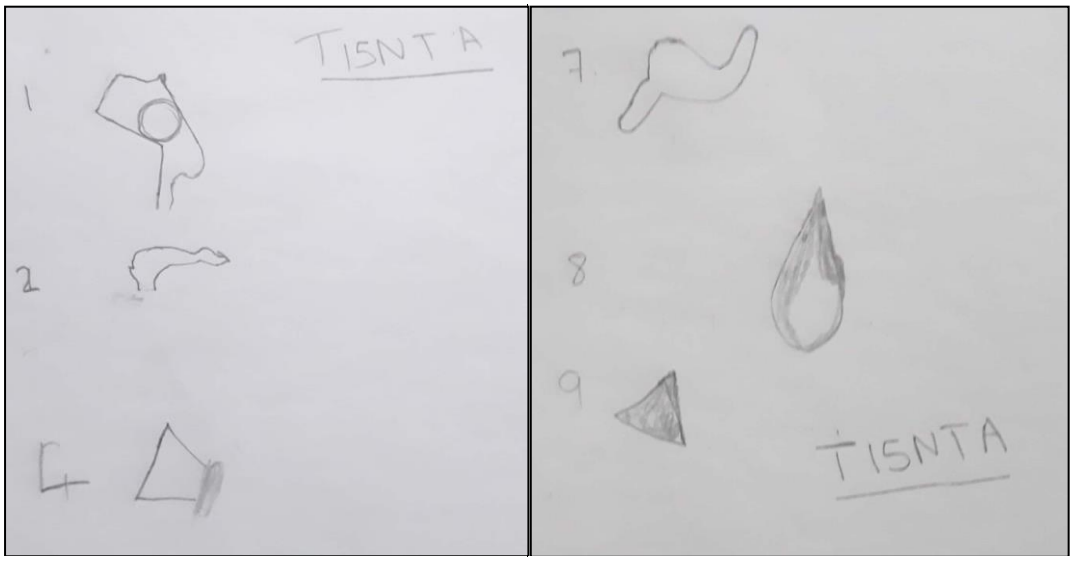

Fig. C8. Chip T15NTA: Schematic diagrams of Mono−phase Type IV fluid inclusions (2, 4, 7, 8 & 9) and a 2−phase Type I fluid inclusion (1).

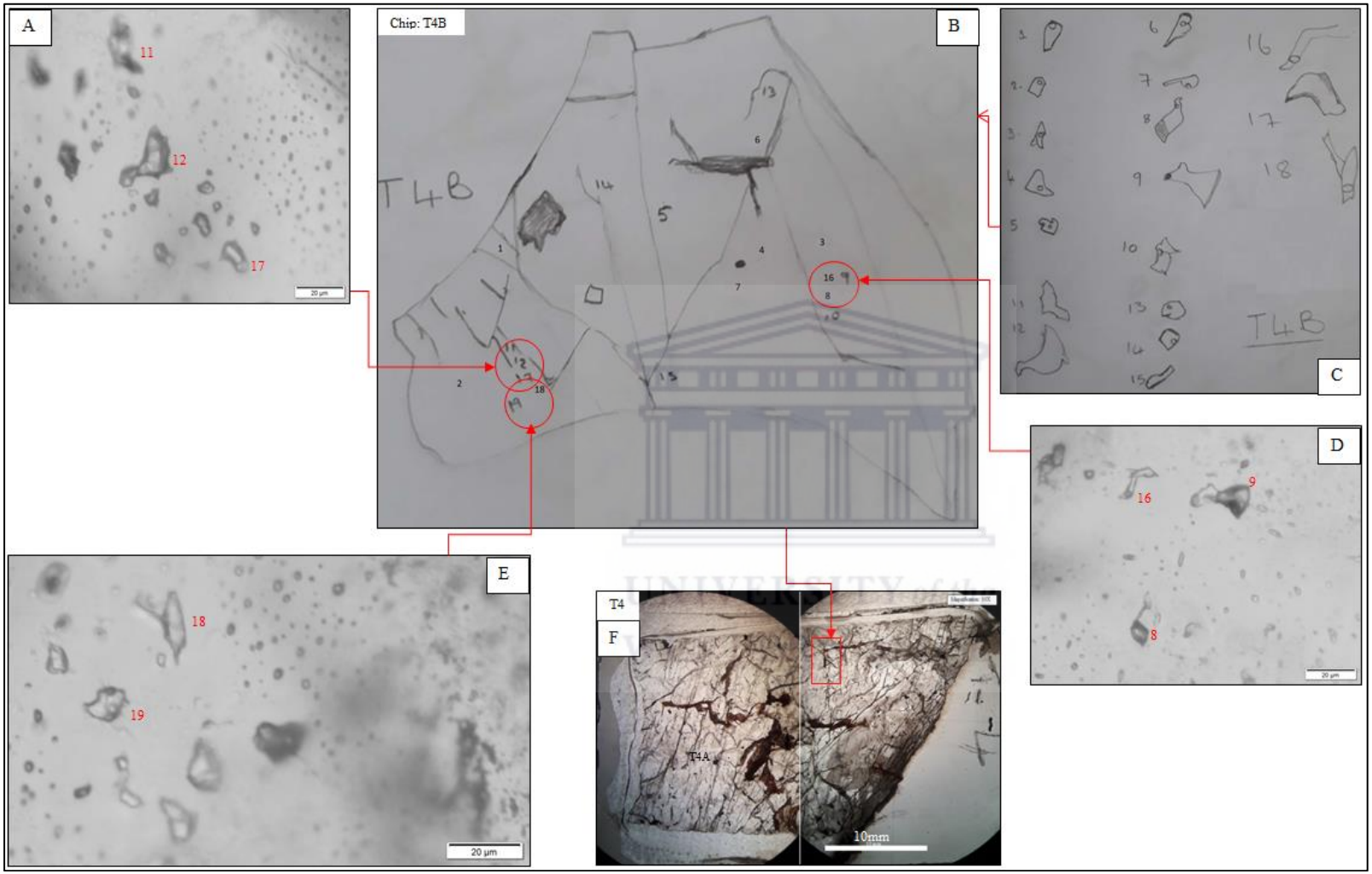

Fig. C9. Coexistence of both mono-phase and bi-phase fluid inclusions in the T4B chip. A. Photomicrograph of a trail of mono-phase fluid inclusions taken at a temperature of −170 °C, B. Another sketch of a chip (T4B) broken from a doubly polished wafer cut from samples collected from trench 4, C. Sketches of fluid inclusions from various parts of chip T4B, D. Mono-phase inclusions (9 and 8) in the same trail with a bi-phase inclusion (16), E. Photomicrograph of a trail of mono-phase fluid inclusions, F. Image of a doubly polished wafer (T4) from trench 4

Appendix D: Zircon CL images for U/Pb dating

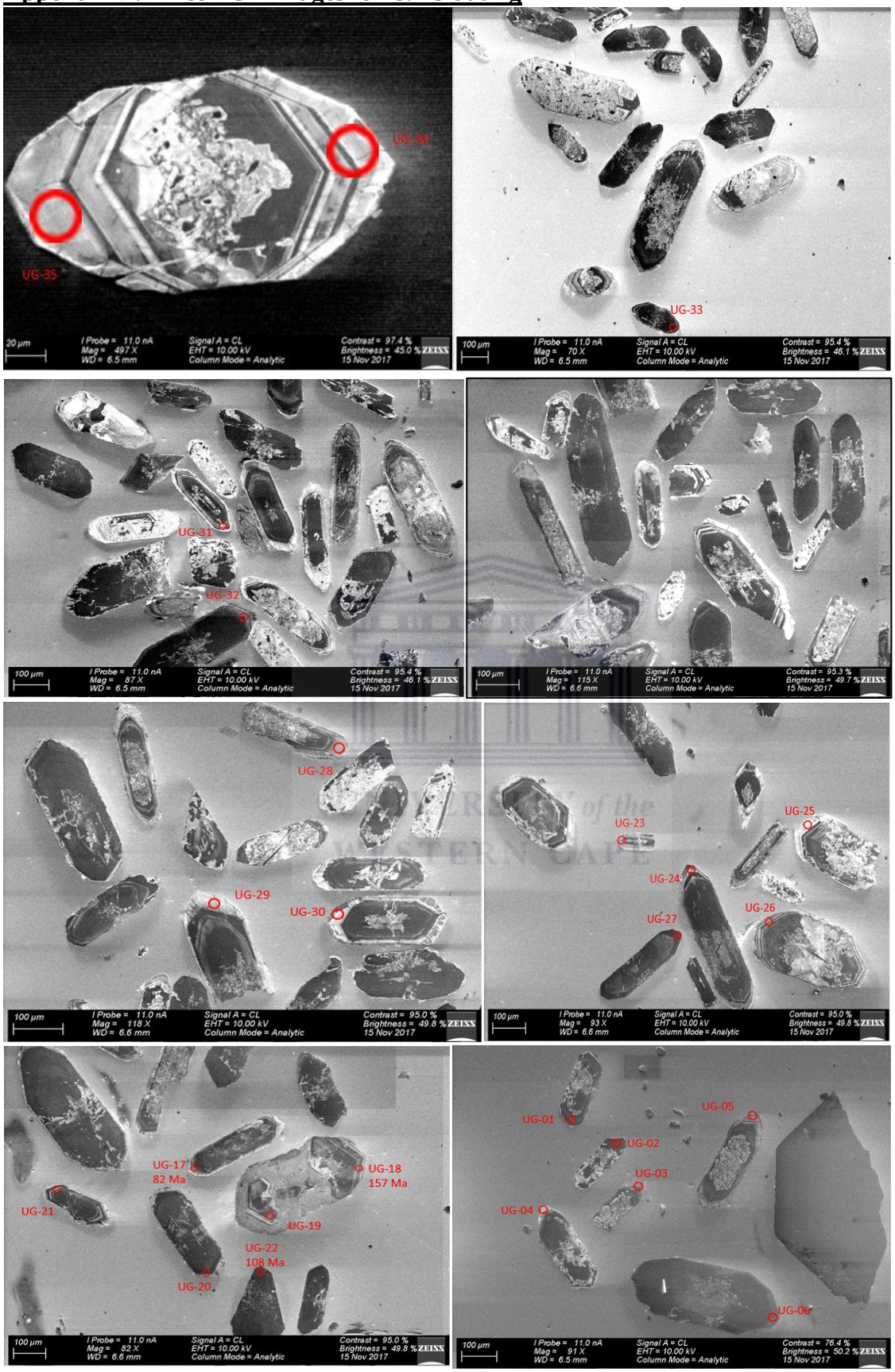

Fig. D1. CL zircon images from the non−foliated granite located in close proximity of the shear zone. Indicated ages are for $^{206}Pb/^{238}U$.

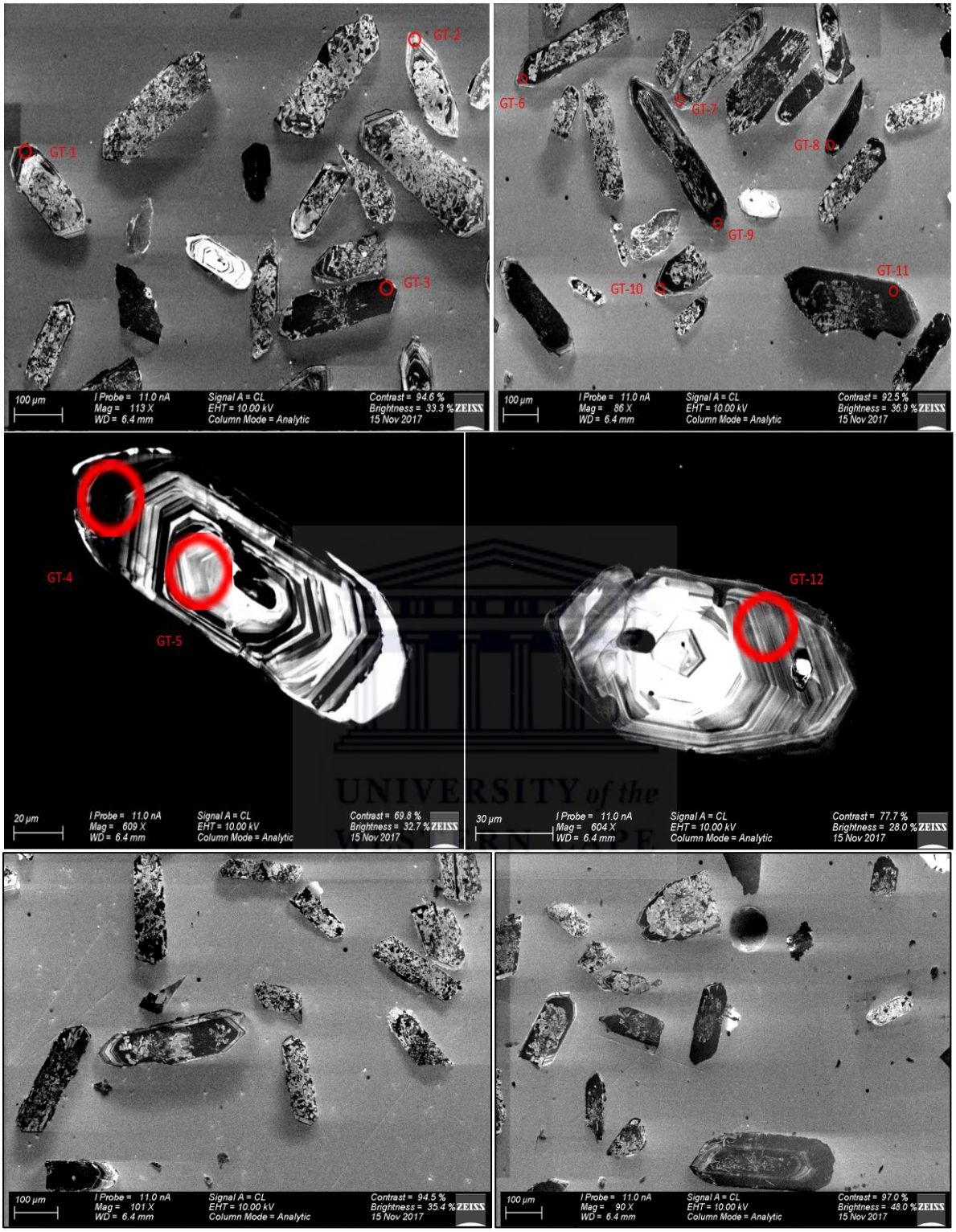

Fig. D2. CL zircon images from the non−foliated granite hosting a mineralized xenolith.

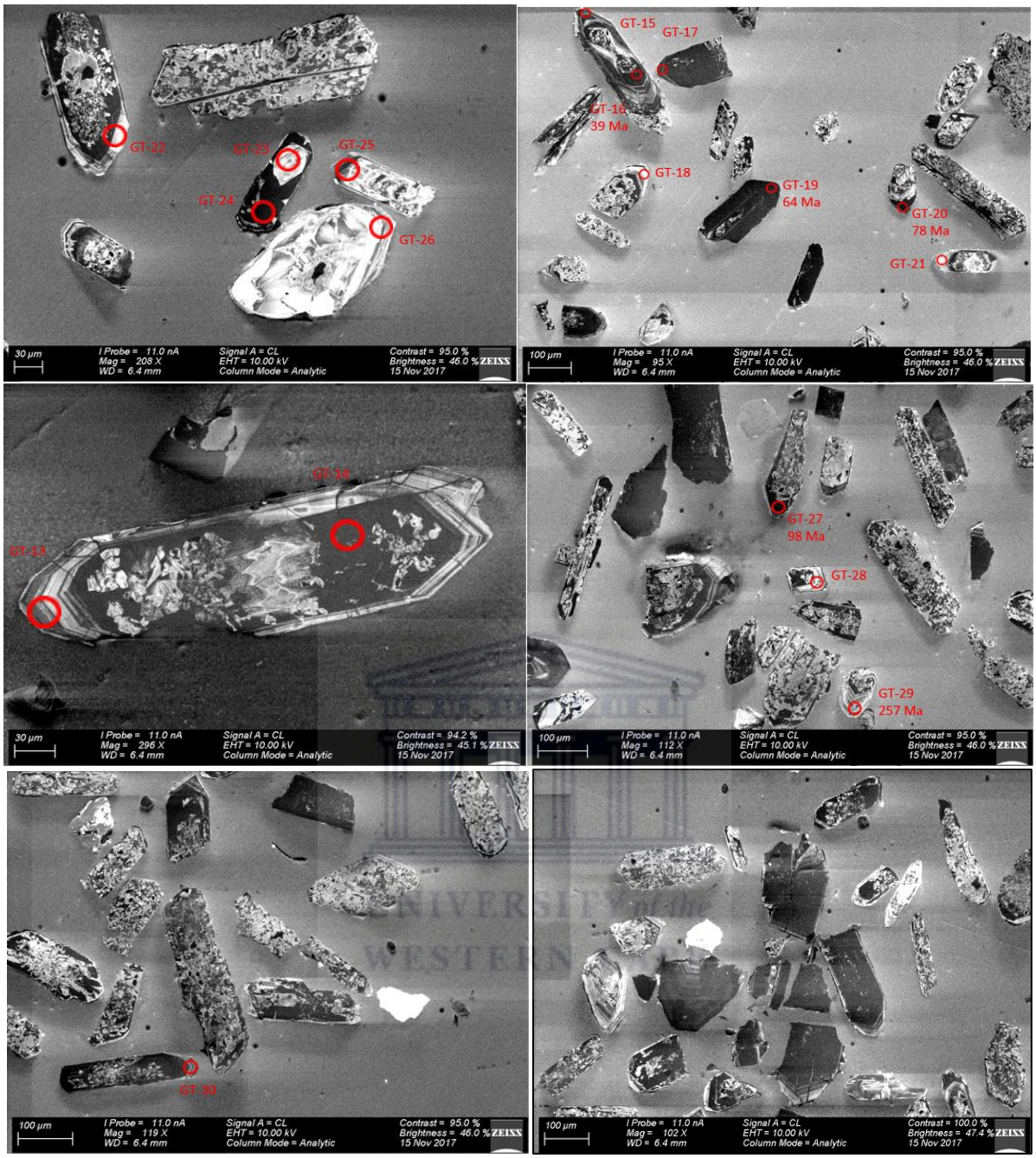

Fig. D3. More CL zircon images from the non−foliated granite hosting a mineralized xenolith. Indicated ages are for $^{206}Pb/^{238}U$.

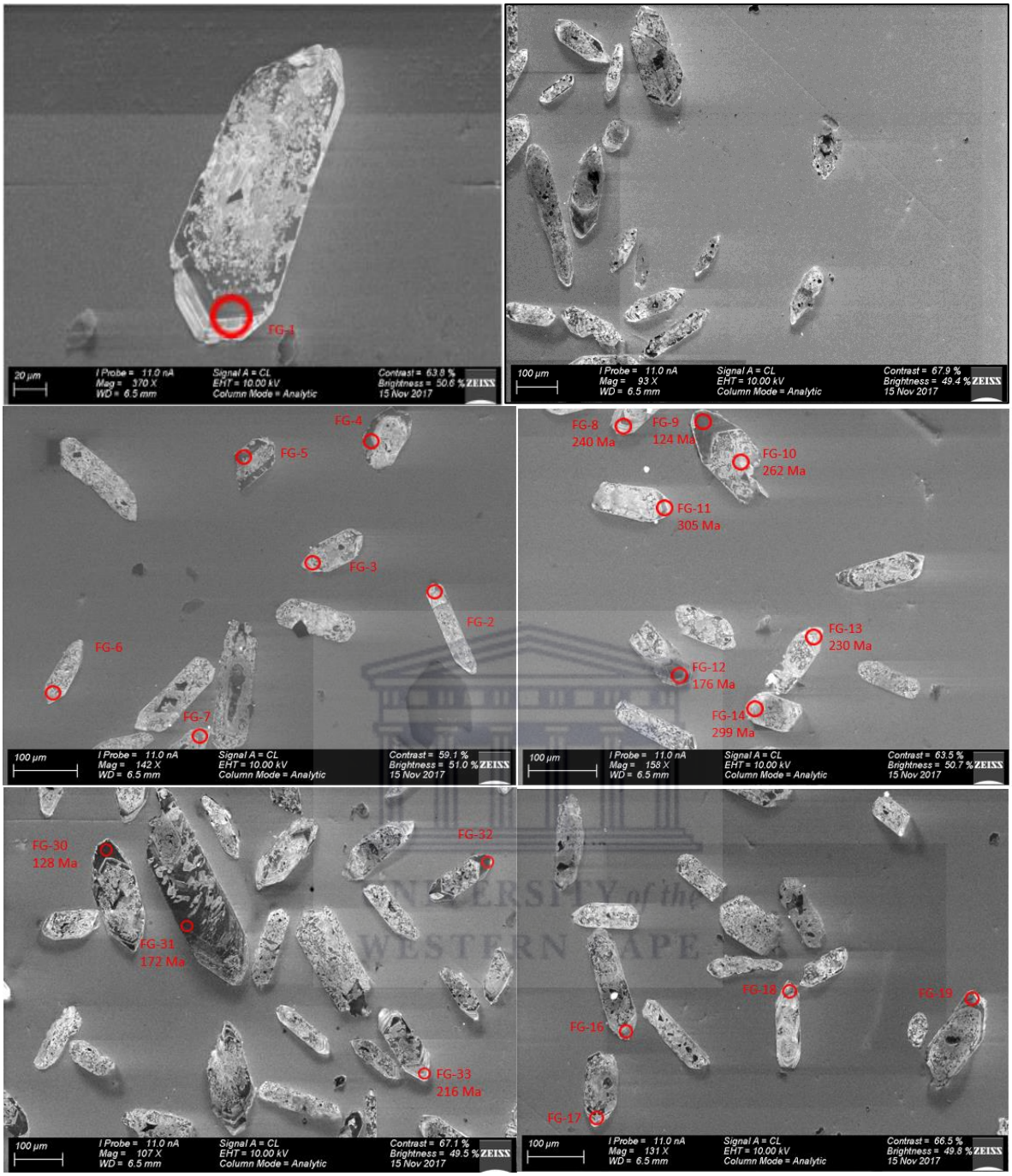

Fig. D4. CL zircon images from the foliated granite located within reach of the shear zone. Indicated ages are for $^{206}Pb/^{238}U$.

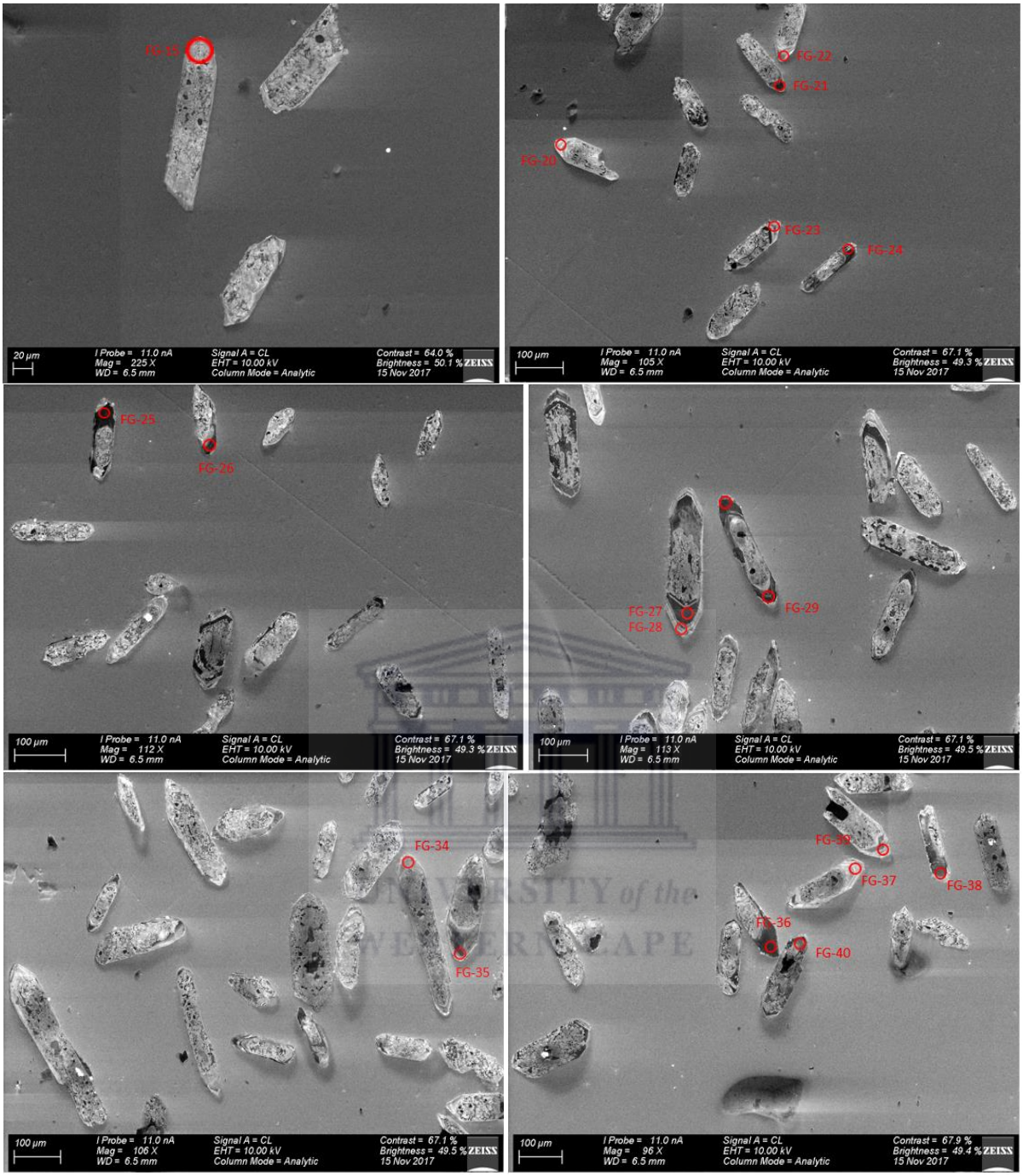

Fig. D5. More CL zircon images from the foliated granite.

Appendix E: XRD spectra

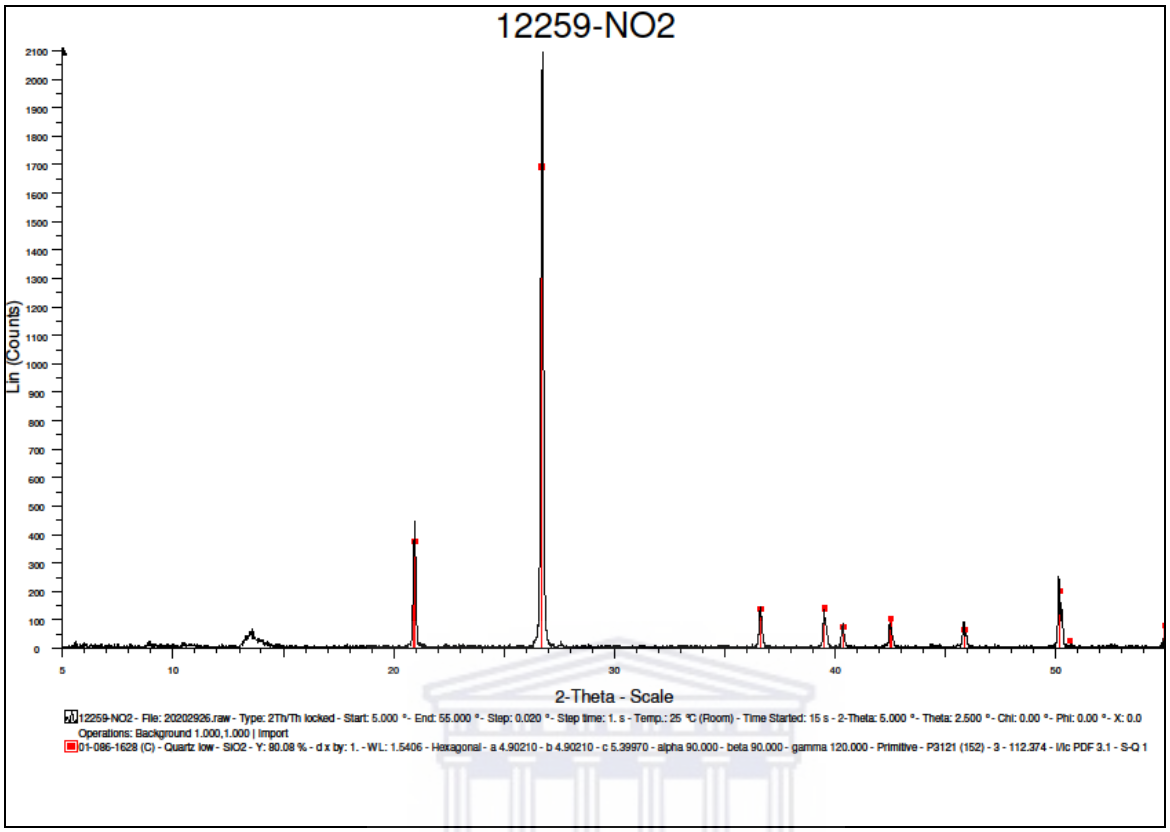

Fig. E1. Sample NO2 XRD spectrum depicting the presence of quartz.

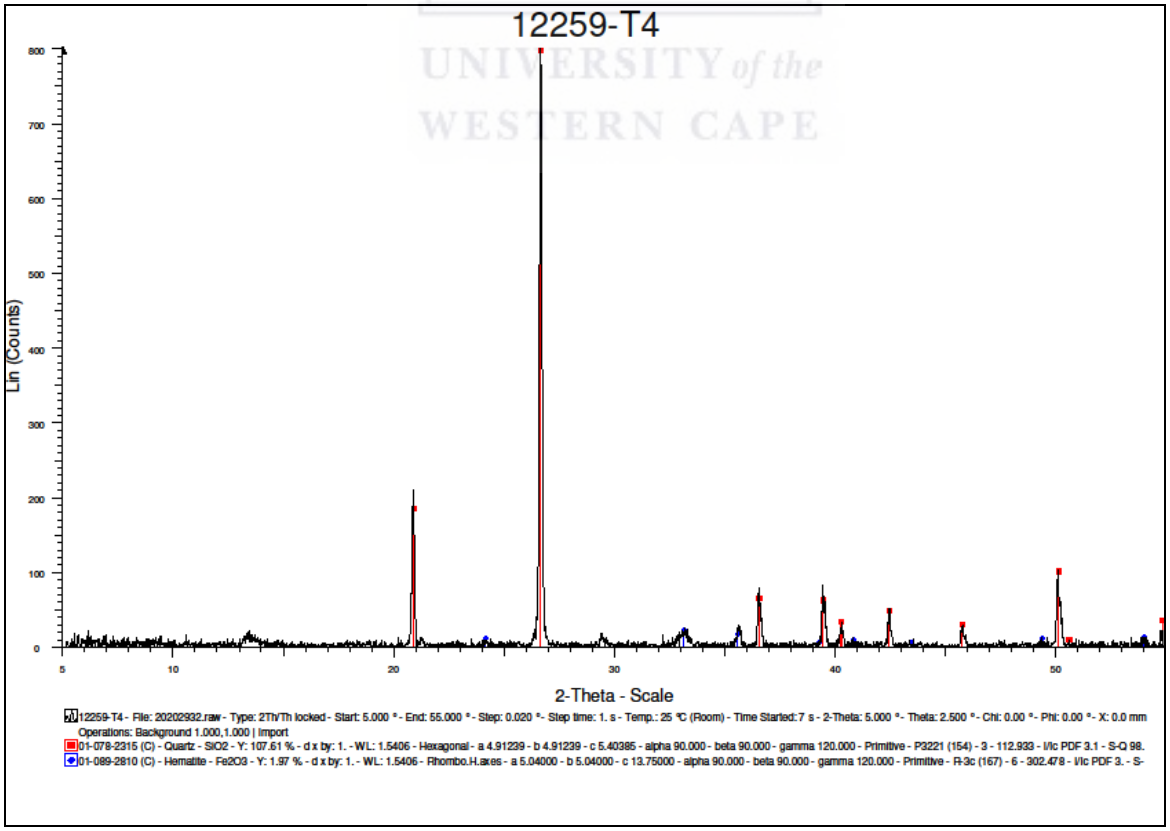

Fig. E2. Sample T4 XRD spectrum depicting the presence of quartz and hematite.

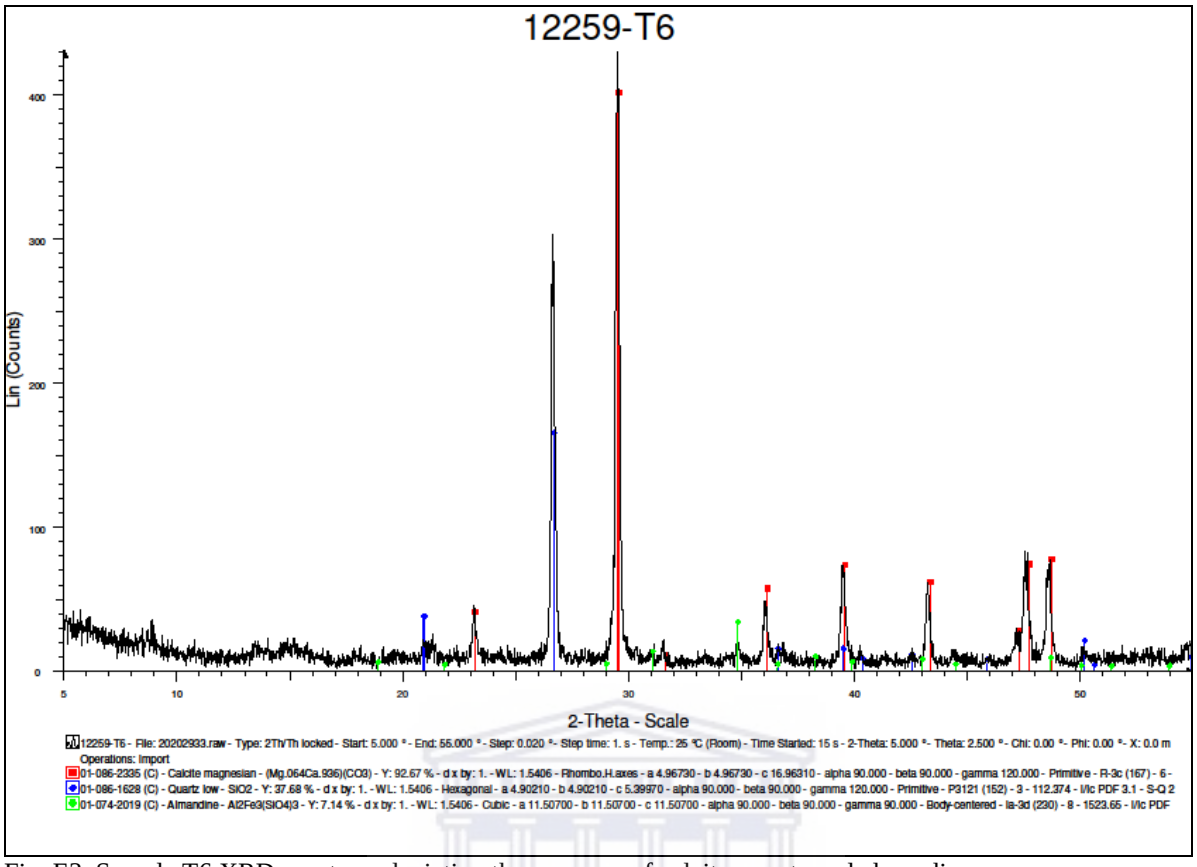

Fig. E3. Sample T6 XRD spectrum depicting the presence of calcite, quartz and almandine.

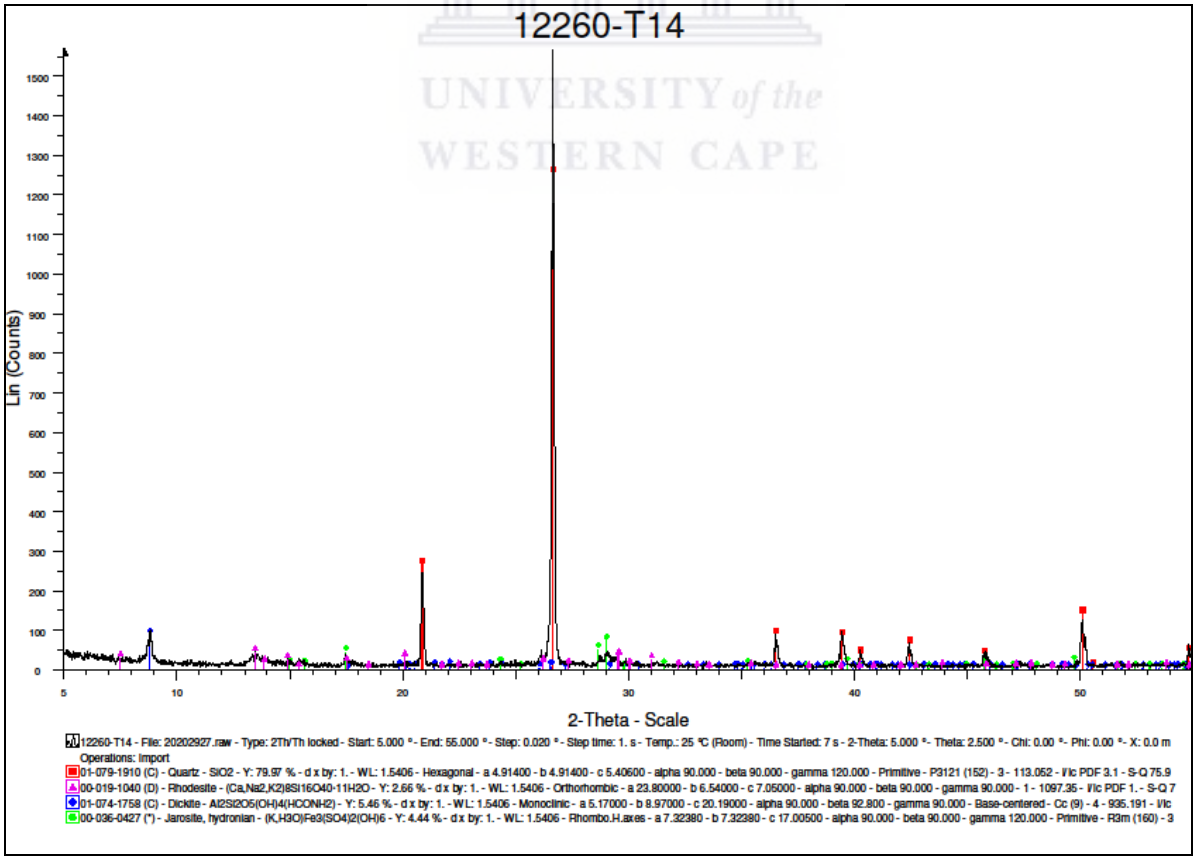

Fig. E4. Sample T14 XRD spectrum depicting the presence of quartz, rhodesite, dickite and jarosite.

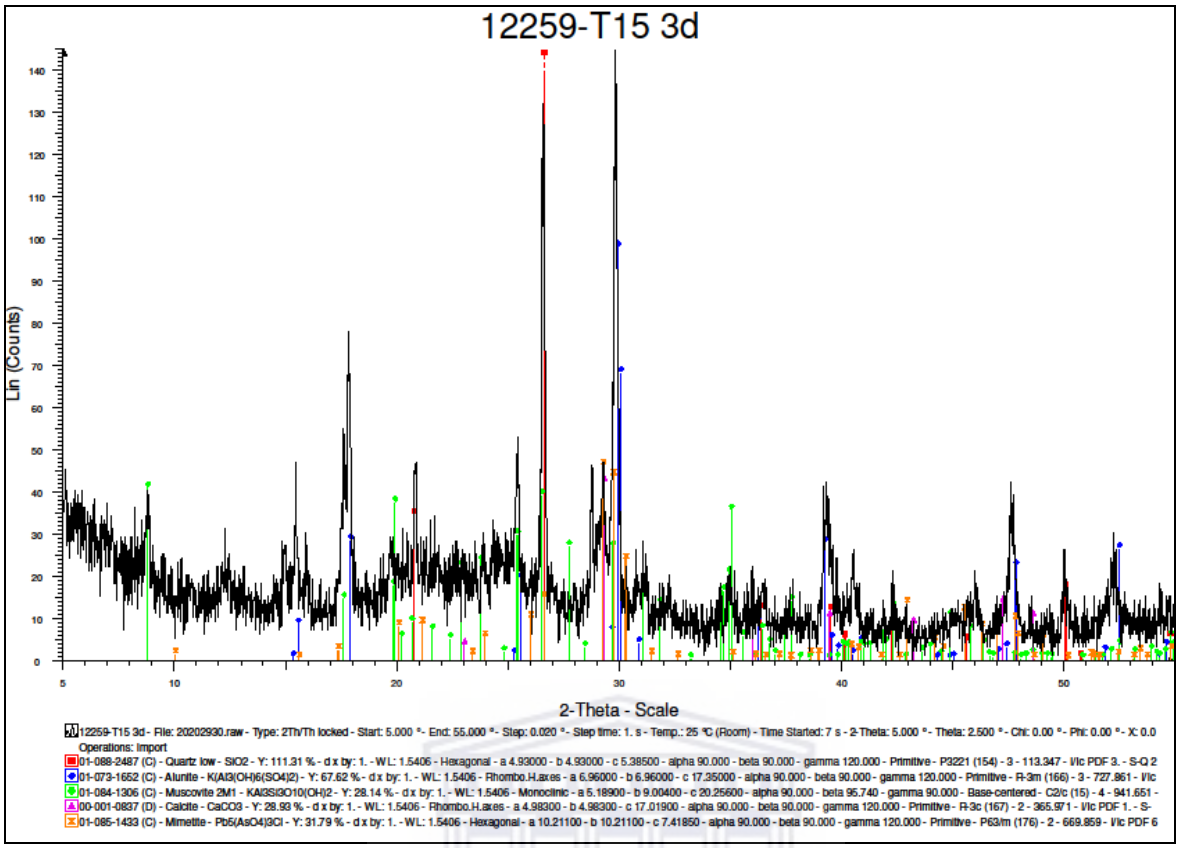

Fig. E5. Sample T15 3d XRD spectrum depicting the presence of quartz, alunite, muscovite, calcite and mimetite.

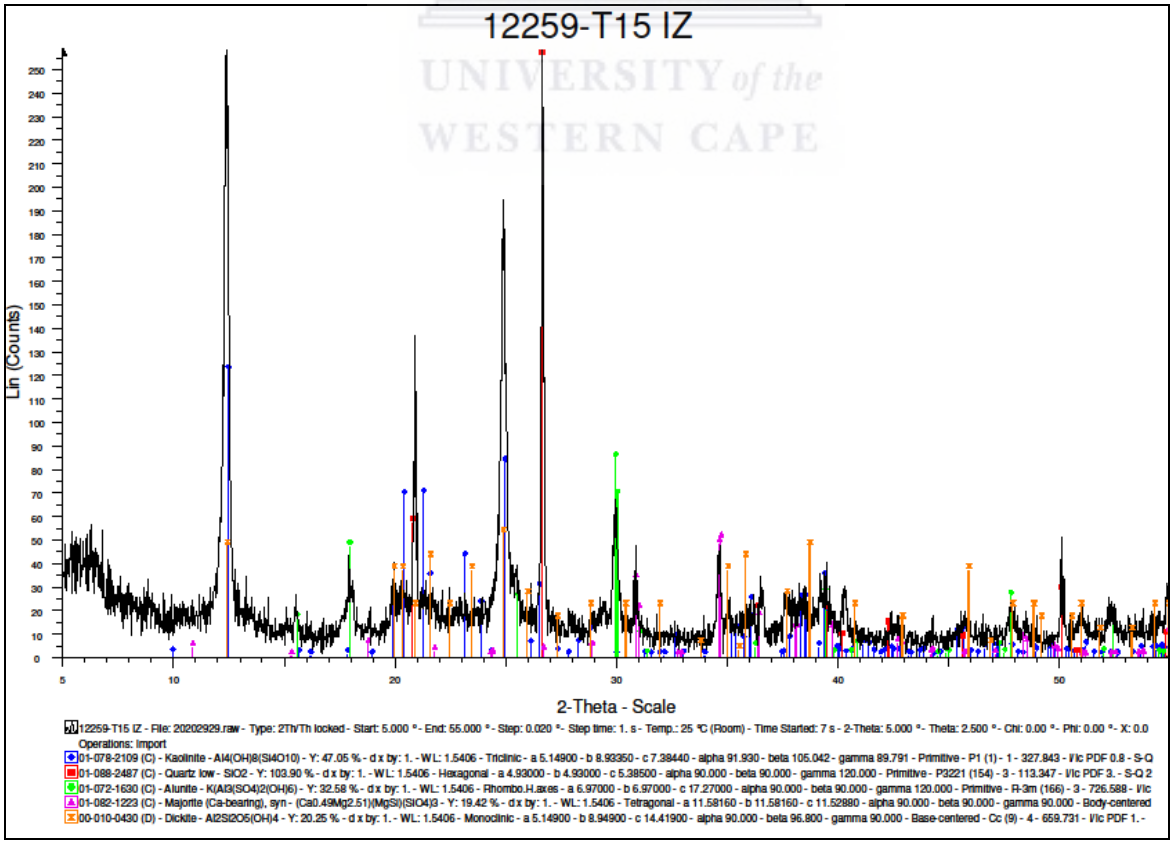

Fig. E6. Sample T15 IZ XRD spectrum depicting the presence of kaolinite, quartz, alunite, majorite and dickite.

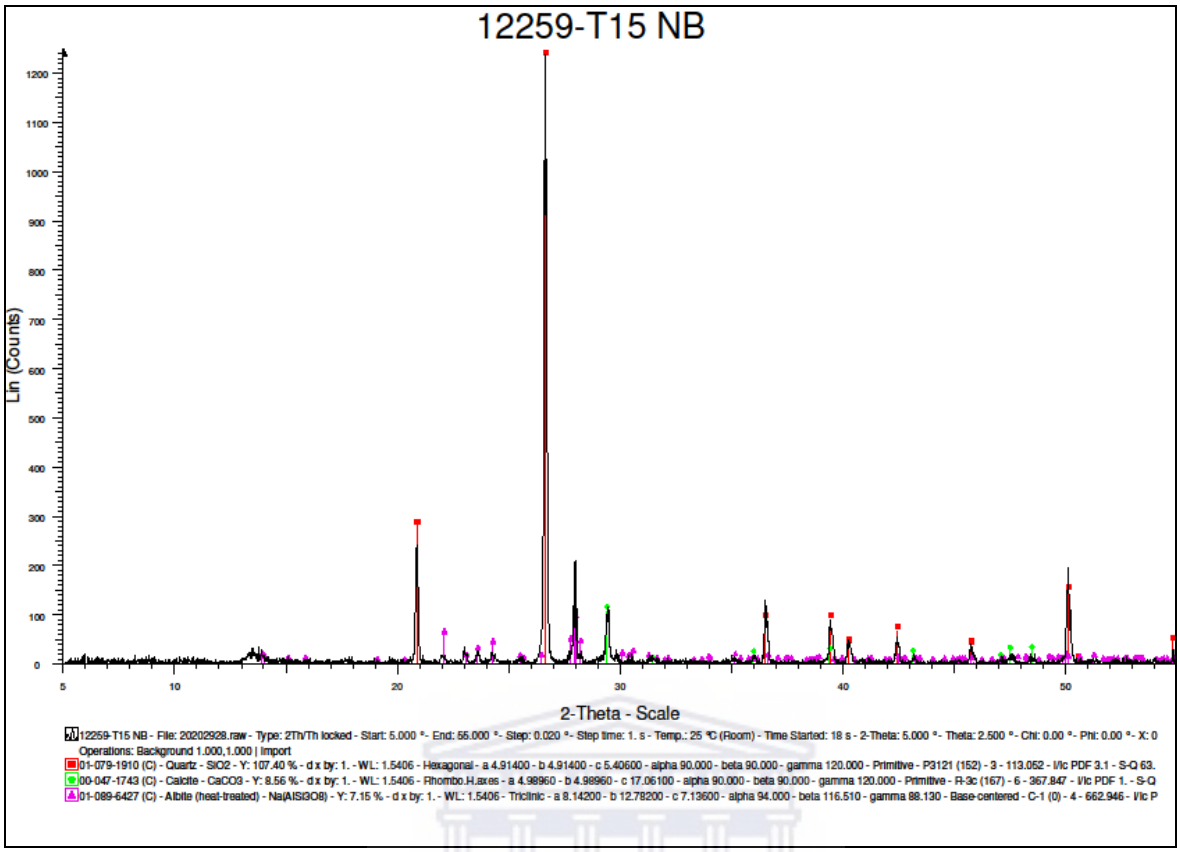

Fig. E7. Sample T15 NB XRD spectrum depicting the presence of quartz, calcite and albite.

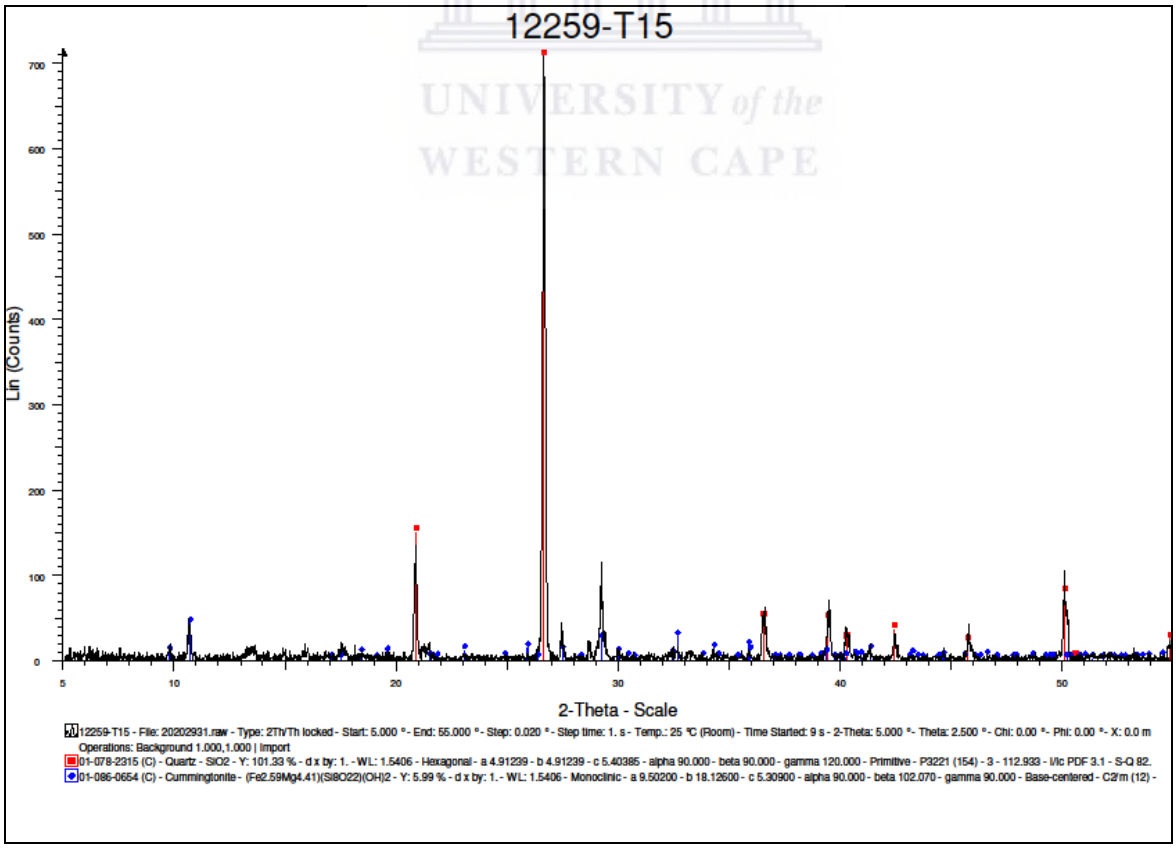

Fig. E8. Sample T15 XRD spectrum depicting the presence of quartz and cummingtonite.

Appendix F: Table F1 Microthermometry data

Order	Chip	Area	FI	Type	petro	RT	size	%vap	Tf1	Ti	Tmice	TmCO2	ThCO2	Mode	Tm cla	Thtot	Mode	Salinity wt% NaCl
1	T4A	SE	a	I	trail	LV	6.4	10	−67		−19.4					153.4	L	22.0
2	T4A	SE	b	I	trail	LV	10.0	10	−42		−1.6					210.1	L	2.7
3	T4A	SE	c	I	trail	LV	4.8	10								178.0	L	
4	T4A	SE	d	I	trail	LV	5.0	10								226.5	L	
5	T4A	SE	e	I	trail	LV	4.0	10								185.5	L	
6	T4A	SE	f	I	trail	LV	5.1	10								249.1	L	
7	T4A	SE	g	I	trail	LV	5.1	10								243.6	L	
8	T4A	SE	h	I	trail	LV	7.1	10	−40		−1.6					191.6	L	2.7
9	T4A	SE	j	I	trail	LV	7.3	10	−41		−1.8					235.0	L	3.1
10	T4A	SE	j1	I	trail	LV	6.3	10								234.1	L	
11	T4A	SE	k	I	trail	LV	6.2	10								220.1	L	
12	T4A	SE	xk	I	trail	LV	5.9	10								205.6	L	
13	T4A	SE	xo	I	trail	LV	3.8	10								152.0	L	
14	T4A	SE	xp	I	trail	LV	17.5	10								172.0	L	
15	T4A	SE	q	I	trail	LV	22.1	10	−84		−22.4					280.9	L	24.0
16	T4A	SE	r	I	trail	LV	10.1	10	−85		−21.9					232.8	L	23.6
17	T4A	SE	xr	I	trail	LV	7.5	10								227.9	L	
18	T4A	SE	s	I	trail	LV	9.9	10	−91		−22.4							24.0
19	T4A	SE	1c	I	trail	LV	12.0	10	−39		−2.2							3.7
20	T4A	SE	1s	IV	trail	V	21.4	100								−124.0	V	
21	T4A	SE	1t	IV	trail	V	21.0	100								−124.0	V	
22	T4A	SE	1	I	is	LV	20.9	10	−34		−3.1					234.7	L	5.1
23	T4A	SE	2	I	is	LV	11.1	10								220.0	L	
24	T4A	SE	11	I	is	LV	10.3	20								222.0	L	
25	T4A	SE	12	I	is	LV	8.3	10								221.6	L	
26	T4A	SE	13	I	trail	LV	15.0	10								225.7	L	
27	T4A	SE	14	I	trail	LV	14.9	10								236.0	L	
28	T4A	Cwest	1	III	trail	LLV	5.3	10	−96			−56.6	25.4	L				
29	T4A	Cwest	2x	I	is	LV	8.8	20								306.5	L	
30	T4A	Cwest	4x	I	is	LV	12.1	20								259.4	L	

Table F1 continues

Order	Chip	Area	FI	Type	petro	RT	size	%vap	Tf1	Ti	Tmice	TmCO2	ThCO2	Mode	Tm cla	Thtot	Mode	Salinity wt% NaCl
31	T4A	Cwest	5	I	is	LV	11.0	10	−34		−1.7							2.9
32	T4A	Cwest	6	III	trail	LV	10.9	10	−96			−56.4	25.5	L				
33	T4A	Cwest	7x	I	trail	LV	10.0	10								287.0	L	
34	T4A	Cwest	10	I	is	LV	9.5	20	−34		−3.6					291.2	L	5.9
35	T4A	Cwest	11x	I	trail	LV	6.2	10								225.6	L	
36	T4A	Cwest	12x	I	trail	LV	6.2	10								241.8	L	
37	T4A	Cwest	19	I	trail	LV	6.6	20								326.5	L	
38	T4A	Cwest	19x	I	trail	LV	7.1	10								329.0	L	
39	T4A	Cwest	19Y	I	is	LV	6.6	10								272.7	L	
40	T4A	Cwest	20	I	trail	LV	8.8	10								291.8	L	
41	T4A	Cwest	21	I	is	LV	11.3	10								255.4	L	
42	T4B		1	I	is	LV	7.5	10	No phase change between −190 and 34°c									
43	T4B		8	I	trail	LV	21.0	20	−39		−6.4							9.7
44	T4B		9	IV	trail	V	24.6	100	−138							−121.4	V	
45	T4B		11	IV	trail	V	21.2	100	−143							−130.0	V	
46	T4B		12	IV	trail	V	23.8	100	−140							−127.0	V	
47	T4B		16	I	trail	LV	16.5	20	−32		−2.9							4.8
48	T4B		17	IV	trail	V	13.3	100	−140							−115.9	V	
49	T14A		1	III	is	L	16.9	0	−95			−57.2	0.2	L				
50	T14A		2	III	trail	LV	15.8	40	−95			−56.8	26.4	L				
51	T14A		3	III	trail	LV	10.6	30	−95			−56.7	27.7	L				
52	T14A		4	III	trail	LV	16.1	40	−95			−57.2	26.8	L				
53	T14A		5	III	trail	LV	24.5	10	−96			−56.8	25.7	L				
54	T14A		6	III	trail	LV	19.2	40	−96			−56.8	25.5	L				
55	T14A		7	III	trail	LV	14.4	50	−95			−57.2	26.9	L				
56	T14A		8	III	trail	LV	17.4	40	−95			−57.2	26.8	L				
57	T14A		8b	III	trail	L	16.4	0	−95			−56.9	25.5	L				
58	T14A		10	III	trail	L	27.2	0	−95			−57.0	15.0	L				

Table F1 continues

Order	Chip	Area	FI	Type	petro	RT	size	%vap	Tf1	Ti	Tmice	TmCO2	ThCO2	Mode	Tm cla	Thtot	Mode	Salinity wt% NaCl
59	T14A		11	V	trail	L	26.5	0	−102			−63.0				−31.4	L	
60	T14A		12	III	trail	LV	14.6	20	−95	−62.7		−57.2	24.2	L				
61	T14A		13	V	trail	L	18.2	0	−102			−62.9						
62	T14A		14	III	trail	LV	13.2	30	−95	−60.0		−57.3	23.2	L				
63	T14A		14a	III	trail	L	7.4	0	−96			−57.2	22.8	L				
64	T14A		14b	III	trail	L	8.5	0	−96			−57.3	22.3	L				
65	T14A		14c	III	trail	L	14.2	0	−95			−57.0						
66	T14A		14Top L	III	trail	L	13.5	0	−95			−57.4	24.6	L				
67	T14A		14Top R	III	trail	L	10.0	0	−95			−57.0						
68	T14A		15	III	trail	L	22.6	0	−99			−58.4			5.6			
69	T14A		21	V	trail	L	13.2	0	−103			−64.8						
70	T14A		22	III	trail	L	27.2	0	−95			−57.4						
71	T14A		23	III	trail	V	14.3	100	−97			−58.4	16.5	V				
72	T14A		24	III	trail	V	10.5	100	−97			−57.5	17.1	V				
73	T14A		25	V	trail	L	19.0	0	−102			−62.1				−22.1	L	
74	T14A		26	V	trail	L	12.8	0	−102			−64.8				−22.4	L	
75	T14A		27	III	trail	LV	16.0	10	−95			−56.6	23.8	L				
76	T14A		28	III	trail	LV	9.8	20	−91			−56.7	25.4	L				
77	T14A		29	III	trail	LV	16.1	30	−95			−56.3	29.2	L				
78	T14A		30	III	trail	L	29.4	0	−93			−56.5	−8.3	L				
79	T14A		31	III	trail	L	16.9	0	−92			−56.5						
80	T14A		32	III	trail	L	16.1	0	No phase change between −190 and 34°c									
81	T14A		35	III	trail	L	12.6	0	−97			−57	11.1	L				
82	T15A		1	I	is	LV	6.6	50	No phase change between −190 and 34°c									
83	T15A		2	IV	trail	V	12.9	100								−84.0	V	
84	T15A		3	IV	trail	V	12.5	100								−84.1	V	

Table F1 continues

Order	Chip	Area	FI	Type	petro	RT	size	%vap	Tf1	Ti	Tmice	TmCO2	ThCO2	Mode	Tm cla	Thtot	Mode	Salinity wt% NaCl
85	T15A		4	IV	trail	V	11.8	100								−107.5	V	
86	T15A		5	IV	trail	V	8.3	100								−79.7	V	
87	T15A		6	IV	trail	V	23.8	100								−88.0	V	
88	T15A		7	IV	trail	V	17.8	100								−80.6	V	
89	T15A		8	IV	trail	V	13.4	100								−73.6	V	
90	T15A		9	IV	trail	V	12.0	100								−106.6	V	
91	T15A		10	IV	trail	V	11.0	100								−101.5	V	
92	T15A		11	IV	trail	V	19.8	100								−71.4	V	
93	T15A		12	IV	trail	V	10.5	100								−89.6	V	
94	T15A		13	IV	trail	V	7.7	100								−75.5	V	
95	T15A		14	IV	trail	V	9.8	100								−75.0	V	
96	T15A		15	IV	trail	V	20.1	100								−100.6	V	
97	T15A		16	IV	trail	V	13.9	100								−102.0	V	
98	T15A		17	IV	trail	V	10.3	100								−109.1	V	
99	T15A		18	IV	trail	V	14.8	100								−110.0	V	
100	T15A		19	IV	trail	V	14.7	100								−100.6	V	
101	T15A		20	IV	trail	V	15.3	100								−109.7	V	
102	T15A		21	IV	trail	V	10.3	100								−109.7	V	
103	T15A		22	IV	trail	V	11.7	100								−109.7	V	
104	T15A		23	IV	trail	V	8.5	100								−111.6	V	
105	T15A		24	IV	trail	V	16.5	100								−108.4	V	
106	T15BaseA		1	IV	trail	V	41.6	100	No phase change between −190 and 34°c									
107	T15BaseA		2	IV	trail	V	30.1	100	No phase change between −190 and 34°c									
108	T15BaseA		3	IV	trail	V	42.4	100	No phase change between −190 and 34°c									
109	T15BaseA		4	IV	trail	V	15.5	100								−106.2	V	

Table F1 continues

Order	Chip	Area	FI	Type	petro	RT	size	%vap	Tf1	Ti	Tmice	TmCO2	ThCO2	Mode	Tm cla	Thtot	Mode	Salinity wt% NaCl
110	T15BaseA		5	IV	trail	V	24.3	100								−105.5	V	
111	T15BaseA		6	IV	trail	V	20.1	100								−110.7	V	
112	T15BaseA		7	IV	trail	V	16.9	100								−104.3	V	
113	T15BaseA		8	IV	trail	V	14.0	100								−110.4	V	
114	T15BaseA		9	IV	trail	V	10.9	100								−110.9	V	
115	T15BaseA		10	IV	trail	V	20.9	100								−112.1	V	
116	T15BaseA		11	IV	trail	V	23.3	100								−90.1	V	
117	T15BaseA		12	IV	trail	V	22.7	100								−85.6	V	
118	T15BaseA		13	IV	trail	V	15.1	100								−116.6	V	
119	T15BaseA		14	IV	trail	V	12.5	100								−115.6	V	
120	T15BaseA		15	IV	trail	V	13.9	100								−116.1	V	
121	T15BaseA		16	IV	trail	V	21.6	100								−114.4	V	
122	T15BaseA		17	IV	trail	V	10.6	100								−109.3	V	
123	T15BaseA		18	IV	trail	V	31.1	100								−109.5	V	
124	T15BaseA		19	IV	trail	V	20.5	100								−114.7	V	
125	T15BaseA		20	IV	trail	V	11.6	100								−113.9	V	
126	T15BaseA		21	IV	trail	V	22.1	100								−75.0	V	
127	T15BaseA		22	IV	trail	V	10.5	100	No phase change between −190 and 34°c									
128	T15BaseA		23	IV	trail	V	9.7	100	No phase change between −190 and 34°c									
129	T15BaseA		24	IV	trail	V	8.3	100	No phase change between −190 and 34°c									
130	A		25	IV	trail	V	13.8	100	No phase change between −190 and 34°c									
131	NO2A		1	I	is	LV	21.5	20	−37						10.5	Leaked at 308°c		
132	NO2A		3	I	is	LV	21.0	20	−36						9.7	291.4	L	

Table F1 continues

Order	Chip	Area	FI	Type	petro	RT	size	%vap	Tf1	Ti	Tmice	TmCO2	ThCO2	Mode	Tm cla	Thtot	Mode	Salinity wt% NaCl
133	NO2A		4	II	is	LVV	16.4	50	−97			−57.7	15.3	L				
134	NO2A		5	I	is	L	9.2	0	−94			−57.4						
135	NO2A		6	I	is	LV	13.7	20	−37						10.4	279.5	L	
136	NO2A		7	I	is	LV	12.4	20	−36						7.0	287.7	L	
137	NO2A		7b	I	is	LV	8.6	20								276.0	L	
138	NO2A		8	II	trail	LVV	24.5	20	−94			−57.2						
139	NO2A		9	II	trail	LVV	18.0	20	−95			−57.2						
140	NO2A		10	III	trail	L	26.5	0	−94			−57.6						
141	NO2A		11	III	trail	L	14.6	0	−96			−57.6	9.1	L				
142	NO2A		12	III	trail	L	10.5	0	−96			−58.3	7.0	L				
143	NO2A		13	III	trail	L	14.5	0	−97			−57.6	17.5	L				
144	NO2A		14	III	trail	L	10.0	0	−97			−57.9	15.5	L				
145	NO2A		15	III	trail	L	10.8	0	−97			−57.7	11.9	L				
146	NO2A		16	III	trail	L	8.3	0	−96			−57.7						
147	NO2A		17	III	trail	L	9.5	0	−97			−57.5	11.3	L				
148	NO2A		18	III	trail	L	10.6	0	−96			−57.7						
149	NO2A		19	III	trail	L	8.4	0	−97			−57.1	11.6	L				
150	NO2A		20	III	trail	L	23.3	0	−96			−57.5	14.4	L				
151	NO2A		21	III	trail	L	13.4	0	−96			−57.8	17.9	L				
152	NO2A		22	I	trail	L	18.9	0	−96			−57.3	17.3	L				
153	NO2A		23	I	trail	LV	31.9	10	−42						3.7			
154	NO2A		24	I	trail	LV	16.4	10	−42						1.5	294.5	L	
155	NO2A		25	I	trail	LV	15.9	10	−42						10.1			
156	NO2A		26	I	trail	LV	18.4	10	−42						6.7			
157	NO2A		27	III	is	LV	12.1	30	−96			−57.2	22.8	L				
158	NO2A		28	III	trail	L	18.4	0	−96			−57.2						
159	NO2A		29	II	is	LV	14.2	50	Decrepitated at 349.6°c									
160	NO2A		30	II	trail	LV	9.9	50	Decrepitated at 345°c									

Table F1 continues

Order	Chip	Area	FI	Type	petro	RT	size	%vap	Tf1	Ti	Tmice	TmCO2	ThCO2	Mode	Tm cla	Thtot	Mode	Salinity wt% NaCl
161	NO2A		31	II	trail	LV	7.0	40	Decrepitated at 346.1°c									
162	T15NT A		1	I	trail	LV	26.6	20	No phase change between −190 and 34°c									
163	T15NT A		2	IV	trail	V	17.1	100	No phase change between −190 and 34°c									
164	T15NT A		4	IV	trail	V	19.6	100								−108.7	V	
165	T15NT A		5	IV	trail	V	12.2	100								−107.0	V	
166	T15NT A		6	IV	trail	V	11.8	100								−108.2	V	
167	T15NT A		7	IV	trail	V	23.5	100								−100.7	V	
168	T15NT A		8	IV	is	V	18.8	100								−101.9	V	
169	T15NT A		9	IV	is	V	14.2	100								−106.8	V	

Table F2 Fluid inclusions type I

Order	Chip	Area	FI	Type	petro	RT	size (μm)	%vap	Tm_{ice}	$T_{m(CL)}$	Th_{tot}	Mode	Bulk density	Raman results (bubble)	Raman Results (liquid)
1	T4A	SE	a	I	trail	LV	6.4	10	−19.4		153.4	L	1.069807		
2	T4A	SE	b	I	trail	LV	10.0	10	−1.6		210.1	L	0.876572	CH_4, weak N_2	H_2O
3	T4A	SE	c	I	trail	LV	4.8	10			178.0	L			H_2O
4	T4A	SE	d	I	trail	LV	5.0	10			226.5	L			H_2O
5	T4A	SE	e	I	trail	LV	4.0	10			185.5	L			
6	T4A	SE	f	I	trail	LV	5.1	10			249.1	L			
7	T4A	SE	g	I	trail	LV	5.1	10			243.6	L			
8	T4A	SE	h	I	trail	LV	7.1	10	−1.6		191.6	L	0.898347		
9	T4A	SE	j	I	trail	LV	7.3	10	−1.8		235.0	L	0.846395		
10	T4A	SE	j1	I	trail	LV	6.3	10			234.1	L			
11	T4A	SE	k	I	trail	LV	6.2	10			220.1	L			
12	T4A	SE	xk	I	trail	LV	5.9	10			205.6	L			
13	T4A	SE	xo	I	trail	LV	3.8	10			152.0	L			
14	T4A	SE	xp	I	trail	LV	17.5	10			172.0	L			
15	T4A	SE	q	I	trail	LV	22.1	10	−22.4		280.9	L			
16	T4A	SE	r	I	trail	LV	10.1	10	−21.9		232.8	L			
17	T4A	SE	xr	I	trail	LV	7.5	10			227.9	L			
18	T4A	SE	s	I	trail	LV	9.9	10	−22.4						
19	T4A	SE	1c	I	trail	LV	12.0	10	−2.2						
20	T4A	SE	1	I	is	LV	20.9	10	−3.1		234.7	L	0.86708	CH_4	H_2O
21	T4A	SE	2	I	is	LV	11.1	10			220.0	L			
22	T4A	SE	11	I	is	LV	10.3	20			222.0	L			
23	T4A	SE	12	I	is	LV	8.3	10			221.6	L			
24	T4A	SE	13	I	trail	LV	15.0	10			225.7	L			
25	T4A	SE	14	I	trail	LV	14.9	10			236.0	L			
26	T4A	Cwest	2x	I	is	LV	8.8	20			306.5	L			

Table F2 continues

Order	Chip	Area	FI	Type	petro	RT	size (μm)	%vap	Tm_{ice}	$T_{m(CL)}$	Th_{tot}	Mode	Bulk density	Raman results (bubble)	Raman Results (liquid)
27	T4A	Cwest	4x	I	is	LV	12.1	20			259.4	L			
28	T4A	Cwest	5	I	is	LV	11.0	10	−1.7						
29	T4A	Cwest	7x	I	trail	LV	10.0	10			287.0	L			
30	T4A	Cwest	10	I	is	LV	9.5	20	−3.6		291.2	L	0.79136		
31	T4A	Cwest	11x	I	trail	LV	6.2	10			225.6	L			
32	T4A	Cwest	12x	I	trail	LV	6.2	10			241.8	L			
33	T4A	Cwest	19	I	trail	LV	6.6	20			326.5	L			
34	T4A	Cwest	19x	I	trail	LV	7.1	10			329.0	L			
35	T4A	Cwest	19Y	I	is	LV	6.6	10			272.7	L			
36	T4A	Cwest	20	I	trail	LV	8.8	10			291.8	L			
37	T4A	Cwest	21	I	is	LV	11.3	10			255.4	L			
38	T4B		7	I	trail	LV	15.1	10						H_2O	
39	T4B		8	I	trail	LV	21.0	20	−6.4					CH_4, N_2	
40	T4B		16	I	trail	LV	16.5	20	−2.9						
41	T4B		18	I	trail	LV	16.48	10						H_2O	
42	NO2A		1	I	is	LV	21.5	20		10.5	Leaked at 308°c				
43	NO2A		3	I	is	LV	21.0	20		9.7	291.4	L			
44	NO2A		6	I	is	LV	13.7	20		10.4	279.5	L			
45	NO2A		7	I	is	LV	12.4	20		7.0	287.7	L			
46	NO2A		7b	I	is	LV	8.6	20			276.0	L			
47	NO2A		23	I	trail	LV	31.9	10		3.7					
48	NO2A		24	I	trail	LV	16.4	10		1.5	294.5	L			
49	NO2A		25	I	trail	LV	15.9	10		10.1					
50	NO2A		26	I	trail	LV	18.4	10		6.7					
51	T4B		1	I	is	LV	7.5	10	No phase change between −190 and 34°c					CH_4, N_2	
52	T15A		1	I	is	LV	6.6	50	No phase change between −190 and 34°c						

Table F2 continues

Order	Chip	Area	FI	Type	petro	RT	size (μm)	%vap	Tm_{ice}	$T_{m(CL)}$	Th_{tot}	Mode	Bulk density	Raman results (bubble)	Raman Results (liquid)
53	T15NTA		1	I	trail	LV	26.6	20	No phase change between −190 and 34°c						

Note: FI: fluid inclusion, NO2A/B: doubly polished vein quartz wafer chip ID; Cwest: central west SE: south east, Petro: petrographic observation referring to an inclusion's occurrence relative to other inclusions and this may be in cluster, trail or isolation, is: isolated, RT: phase(s) present in an inclusion at room temperature, L: liquid, V: vapour, %Vap: percentage of vapour in an inclusion, $T_{m(ice)}$: ice melting temperature, $T_{m(CL)}$: clathrate melting temperature, T_h: total homogenization temperature, Mode: the resulting phase upon homogenization.

Table F3 fluid inclusions type II

Order	Chip	FI	Type	petro	RT	Size (μm)	%vap	Tf1	$T_{m(CO2)}$	$T_{h(CO2)}$	Mode	Raman results (bubble)	Raman results (liquid)
1	NO2A	4	II	trail	LVV	16.4	50	−97	−57.7	15.3	L		
2	NO2A	8	II	trail	LVV	24.5	20	−94	−57.2				
3	NO2A	9	II	trail	LVV	18.0	20	−95	−57.2				
4	NO2B	1	II	trail	LV	8.3	30					CO_2, H_2O	H_2O
5	NO2B	2	II	trail	LV	8.1	30					CO_2, CH_4, N_2, weak H_2O	H_2O, CO_2
6	NO2B	3	II	trail	LV	12.1	30					CO_2, H_2O, N_2	H_2O, CO_2
7	NO2B	4	II	trail	LV	6.5	20					CO_2, CH_4, H_2O, N_2	H_2O, CO_2, CH_4
8	NO2A	29	II	trail	LV	14.2	50	Decrepitated at 349.6°C					
9	NO2A	30	II	trail	LV	9.9	50	Decrepitated at 345°C					
10	NO2A	31	II	trail	LV	7.0	40	Decrepitated at 346.1°C					

Note: FI: fluid inclusion, NO2A/B: doubly polished vein quartz wafer chip ID, Petro: petrographic observation referring to an inclusion's occurrence relative to other inclusions and this may be in cluster, trail or isolation, RT: phase(s) present in an inclusion at room temperature, L: liquid, V: vapour, %Vap: percentage of vapour in an inclusion, Tf1: nucleation/ freezing temperature obtained during the freezing process, $T_{m(CO2)}$: carbon dioxide melting temperature, $T_{h(CO2)}$: carbon dioxide homogenization temperature, Mode: the resulting phase upon homogenization.

Table F4 fluid inclusions type III

Order	Chip	Area	FI	Type	petro	RT	size (μm)	%vap	$T_{m(CO2)}$	$T_{h(CO2)}$	Mode	$X(CO_2)$	$X(CH_4)$	Bulk density (g/cc)	Raman results (bubble)	Raman results (liquid)
1	T4A	Cwest	6	III	trail	LV	10.9	10	−56.4	25.5	L					
2	T14A		1	III	is	L	16.9	0	−57.2	0.2	L	0.9833	0.0167	0.909373		
3	T14A		2	III	trail	LV	15.8	40	−56.8	26.4	L					
4	T14A		3	III	trail	LV	10.6	30	−56.7	27.7	L					
5	T14A		4	III	trail	LV	16.1	40	−57.2	26.8	L					
6	T14A		5	III	trail	LV	24.5	10	−56.8	25.7	L					
7	T14A		6	III	trail	LV	19.2	40	−56.8	25.5	L					
8	T14A		7	III	trail	LV	14.4	50	−57.2	26.9	L					
9	T14A		8	III	trail	LV	17.4	40	−57.2	26.8	L					CO_2, CH_4, N_2
10	T14A		8b	III	trail	L	16.4	0	−56.9	25.5	L					
11	T14A		10	III	trail	L	27.2	0	−57.0	15.0	L	0.9875	0.0125	0.431378		
12	T14A		12	III	trail	LV	14.6	20	−57.2	24.2	L					
13	T14A		14	III	trail	LV	13.2	30	−57.3	23.2	L					
14	T14A		14a	III	trail	L	7.4	0	−57.2	22.8	L					
15	T14A		14b	III	trail	L	8.5	0	−57.3	22.3	L	0.9833	0.0167	0.735901		
16	T14A		14c	III	trail	L	14.2	0	−57.0							

Table F4 continues

Order	Chip	Area	FI	Type	petro	RT	size (μm)	%vap	$T_{m(CO2)}$	$T_{h(CO2)}$	Mode	$X(CO_2)$	$X(CH_4)$	Bulk density (g/cc)	Raman results (bubble)	Raman results (liquid)
17	T14A		14Top L	III	trail	L	13.5	0	−57.4	24.6	L					
18	T14A		14Top R	III	trail	L	10.0	0	−57.0							
19	T14A		15	III	trail	L	22.6	0	−58.4						CO_2, CH_4, N_2	
20	T14A		22	III	trail	L	27.2	0	−57.4							
21	T14A		23	III	trail	V	14.3	100	−58.4	16.5	V	0.9208	0.0792	0.200501		
22	T14A		24	III	trail	V	10.5	100	−57.5	17.1	V	0.9667	0.0333	0.188217		
23	T14A		27	III	trail	LV	16.0	10	−56.6	23.8	L					
24	T14A		28	III	trail	LV	9.8	20	−56.7	25.4	L					
25	T14A		29	III	trail	LV	16.1	30	−56.3	29.2	L				CO_2	CO_2
26	T14A		30	III	trail	L	29.4	0	−56.5	−8.3	L					
27	T14A		31	III	trail	L	16.9	0	−56.5							
28	T14A		35	III	trail	L	12.6	0	−57	11.1	L					
29	NO2A		5	III	is	L	9.2	0	−57.4							
30	NO2A		10	III	trail	L	26.5	0	−57.6							
31	NO2A		11	III	trail	L	14.6	0	−57.6	9.1	L	0.9625	0.0375	0.827827		
32	NO2A		12	III	trail	L	10.5	0	−58.3	7.0	L	0.95	0.05	0.829531		

Table F4 continues

Order	Chip	Area	FI	Type	petro	RT	size (μm)	%vap	$T_{m(CO2)}$	$T_{h(CO2)}$	Mode	$X(CO_2)$	$X(CH_4)$	Bulk density (g/cc)	Raman results (bubble)	Raman results (liquid)
33	NO2A		13	III	trail	L	14.5	0	−57.6	17.5	L	0.9667	0.0333	0.766083		
34	NO2A		14	III	trail	L	10.0	0	−57.9	15.5	L	0.95	0.05	0.761611		
35	NO2A		15	III	trail	L	10.8	0	−57.7	11.9	L					
36	NO2A		16	III	trail	L	8.3	0	−57.7							
37	NO2A		17	III	trail	L	9.5	0	−57.5	11.3	L					
38	NO2A		18	III	trail	L	10.6	0	−57.7							
39	NO2A		19	III	trail	L	8.4	0	−57.1	11.6	L	0.9854	0.0146	0.425425		
40	NO2A		20	III	trail	L	23.3	0	−57.5	14.4	L	0.9667	0.0333	0.794672		
41	NO2A		21	III	trail	L	13.4	0	−57.8	17.9	L	0.9562	0.0438	0.746316		
42	NO2A		22	III	trail	L	18.9	0	−57.3	17.3	L					
43	NO2A		27	III	is	LV	12.1	30	−57.2	22.8	L	0.9833	0.0167	0.730912		
44	NO2A		28	III	trail	L	18.4	0	−57.2							

Note: FI: fluid inclusion, T14A and NO2A: doubly polished vein quartz wafer chip ID, Cwest: central west, Petro: petrographic observation referring to an inclusion's occurrence relative to other inclusions and this may be in cluster, trail or isolation, is: isolated, RT: phase(s) present in an inclusion at room temperature, L: liquid, V: vapour, %Vap: percentage of vapour in an inclusion, T_{mCO2}: carbon dioxide melting temperature, T_{hCO2}: carbon dioxide homogenization temperature, Mode: the resulting phase upon homogenization, $X(CO_2)$ and $X(CH_4)$: CO_2 and CH_4 composition ratios respectively, where the area is not given i.e. T14A and NO2A; the chip was not divided into areas.

Table F5 fluid inclusions type IV

Order	Chip	FI	Type	petro	RT	size	%vap	$T_{h(CH4±H2O±N2)}$	Mode	$X(CH_4)$	$X(H_2O-N_2)$	Bulk density (g/cc)	Raman results
1	T4A	1s	IV	trail	V	21.4	100	−124.0	V	0.95	0.05	0.0016774	
2	T4A	1t	IV	trail	V	21.0	100	−124.0	V	0.95	0.05	0.0016774	
3	T4B	9	IV	trail	V	24.6	100	−121.4	V	0.95	0.05	0.0021637	
4	T4B	11	IV	trail	V	21.2	100	−130.0	V	0.97	0.03	0.001479	
5	T4B	12	IV	trail	V	23.8	100	−127.0	V	0.96	0.04	0.0015349	
6	T4B	17	IV	trail	V	13.3	100	−115.9	V	0.93	0.07	0.002601	
7	T15A	2	IV	trail	V	12.9	100	−84.0	V	0.84	0.16	0.0126177	
8	T15A	3	IV	trail	V	12.5	100	−84.1	V	0.84	0.16	0.0125376	
9	T15A	4	IV	trail	V	11.8	100	−107.5	V	0.91	0.09	0.0041561	
10	T15A	5	IV	trail	V	8.3	100	−79.7	V	0.83	0.17	0.0155423	
11	T15A	6	IV	trail	V	23.8	100	−88.0	V	0.85	0.15	0.0103898	
12	T15A	7	IV	trail	V	17.8	100	−80.6	V	0.83	0.17	0.014697	
13	T15A	8	IV	trail	V	13.4	100	−73.6	V	0.81	0.19	0.0200482	
14	T15A	9	IV	trail	V	12.0	100	−106.6	V	0.91	0.09	0.0044656	
15	T15A	10	IV	trail	V	11.0	100	−101.5	V	0.89	0.11	0.0054587	
16	T15A	11	IV	trail	V	19.8	100	−71.4	V	0.8	0.2	0.021618	

Table F5 continues

Order	Chip	FI	Type	petro	RT	Size (µm)	%vap	$T_{h(CH4±H2O±N2)}$	Mode	$X(CH_4)$	$X(H_2O-N_2)$	Bulk density (g/cc)	Raman results
17	T15A	12	IV	trail	V	10.5	100	−89.6	V	0.86	0.14	0.0100022	
18	T15A	13	IV	trail	V	7.7	100	−75.5	V	0.82	0.18	0.0189452	
19	T15A	14	IV	trail	V	9.8	100	−75.0	V	0.81	0.19	0.0184341	
20	T15A	15	IV	trail	V	20.1	100	−100.6	V	0.89	0.11	0.0058364	
21	T15A	16	IV	trail	V	13.9	100	−102.0	V	0.89	0.11	0.0052585	
22	T15A	17	IV	trail	V	10.3	100	−109.1	V	0.91	0.09	0.0036525	
23	T15A	18	IV	trail	V	14.8	100	−110.0	V	0.91	0.09	0.0033935	
24	T15A	19	IV	trail	V	14.7	100	−100.6	V	0.89	0.11	0.0058364	
25	T15A	20	IV	trail	V	15.3	100	−109.7	V	0.91	0.09	0.003478	
26	T15A	21	IV	trail	V	10.3	100	−109.7	V	0.91	0.09	0.003478	
27	T15A	22	IV	trail	V	11.7	100	−109.7	V	0.91	0.09	0.003478	
28	T15A	23	IV	trail	V	8.5	100	−111.6	V	0.92	0.08	0.0033213	
29	T15A	24	IV	trail	V	16.5	100	−108.4	V	0.91	0.09	0.0038658	
30	T15N Lower vein	4	IV	trail	V	15.5	100	−106.2	V	0.9	0.1	0.0041694	
31	T15N Lower vein	5	IV	trail	V	24.3	100	−105.5	V	0.9	0.1	0.004404	
32	T15N Lower vein	6	IV	trail	V	20.1	100	−110.7	V	0.92	0.08	0.0035814	

Table F5 continues

Order	Chip	FI	Type	petro	RT	Size (µm)	%vap	$T_{h(CH4±H2O±N2)}$	Mode	$X(CH_4)$	$X(H_2O-N_2)$	Bulk density (g/cc)	Raman results
33	T15N Lower vein	7	IV	trail	V	16.9	100	−104.3	V	0.9	0.1	0.0048334	CH_4, N_2
34	T15N Lower vein	8	IV	trail	V	14.0	100	−110.4	V	0.92	0.08	0.0036721	
35	T15N Lower vein	9	IV	trail	V	10.9	100	−110.9	V	0.92	0.08	0.0035221	
36	T15N Lower vein	10	IV	trail	V	20.9	100	−112.1	V	0.92	0.08	0.0031841	
37	T15N Lower vein	11	IV	trail	V	23.3	100	−90.1	V	0.86	0.14	0.0096733	
38	T15N Lower vein	12	IV	trail	V	22.7	100	−85.6	V	0.85	0.15	0.0121482	
39	T15N Lower vein	13	IV	trail	V	15.1	100	−116.6	V	0.93	0.07	0.0024435	CH_4, N_2
40	T15N Lower vein	14	IV	trail	V	12.5	100	−115.6	V	0.93	0.07	0.0026712	
41	T15N Lower vein	15	IV	trail	V	13.9	100	−116.1	V	0.93	0.07	0.0025551	
42	T15N Lower vein	16	IV	trail	V	21.6	100	−114.4	V	0.93	0.07	0.0029687	
43	T15N Lower vein	17	IV	trail	V	10.6	100	−109.3	V	0.91	0.09	0.0035935	
44	T15N Lower vein	18	IV	trail	V	31.1	100	−109.5	V	0.91	0.09	0.0035353	CH_4, N_2
45	T15N Lower vein	19	IV	trail	V	20.5	100	−114.7	V	0.93	0.07	0.0028917	
46	T15N Lower vein	20	IV	trail	V	11.6	100	−113.9	V	0.93	0.07	0.003101	CH_4, N_2
47	T15N Lower vein	21	IV	trail	V	22.1	100	−75.0	V	0.81	0.19	0.0184341	
48	T15N Upper vein	4	IV	trail	V	19.6	100	−108.7	V	0.91	0.09	0.0037731	
49	T15N Upper vein	5	IV	trail	V	12.2	100	−107.0	V	0.91	0.09	0.0043256	

Table F5 continues

Order	Chip	FI	Type	petro	RT	Size (µm)	%vap	$T_{h(CH4±H2O±N2)}$	Mode	$X(CH_4)$	$X(H_2O-N_2)$	Bulk density (g/cc)	Raman results
50	T15N Upper vein	6	IV	trail	V	11.8	100	−108.2	V	0.91	0.09	0.0039287	
51	T15N Upper vein	7	IV	trail	V	23.5	100	−100.7	V	0.89	0.11	0.0057933	
52	T15N Upper vein	8	IV	is	V	18.8	100	−101.9	V	0.89	0.11	0.005298	
53	T15N Upper vein	9	IV	is	V	14.2	100	−106.8	V	0.91	0.09	0.0043951	
54	T15N Lower vein	1	IV	trail	V	41.6	100	No phase change between -190 and 34°C					
55	T15N Lower vein	2	IV	trail	V	30.1	100	No phase change between -190 and 34°C					
56	T15N Lower vein	3	IV	trail	V	42.4	100	No phase change between -190 and 34°C					
57	T15N Lower vein	22	IV	trail	V	10.5	100	No phase change between -190 and 34°C					
58	T15N Lower vein	23	IV	trail	V	9.7	100	No phase change between -190 and 34°C					
59	T15N Lower vein	24	IV	trail	V	8.3	100	No phase change between -190 and 34°C					
60	T15N Lower vein	25	IV	trail	V	13.8	100	No phase change between -190 and 34°C					
61	T15N Upper vein	2	IV	trail	V	17.1	100	No phase change between -190 and 34°C					

Note: FI: fluid inclusion, T15A, T15N Upper vein and T15N Lower vein: doubly polished vein quartz wafer chip ID, Petro: petrographic observation referring to an inclusion's occurrence relative to other inclusions and this may be in cluster, trail or isolation, is: isolated, RT: phase(s) present in an inclusion at room temperature, V: vapour, %Vap: percentage of vapour in an inclusion, T_h: total homogenization temperature, Mode: the resulting phase upon homogenization, $X(CO_2)$ and $X(CH_4)$: CO_2 and CH_4 composition ratios respectively.

Table F6 fluid inclusions type V

Order	Chip	FI	Type	petro	RT	Size (µm)	%vap	$T_{m(CO2)}$	T_h	Mode	Raman results
1	T14A	11	V	trail	L	26.5	0	−63.0	−31.4	L	
2	T14A	13	V	trail	L	18.2	0	−62.9			
3	T14A	21	V	trail	L	13.2	0	−64.8			
4	T14A	25	V	trail	L	19.0	0	−62.1	−22.1	L	CO_2, CH_4, N_2
5	T14A	26	V	trail	L	12.8	0	−64.8	−22.4	L	CO_2, CH_4, N_2

Note: FI: fluid inclusion, T14A: doubly polished vein quartz wafer chip ID, Petro: petrographic observation referring to an inclusion's occurrence relative to other inclusions and this may be in cluster, trail or isolation, RT: phase(s) present in an inclusion at room temperature, L: liquid, %Vap: percentage of vapour in an inclusion, T_{mCO2}: carbon dioxide melting temperature, T_{hCO2}: total homogenization temperature, Mode: the resulting phase upon homogenization.

Appendix G: $^{40}Ar/^{39}Ar$ dating data table Sample NO 2 grain 1 and 2

Ar isotope and age data for sample: No−2, Grain 1

Calculated at 11−28−2017 − 12:57:11

J−value used: 0.008712 +/− 0.000021

Ca/K and Cl/K factors: 1.9557 +/− 0.0118 0.1226 +/− 0.0015 from file: Irrad_2017_Aug_23_Jvals.csv

Exponential fractionation factor: −0.298

Common 40Ar/36Ar value used: 298.56 +/− 0.30

number of steps: 9

Step name	40.0 (nA)	2SE Abs	(nA)	2SE Abs	39.0 (nA)	2SE Abs	(nA)	2SE Abs	38.0 (nA)	2SE Abs
2892_No−2 _h−p_16_1_10.36A		35.96755		isotopes	2892	0.001445	1.54E−05	6.48E−07	1.34E−06	5.13E−06
2894_No−2_ h−p_16_1_10.76A	1.51E−05	1.73E−06	5.38E−06	1.34E−06	2894	0.007598	1.88E−05	2.44E−05	1.40E−06	1.76E−05
2895_No−2_ h−p_16_1_11.00A	4.09E−05	1.85E−06	5.59E−06	1.13E−06	2895	0.155974	1.26E−04	0.00054	2.87E−06	3.63E−05
2896_No−2_ h−p_16_1_11.24A	0.000465	3.81E−06	2.98E−05	1.42E−06	2896	0.012296	2.24E−05	2.11E−05	1.56E−06	4.7E−06
2897_No−2_ h−p_16_1_11.48A	−5.2E−07	1.46E−06	7.92E−07	1.07E−06	2897	1.462217	2.44E−04	0.003045	9.38E−06	4.62E−05
2899_No−2_ h−p_16_1_11.72A	−4.6E−06	1.62E−06	9.29E−06	1.38E−06	2899	0.502871	9.34E−05	0.001085	4.64E−06	1.65E−05
2900_No−2_ h−p_16_1_11.96A	1.68E−05	1.78E−06	8.21E−06	8.75E−07	2900	1.297014	1.48E−04	0.002658	6.00E−06	4.13E−05
2901_No−2_ h−p_16_1_12.20A	3.77E−05	1.89E−06	1.87E−05	1.35E−06	2901	0.06185	5.17E−05	0.000206	1.82E−06	5E−06
2902_No−2_ h−p_16_1_12.44A	9.25E−06	1.23E−06	3.48E−06	1.37E−06	2902	0.043872	2.23E−05	7.41E−05	1.37E−06	4.88E−06

Grain 1 Ar/ Ar data table continues

Step name	39/40 Ca+KCorr	sigma	36/40 Ca+KCorr	sigma	37/39 Ca+KCorr	sigma	38/39 Ca+KCorr	sigma	40/39 rad	sigma
2892_No−2 _h−p_16_1_10.36A	0.000428	9.06E−03	0.003605	1.54E−02	54.0317	272.7247	6.588512	33.2812	−178.518	15558.53
2894_No−2_ h−p_16_1_10.76A	0.003179	3.80E−04	0.00071	3.92E−03	3.735464	0.664265	0.675629	0.177742	247.8435	44.83677
2895_No−2_ h−p_16_1_11.00A	0.003431	3.62E−05	0.000183	1.72E−05	1.919725	0.045672	0.056731	0.007827	275.5152	3.451994
2896_No−2_ h−p_16_1_11.24A	0.0017	2.81E−04	6.25E−05	1.36E−03	0	0	0.214315	0.147565	577.2816	87.25275
2897_No−2_ h−p_16_1_11.48A	0.002067	1.27E−05	6.16E−06	3.17E−06	0	0	0.014508	0.000995	482.9256	2.940158
2899_No−2_ h−p_16_1_11.72A	0.002143	1.83E−05	1.58E−05	4.45E−06	0.03437	0.008881	0.013657	0.003786	464.5336	4.057043
2900_No−2_ h−p_16_1_11.96A	0.002034	9.76E−06	1.4E−05	2.14E−06	0.031541	0.003863	0.014141	0.001345	489.521	2.194067
2901_No−2_ h−p_16_1_12.20A	0.003307	5.74E−05	5.44E−05	3.74E−03	0.099902	0.032361	0.020981	0.010814	297.5175	6.864771
2902_No−2_ h−p_16_1_12.44A	0.001677	5.95E−05	0.0001	1.49E−03	0.116833	0.089905	0.054142	0.029896	578.4023	24.73691

Grain 1 Ar/ Ar data table continues

Step name	%39Ar	Age Ma	+/−95%	Incl(1/0)	Ca/K	sigma	Cl/K	sigma
2892_No−2 _h−p_16_1_10.36A	0.008209	0	8172.709	0	105.6711	533.3747	0.807872	4.080897
2894_No−2_ h−p_16_1_10.76A	0.318868	2076.068	464.4601	0	7.305538	1.299867	0.082844	0.021818
2895_No−2_ h−p_16_1_11.00A	7.053636	2208.785	33.92647	0	3.754453	0.092149	0.006956	0.000963
2896_No−2_ h−p_16_1_11.24A	0.275178	3242.483	444.3673	0	0	0	0.026279	0.018097
2897_No−2_ h−p_16_1_11.48A	39.775	2977.952	23.22875	1	0	0	0.001779	0.000124
2899_No−2_ h−p_16_1_11.72A	14.1809	2921.546	30.11971	1	0.067218	0.017374	0.001675	0.000465
2900_No−2_ h−p_16_1_11.96A	34.72533	2997.757	21.15622	1	0.061686	0.007565	0.001734	0.000166
2901_No−2_ h−p_16_1_12.20A	2.693726	2307.76	59.90501	0	0.195382	0.0633	0.002573	0.001326
2902_No−2_ h−p_16_1_12.44A	0.969149	3245.403	130.7563	0	0.228493	0.175835	0.006639	0.003667

Weighted average of included steps

37/39corr	sigma	38/39corr	sigma	40/39 rad	sigma	%39Ar sum	Age Ma	+/−95%	Ca/K	sigma	Cl/K	sigma
0.032361	3.90E−03	0.014228	9.21E−04	482.5744	1.651539	88.68123	2976.891	18.14525	0.06329	0.007641	0.001745	0.000115

Inverse isochron calculation results

40Ar/39Ar(I)	sigma	40Ar/36Ar	sigma	app. age	+/−95%
438.801	1203.9	−19248.9	38227.23	2839.546	4618.754

End Of Results

Ar isotope and age data for sample: No−2, Grain 2

Calculated at 11−28−2017 − 13:00:44

J−value used: 0.008714 +/− 0.000024

Ca/K and Cl/K factors: 1.9557 +/− 0.0375 0.1226 +/− 0.0030 from file: Irrad_2017_Aug_23_Jvals.csv

Exponential fractionation factor: −0.298

Common 40Ar/36Ar value used: 298.56 +/− 0.30

Number of steps: 14

Step name	40.0 (nA)	2SE Abs	(nA)	2SE Abs	39.0 (nA)	2SE Abs	(nA)	2SE Abs	38.0 (nA)	2SE Abs
2907_No−2_ h−p_60_2_9.80A		35.96755		isotopes	2907	0.024628	1.93E−05	0.00125	5.42E−06	3.53E−05
2908_No−2_ h−p_60_2_10.05A	6.7E−05	1.84E−06	1.8E−05	1.19E−06	2908	0.059795	7.34E−05	0.001952	4.47E−06	3.48E−05
2909_No−2_ h−p_60_2_10.29A	0.000263	3.21E−06	3.09E−05	1.20E−06	2909	0.148199	7.16E−05	0.004145	1.26E−05	8.26E−05
2910_No−2_ h−p_60_2_10.54A	0.000144	2.24E−06	4.45E−05	1.35E−06	2910	0.601515	6.03E−04	0.017392	1.99E−05	0.000251
2912_No−2_ h−p_60_2_10.78A	2.62E−05	2.02E−06	3.76E−05	2.56E−06	2912	1.518708	2.76E−04	0.04432	3.07E−05	0.00059
2913_No−2_ h−p_60_2_11.03A	7.75E−05	1.51E−06	4.71E−05	1.60E−06	2913	1.925804	2.21E−04	0.05617	3.40E−05	0.000736
2914_No−2_ h−p_60_2_11.28A	9.23E−06	2.02E−06	2.23E−05	1.35E−06	2914	3.138328	3.99E−04	0.091396	4.17E−05	0.001191
2915_No−2_ h−p_60_2_11.52A	8.64E−06	1.42E−06	2.29E−05	1.70E−06	2915	3.846795	5.14E−04	0.111999	4.99E−05	0.001472
2917_No−2_ h−p_60_2_11.77A	2.2E−05	1.62E−06	3.49E−05	1.81E−06	2917	1.701123	4.00E−04	0.049699	2.05E−05	0.000653
2918_No−2_ h−p_60_2_12.02A	2.85E−06	2.12E−06	7.38E−06	1.74E−06	2918	2.480095	4.24E−04	0.072863	4.36E−05	0.000982
2919_No−2_ h−p_60_2_12.26A	1.49E−05	1.46E−06	1.29E−05	1.79E−06	2919	2.259178	4.91E−04	0.066801	3.75E−05	0.000937
2920_No−2_ h−p_60_2_12.51A	1.56E−06	1.71E−06	1.54E−05	1.15E−06	2920	2.563939	3.13E−04	0.07545	4.00E−05	0.001008
2922_No−2_ h−p_60_2_12.75A	−1.5E−06	1.38E−06	4.49E−06	1.32E−06	2922	0.427501	1.03E−04	0.012585	1.28E−05	0.000177
2923_No−2_ h−p_60_2_13A	−5.2E−06	1.70E−06	3.93E−06	1.22E−06	2923	0.646941	1.58E−04	0.018836	1.89E−05	0.000243

Grain 2 Ar/Ar data table continues

Step name	39/40 Ca+KCorr	sigma	36/40 Ca+KCorr	sigma	37/39 Ca+KCorr	sigma	38/39 Ca+KCorr	sigma	40/39 rad	sigma
2907_No−2_ h−p_60_2_9.80A	0.050513	4.25E−04	0.00071	8.99E−05	0.119761	0.008097	0.025387	0.002082	15.60293	0.575245
2908_No−2_ h−p_60_2_10.05A	0.032445	1.67E−04	0.000499	3.92E−05	0.300563	0.009104	0.014831	0.001545	26.22984	0.370969
2909_No−2_ h−p_60_2_10.29A	0.0278	1.65E−04	0.000291	1.78E−05	0.077871	0.003003	0.0178	0.000991	32.84849	0.293912
2910_No−2_ h−p_60_2_10.54A	0.02874	8.49E−05	6.06E−05	9.04E−06	0.00337	0.000632	0.013927	0.000337	34.1657	0.128145
2912_No−2_ h−p_60_2_10.78A	0.029009	4.10E−05	3.01E−05	1.90E−06	0.003906	0.000186	0.013025	0.00017	34.16282	5.54E−02
2913_No−2_ h−p_60_2_11.03A	0.028992	3.49E−05	1.12E−05	1.36E−06	0.000367	0.000196	0.012933	0.000156	34.37607	4.24E−02
2914_No−2_ h−p_60_2_11.28A	0.028948	2.68E−05	7.08E−06	1.15E−06	0.000211	8.43E−05	0.012889	0.000151	34.47119	3.52E−02

Grain 2 Ar/Ar data table continues

Step name	39/40 Ca+KCorr	sigma	36/40 Ca+KCorr	sigma	37/39 Ca+KCorr	sigma	38/39 Ca+KCorr	sigma	40/39 rad	sigma
2915_No−2_ h−p_60_2_11.52A	0.028941	2.69E−05	8.81E−06	9.09E−07	0.000439	7.87E−05	0.012988	0.000139	34.46253	3.22E−02
2917_No−2_ h−p_60_2_11.77A	0.029041	2.77E−05	4.21E−06	9.24E−05	0.000128	0.000233	0.013002	0.000202	34.39098	3.66E−02
2918_No−2_ h−p_60_2_12.02A	0.029204	3.57E−05	5.03E−06	1.74E−06	0.000458	0.000109	0.013337	0.000179	34.19038	4.53E−02
2919_No−2_ h−p_60_2_12.26A	0.029393	3.50E−05	6.62E−06	9.34E−07	5.2E−05	0.000139	0.013882	0.000131	33.95463	4.02E−02
2920_No−2_ h−p_60_2_12.51A	0.029252	3.02E−05	1.7E−06	1.39E−05	0	0	0.01325	0.000229	34.16844	3.78E−02
2922_No−2_ h−p_60_2_12.75A	0.029264	6.04E−05	8.93E−06	6.33E−05	0	0	0.013862	0.000581	34.08057	8.92E−02
2923_No−2_ h−p_60_2_13A	0.028942	5.88E−05	1.7E−05	9.89E−06	0	0	0.012713	0.000485	34.37646	8.79E−02

Grain 2 Ar/Ar data table continues

Step name	%39Ar	Age Ma	+/−95%	Incl(1/0)	Ca/K	sigma	Cl/K	sigma
2907_No−2_ h−p_60_2_9.80A	0.19985	230.0614	15.71847	0	0.234219	0.016459	0.003113	0.000267
2908_No−2_ h−p_60_2_10.05A	0.312391	371.4874	9.37891	0	0.587819	0.021065	0.001819	0.000195
2909_No−2_ h−p_60_2_10.29A	0.663398	454.2791	7.886798	0	0.152294	0.006558	0.002183	0.000133
2910_No−2_ h−p_60_2_10.54A	2.783224	470.3122	4.613563	1	0.006592	0.001242	0.001708	5.9E−05
2912_No−2_ h−p_60_2_10.78A	7.092899	470.2773	3.267521	1	0.007639	0.000392	0.001597	4.45E−05
2913_No−2_ h−p_60_2_11.03A	8.989212	472.8597	3.41126	1	0.000718	0.000383	0.001586	4.35E−05
2914_No−2_ h−p_60_2_11.28A	14.62664	474.0104	3.393105	1	0.000413	0.000165	0.00158	4.31E−05
2915_No−2_ h−p_60_2_11.52A	17.92401	473.9056	3.175777	1	0.000858	0.000155	0.001593	4.28E−05
2917_No−2_ h−p_60_2_11.77A	7.953578	473.0401	3.348292	1	0.00025	0.000455	0.001594	4.64E−05
2918_No−2_ h−p_60_2_12.02A	11.6609	470.6112	3.370836	1	0.000895	0.000214	0.001635	4.58E−05
2919_No−2_ h−p_60_2_12.26A	10.69083	467.7527	3.268522	1	0.000102	0.000272	0.001702	4.49E−05
2920_No−2_ h−p_60_2_12.51A	12.07464	470.3454	3.346795	1	0	0	0.001625	4.89E−05
2922_No−2_ h−p_60_2_12.75A	2.014129	469.2803	3.933005	1	0	0	0.0017	8.26E−05
2923_No−2_ h−p_60_2_13A	3.014297	472.8644	3.933897	1	0	0	0.001559	7.08E−05

Weighted average of included steps of Ar/Ar dating given above

37/39corr	sigma	38/39corr	sigma	40/39 rad	sigma	%39Ar sum	Age Ma	+/−95%	Ca/K	sigma	Cl/K	sigma
0.000713	5.30E−05	0.013178	5.89E−05	34.28694	1.44E−02	98.82436	471.7808	3.252454	0.001394	0.000107	0.001616	4.04E−05

Inverse isochron calculation results

40Ar/39Ar(I)	sigma	40Ar/36Ar	sigma	app. age	+/−95%
34.50644	8.154657	613.1623	415.1751	474.4366	194.8292

End Of Results

Appendix H: LA-ICP MS analytical results from U/Pb dating of the reference material

						Data for Tera-Wasserburg plot [a]				Data for Wetherill plot [a]					Dates (Ma)									Concordance [b]
Spot number	^{206}Pb (CPS)	^{204}Pb (CPS)	^{206}Pb/ ^{204}Pb	U (ppm)	Th/ U	^{238}U/^{206}Pb	2 s	^{207}Pb/^{206}Pb	2 s	^{207}Pb/^{235}U	2 s	^{206}Pb/^{238}U	2 s	rho	^{207}Pb/^{206}Pb	2 s	2s sys	^{206}Pb/^{238}U	2 s	2s sys	^{207}Pb/^{235}U	2 s	2s sys	%
Ples - 1	94800	b.d.	b.d	367	0.10	18.60	0.29	0.0546	0.0011	0.4049	0.0094	0.0538	0.0009	0.68	369	45	47	338	5	8	344	7	9	98
Ples - 2	99000	b.d.	b.d	402	0.13	18.93	0.30	0.0546	0.0011	0.3993	0.0092	0.0528	0.0008	0.68	372	43	47	332	5	8	341	7	9	97
Ples - 3	82600	b.d.	b.d	324	0.10	18.21	0.28	0.0530	0.0012	0.4034	0.0099	0.0549	0.0008	0.62	303	48	53	345	5	8	343	7	10	100
Ples - 4	83000	b.d.	b.d	336	0.10	18.67	0.29	0.0539	0.0012	0.3996	0.0096	0.0536	0.0008	0.65	348	49	52	336	5	8	341	7	10	99
Ples - 5	86400	b.d.	b.d	347	0.10	18.55	0.29	0.0535	0.0011	0.3989	0.0095	0.0539	0.0008	0.65	326	47	49	339	5	8	340	7	10	100
Ples - 6	92400	b.d.	b.d	360	0.10	18.61	0.28	0.0542	0.0011	0.4026	0.0093	0.0537	0.0008	0.64	356	45	47	337	5	8	343	7	9	98
Ples - 7	91400	b.d.	b.d	372	0.10	18.53	0.28	0.0528	0.0011	0.3939	0.0094	0.0540	0.0008	0.64	301	49	51	339	5	8	336	7	9	101
Ples - 8	91800	b.d.	b.d	381	0.10	18.69	0.29	0.0535	0.0011	0.3942	0.0096	0.0535	0.0008	0.64	331	48	50	336	5	8	337	7	9	100
Ples - 9	88900	b.d.	b.d	367	0.10	18.60	0.29	0.0537	0.0012	0.3977	0.0095	0.0538	0.0009	0.66	332	48	52	338	5	8	340	7	9	99
Ples - 10	85000	b.d.	b.d	356	0.13	18.72	0.29	0.0531	0.0011	0.3899	0.0092	0.0534	0.0008	0.67	317	47	48	336	5	8	334	7	9	100
Ples - 11	77200	b.d.	b.d	320	0.10	18.40	0.30	0.0533	0.0012	0.3974	0.0097	0.0544	0.0009	0.68	314	47	52	341	6	8	339	7	9	101
Ples - 12	77100	b.d.	b.d	319	0.10	18.30	0.29	0.0534	0.0012	0.4011	0.0099	0.0547	0.0009	0.64	327	50	52	343	5	8	343	7	8	100
Ples - 13	91200	b.d.	b.d	385	0.11	18.45	0.29	0.0538	0.0011	0.4031	0.0099	0.0542	0.0009	0.64	347	46	48	340	5	8	343	7	10	99
Ples - 14	72600	b.d.	b.d	309	0.10	18.49	0.30	0.0543	0.0012	0.4018	0.0099	0.0541	0.0009	0.66	354	50	51	340	5	8	343	7	9	99
Ples - 15	84300	b.d.	b.d	368	0.11	18.64	0.30	0.0530	0.0011	0.3933	0.0092	0.0537	0.0009	0.69	314	48	50	337	5	8	337	7	9	100
Ples - 16	80500	b.d.	b.d	343	0.09	18.26	0.30	0.0529	0.0012	0.3994	0.0096	0.0548	0.0009	0.69	303	49	53	344	6	8	340	7	10	101
Ples - 17	89900	b.d.	b.d	389	0.10	18.60	0.29	0.0536	0.0011	0.3968	0.0092	0.0538	0.0009	0.68	334	46	48	338	5	8	339	7	9	100
Ples - 18	81600	b.d.	b.d	353	0.10	18.67	0.28	0.0537	0.0011	0.3949	0.0090	0.0536	0.0008	0.66	334	45	48	336	5	8	337	7	9	100
Ples - 19	87500	b.d.	b.d	381	0.10	18.52	0.28	0.0545	0.0012	0.4053	0.0098	0.0540	0.0008	0.64	361	48	51	339	5	8	345	7	10	98
Ples - 20	86400	b.d.	b.d	372	0.10	18.50	0.28	0.0533	0.0011	0.3964	0.0092	0.0541	0.0008	0.65	316	45	48	339	5	8	338	7	9	100
Ples - 21	94800	b.d.	b.d	407	0.11	18.29	0.27	0.0536	0.001	0.4053	0.0092	0.0547	0.0008	0.66	337	42	44	343	5	8	345	7	9	100

Uncertainties quoted without components related to systematic error unless otherwise stated. Total systematic uncertainties (s sys): ^{206}Pb/^{238}U = 1.8 %; ^{207}Pb/^{206}Pb = 0.5 (2s).

[a] Data not corrected for common Pb

[b] Concordance calculated as: (^{206}Pb^{238}U date/^{207}Pb^{235}U date)*100

Appendix I: LA-ICP MS analytical results from U/Pb dating of the foliated granite sample (FG)

						Data for Tera-Wasserburg plot [a]				Data for Wetherill plot [a]					Dates (Ma)									Concordance [b]
Spot number	^{206}Pb (CPS)	^{204}Pb (CPS)	^{206}Pb/^{204}Pb	U (ppm)	Th/U	^{238}U/^{206}Pb	2 s	^{207}Pb/^{206}Pb	2 s	^{207}Pb/^{235}U	2 s	^{206}Pb/^{238}U	2 s	rho	^{207}Pb/^{206}Pb	2 s	2s sys	^{206}Pb/^{238}U	2 s	2s sys	^{207}Pb/^{235}U	2 s	2s sys	%
FG - 3	753000	b.d.	b.d	4190	0.02	24.81	0.36	0.1048	0.0016	0.5814	0.0110	0.0403	0.0006	0.76	1708	28	30	255	4	6	465	7	10	55
FG - 5	1175000	b.d.	b.d	15570	0.03	59.38	0.92	0.2326	0.0034	0.5386	0.0100	0.0168	0.0003	0.83	3066	24	25	108	2	3	437	7	10	25
FG - 6	250000	b.d.	b.d	1250	0.06	23.50	0.40	0.1088	0.0031	0.6360	0.0170	0.0426	0.0007	0.64	1762	54	55	269	5	7	499	11	14	54
FG - 7	844000	b.d.	b.d	5330	0.02	27.13	0.44	0.0992	0.0017	0.5050	0.0098	0.0369	0.0006	0.84	1608	37	40	233	4	6	415	7	9	56
FG - 8	869000	b.d.	b.d	5170	0.01	26.39	0.40	0.0827	0.0014	0.4312	0.0096	0.0379	0.0006	0.69	1255	34	35	240	4	6	364	7	9	66
FG - 9	1147000	b.d.	b.d	13420	0.01	51.44	0.85	0.2646	0.0043	0.7079	0.0140	0.0194	0.0003	0.83	3268	26	27	124	2	3	543	8	12	23
FG - 10	748400	b.d.	b.d	4092	0.00	24.08	0.35	0.0713	0.0025	0.4069	0.0150	0.0415	0.0006	0.40	964	62	72	262	4	6	347	11	12	76
FG - 11	450000	b.d.	b.d	1890	0.03	20.61	0.32	0.1160	0.0029	0.7730	0.0230	0.0485	0.0008	0.52	1888	39	46	305	5	7	581	12	16	53
FG - 12	1165000	b.d.	b.d	9020	0.01	36.08	0.55	0.1692	0.0051	0.6430	0.0220	0.0277	0.0004	0.44	2522	56	57	176	3	4	502	14	17	35
FG - 13	725000	b.d.	b.d	4520	0.02	27.56	0.44	0.1005	0.002	0.5026	0.0110	0.0363	0.0006	0.73	1626	36	38	230	4	5	413	7	10	56
FG - 14	775000	b.d.	b.d	3600	0.06	21.04	0.32	0.0814	0.0015	0.5314	0.0110	0.0475	0.0007	0.74	1220	38	39	299	5	7	432	8	10	69
FG - 15	795000	b.d.	b.d	3822	0.03	21.27	0.38	0.0810	0.0011	0.5251	0.0110	0.0470	0.0008	0.84	1218	28	31	296	5	7	428	7	10	69
FG - 16	370000	b.d.	b.d	1403	0.02	18.76	0.30	0.0764	0.0012	0.5615	0.0110	0.0533	0.0008	0.80	1104	34	35	335	5	8	452	7	10	74
FG - 17	579000	b.d.	b.d	2121	0.01	17.91	0.28	0.0982	0.002	0.7550	0.0170	0.0559	0.0009	0.68	1583	37	39	350	5	8	571	10	13	61
FG - 18	635000	b.d.	b.d	3810	0.02	27.34	0.40	0.0772	0.0011	0.3897	0.0069	0.0366	0.0005	0.83	1122	28	30	232	3	5	334	5	7	69
FG - 19	643000	b.d.	b.d	3630	0.01	27.79	0.50	0.1376	0.0038	0.6840	0.0250	0.0360	0.0007	0.49	2185	49	51	228	4	6	527	15	19	43
FG - 20	648000	b.d.	b.d	3080	0.01	21.59	0.36	0.0832	0.0017	0.5287	0.0120	0.0463	0.0008	0.74	1268	40	41	292	5	7	431	8	11	68
FG - 21	492000	b.d.	b.d	3060	0.02	31.42	0.48	0.1345	0.0025	0.5900	0.0130	0.0318	0.0005	0.70	2151	33	35	202	3	5	470	9	12	43
FG - 22	788000	b.d.	b.d	3915	0.00	22.29	0.35	0.0689	0.0011	0.4263	0.0085	0.0449	0.0007	0.79	894	32	35	283	4	7	360	6	8	78
FG - 23	982000	b.d.	b.d	8310	0.01	37.81	0.67	0.1379	0.0027	0.5046	0.0110	0.0265	0.0005	0.82	2196	34	35	168	3	4	415	8	10	41
FG - 26	999600	b.d.	b.d	7860	0.02	34.98	0.60	0.1069	0.0015	0.4224	0.0080	0.0286	0.0005	0.90	1745	26	27	182	3	4	358	6	8	51
FG - 27	928000	b.d.	b.d	6630	0.01	35.04	0.52	0.2171	0.0029	0.8536	0.0160	0.0285	0.0004	0.79	2956	21	23	181	3	4	626	9	13	29
FG - 28	882000	b.d.	b.d	6270	0.01	32.62	0.47	0.1315	0.0024	0.5557	0.0110	0.0307	0.0004	0.72	2110	33	35	195	3	4	448	8	10	43

	Appendix I continues					Data for Tera-Wasserburg plot [a]				Data for Wetherill plot [a]					Dates (Ma)									Concordance [b]
Spot number	^{206}Pb (CPS)	^{204}Pb (CPS)	$^{206}Pb/^{204}Pb$	U (ppm)	Th/U	$^{238}U/^{206}Pb$	2 s	$^{207}Pb/^{206}Pb$	2 s	$^{207}Pb/^{235}U$	2 s	$^{206}Pb/^{238}U$	2 s	rho	$^{207}Pb/^{206}Pb$	2 s	2s sys	$^{206}Pb/^{238}U$	2 s	2s sys	$^{207}Pb/^{235}U$	2 s	2s sys	%
FG - 30	1028000	b.d.	b.d	11470	0.01	49.78	0.94	0.2543	0.005	0.7080	0.0190	0.0201	0.0004	0.70	3202	29	32	128	2	3	542	11	15	24
FG - 31	1482000	b.d.	b.d	12600	0.00	36.98	0.72	0.1970	0.003	0.7380	0.0180	0.0270	0.0005	0.80	2799	25	26	172	3	5	561	10	14	31
FG - 33	664000	b.d.	b.d	4480	0.00	29.42	0.53	0.0697	0.0013	0.3268	0.0075	0.0340	0.0006	0.78	911	39	41	216	4	5	288	6	7	75
FG - 34	590000	b.d.	b.d	3310	0.01	27.32	0.40	0.1035	0.0028	0.5197	0.0170	0.0366	0.0005	0.44	1682	43	51	232	3	5	425	11	13	55
FG - 35	1007000	b.d.	b.d	8850	0.01	39.71	0.60	0.1621	0.002	0.5624	0.0096	0.0252	0.0004	0.88	2476	21	23	160	2	4	453	6	9	35
FG - 37	567000	b.d.	b.d	3600	0.00	29.99	0.43	0.0635	0.00098	0.2927	0.0060	0.0333	0.0005	0.70	719	34	36	211	3	5	261	5	7	81
FG - 38	830000	b.d.	b.d	8050	0.01	41.79	1.03	0.1390	0.0043	0.4559	0.0110	0.0239	0.0006	0.99	2205	49	51	152	4	5	381	8	10	40
FG - 39	837000	b.d.	b.d	4920	0.01	26.69	0.38	0.1402	0.0034	0.7250	0.0190	0.0375	0.0005	0.55	2209	43	45	237	3	5	552	12	15	43
FG - 40	544000	b.d.	b.d	3850	0.02	35.64	0.57	0.1295	0.0029	0.5014	0.0140	0.0281	0.0005	0.57	2087	33	40	178	3	4	412	8	12	43

Uncertainties quoted without components related to systematic error unless otherwise stated. Total systematic uncertainties (s sys): $^{206}Pb/^{238}U$ = 1.8 %; $^{207}Pb/^{206}Pb$ = 0.5 (2s).

[a] Data not corrected for common Pb

[b] Concordance calculated as: (^{206}Pb-^{238}U date/^{207}Pb-^{235U} date)*100

Appendix J: LA-ICP MS analytical results from U/Pb dating of the foliated granite sample (GT) - trench 9

						Data for Tera-Wasserburg plot [a]				Data for Wetherill plot [a]					Dates (Ma)									Concordance [b]
Spot number	^{206}Pb (CPS)	^{204}Pb (CPS)	^{206}Pb/^{204}Pb	U (ppm)	Th/U	^{238}U/^{206}Pb	2 s	^{207}Pb/^{206}Pb	2 s	^{207}Pb/^{235}U	2 s	^{206}Pb/^{238}U	2 s	rho	^{207}Pb/^{206}Pb	2 s	2s sys	^{206}Pb/^{238}U	2 s	2s sys	^{207}Pb/^{235}U	2 s	2s sys	%
GT - 3	843000	b.d.	b.d	21170	0.04	105.75	1.57	0.3570	0.0053	0.4657	0.0082	0.0095	0.0001	0.84	3734	22	24	61	1	2	388	6	8	16
GT - 4	493000	b.d.	b.d	1145	0.15	9.92	0.15	0.0988	0.0015	1.3720	0.0260	0.1008	0.0015	0.79	1599	29	31	619	9	14	876	11	16	71
GT - 5	392000	b.d.	b.d	629	0.45	7.26	0.11	0.0938	0.002	1.7800	0.0480	0.1378	0.0021	0.57	1493	42	44	832	12	19	1035	18	24	80
GT - 6	838000	b.d.	b.d	15230	0.40	77.04	1.60	0.3026	0.0056	0.5389	0.0110	0.0130	0.0003	0.99	3480	29	31	83	2	3	438	7	10	19
GT - 11	921000	b.d.	b.d	20030	0.05	94.38	1.43	0.3379	0.0052	0.4921	0.0090	0.0106	0.0002	0.83	3651	24	26	68	1	2	406	6	9	17
GT - 12	407000	b.d.	b.d	1212	0.21	12.93	0.18	0.0624	0.00091	0.6625	0.0120	0.0773	0.0011	0.79	678	31	33	480	7	11	516	7	11	93
GT - 14	727000	b.d.	b.d	20400	0.20	115.21	2.12	0.3556	0.0052	0.4250	0.0073	0.0087	0.0002	0.99	3728	22	24	56	1	2	360	5	8	15
GT - 16	628000	b.d.	b.d	24170	0.16	165.40	2.43	0.3938	0.0047	0.3280	0.0055	0.0060	0.0001	0.88	3883	19	21	39	1	2	288	4	7	14
GT - 19	754700	b.d.	b.d	18470	0.07	99.50	1.88	0.4050	0.0057	0.5615	0.0110	0.0101	0.0002	0.97	3925	21	23	64	1	2	452	7	10	14
GT - 20	943000	b.d.	b.d	18900	0.34	82.03	1.55	0.3638	0.006	0.6117	0.0110	0.0122	0.0002	0.99	3766	26	29	78	2	3	484	7	10	16
GT - 22	561000	b.d.	b.d	5170	0.07	38.31	0.62	0.1405	0.0022	0.5045	0.0110	0.0261	0.0004	0.74	2229	26	29	166	3	4	414	7	10	40
GT - 26	615100	b.d.	b.d	3088	0.92	20.81	0.32	0.1465	0.0025	0.9700	0.0210	0.0481	0.0007	0.70	2303	30	31	303	5	7	687	11	15	44
GT - 27	829000	b.d.	b.d	12640	0.04	64.98	1.10	0.2668	0.0049	0.5635	0.0130	0.0154	0.0003	0.73	3279	30	31	98	2	2	453	9	12	22
GT - 29	810000	b.d.	b.d	4870	0.05	24.60	0.45	0.0806	0.0015	0.4504	0.0130	0.0407	0.0008	0.64	1209	34	38	257	5	6	377	9	11	68
GT - 30	720000	b.d.	b.d	4790	0.03	26.88	0.55	0.1438	0.004	0.7330	0.0200	0.0372	0.0008	0.75	2262	54	56	236	5	6	557	11	15	42

Uncertainties quoted without components related to systematic error unless otherwise stated. Total systematic uncertainties (s sys): ^{206}Pb/^{238}U = 1.8 %; ^{207}Pb/^{206}Pb = 0.5 (2s).

[a] Data not corrected for common Pb

[b] Concordance calculated as: (^{206}Pb-^{238}U date/^{207}Pb-^{235U} date)*100

Appendix K: LA-ICP MS analytical results from U/Pb dating of the non-foliated granite sample (UG)

						Data for Tera-Wasserburg plot [a]				Data for Wetherill plot [a]					Dates (Ma)								Concordance [b]
Spot number	^{206}Pb (CPS)	^{204}Pb (CPS)	^{206}Pb/^{204}Pb	U (ppm)	Th/U	^{238}U/^{206}Pb	2 s	^{207}Pb/^{206}Pb	2 s	^{207}Pb/^{235}U	2 s	^{206}Pb/^{238}U	2 s	rho	^{207}Pb/^{206}Pb	2 s	2s sys	^{206}Pb/^{238}U	2 s	2s sys	^{207}Pb/^{235}U	2 s	2s sys	%
UG - 5	537000	b.d.	b.d	4330	0.01	34.03	0.53	0.0675	0.0011	0.2750	0.0055	0.0294	0.0005	0.78	849	36	39	187	3	4	247	4	6	76
UG - 7	684000	b.d.	b.d	8450	0.42	54.47	0.86	0.2174	0.0032	0.5514	0.0096	0.0184	0.0003	0.91	2959	24	25	117	2	3	446	6	10	26
UG - 8	946000	b.d.	b.d	11590	0.18	54.56	0.83	0.2219	0.0028	0.5621	0.0110	0.0183	0.0003	0.78	2992	20	22	117	2	3	453	7	10	26
UG - 9	892000	b.d.	b.d	10010	0.17	49.83	0.74	0.1605	0.0018	0.4450	0.0078	0.0201	0.0003	0.85	2459.7	20	21	128	2	3	374	5	8	34
UG - 10	596600	b.d.	b.d	8160	0.23	59.49	0.92	0.1503	0.0022	0.3496	0.0065	0.0168	0.0003	0.83	2344	25	27	108	2	2	304	5	7	35
UG - 12	879000	b.d.	b.d	3040	0.01	15.37	0.22	0.0585	0.00085	0.5266	0.0092	0.0651	0.0009	0.81	542	31	34	406	6	9	429	6	9	95
UG - 13	805000	b.d.	b.d	14850	0.19	77.76	1.27	0.1653	0.0022	0.2938	0.0053	0.0129	0.0002	0.91	2508	23	24	83	1	2	262	4	6	32
UG - 14	973000	b.d.	b.d	12570	0.04	54.23	0.94	0.1653	0.0023	0.4209	0.0079	0.0184	0.0003	0.92	2507	24	25	118	2	3	357	6	8	33
UG - 15	957000	b.d.	b.d	7500	0.02	33.40	0.52	0.0736	0.0012	0.3055	0.0060	0.0299	0.0005	0.80	1026	33	35	190	3	4	271	5	7	70
UG - 16	554400	b.d.	b.d	8210	0.07	65.75	0.91	0.2060	0.0027	0.4327	0.0075	0.0152	0.0002	0.80	2870	22	23	97	1	2	365	5	8	27
UG - 17	813000	b.d.	b.d	14850	0.07	78.19	1.28	0.1716	0.0023	0.3025	0.0057	0.0128	0.0002	0.87	2570	22	24	82	1	2	269	4	6	30
UG - 18	729000	b.d.	b.d	6510	0.03	40.55	0.64	0.1109	0.0016	0.3767	0.0080	0.0247	0.0004	0.74	1811	25	28	157	2	4	325	6	8	48
UG - 22	602200	b.d.	b.d	8170	0.05	59.31	0.91	0.1731	0.0028	0.4019	0.0074	0.0169	0.0003	0.84	2584	27	28	108	2	3	343	5	8	31
UG - 24	479000	b.d.	b.d	3040	0.12	30.61	0.46	0.0698	0.0014	0.3148	0.0074	0.0327	0.0005	0.64	911	43	45	207	3	5	278	6	8	75
UG - 26	1024000	b.d.	b.d	7840	0.02	31.88	0.61	0.0661	0.0012	0.2859	0.0061	0.0314	0.0006	0.90	803	37	40	199	4	5	255	5	6	78
UG - 27	470000	b.d.	b.d	11540	0.51	108.84	1.66	0.1941	0.0025	0.2453	0.0044	0.0092	0.0001	0.85	2771	23	25	59	1	2	223	4	5	26
UG - 29	506000	b.d.	b.d	2790	0.05	24.39	0.33	0.0675	0.0011	0.3811	0.0077	0.0410	0.0006	0.68	841	35	36	259	4	6	328	6	8	79
UG - 32	783300	b.d.	b.d	8755	0.14	52.14	0.76	0.2076	0.003	0.5478	0.0100	0.0192	0.0003	0.80	2882	23	25	122	2	3	443	7	10	28
UG - 33	564000	b.d.	b.d	7240	0.22	60.10	1.01	0.1420	0.0024	0.3246	0.0067	0.0166	0.0003	0.82	2243	28	31	106	2	3	285	5	7	37
UG - 34	621000	b.d.	b.d	4310	0.14	30.64	0.44	0.0739	0.0011	0.3320	0.0060	0.0326	0.0005	0.80	1030	30	32	207	3	5	291	5	7	71
UG - 35	658100	b.d.	b.d	4960	0.16	31.65	0.48	0.0725	0.0011	0.3157	0.0061	0.0316	0.0005	0.79	994	31	33	201	3	5	278	5	7	72

Uncertainties quoted without components related to systematic error unless otherwise stated. Total systematic uncertainties (s sys): ^{206}Pb/^{238}U = 1.8 %; ^{207}Pb/^{206}Pb = 0.5 (2s).

[a] Data not corrected for common Pb

[b] Concordance calculated as: (^{206}Pb-^{238}U date/^{207}Pb-^{235U} date)*100

Appendix L: Concordia diagram of the secondary zircon reference material

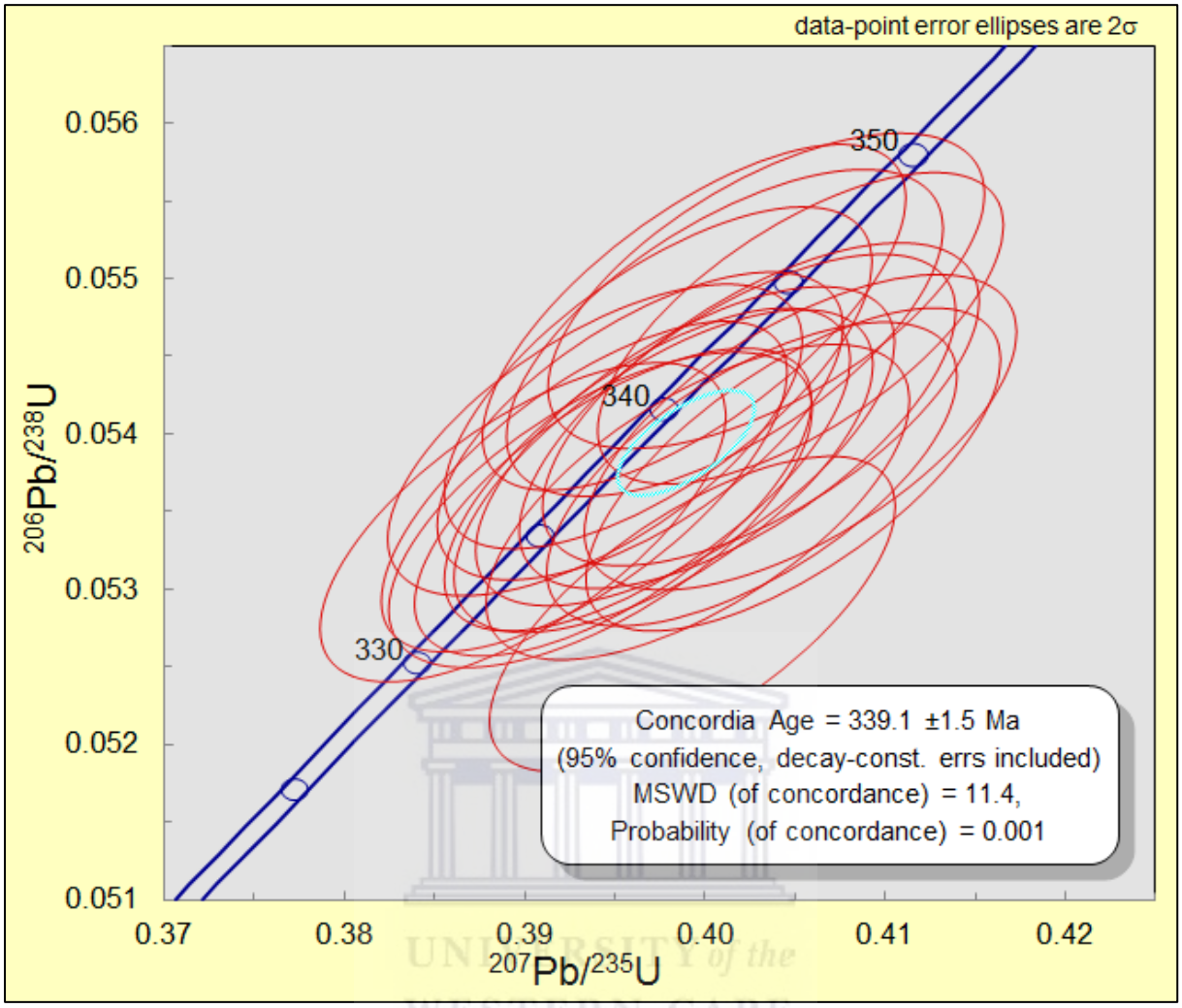

Fig. L1. (a) Concordia diagram of the secondary zircon reference material which was used to validate the data.

Appendix M: Raman spectroscopy figures

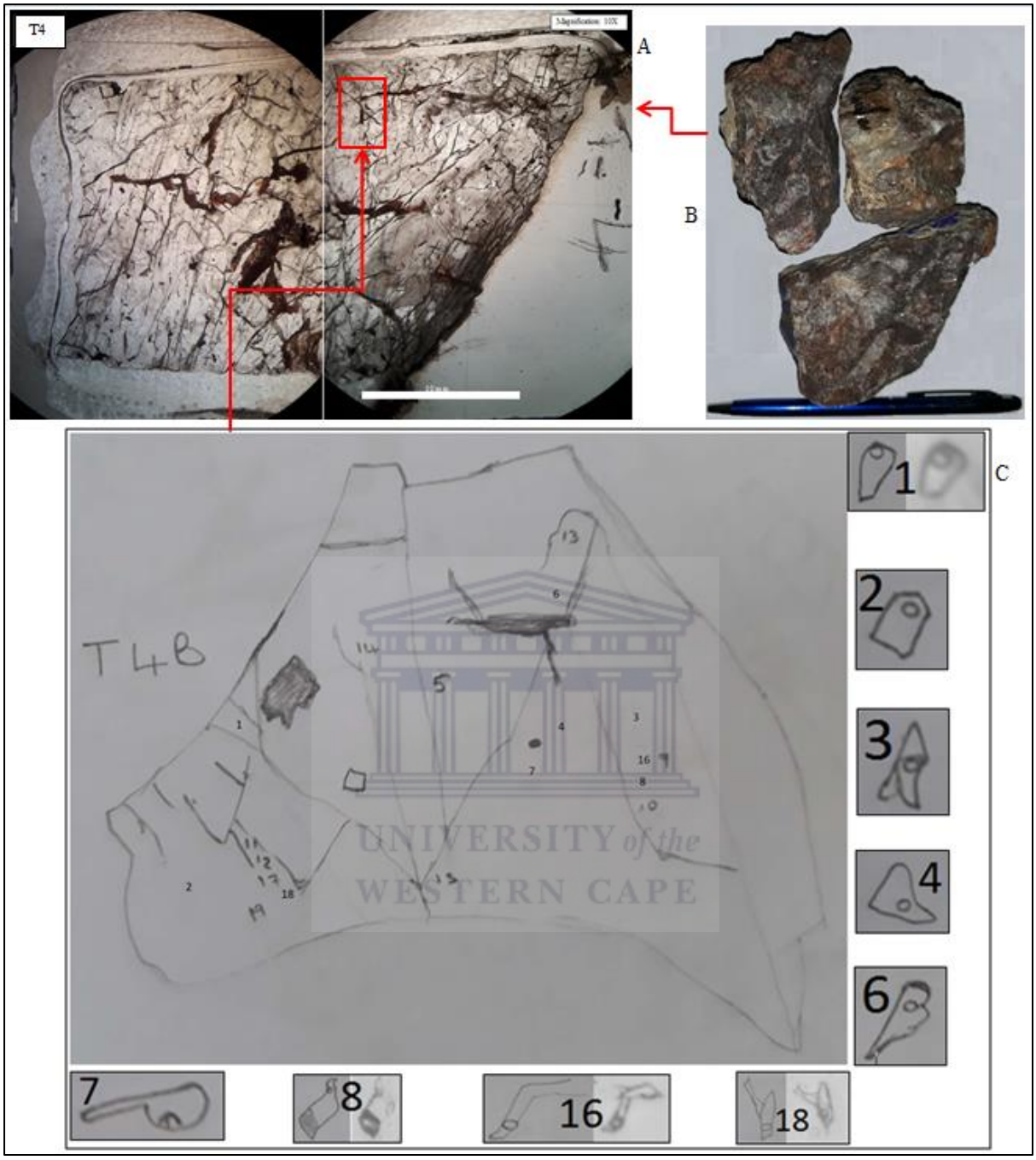

Fig. M1. Fluid inclusions analysed by Raman spectroscopy: A. Image of a double polished wafer indicating the locality chip T4B, B. Vein quartz samples from where the double polished wafers were cut, C. Sketch of a double polished vein quartz wafer chip (T4B) indicating positions of fluid inclusions; around it are photomicrographs and sketches of the fluid inclusions marked in the chip, four of which (1, 7, 8 & 18) were analysed by Raman spectroscopy.

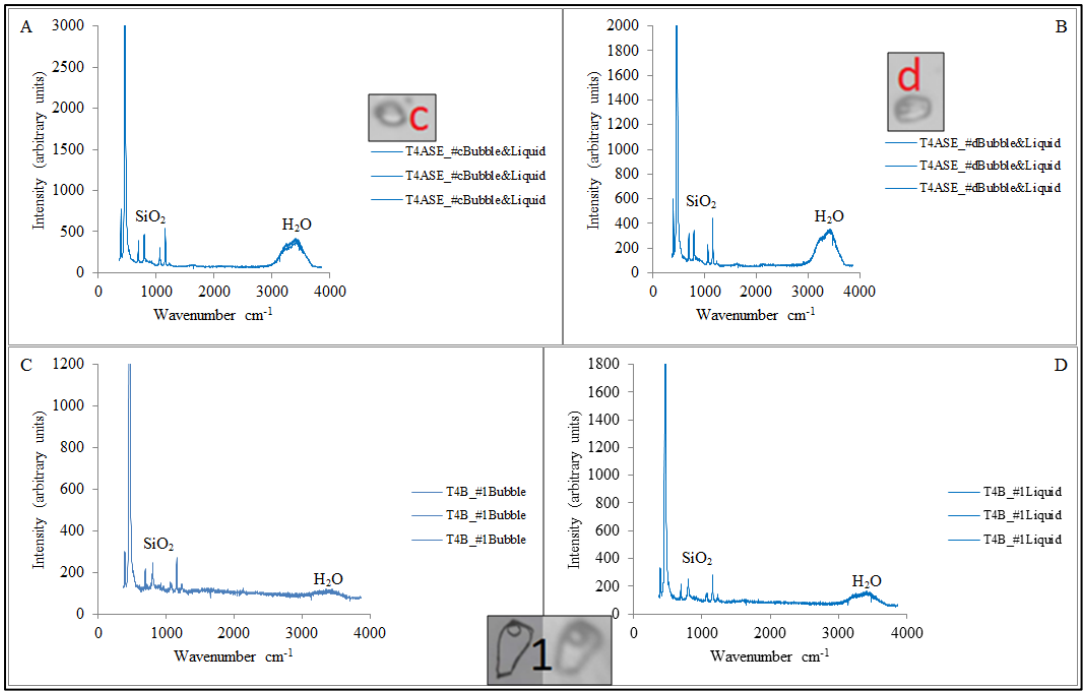

Fig. M2. Raman spectra for fluid inclusions c, d & 1 in chip T4A and T4B from trench 4. The inserts images are photomicrographs and sketches of the analysed fluid inclusions. A - C. Bubble and liquid spectra of inclusions c, d & 1 depicting the presence of H_2O.

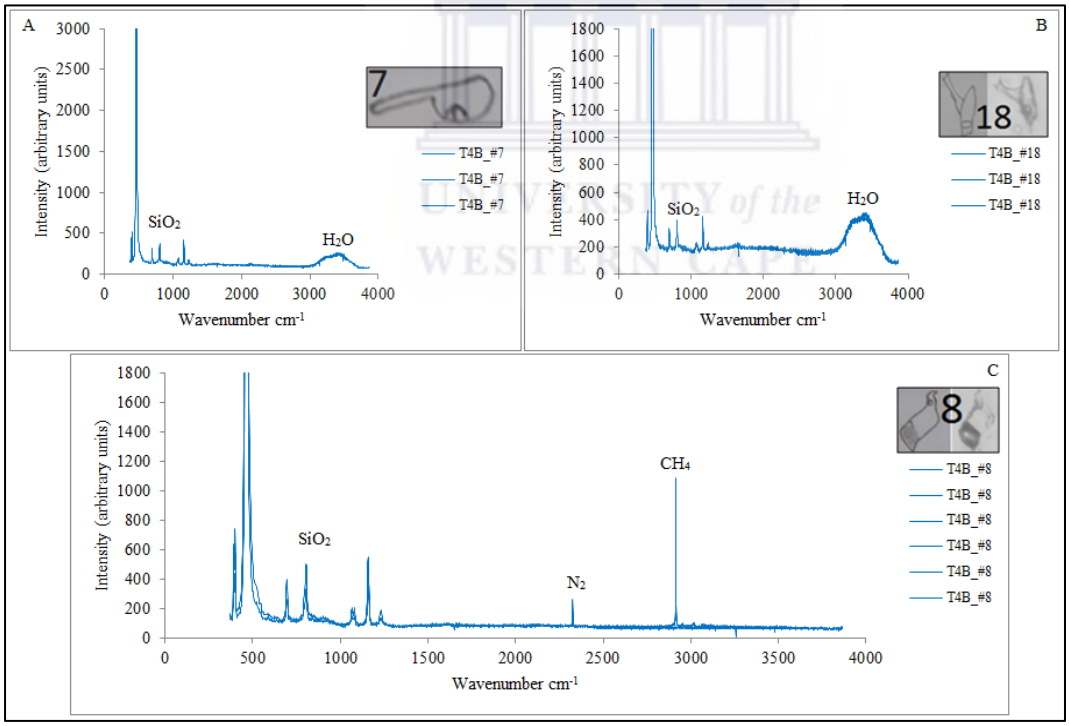

Fig. M3. Raman spectra for fluid inclusions 7, 18 and 8 in chip T4B from trench 4. The insert images are photomicrographs of the analysed fluid inclusions. A. and B. Spectra from inclusions 7 and 18 showing the presence of H_2O, C. Bubble spectrum showing the presence of CH_4 and N_2. Other peaks are as a result of the host rock matrix (quartz).

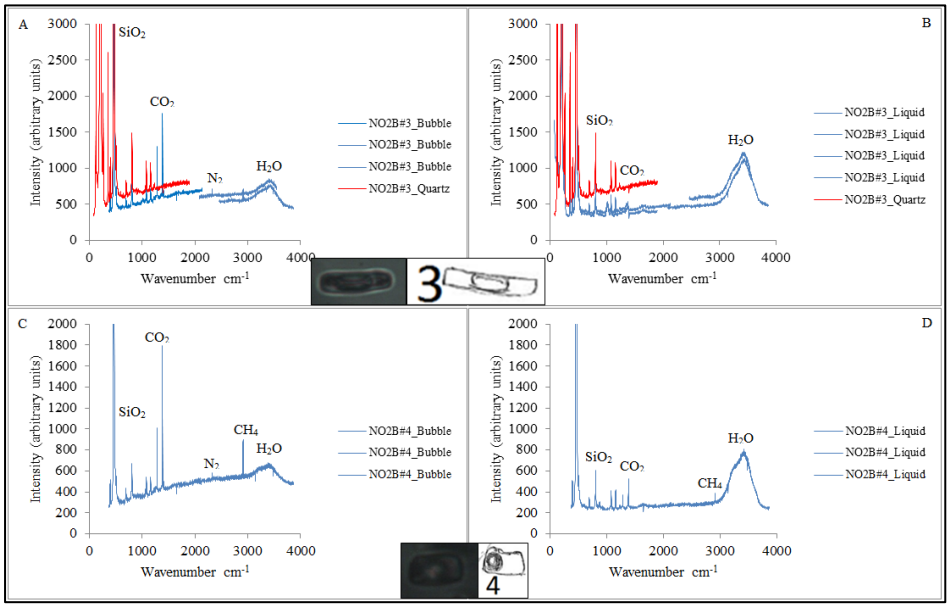

Fig. M4. Raman spectra for fluid inclusions 3 and 4 in chip NO2B from sampling point NO2. The insert images are photomicrographs of the analysed fluid inclusions. A. Spectra showing the presence of SiO_2, CO_2, N_2 and H_2O, B. Spectra showing the presence of H_2O, CO_2 and SiO_2, C. Spectrum showing the presence of CO_2, CH_4, N_2 and H_2O, D. Spectrum showing the presence of H_2O, CO_2 and CH_4. Red spectra in A and B are for quartz, the blue spectra in A and C are for bubbles, the blue spectra in B and D are for liquid.

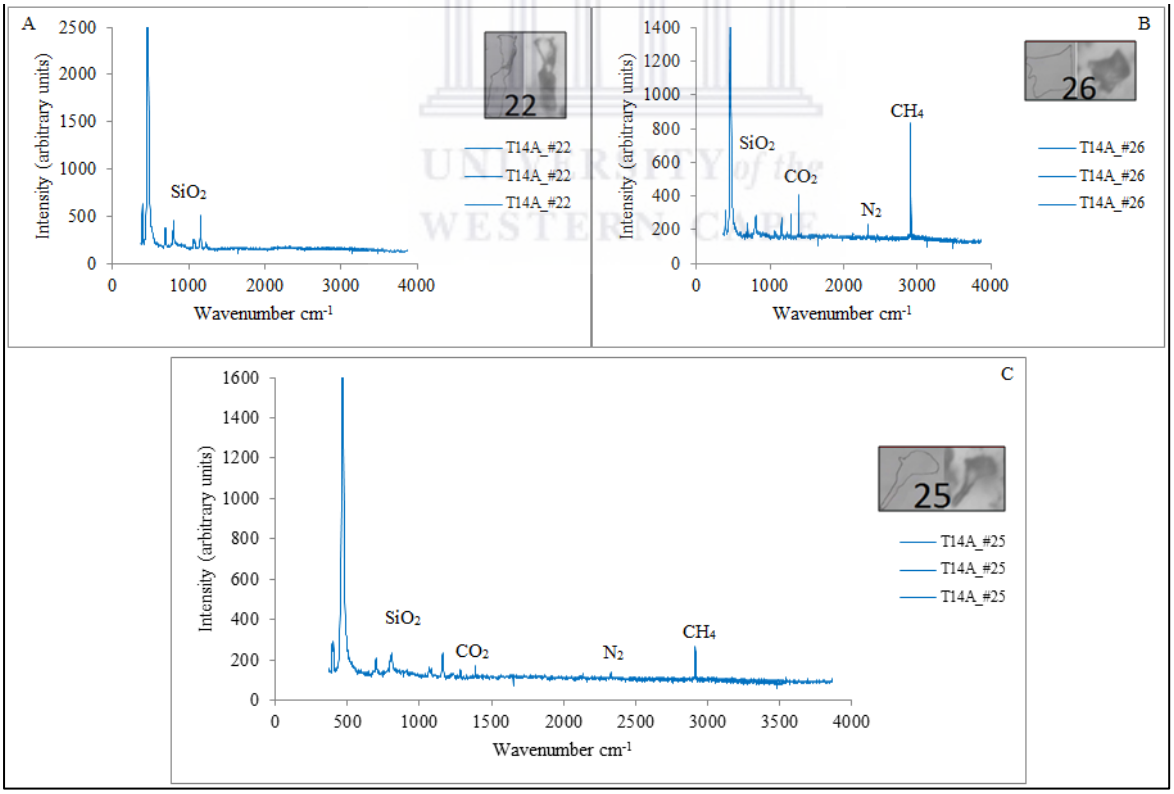

Fig. M5. Raman spectra for fluid inclusions 22, 25 and 26 in chip T14A from trench 14. The insert images are photomicrographs and sketches of the analysed fluid inclusions. A. Inclusion 22 gave no gas peaks, B. Spectrum showing the presence of CO_2, CH_4, and very minor N_2, C. Spectrum showing the presence of CO_2, CH_4, and weak N_2.

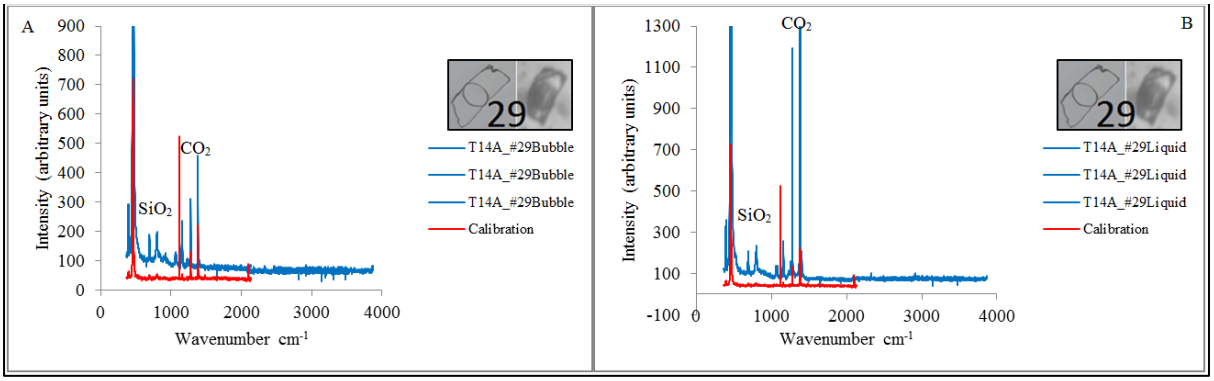

Fig. M6. Raman spectra for fluid inclusion 29 in chip T14A from trench 14. The insert images are photomicrographs and sketches of the analysed fluid inclusion. A. Bubble spectrum of inclusion 29 showing the presence of CO_2, B. Liquid spectrum of inclusion 29 showing the presence of CO_2. The red spectra are for calibration.

Appendix N: RB-Sr whole-rock dates of granitoids and pegmatites

Table N1: RB-Sr whole-rock dates of granitoids and pegmatites. Errors in dates and $(^{87}Sr/^{86}Sr)_I$ ratios reported at 95% confidence level (Steven, 1993)

Locality	Lithology	Age (Ma)	$(^{87}Sr/^{86}Sr)_I$	MSWD
Ohere Oos	Salem granitoid	542±11	0.7062±.0002	0.13
Ohere	Leucogranite	506±135	0.7107±.0214	1.4
Kohero Tin mine	Stanniferous pegmatite	492±11	0.7267±.0002	1.10
Sandamap Noord	Leucogranite phacolith (FG in this thesis)	512±19	0.7153±.0030	0.67
Sandamap Noord	Pegmatite (UG & GT in this thesis)	473±23	0.7267±.0072	0.05
Sandamap Noord	Stanniferous pegmatite (located roughly 3 km south of Sandamap shear zone)	468±14	0.7238±0028	3.17

Errors in dates and $(^{87}Sr/^{86}Sr)_I$ ratios reported at 95% confidence level

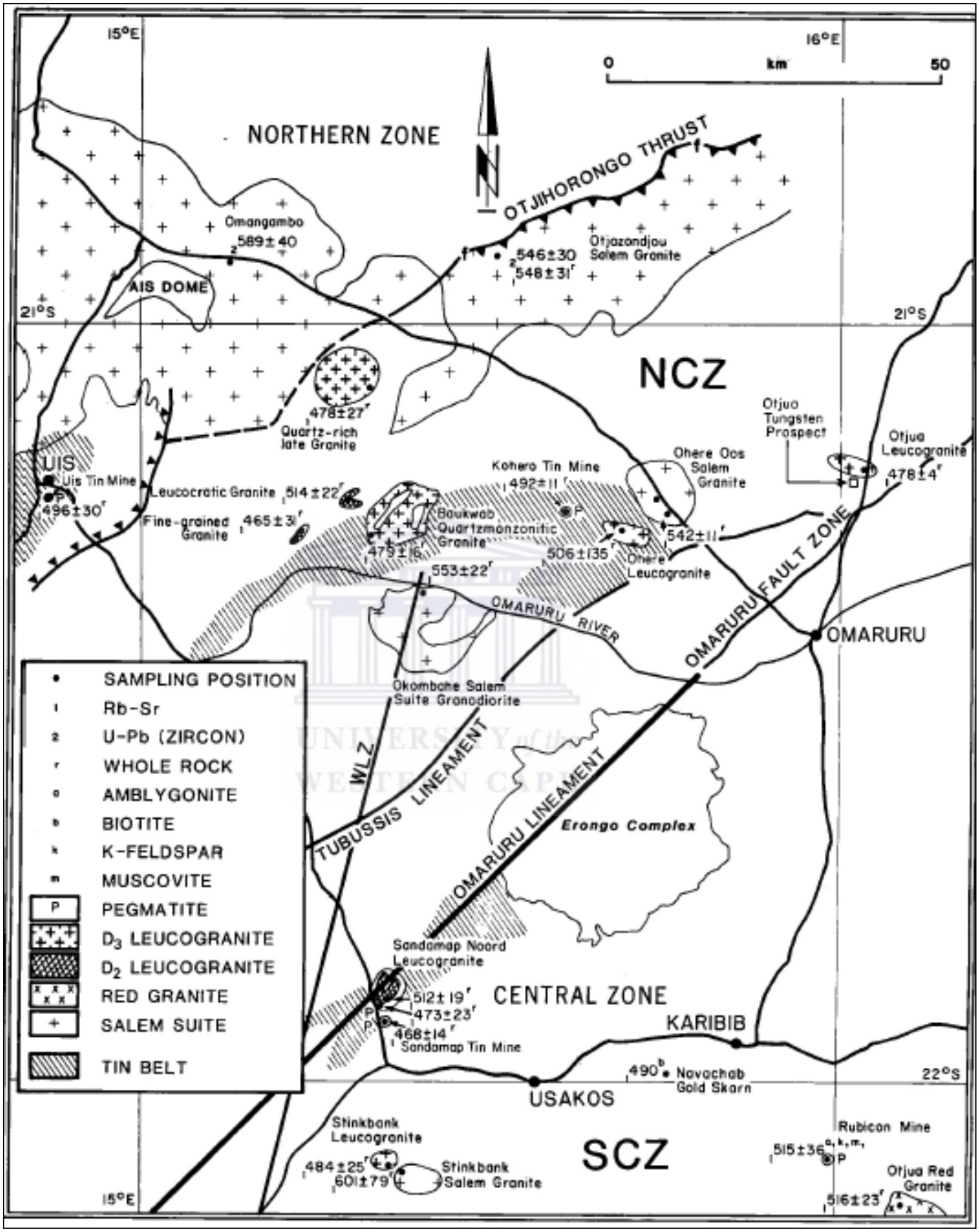

Fig. N1. Whole rock and mineral emplacement ages from central Namibia (After Steven, 1993).

Appendix O: Research Materials and methods

O.1 Fire assay

The fire assay procedure, as given in Sein *et al.* (2017), was used. Precious metals were separated and accumulated by using a lead collection procedure, where 40g of sample-flux mixtures in cupels were placed in the furnace heated to temperatures from 900 – 1000°C. The precious metals were then separated from the lead button by an absorption process (cupellation). A standard reference material with known contents of metals was used during the process together with the samples to be analyzed. This was done for the purpose of keeping control of the whole process and ensuring quality control and quality assurance (Sein *et al.*, 2017). After the cupellation process, prills containing precious metals and some platinum group elements (PGEs) were cooled and dissolution was done by heating for 10 minutes on the hot plate after adding 1 ml of nitric acid (HNO_3) allowing complete dissipation of nitrous fumes. This was followed by rinsing with water and 4 ml hydrochloric acid (HCl) and heating for another 10 minutes. Cooling followed and finally 1 ml lanthanum nitrate solution was added before analysis by ICP-OES.

O.2 Analytical procedure: XRD

A D8 Advance XRD instrument equipped with LYNXEYE detector, housed at the Geological Survey of Namibia, was used. Approximately 1g of each sample was pulverised and few drops of ethanol added for the sample to stick to the disc. The wet sample was placed on a silicon disc surface and left to dry. Once dried, the disc was placed on the sample tray inside the machine for analysis. Generator settings when the instrument is not running are: 20kV and 5 mA. Operating Voltages and current are 40 kV and 40 mA. Scan parameters are 5 to 55°, 1° beam divergence slit and a complete scan time is 41 minutes 41 seconds per batch of samples.

O.3 Analytical procedure: Fusion XRF

Pulverised samples were dried at 105°C and then heated at 950°C for the calculation of LOI (Loss on Ignition). An amount of 10g of each sample was mixed with 1g of Li Borate flux

(binder) and the mixture was then fused in platinum crucibles to form glass beads. Measurements on glass beads were then carried out by XRF against calibration curves created by a range of CRMs (Certified Reference Materials) made in the same way and the results reported as oxides. The flux used for the fusion is a Claisse Lithium Tetra- / Meta-Borate with a little Li Bromide acting as a releasing agent. The fusing process was done using a semi-automatic Claisse M4 fusion instrument. The XRF instrument used is a PAnalytical / Philips PW2400 fitted with a 3kW Rh-target end window X-Ray tube.

O.4 Analytical procedure: ICP-OES

The Spectro Arcos ICP-OES is equipped with charge-coupled device (CCD) detectors and side-on plasma interface (SPI) (radial view) which limits the matrix effects. The operating conditions were as follows: plasma power was 1400 watts (W), pump speed was 30 revolutions per minute (rpm), the coolant flow was 14 litres per minute (L/min), auxiliary flow was 2.1 litres per minute (L/min), and nebuliser cross-flow was 0.80 litres per minute (L/min).

In addition to the conditions stated above, the sample injection mode was by continuous nebulisation and the signal processing or line measurement was based on the peak height. Polynomial plotted background corrected the background. The aqueous standards solutions were prepared by dilution from stock individual standards of 1000 $mg.L^{-1}$. All standards contained 10% (v/v) HNO_3 for acidification and so the samples were matrix matched with the standards. Plots of emission intensity (cps) versus concentration were constructed using ICP-OES spectroscopy. A 7-point calibration on all the elements was plotted to determine the unknown.

O.5 Microthermometry and Raman spectroscopy

An optical petrographic microscope at the University of the Western Cape (UWC) was used to study and characterise fluid inclusions in doubly polished thick sections. The samples were studied under transmitted plane-polarized white light. The study was aimed at characterizing the inclusions in terms of abundance, phases, assemblages, morphology, sizes and relative inclusion volumes.

Microthermometry

A Linkam THMSG600 heating-freezing stage with a temperature range between −196°C and 600°C, housed at the Department of Geological Sciences, University of Cape Town (UCT) was used. The stage is connected to a TMS94 programmable thermal control unit, which allows controlled heating and cooling rates of between 0.1°C and 90°C per minute. The stage is mounted on an Olympus BX53 transmitted light microscope fitted with 10×, 50× and 100× long-working distance lenses. In addition, a 2× magnification changer enables maximum magnifications for small (5µm) inclusions.

Stage calibration was done using pure CO_2 inclusions in quartz (verified with Raman analyses) at the triple point of CO_2 (−56.6°C) and homogenization temperatures of synthetic H_2O inclusions in quartz for calibration up to 10°C. Low temperature phase transitions (<10 °C) are estimated to have a precision of 0.2°C, and homogenization measurements of H_2O inclusions have a precision of 5°C.

Raman Spectroscopy

Fluid inclusions in chips from the doubly polished wafers described were analysed using Raman spectroscopy at the University of the Witwatersrand in order to determine the qualitative content of the fluid inclusions. Raman spectra were acquired using the 514.5 nm line of a Lexel Model 95 SHG argon ion laser and a Horiba LabRAM HR Raman spectrometer coupled to an Olympus BX41 microscope. Data were acquired using LabSpec v5. Software at the Department of Physics, the University of the Witwatersrand. Analyses were done by focusing the argon ion laser beam onto the fluid inclusion using a 100× objective with 0.90 numerical aperture. The backscattered light was dispersed via a 600 lines/mm grating onto a liquid nitrogen cooled charge-coupled device (CCD) detector. The laser beam spot diameter is about 1 µm.

O.6 Principles behind Raman spectroscopy technique

Raman spectroscopy is the quantification of the photons emitted from inelastic scattering of light by matter in its solid, liquid, or gas state (Frezzotti *et al.*, 2012). With inelastic scattering the monochromatic light scattered by matter holds radiations with frequencies different from

that of the exciting light as opposed to Rayleigh or elastic scattering which happens when the transition starts and ends at the same vibrational energy level without loss of energy (Frezzotti *et al.*, 2012). The interaction of the exciting light with the vibrational modes in the sample produces losses and gains of energy in the incident beam, referred to as Stokes and anti−Stokes scattering, respectively (Burke, 2001), in other words a change to lower and higher frequencies in the scattered light (Frezzotti *et al.*, 2012). A Raman spectrum is a plot of the intensity of the scattering (in arbitrary units) versus the frequency of scattered light (i.e., Raman vibrational modes/ wave number) in frequency units (Frezzotti *et al.*, 2012; Burke, 2001). The peaks in the spectrum equate to the energies of the vibrational modes of the different molecules/ substances in the sample (Burke, 2001). The species contained in the fluid inclusions were identified with the aid of data on vibrational modes for different species given in Frezzotti *et al.* (2012) and Burke (2001).

O.7 Argon-argon dating, Sample preparation and analysis

A total of 50 samples (minerals separates), ranging in weight from 0.2 – 1 mg, enclosed in aluminum foil, were placed in a silica glass tube of 1 cm diameter. This was followed by vacuum sealing of the tube and 20 hours irradiation in position B2W (not cadmium-shielded) of the 20 MW SAFARI-1 nuclear reactor at Pelindaba, Pretoria, by NTP®, a subsidiary of the Nuclear Energy Corporation of South Africa (NECSA) which specializes in the production of isotopes intended for medical purposes.

After irradiation, samples were baked at a temperature of about 220℃ for 3 hours. The gas released from samples for analytical purposes was done by stepwise heating, using a defocused beam from a SPECTRON® continuous Nd-YAG 1064 nm laser, which has the capacity to produce up to 9W. Step-heating analyses were performed at the Department of Geology, University of Johannesburg. There were between 8 and 15 heating steps per grain, at a current between 9.5-12A, generating temperatures between 600˚C and 1300˚C, when fusion occurs. The gas that was extracted from each heating step was decontaminated using SAES APG10 getters, one at room temperature and the other at 400˚C ahead of introduction to the MAP 215-50 mass spectrometer for analysis. Blank measurements were dispersed in succession of every three or four analyses.

O.8 U-Pb dating Reasearch equipment

An ASI Resolution M-50-SE Excimer laser coupled to a Thermo Element 2 sector field single-cell inductively coupled plasma mass spectrometry (SF SC ICP-MS) at CAF (Stellenbosch University) was utilized for U-Pb isotope dating of zircons from intrusive bodies (foliated granite, non-foliated granite and dolerite dyke). The Map 215-50 Noble Gas Mass Spectrometer, equipped with a Nd-YAG laser housed at SPECTRUM (the Central Analytical Facility of the Faculty of Science, University of Johannesburg), was utilized for $^{40}Ar/^{39}Ar$ isotope dating of hydrothermal micas in vein quartz samples in order to date the age of the mineralizing event.

A super-panner (Fig.1) was used for heavy mineral separation. The super-panner has a 'V' shaped tray and the bottom of the tray is wider than the head. The tray was wetted with water and a sample (pulverized, +300 microns in this study) was placed on the tray at the head. When in operation the tray moves back and forth in a motion parallel to the length of the tray. This motion results in an 'end-knock' which 'throws' the heavier minerals upstream towards the head of the tray and the lighter minerals downstream towards the bottom of the tray. At the bottom of the tray the lighter minerals are sucked into a vacuum suction flask and discarded if no longer required.

Fig. O.1. Super-panner, which was used for heavy mineral separation of zircon grains, housed at the Central Analytical Facility (CAF), Stellenbosch University.

A Frantz Isodynamic Magnetic Separator Model L-1 was used to further separate the most magnetic material from non-magnetic material so that the volume of sample to be separated by heavy liquid separation was reduced. With this equipment, induced magnetic fields at different electric current settings interact with mineral grains as they pass through the magnetic field at a set slope and tilt to separate the sample according to the magnetic susceptibility of the mineral grains (Fig. 2). The target mineral, zircon, has a very low magnetic susceptibility. According to Chisholm et al. (2014), the Frantz magnetic separator is the only piece of equipment in a mineral separation laboratory that allows for refined mechanical discrimination of high quality zircons for isotopic analysis.

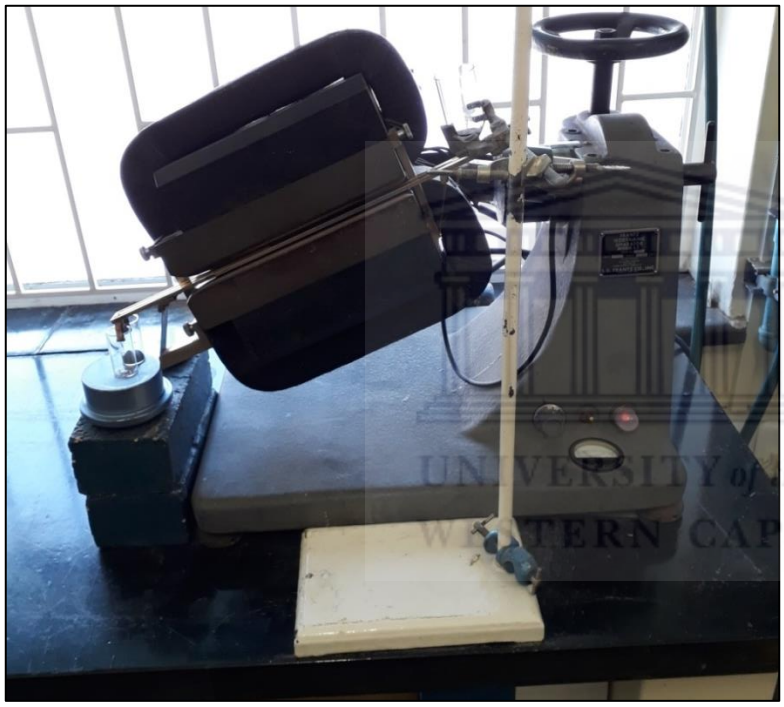

Fig. O.2. The Frantz Magnetic Separator housed at the Central Analytical Facility (CAF), Stellenbosch University.

O.9 U-Pb dating, Sample preparation and analysis

Five (5) kg of each the three plutonic rock samples (foliated granite, non-foliated granite and dolerite dyke) were crushed and sieved at the Geological Survey of Namibia by means. Further sample preparation (zircon separation) was carried out at CAF, Stellenbosch University. Samples collected in the 300µm sieve were used for zircon separation. All samples were washed in water to remove excess dust followed by panning on the superpanner. The collected heavy minerals were separated by Heavy Liquids using

Tetrabromoethane (TBE). Samples were then dried overnight in an oven followed by the separation of magnetic from non-magnetic minerals using a hand magnet and thereafter a Frantz Isodynamic Magnetic Separator. The separation process was finalized by zircon picking using a stereoscopic microscope. This was followed by mounting of the zircons in 25 mm epoxy resin discs which were polished to expose the interior of the mineral grains. All zircons were CL-imaged prior to laser ablation (LA) U-Pb work using a Zeiss Merlin scanning electron microscope (SEM) equipped with a cathodoluminescent (CL) detector at the Central Analytical Facilities (CAF), Stellenbosch University.

Laser ablation U-Pb geochronological analyses were carried out at CAF, Stellenbosch University, by utilizing a 193 nm wavelength ASI Resolution laser ablation system coupled with a Thermo Scientific Element 2 single collector magnetic sector field inductively coupled plasma mass spectrometer (SC-SF-ICP-MS).

At the beginning of each analytical session, the mass spectrometer was adjusted by ablating a line scan on the standard reference glass material (NIST620 glass). The lenses, gas flows, and torch position were adjusted while measuring ^{206}Pb, ^{238}U and $^{238}U^{16}O$ to yield steady signals and high intensity on ^{206}Pb and ^{238}U, as well as low oxide rates ($^{238}U^{16}O/^{238}U < 0.3\%$). The ablated material from zircon samples was transported into the ICP-MS from the laser cell using a continuous flow of He gas at a flow rate of 0.35 l/min. Signals of mass-to charge ratio (m/z) 202, 204, 206, 207, 208, 232, 235 and 238 were obtained in electrostatic scan mode. The ^{202}Hg signal was collected for correcting the isobaric interference of ^{204}Hg on ^{204}Pb. The isotopic analysis was computer controlled meaning the functions of the laser and ICP-MS software packages were coordinated to permit automated execution. A single analytical session can consist of up to analytical 500 measurements.

Any common Pb on blank sample surfaces emanating from the sample preparation stage was eliminated by pre-ablating each spot before the gas blank measurement and this was done by firing two laser shots. Zircon GJ-1 was used as a matrix-matched primary reference material for the purpose of correcting mass discrimination on measured isotope ratios in unknown samples and correction for instrumental drift at the same time. Normalization values are based on ratios determined by Isotope Dilution Thermal ionization mass spectrometry (ID-TIMS) reported in Horstwood et al. (2016). Each analytical session, which consisted of 13 unknowns, the zircon reference materials GJ-1 (Jackson et al., 2004) and Plešovice (Sláma et

al., 2008) were measured. Plešovice zircon was through analysis utilized as a secondary reference material to authenticate the results and determine the quality of the data for each analytical session. The laser sampling protocol utilized a 26 µm static spot and a fluence of 2.0 J/cm^2. A combination of the software package Iolite v.3.5 (Paton et al., 2011), with Vizual Age (Petrus and Kamber, 2012) was used for data reduction.

A combination of the software package Iolite v.3.5 (Paton et al., 2011), with Vizual Age (Petrus and Kamber, 2012) was used for data reduction. An exponential model of laser-induced elemental fractionation (LIEF), attained by combining the isotopic ratios of the primary reference material from the entire session, was used for correction of time-dependent down-hole elemental fractionation in the unknowns, under the assumption of the same fractionation behaviour in the reference material and the unknowns. After correction for drift, LIEF and normalization to the main reference material (performed in Iolite), uncertainty components for systematic errors were propagated by quadratic addition in line with the recommendations of Horstwood et al. (2016).

The value of the total decay constant of ^{40}K used is 5.554 ± 0.014 × 10^{-10} yr^{-1} (Kossert and Günther, 2004; Renne et al., 2010). The McClure Mountain hornblende (MMhb, with an age of 523.1 ± 1 Ma, Renne et al., 1998) was utilized as a fluence monitor. Multigrain aliquots of MMhb were placed at the top, middle and bottom of the irradiation sample pile, and generated J-values fitted to a curve. Despite the fact that MMhb has been described to give a variety of values (Baksi et al., 1996; Renne et al., 1998), the analyzing lab (University of Johannesburg) found that this monitor yields consistent J-values and in particular Ca/K and Cl/K factors. A J value of 0.008714 ± 0.000024 is reported. The J value is a dimensionless irradiation-related parameter that is determined by using standards of known age to monitor the neutron flux in the reactor. The background decay and reactor-induced correction factors are Ca/K = 1.9557 ± 0.0375 and Cl/K = 0.1236 ± 0.0030. Run regressions, corrections and age calculations were achieved using in-house developed software, which encompasses full error propagation (incorporating uncertainties of the decay constant and J-values) utilizing Monte Carlo simulations.

During irradiation, neutrons may react with calcium (Ca), argon (Ar) and chlorine (Cl) in the sample other than ^{39}K to produce interfering isotopes of argon (^{36}Ar, ^{37}Ar, ^{38}Ar, ^{39}Ar and ^{40}Ar) and these have to be corrected for and the resulting errors have to be accurately monitored. Mass fractionation correction was done using the exponential law (Ranen and

Jacobsen, 2008; Gopalan, 2002; Young et al., 2002). The exponential fractionation factor = -0.298. The ratio for $^{40}Ar/^{36}Ar$ used for atmospheric Ar contamination correction is 298.56 ± 0.31 (Lee et al., 2006). Uncertainties in the data are expressed at the 95% level.

Appendix P: Variances between the uranium concentration in zircons and the concordance %

Table P1 Variances between the uranium concentration in zircons and the concordance % in the foliated granite (FG).

Sample ID	Concordance [b] %	U (ppm)	Dates (Ma)			Ablated zircon zone	Image showing ablation spots
			$^{207}Pb/^{206}Pb$	$^{206}Pb/^{238}U$	$^{207}Pb/^{235}U$		
FG-37	81	3600	719	211	261	Outer	
FG-22	78	3915	894	283	360	Outer	
FG-9	23	13420	3268	124	543	Outer	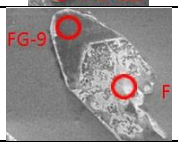

Concordance calculated as: ($^{206}Pb^{238}U$ date/$^{207}Pb^{235}U$ date)*100

Table P2 Variances between the uranium concentration in zircons and the concordance % in the non-foliated granite (GT) which hosts a mineralized xenolith at trench 9.

Sample ID	Concordance [b] %	U (ppm)	Dates (Ma)			Ablated zircon zone	Image showing ablation spots
			$^{207}Pb/^{206}Pb$	$^{206}Pb/^{238}U$	$^{207}Pb/^{235}U$		
GT-12	93	1212	678	480	516	Inner	
GT-4	71	1145	1599	619	876	Outer	
GT-19	14	18470	3925	64	452	Outer	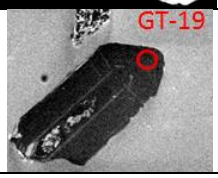

Concordance calculated as: ($^{206}Pb^{238}U$ date/$^{207}Pb^{235}U$ date)*100

Table P3 Variances between the uranium concentration in zircons and the concordance % in the non-foliated granite (UG).

Sample ID	Concordance [b] %	U (ppm)	Dates (Ma)			Ablated zircon zone	Image showing ablation spots
			$^{207}Pb/^{206}Pb$	$^{206}Pb/^{238}U$	$^{207}Pb/^{235}U$		
UG-12	95	3040	542	406	429	Outer	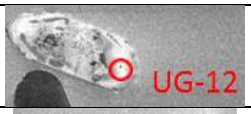
UG-29	79	2790	841	259	328	Outer	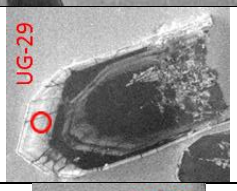
UG-27	26	11540	2771	59	223	Outer	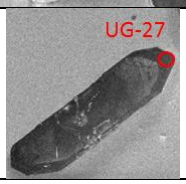

Concordance calculated as: ($^{206}Pb^{238}U$ date/$^{207}Pb^{235}U$ date)*100